Imperial College London

Permeation of High Pressure CO_2 in Semicrystalline Polymers

Tianyi Hu

July 2021

Supervisor: Dr. Christopher J. Tighe

Department of Chemical Engineering

Imperial College London

Submitted in fulfilment of the requirements for the degree of
Doctor of Philosophy in Chemical Engineering of Imperial College London
and the Diploma of Imperial College London

Abstract

With climate change becoming a major global concern, carbon capture and storage (CCS) has been the subject of intense research activity around the world. Although the benefits of CCS have been well recognised for decades, extensive industrial applications have not been realised. Particularly, there is a gap in research on the handling of high pressure CO_2, despite the abundant work dealing with lower pressure CO_2. This thesis focuses on the permeation process of CO_2 through semicrystalline polymeric materials under high pressures, to gain a better understanding on the diffusion and sorption mechanisms in the CO_2-polymer systems. The work presented in this thesis provides fundamental data, which could be used to guide the selection of suitable polymeric seals and liners in CCS applications, and may also be applied to other permeation-related processes involving CO_2-polymer systems under high pressures.

This thesis develops new experimental and modelling techniques to investigate the permeation behaviour of CO_2 through semicrstalline polymers under high pressures. (i) An experimental setup for permeation measurements was designed and constructed. (ii) Continuous permeation experiments of CO_2 in two commonly used semicrystalline polymers, polytetrafluoroethylene (PTFE) and high density polyethelene (HDPE), were carried out at various temperatures ranging from 28 to 50 °C and pressures up to 600 bar. (iii) The experimental data was fitted to a diffusion model, which incorporated the free volume theory to describe the concentration-dependence of the diffusivity. The model was first nondimensionalised, and then simplified using assumptions, which were subsequently shown to be valid. A simple graphical method, which requires no numerical equation solvers, was proposed for model validation and parameter estimation. The obtained results were in excellent agreement with those obtained with the numerical solver. (iv) The effect of pressure on diffusion was characterised from the near-instantaneous flux drops, which were observed when the pressure was increased following steady states of permeation. (v) The solubilities derived from the permeation measurements were fitted to the Sanchez-Lacombe equation of state, and excellent fits were obtained between the two. On the basis of the experimental and modelling results, transport properties and free-volume parameters were successfully estimated; these were compared with data found in the literature under similar conditions.

Declaration of Originality

I hereby certify that the work presented in this thesis is the result of my own investigations during the PhD project undertaken at the Department of Chemical Engineering at Imperial College London between November 2017 and July 2021. All else is referenced and properly acknowledged.

Tianyi Hu

July 2021

Copyright Declaration

The copyright of this thesis rests with the author. Unless otherwise indicated, its contents are licensed under a Creative Commons Attribution-Non Commercial 4.0 International Licence (CC BY-NC). Under this licence, you may copy and redistribute the material in any medium or format. You may also create and distribute modified versions of the work. This is on the condition that: you credit the author and do not use it, or any derivative works, for a commercial purpose. When reusing or sharing this work, ensure you make the licence terms clear to others by naming the licence and linking to the licence text. Where a work has been adapted, you should indicate that the work has been changed and describe those changes. Please seek permission from the copyright holder for uses of this work that are not included in this licence or permitted under UK Copyright Law.

There is only one heroism in the world: it is to see the world as it is, and to love it.

— Romain Rolland

Acknowledgements

I would like to thank my supervisor Dr. Chris Tighe for his supervision and assistances throughout my time at Imperial College London. As a diffident person who has been used to seeing herself as a nobody among many intelligent people, I have received praise from Chris during the past four years more than the sum of what I had received from all others over the 22 years in my life before. No matter whether the praise truly reflects my academic capability, it to a large extent encouraged me to take on the PhD project from scratch and challenge myself on facing difficulties during my research. Without the guidance and help from Chris, I would not have been able to accomplish the project. Most importantly, in my future career, there would always be a voice in my head reminding me that I was once trusted by someone and I will not let him down.

I would like to thank the Department of Chemical Engineering at Imperial College London for offering me a Departmental PhD scholarship. I would also like to thank Prof. Serafim Kalliadasis and Dr. Vijesh Bhute for offering me a GTA position for Mathematics 1 for three years. It has been a rewarding experience for me to interact with the students and even learn from them. I would like to thank my dear colleagues in the group and those kind staff members who showed me positive attitudes towards research and life. They helped me become a responsible and caring chemical engineer. A non-exhaustive list of these people includes: Mario Almeida, Janet Skitt, Parth Shah, Nathan Allcock, Artur Andrade, Sirong He, Tony Meredith, Richard Wallington, Jonathon Henton, Samuel Jones, Chin Lang, Patricia Carry, Susi Underwood, Anusha Sri-Pathmanathan, Keith Walker, Severine Toson, and Pim Amrit.

I would like to thank my family for offering me a warm home, a place where I can always go back, wherever I leave for. In the coming future, I hope I will spend more time with you. Last but not the least, I would like to thank me for working hard and for being myself.

Contents

Abstract **i**

Acknowledgements **iv**

List of Figures **xi**

List of Tables **xv**

Nomenclature **xvii**

1 Introduction **1**

1.1 Climate Change and CCS 1

1.2 Permeation-Related Processes in CCS 3

1.2.1 Polymeric Membranes for CO_2 Separation 4

1.2.2 Pipeline Corrosion and Polymeric Barriers 5

1.2.3 Leakage and Polymeric Seals 6

1.3 Project Motivations and Scientific Significance 9

1.4 Objectives and Scope 10

1.5 Structure of the Thesis 11

2 Literature Review **12**

2.1 Introduction 12

2.2 Solution-Diffusion *vs.* Pore-Flow 12

2.3 Transport Properties 14

2.3.1 Permeability 14

2.3.2 Diffusivity 15

2.3.3 Solubility 17

2.4 Free Volume Theory 20

2.4.1 Free Volume in Glassy and Rubbery Polymers 20

2.4.2 Free Volume Models 21

2.5 Equations of State for Penetrant-Polymer Systems 30

2.5.1 Equations of State 30

2.5.2 Sanchez-Lacombe EOS 32

2.6 Factors Affecting the Transport Properties 33

2.6.1 Effects of Temperature 33

2.6.2 Effects of Pressure 35

2.6.3 Effects of Crystallinity 36

2.7 Experimental Techniques 38

2.7.1 Sorption-Desorption 38

2.7.2 Permeation 40

2.8 Concluding Remarks 41

3 Experimental **43**

3.1 Introduction . . . 43

3.2 Materials . . . 43

3.2.1 Gas Specifications . . . 43

3.2.2 Polymer Characterisation . . . 44

3.3 Experimental Design . . . 47

3.3.1 Permeation Setup . . . 47

3.3.2 Safety Aspects . . . 50

3.3.3 Apparatus . . . 52

3.4 Experimental Procedure . . . 56

3.5 Experimental Methodology . . . 59

3.6 Systematic and Random Errors . . . 60

3.7 Repeatability . . . 62

4 Transient Permeation Following a Single Pressure Step **64**

4.1 Introduction . . . 64

4.1.1 Background . . . 64

4.1.2 Aims . . . 66

4.2 Model Development . . . 67

4.2.1 Constant Diffusivity . . . 67

4.2.2 Free Volume Model . . . 68

4.2.3 Nondimensionalised Model . . . 71

4.3 Full Model *vs.* Simplified Model . . . 73

4.3.1 Dimensionless Diffusivity D' . . . 74

4.3.2 Dimensionless Flux F' . . . 75

4.4 Early Approximation Method . . . 76

4.5 Procedure for Graphical Analysis . . . 82

4.6 Transient Flux Measurements . . . 83

4.7 Analysis of Steady-State Flux . . . 94

4.7.1 Derivation for $U/(WV')$ . . . 94

4.7.2 Estimation of Parameter Values . . . 97

4.7.3 Discussion on the Estimated Parameters . . . 101

4.8 Concluding Remarks . . . 103

5 Transient Permeation Following Successive Pressure Steps 105

5.1 Introduction . . . 105

5.1.1 Background . . . 105

5.1.2 Aims . . . 106

5.2 Stepwise Model Development . . . 107

5.2.1 Diffusion Equations . . . 107

5.2.2 Permeation Flux . . . 109

5.3 Constants $\tilde{a}$, $\tilde{b}$ and $\tilde{c}$ . . . 110

5.4 Estimation of $D_i'(X=0)$ . . . 111

5.5 Measurements of Steady-State Flux for Step i . . . 112

5.6 Determination of $\tilde{a}$, $\tilde{b}$ and $\tilde{c}$ . . . 117

5.7 Estimations of Free-Volume Parameters . . . 118

5.7.1 Estimating A_d . . . 118

5.7.2 Estimating β_p . . . 121

5.7.3 Estimating B_d . . . 124

5.8 Estimation of W_i, $U_i/(W_iV')$ and $D_i'(X=0)$ . . . 125

5.9 Comparison of Measured *vs.* Modelled Fluxes . . . 130

5.10 Concluding Remarks . . . 132

6 Solubility Analysis **133**

6.1 Introduction . . . 133

6.2 Theoretical . . . 134

6.2.1 Equilibrium Solubility . . . 134

6.2.2 Sanchez-Lacombe (SL) EOS . . . 134

6.3 Results and Discussion . . . 136

6.3.1 Solubility Measurements . . . 136

6.3.2 Modelling Solubility Using the SL EOS . . . 145

6.4 Concluding Remarks . . . 157

7 Conclusions **159**

7.1 Summary . . . 160

7.2 Outlook . . . 162

Appendices **165**

A Sorption Experiment **166**

A.1 Process Description 166

A.2 Procedure 169

B gPROMS Modelling **171**

C Flux Approximation Plots **174**

C.1 Simplified Model 174

C.2 Full Model with $W = 5$ 177

D Experimental Runs Explained **180**

E ASPEN Modelling of Solubility **182**

F Drawings of Permeation Cell **185**

G Access to the Data **188**

Bibliography **189**

List of Figures

1.1 Schematic diagram showing the three steps of the CCS chain, and their respective operating conditions presented on the CO_2 phase diagram retrived from [7]. The diagrams were plotted using data and information collected from [6, 8–11]. The rectangle region with blue dash boundaries on the CO_2 phase diagram refers to the experimental conditions in this work. 2

1.2 Various processes involved in the three steps of CCS. The highlighted processes are those related to permeation of CO_2 in polymers. 4

1.3 Schematic diagram of the semicrystalline morphology, showing the amorphous regions and the crystallites. 6

1.4 Solubility parameters and chemical resistance of various semicrystalline polymers. Data for solubility parameter at room temperature: PTFE [60, 61], HDPE (high density polyethelene) [62, 63], EPDM [64, 65], PVDF (polyvinylidene difluoride) [66], PP (Polypropylene) [67], and liquid CO_2 [68]. Information on chemical resistance at 20 °C and 60 °C: PTFE, EPDM, PVDF, and PP [69]; HDPE [70, 71]. 7

2.1 Schematic representation of permeation through a polymeric membrane according to solution-diffusion transport model (L denotes the membrane thickness). . 13

2.2 Plot of Q_t *vs.* t, showing the "time lag" of a cumulative permeation curve approching steady state. 15

2.3 Isotherm plots of sorbed concentration *vs.* pressure for the five typical sorption modes (diagram reprodcued from [79]). 17

2.4 The specific volume of a polymer as a function of temperature, with free volume and occupied volume shown in the graph. 21

3.1 (a) PTFE sample; (b) HDPE sample. 44

3.2 DSC curves of the samples. 45

3.3 Process flow diagram for permeation experiments (1 of 2). 48

3.4 (a) ISCO 260D pump (P-1); (b) ISCO 65D pump (P-2). 52

3.5 Permeation cell (PC): (1) circlip; (2) cap; (3) sleeve; (4) top plug; (5) dowel; (6) dip tube; (7) bottom plug. 53

3.6 The infrared (IR) gas analyser (LI-COR LI-850) gas analyser used in this work. 54

3.7 (a) Mass flow controller (MKS Instruments); (b) pressure transmitter (WIKA); (c) Thermocouple (TC Ltd). 56

3.8 Breakthrough curves of CO_2 flux against time, obtained from repeating runs of CO_2 through PTFE and HDPE. 62

4.1 Comparisons of the breakthrough curves of CO_2 flux against time, obtained from the permeation experiments, by applying the time-lag method with a constant diffusivity, or by using the free volume model with a thermodynamic diffusivity, for the two polymers. 65

4.2 Plots of flux and pressure against time in a successive permeation experiment for PTFE and HDPE. 65

4.3 Dimensionless diffusivity D' as a function of the dimensionless time τ, and the dimensionless distance X, with $D'(X = 0) = 1.5$, which was used for illustration. For each value of τ, the upper curve is the one obtained using the full nondimensionalised model, Eq. (4.30), with $W = 5$; and the lower curve is the one obtained using the simplified nondimenisionalised model, Eq. (4.38). 74

4.4 Plot of the normalised dimensionless flux, as a function of the dimensionless time τ. For each value of $D'(X = 0)$, the upper curve is the one obtained using the full nondimensionalised model, Eq. (4.30) and Eq. (4.36), with $W = 5$; and the lower curve is the one obtained using the simplified nondimensionalised model, Eq. (4.38) and Eq. (4.36). 76

4.5 Plot of $\ln\left[\tau^{1/2}F'/F'(\tau = \infty)\right]$ against $1/\tau$ for the early breakthrough obtained from the full nondimensionalised model, Eq. (4.30) and Eq. (4.36), with $W = 5$ and $D'(X = 0) = 1.5$. 78

4.6 Plot of $D'(X = 0)$ *vs.* $2c - \ln|k|$. For the simplified model: $D'(X = 0) = 11.5(2c - \ln|k|)^2 - 34.0(2c - \ln|k|) + 26.0$. For the full model with $W = 5$: $D'(X = 0) = 9.8(2c - \ln|k|)^2 - 28.5(2c - \ln|k|) + 21.5$. 81

4.7 Plot of μ *vs.* $D'(X = 0)$. For the simplified model: $\mu = 8.0 \times 10^{-4}[D'(X = 0)]^2 - 1.9 \times 10^{-2}D'(X = 0) + 2.7 \times 10^{-1}$. For the full model with $W = 5$: $\mu = 2.2 \times 10^{-4}[D'(X = 0)]^2 - 2.1 \times 10^{-2}D'(X = 0) + 2.7 \times 10^{-1}$. 81

4.8 A diagram showing the procedure for estimating the values of transport properties, which can characterise a permeation process. 82

4.9 Early approximation plots and fitting of modelling results to experimental data for the runs. 85

4.10 Plot of Ω_s (Ω_W) *vs.* $2c - \ln|k|$. For the simplified model: $\Omega_s = 1.38(2c - \ln|k|)^2 - 6.44(2c - \ln|k|) + 7.83$. For the full model with $W = 5$: $\Omega_W = 1.24(2c - \ln|k|)^2 - 5.94(2c - \ln|k|) + 7.41$. 95

4.11 Plot of $(-\partial D'/\partial X)_{X=1,\tau=\infty}$ *vs.* $D'(X=0)$. For the simplified model: $(-\partial D'/\partial X)_{X=1,\tau=\infty} = D'(X=0) - 1$. For the full model with $W = 5$: $(-\partial D'/\partial X)_{X=1,\tau=\infty} = 0.14[D'(X=0)]^2 + 0.77[D'(X=0)] - 0.92$. 96

5.1 Plots of flux and pressure against time in a successive permeation experiment for PTFE and HDPE. 106

5.2 Comparison of the modelled $D_{T,i}(T, p_i, 0)$ by optimisation (dashed) and the experimentally obtained $D_{T,i}(T, p_i, 0)$ (symbols) for the eight runs. 117

5.3 Comparison of the experimental flux curves and the modelled flux curves, with three runs as examples. 131

6.1 Pressure dependences of P_i, $D_{T,i}(X=0)$ and $C_i(X=0)$ for the eight runs, with uncertainties shown by the error bars on the plots. Linear fits for the data points of $C_i(X=0)$ are shown, with slopes presented in Table 6.1. 137

6.2 Comparison of the experimental solubility and the modelled solubility with SL EOS for PTFE and HDPE. 147

6.3 Flow diagram showing the procedure for estimating V_i', U_i and γ_i. 150

List of Tables

2.1 Typical sorption modes, with their respective expressions, dominant interactions, and examples. 18

2.2 A non-exclusive summary of the literature applying the Vrentas-Duda theory and Fujita's theory of free volume. 26

3.1 Purchase information and specifications for the gases used in this work. 44

3.2 Characteristics of the polymer samples. 45

4.1 Values of the parameters used for early approximation, for the simplified model, and the full model with $W = 5$, and the relative difference between the two. . . 80

4.2 9 experimental runs of transient permeation, with the experimental conditions specified. 83

4.3 Values of the parameters estimated for the permeation runs, by applying the early approximation method with the simplified model, and the full model with $W = 5$; and the optimised values obtained using gPROMS. 91

4.4 Summary and comparison of the estimated transport coefficients and the lumped parameter for the runs, with the approaches of the time-lag method, graphical method with the simplified model and the full model with $W = 5$, and gPROMS optimisation. 97

5.1 Experimental results for the continuous runs: $F_m(t_i = 0)$ and $F_m(t_i = \infty)$ obtained using Eq. (3.2), F'_{i+1} obtained using Eq. (5.15), and $D_{T,i}(T, p_i, 0)$ obtained using Eq. (5.16). 113

5.2 The values of $\tilde{a}$, $\tilde{b}$ and $\tilde{c}$, estimated by the optimisation method described in Section 5.3; and the free-volume parameters obtained as described in Section 5.7. 119

5.3 The values of $v_f(T, 0, 0)$ calculated based on formulations and data from various sources. 122

5.4 Estimated values of W_i, $U_i/(W_i V')$, and $D'_i(X = 0)$, obtained from Eq. (5.5), Eq. (5.27), and Eq. (5.26), respectively, for the eight runs. 125

6.1 The solubility coefficient, S, obtained from the linear fits of $C_i(X = 0)$ *vs.* p_i in Figure 6.1 for the runs. 143

6.2 Pure-component parameters (p^*, characteristic pressure; ρ^*, characteristic density; T^*, characteristic temperature) for CO_2, PTFE and HDPE in the SL EOS. 145

6.3 Optimised binary interaction parameters, k_{ij} and η_{ij}, obtained by minimising the sum of the squared differences between the experimental solubilities and those modelled with SL EOS. 148

6.4 Estimated values of V'_i, U_i, and γ_i for the runs, determined using the procedure shown in Figure 6.3. 150

Nomenclature

Greek Letters

α'	Constant in Eq. (2.24)	
α_c	Constant related to concentration in Eq. (2.39)	
α_g	Volume expansion coefficient of the glassy polymer	K^{-1}
α_r	Volume expansion coefficient of the rubbery polymer	K^{-1}
β	Parameter defined by Eq. (2.10)	
β'	Constant in Eq. (2.24)	
β_h	Constant related to hydrostatic pressure effect in Eq. (2.39)	bar^{-1}
β_p	Compressibility	bar^{-1}
χ	Flory-Huggins interaction parameter	
ϵ	Characteristic interaction energy per segment	J
ϵ^*_{ij}	SL EOS cross parameter	
η_{ij}	SL EOS binary parameter	
γ	Concentration coefficient	
γ'	A numerical factor between 0.5 and 1	

γ''	free-volume parameter in Eq. (2.25)	
λ	Flux-approximation constant	
μ	Flux-approximation constant	
ν	Volume fraction of the penetrant in the mixture	
ω_i	Weight fraction of component i	
ω_p	Mass of the jumping units of the polymer	kg
Ω_s	Constant	
ω_s	Mass of the jumping units of the solvent	kg
Ω_W	Constant	
$\overline{\beta}$	Parameter defined by Eq. (2.18)	
ϕ_1	Volume fraction of the penetrant in the polymer	
ϕ_a	Amorphous volume fraction of the polymer	
ϕ_i	Volume fraction of component i	
ϕ_s	Volume fraction of the solvent in the polymer solution	
Ψ	Detour ratio	
ψ	Chain immobilisation factor	
ρ	Density of the system	kg m^{-3}
ρ^*	Characteristic density for pure component	kg m^{-3}
σ	Constant related to polymer-penetrant interaction in Eq. (2.40)	
τ	Dimensionless time	

τ_k	Ratio of evaporation energy to activation energy	
$\tau_{k,\text{pure}}$	Ratio of the evaporation energy to the viscous energy in pure limits	
Θ	Time lag	s
$\tilde{\rho}$	Reduced density	
ς	Tortuosity factor	
ξ	A dimensionless quantity in Eq. (2.14)	
ζ	Blocking factor	

Roman Letters

ΔH_m^0	Enthalpy of fusion of the 100% crystalline poymer	J kg^{-1}
ΔH_m	Enthalpy of fusion	J kg^{-1}
ΔH_S	Apparent heat of solution	J mol^{-1}
$\hat{V}^*_{\text{pen.}}$	Molecular core volume of the penetrant	m^3 mol^{-1}
$\overline{B}_d$	Parameter in Eq. (2.16)	
$\overline{f}_p^0$	Fractional free volume of the pure polymer	
$\overline{f}_s^*$	Fractional free volume associated with the solvent at $\phi_s \to 0$	
$\tilde{a}$	Constant as defined in Eq. (5.17)	m^2 s^{-1}
$\tilde{b}$	Constant as defined in Eq. (5.18)	bar
$\tilde{c}$	Constant as defined in Eq. (5.19)	bar
$\tilde{p}$	Reduced pressure	
$\tilde{T}$	Reduced temperature	

A	Surface area of the polymer disc exposed to CO_2	m^2
a	Thermodynamic activity	
A_d	free-volume parameter	m^2 mol s^{-1} J^{-1}
b	Langmuir affinity parameter	
B_D	Penetrant-free volume interaction parameter for diffusivity	
B_d	Parameter in Eq. (2.8)	
B_P	Penetrant-free volume interaction parameter for permeability	
B_S	Penetrant-free volume interaction parameter for solubility coefficient	
C	Concentration of the penetrant in the mixture	m^3(STP) m^{-3}(mixture)
c	$y-$intercept of the straight line for flux approximation	
C'_H	Langmuir sorption capacity	
c_{BET}	BET constant	
C_h	Equilibrium concentration of the penetrant at the high pressure surface of the membrane	m^3(STP) m^{-3}(mixture)
C_l	Equilibrium concentration of the penetrant at the low pressure surface of the membrane	m^3(STP) m^{-3}(mixture)
C_s	Parameter in Eq. (2.8)	
D	Constant diffusivity	m^2 s^{-1}
d	Diameter of the polymer sheet	m
D'	Dimensionless diffusion coefficient	
D'_0	Diffusion coefficient at $p = 0$ and $C = 0$ in Eq. (2.39)	m^2 s^{-1}

D^*	Diffusivity of the penetrant in completely amorphous polymer	$m^2\ s^{-1}$
D_0	Pre-exponential factor in Eq. (2.25)	$m^2\ s^{-1}$
D_a	Diffusivity of the penetrant in the amorphous phase of a semicrystalline polymer	$m^2\ s^{-1}$
D_M	Mutual diffusion coefficient	$m^2\ s^{-1}$
D_T	Thermodynamic diffusivity	$m^2\ s^{-1}$
$D_T(T,p,0)$	Thermodynamic diffusion coefficient for infinite dilution of the penetrant at T and p	$m^2\ s^{-1}$
D_T^0	Thermodynamic diffusivity at $\phi_s \to 0$	$m^2\ s^{-1}$
D_{00}	Pre-exponential constant for diffusivity in Eq. (2.33)	$m^2\ s^{-1}$
E_a	Activation energy	$J\ mol^{-1}$
E_D	Activation energy of diffusivity	$J\ mol^{-1}$
E_P	Activation energy of permeability	$J\ mol^{-1}$
F	Permeation flux of the penetrant	$mol\ m^{-2}\ s^{-1}$
f	Fractional free volume	
F'	Dimensionless flux	
F'_{i+1}	Ratio of $F(t_{i+1}=0)$ to $F(t_i=\infty)$	
F_i^m	Mass flux of component i	$kg\ m^{-2}\ s^{-1}$
F_m	Measured permeation rate of CO_2	$m^3(STP)\ m^{-2}\ s^{-1}$
f_p	Fractional free volume of the pure polymer	
f_s	Fractional free volume of the pure solvent	
i	Step in a measurement	

k	Slope of the straight line for flux approximation	
k_B	Boltzmann's constant	J K^{-1}
k_D	Henry's law coefficient	bar^{-1}
K_P	Henry's constant	bar
k_{ij}	SL EOS binary parameter	
L	Thickness of the polymer sheet	m
m	Number of lattice sites per molecule in Eq. (2.27)	
$M_{\text{pen.}}$	Molecular weight of the penetrant	kg mol^{-1}
m_s	Solvent mobility	
M_W	Molecular weight	
N	Number of molecules in the system in Eq. (2.27)	
n	Total number of steps in a measurement	
N_0	Number of empty sites in Eq. (2.27)	
N_r	Total number of lattice sites in Eq. (2.27)	
P	Permeability	barrer
p	Pressure	bar
P^*	Permeability of the penetrant in completely amorphous polymer	barrer
p^*	Characteristic pressure for pure component	bar
p_0	Saturation pressure	bar
P_a	Permeability of the penetrant in the amorphous phase of a semicrystalline polymer	barrer

p_h	High pressure (side) of the polymer	Pa
p_l	Low pressure (side) of the polymer	Pa
P_{00}	Pre-exponential constant for permeability in Eq. (2.32)	barrer
Q	Sum of squared differences in Eq. (5.21)	
q	Flowrate of the sweeping stream	$m^3\ s^{-1}$
Q_t	Total amount of diffusing CO_2 in t	$m^3\ m^{-2}$
R	Ideal gas constant	$J\ K^{-1}\ mol^{-1}$
r	Size parameter	
S	Solubility coefficient	Pa^{-1}
S^*	Solubility coefficient of the penetrant in completely amorphous polymer	Pa^{-1}
$s_{\text{pen.}}$	Molar surface area of the penetrant molecules	$m^2\ mol^{-1}$
S_a	Solubility coefficient of the penetrant in the amorphous phase of a semicrystalline polymer	Pa^{-1}
S_{00}	Pre-exponential constant for solubility coefficient in Eq. (2.34)	Pa^{-1}
T	Temperature	K
t	Time	s
T^*	Characteristic temperature for pure component	K
T_g	Glass transition temperature	K
T_m	Melting temperature	K
U	Dimensionless group	
V	Specific volume of the polymer	$m^3\ kg^{-1}$

v	Adsorbed volumetric quantity of the penetrant	m^3
V'	Ratio of $V_{T,p}$ to $V_{273K,1atm}$	
v^*	Closed-packed volume of a segment	$m^3\ mol^{-1}$
V_0	Occupied specific volume of the polymer	$m^3\ kg^{-1}$
V_F	Specific free volume of the polymer	$m^3\ kg^{-1}$
V_f	Molar free volume in Eq. (2.23)	$m^3\ mol^{-1}$
$v_f(T,p,\nu)$	Polymer fractional free volume in Eq. (4.6)	
$v_f^*(T,p,0)$	Fractional free volume of the pure polymer at p and T in Eq. (4.7)	
V_i	Specific volume of component i	$m^3\ kg^{-1}$
V_k	Partial molar volume of component k	
v_m	Monolayer adsorbed volumetric quantity of the penetrant	m^3
v_p	Specific volume of the pure polymer	$m^3\ kg^{-1}$
v_p^0	Specific volume of the pure polymer at 0 K	$m^3\ kg^{-1}$
v_s	Specific volume of the pure solvent	$m^3\ kg^{-1}$
v_s^0	Specific volume of the pure solvent at 0 K	$m^3\ kg^{-1}$
$V_{273K,1atm}$	Specific volume of the penetrant at standard conditions	m^3(STP) kg^{-1}
v_{hs}	Specific critical hole volume of a jumping unit of the solvent	$m^3\ kg^{-1}$
v_{ij}^*	SL EOS cross parameter	
$V_{T,p}$	Specific volume of the penetrant at T and p	$m^3\ kg^{-1}$
W	Dimensionless group	

X	Dimensionless distance	
x	Position in the polymer sheet	m
X_c	Degree of crystallinity of the polymer	
x_k	Mole fraction of component k	
y_{CO_2}	Molar fraction of CO_2 in the sweeping stream	

Abbreviations

CCS	Carbon capture and storage
COC	Cyclic olefin copolymer
DC	Dose cell
DMA	Dynamic mechanical analysis
DSC	Differential scanning calorimetry
EOS	Equation of state
EPDM	Ethylene propylene diene monomer
HDPE	High density polyethelene
IR	Infrared
LCST	Lower critical solution temperature
LDPE	Low density polyethylene
LJD	Lennard-Jones and Devonshire
MCT	Mercury cadmium telluride
MOF	Metal organic framework
PBS	Poly(butylene succinate)

PBSA	Poly(butylene succinate-co-adipate)
PC	Polycarbonate or permeation cell depending on the context
PDMS	Polydimenthylsiloxane
PE	Polyethelene
PEAA	Poly(ethylene-co-acrylic acid)
PED	Pressure Equipment Directive
PMMA	Poly(methyl methacrylate)
PP	Polypropylene
PPO	Poly(phenylene oxide)
PSUL	Polysulfone
PTFE	Polytetrafluoroethylene
PVDF	Polyvinylidene difluoride
RC	Reference cell
SAFT	Statistical associating fluid theory
SD	Standard deviation
SL	Sanchez-Lacombe
STP	Standard temperature and pressure
TC	Test cell
UCST	Upper critical solution temperature
UV	Ultraviolet
WLF	Williams-Landel-Ferry

Chapter 1

Introduction

This thesis investigates the process of permeation of high pressure CO_2 in semicrystalline polymers, for applications such as polymer lining, sealing, and coating in carbon capture and storage (CCS) sector. In this chapter, background information on climate change and CCS is provided. The processes related to CO_2 transport in polymers in a CCS chain are introduced. Following the project motivations and the scientific significance, the objectives and the scope of the project are stated. An outline of the thesis is given at the end of this chapter.

1.1 Climate Change and CCS

The past year of 2020 has witnessed major commitments by a host of countries to cut carbon emissions and eventually reach "net zero" targets within the next few decades [1]. Rather than being just political statements, these commitments are increasingly likely to be fulfilled, with the promising signals that the US seems to be moving back on track for the Paris Agreement [2], that China has pledged peak emissions before 2030 and carbon neutrality by 2060 [3], that countries responsible for more than 65% of global emissions and more than 70% of the world economy have been making detailed plans and legislation to reach the goals [1], and that the COVID-19 [4] pandemic recovery promotes clean energy investments and low-carbon technologies to tackle climate change [1].

Meeting the net-zero target requires both the reduction on carbon emission by substituting fossil fuels with clean energy sources, and the removal of released carbon dioxide with CCS techniques. A CCS chain consists of three primary steps: firstly, capturing CO_2 from emission sources and separating it from other gases; secondly, compressing it to form supercritical or dense phase CO_2 and transporting it via pipelines or ships to a storage site; and thirdly, injecting it into oil and gas wells or saline aquifers for long term storage [5, 6]. As shown in Figure 1.1, high pressure conditions can be involved in the operations for these steps. The resulting supercritical or dense phase CO_2, particularly with the existence of impurities produced from the emission sources, can cause devastating damage to the pipeline and the polymeric seals and liners.

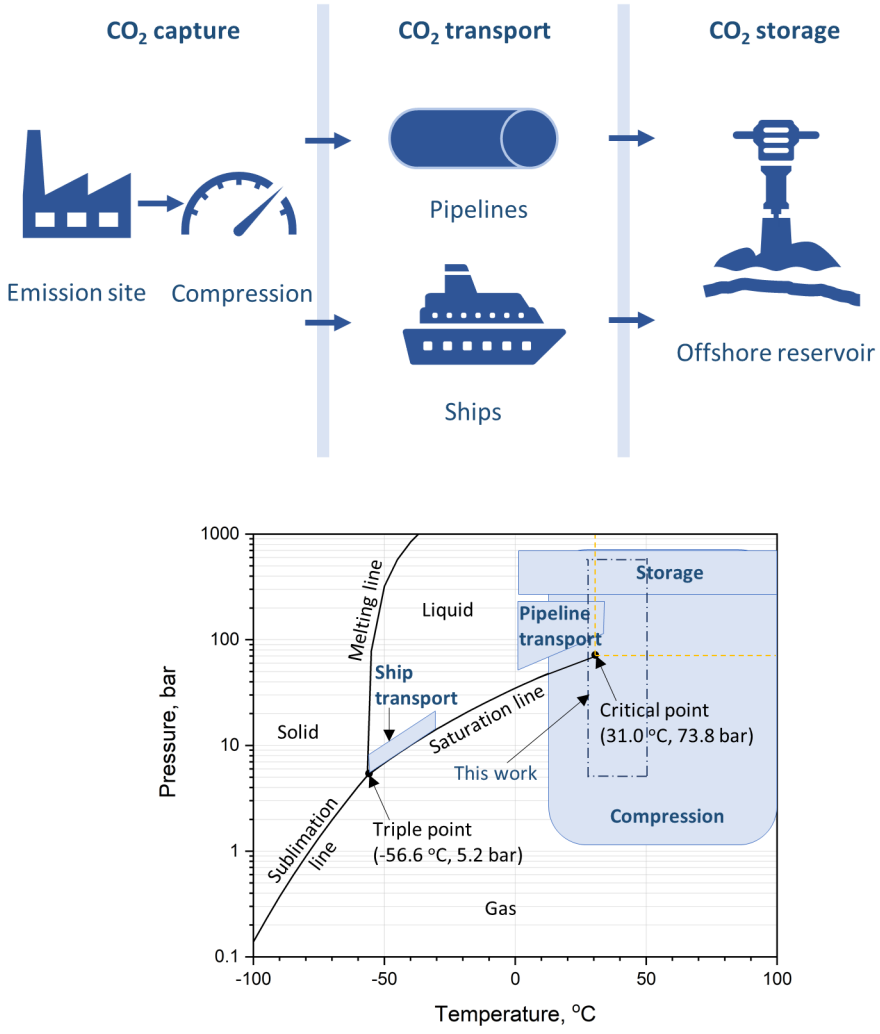


Figure 1.1: Schematic diagram showing the three steps of the CCS chain, and their respective operating conditions presented on the CO_2 phase diagram retrived from [7]. The diagrams were plotted using data and information collected from [6, 8–11]. The rectangle region with blue dash boundaries on the CO_2 phase diagram refers to the experimental conditions in this work.

This damage, including the corrosion of the metallic pipeline [12–16], and the degradation of seals, liners, coatings and other protective layers [17–19], can severely shorten the service life of these components and negatively impact the cost effectiveness of the CCS chain. To tackle these issues and to develop a better understanding of these processes under high pressure environments, research on the transport behaviour of high pressure CO_2 in polymeric materials is required.

In comparison to the abundant resources and studies on lower pressure gaseous CO_2, which are readily available in literature, *e.g.* [20–30], studies, especially experimental works, on the transport phenomena of high pressure CO_2 are relatively scarce, despite an increasing number of papers emerging [31–36]. To enrich the database for CO_2-polymer systems under high pressures, and develop reliable methods for investigating polymer issues due to CO_2 permeation in a CCS chain, experimental and modelling work has been conducted in this project. The work was conducted under a range of conditions, with the temperature ranging from 28 °C to 50 °C and the pressure ranging from 5 bar to 600 bar, as shown by the blue outlined rectangle in Figure 1.1. The methods developed and the results obtained can be applied to the specific permeation-related processes in a CCS chain.

1.2 Permeation-Related Processes in CCS

A CCS chain consists of a series of processes, with various techniques involved, as shown in Figure 1.2. After CO_2 is captured from power plants or other industrial sites, it needs to be separated from the additional components in the stream, by means of *e.g.* physical adsorption [37], absorption and stripping with aqueous amine [38], membrane technologies [39], metal organic frameworks (MOFs) [40], and chemical looping [41]. Subsequently, CO_2 is transported to the storage sites through either pipelines or ships, the latter of which normally require cryo-compressed conditions to obtain liquefied CO_2 [42]. Throughout transportation, all polymeric materials used in tubes, pipes, pumps, compressors and other components for corrosion prevention and sealing purposes, can be exposed to CO_2 and the impurities under

the corresponding operating conditions. The performance of these polymeric materials has significant impacts on safety, efficiency, profits and environmental issues. After CO_2 has been transported to the storage sites, it is injected into depleted oil/gas fields, and is sealed by impermeable rock formations [11]. This thesis focuses on CO_2-polymer systems in permeation-related processes, which are the highlighted ones in white colour as shown in Figure 1.2.

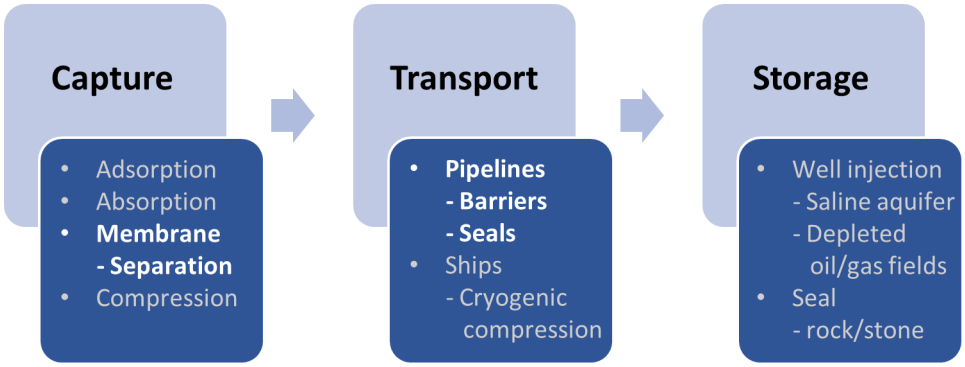


Figure 1.2: Various processes involved in the three steps of CCS. The highlighted processes are those related to permeation of CO_2 in polymers.

1.2.1 Polymeric Membranes for CO_2 Separation

Despite the long history of the modern membrane separation industry beginning in the 1960s [43], the use of membranes for gas separation in a CCS chain is a relatively new technology, compared with solvent absorption, which is a mature technology for CO_2 separation and has been applied commercially. However, recent advancements in membrane materials for large-scale CO_2 capture and separation make membrane technology a more competitive choice over solvent absorption in the future, with the following advantages. Firstly, it involves less chemicals in the operation than the solvent absorption method, which can lead to significant environmental impacts [44, 45]. Secondly, membrane operations are less energy intensive and have lower capital costs than absorption processes [45]. Thirdly, membranes are suitable for offshore applications, owing to their ease of installation, operation and maintenance [46].

Various types of membrane materials exist for CO_2 separation [47, 48], such as polymeric, inorganic and carbon membranes, *etc.* This thesis focuses on the gas transport through polymeric membranes, which are generally non-porous, by a solution-diffusion mechanism [49], whereby

gas permeation is decribed by the thermodynamic sorption within the membrane and its kinetic diffusion through the polymer matrix. There is a trade-off of permeance and selectivity of CO_2 [50], which are the two key parameters characterising the separation performance of the polymeric membrane. Methods should be explored to maximise both permeance and selectivity by manipulating the chemical composition of the polymer and the conditions for its preparation [39]. Meanwhile, research on the high-temperature stability of the polymeric membranes needs to be conducted, to improve the high-temperature resistance of membranes [47].

1.2.2 Pipeline Corrosion and Polymeric Barriers

Being one of the major factors affecting the structural integrity and the economics of a CCS chain in large scale, corrosion of the pipeline remains an issue, due to the technological gap in understanding the transport behaviour of CO_2 and its various impurities in metallic and polymeric materials in dry and wet environments. Corrosion issues have been seldomly reported for pipeline steels exposed to pure, dry CO_2 [51]. However, in the presence of impurities such as SO_x, NO_x, O_2, CO, and H_2S [52], which are captured along with CO_2 from fossil-fuelled power plants, high corrosion rates of carbon steel in aqueous enviroments were reported [53]. Consequently, polymeric materials are normally used as barriers to avoid the contact between gases and the pipeline, so as to protect the metallic components from corrosion, and thus decelerate the failure of the metals and prolong their service life.

Evaluation of the effectiveness of the polymeric barriers for corrosion prevention needs to be conducted, on the basis of an understanding of the interactions between the gas components and the polymeric materials, under a variety of working conditions. First of all, CO_2 may induce swelling or platicisation effects [36], which could accelerate the diffusion and increase the uptake of the gas components in the polymers, leading to failures of the barrier materials. Furthermore, in spite of its trace amount in the CO_2 stream, water could react with CO_2 to form carbonic acid, with SO_x to form sulphric acid, or with NO_x to form nitric acid [54, 55], causing damages to the polymeric barriers [51]. The resistance to acids can be used as a criterion for selecting appropriate polymer materials. For instance, elastomers such as ethylene propylene diene

monomer (EPDM) and natural rubber, are less stable towards sulphuric and nitric acids, than polypropylene, polyethylene and polytetrafluoroethylene (PTFE) [56], which are considered as suitable candidates for CO_2 streams containing small amounts of SO_x and NO_x. In addition, perfluoropolymers (mainly PTFE copolymers) exhibit anomalously low permeability of H_2S compared to nonfluorinated polymers [57], making the former superior for being used as the barrier materials.

1.2.3 Leakage and Polymeric Seals

Elastomeric seals are commonly used for pipeline sealing, which is essential for preventing leakage and maintaining pressure in the CO_2 transport system. In many cases, for economic reasons, the CO_2 transport system is adapted from the existing pipeline infrastructure used in the oil and gas industry. Specifically, over 6500 km of CO_2 pipelines, primarily in the US, are used for enhanced oil recovery (EOR) operations [58]. However, the CO_2 used for EOR is quite pure, whilst the CO_2 stream in a CCS chain normally contains impurities, which could interact with the polymeric materials, as discussed in Section 1.2.2. As a result, to avoid seal failure, the suitability of the polymeric seals used for EOR operations needs to be evaluated for CCS applications [59].

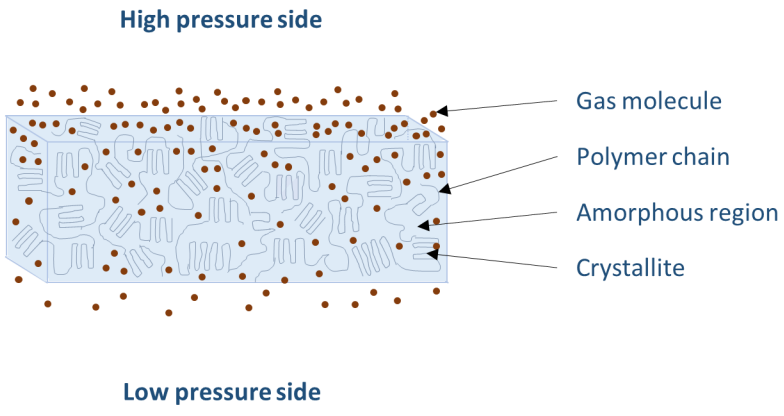
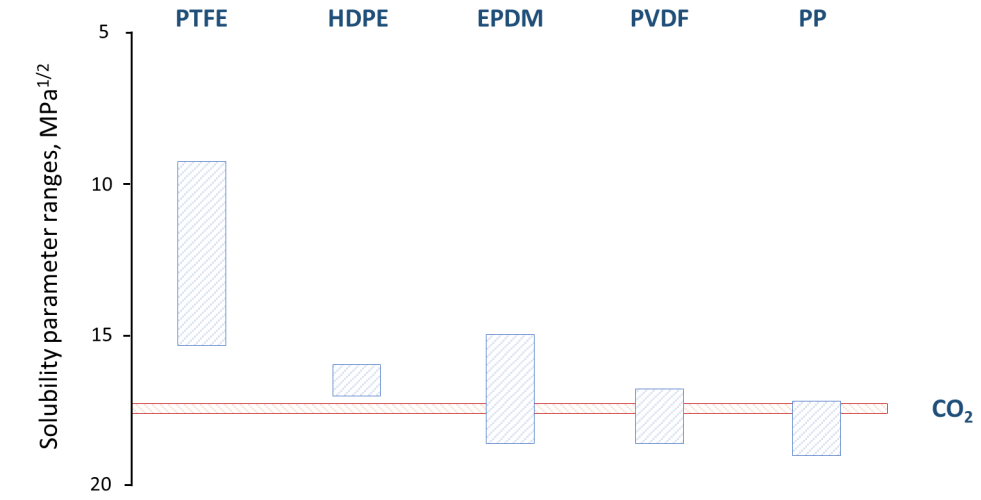


Figure 1.3: Schematic diagram of the semicrystalline morphology, showing the amorphous regions and the crystallites.

The morphology of polymers also has an impact on the gas transport process. Polymers nor-

mally exhibit two types of morphology in the solid state: amorphous and semicrystalline. In an amorphous polymer, molecules are randomly oriented and thus there is little long range structure. A semicrystalline polymer is comprised of amorphous regions and regions of dense crystallites, as shown in Figure 1.3. Gas molecules can only penetrate through the amorphous regions, whilst the crystallites are typically assumed to be comparatively impenetrable and result in the polymer properties of rigidity and good chemical resistance [20].



	PTFE		HDPE		EPDM		PVDF		PP	
	20 °C	60 °C	20 °C	60 °C	20 °C	60 °C	20 °C	60 °C	20 °C	60 °C
H_2S	A	A	A	A	A	A	A	A	A	A
SO_2	A	A	A	A	A	A	A	A	A	A
CO	A	A	A	A	A	A	A	A	A	A
N_2O	A	A	A	A	A	A	A	A	A	A
NH_3	A	A	A	A	A	A	A	A	A	B
Water	A	A	A	A	A	A	A	A	A	A
Amines	A	A	A		A		B	C	A	B

A Excellent (recommended) B Slowly attacked

C Limited resistance Not known

Figure 1.4: Solubility parameters and chemical resistance of various semicrystalline polymers. Data for solubility parameter at room temperature: PTFE [60, 61], HDPE (high density polyethelene) [62, 63], EPDM [64, 65], PVDF (polyvinylidene difluoride) [66], PP (Polypropylene) [67], and liquid CO_2 [68]. Information on chemical resistance at 20 °C and 60 °C: PTFE, EPDM, PVDF, and PP [69]; HDPE [70, 71].

Figure 1.4 shows the properties of a non-exhaustive list of semicrystalline polymers (PTFE, HDPE, EPDM, PVDF and PP), which are considered to be suitable candidates for polymeric seals in CCS applications. These properties refer to the solubility parameters, which show the affinity of the polymers with CO_2, and their chemical resistance with respect to various contaminants.

As can be seen from Figure 1.4, compared with PTFE and HDPE, the other polymers have similar solubility parameters to liquid CO_2, making it easier for CO_2 to dissolve into these polymers and swell them. The solubility parameters may suggest that PTFE and HDPE tend to be stable in an environment of liquid CO_2. In addition, they seem to possess excellent resistance to various contaminants in a wide temperature range from 20 °C to 60 °C. As a result, PTFE and HDPE are considered two promising candidates for CCS applications. Thus, they have been chosen as the representative semicrystalline polymers to be studied in this work.

PTFE, degraded by few chemicals, has so far been regarded as one of most chemically resistant polymers among thermoplastics [72], which refer to a class of polymers that can be softened and melted by applying heat [73]. This inertness arises from its molecular structure of carbon-carbon bonds and carbon-fluorine bonds, both of which are extremely strong [74]. Owing to the size of the fluorine atom, a uniform and continuous covering can be formed around the carbon-carbon bonds to protect them from chemical attack, contributing to chemical resistance and stability of the molecule [74]. These superior properties of PTFE result in its applications in polymer lining, fittings, valves, pumps and other components for transport purposes.

HDPE is another widely used thermoplastic. The semicrystalline morphology, which is composed of a hard crystalline phase and a soft amorphous phase, results in the high modulus of elasticity of HDPE, as well as its high impact toughness [75]. The excellent chemical resistance of HDPE, especially to polar compounds, arises from the relatively inert carbon-carbon and carbon-hydrogen bonds, which make it resistant to most types of chemical attack [76]. The advantages of relatively low cost, excellent flexibility and resistance to impact damage distinguish HDPE as one of the most common types of plastic used in both industry and daily life.

1.3 Project Motivations and Scientific Significance

This project is motivated by two factors: industrial needs and research gaps, for the usage of polymeric materials in CCS applications. Firstly, from the industrial point of view, polymeric materials are desirable in a CCS system, for their excellent flexibility, sealing properties, resistance to degradation, low weight, and low cost compared to metals. Experimental data and test methods are required to understand the transport behaviour of CO_2 and impurities in the engineering polymers, and to evaluate the performance of these polymers under specified conditions. As a result, suitable polymers can be selected or developed for specific CCS applications, and operating efficiency as well as profits can be maximised.

Secondly, despite the increasing amount of research into the subject of CCS, and more specifically the application of polymers for CCS, research gaps still exist in several aspects. Most work has been done in a relatively low pressure range of 1 - 100 bar, which is outside the operating ranges for many CCS processes, as can be seen from Figure 1.1. Furthermore, regarding impurities, various components and compositions may occur in a CO_2 stream, depending on its source and the applied capturing method. Therefore, comprehensive experimental data are in demand for effective comparison and evaluation. Moreover, in addition to experiments, which are normally time-consuming, expensive and sometimes dangerous to conduct, it is necessary to develop accurate models, which can be used for estimation and prediction.

As a scientific project, the work presented in this thesis could have the following contributions to the research community: (1) Data acquisition - the permeation data for CO_2 in semicrystalline polymers under various temperatures and elevated pressures can be used as a guide for material selection or a reference for other researchers. (2) Experimental method - a high-pressure permeation rig has been built and operated under a safe code of practice, the experience of which can be used for reference, and can be replicated by others. (3) Model development - the modelling of the permeation process, with either analytical or numerical methods, assists the development of theories, which help elucidate the mechanisms behind the permeation behaviour.

1.4 Objectives and Scope

It is a primary goal in this work that the obtained data and the developed methods would contribute to a better understanding of the permeation mechanisms involved in CCS applications, and a more effective selection of suitable polymeric materials for these processes. In accordance with this overall goal, the scientific and engineering objetives are: (i) to build a reliable high-pressure permeation rig; (ii) to develop experimental methodologies for data acquisition; (iii) to derive and simplify phenomenological models that help elucidate fundamental properties from the permeation measurements.

Under the relatively broad topic of high pressure gas permeation through semicrystalline polymers, this work was specifically refined to the following scope:

- Permeation experiments: despite the multi-functional feature of the high pressure rig, which can be used to conduct separate permeation and sorption experiments (briefly described in Appendix A) under high pressures, this project has a focus on the permeation experiments, which were conducted under three temperatures (28 °C, 35 °C and 50 °C), and under pressures ranging from 5 bar to 600 bar.

- CO_2-polymer systems: to form a basis for further permeation study of complex high-pressure systems, this project investigates the permeation process of pure CO_2 in two representative semicrystalline polymers: PTFE and HDPE.

- Modelling: a free volume model, together with the Sanchez-Lacombe (SL) equation of state (EOS), is used to fit the experimentally measured transient permeation curves, using the tools of Matlab, gPROMS and Aspen Plus. In addition, graphical and analytical methods, which only require Microsoft Excel, are also developed for modelling the same process.

1.5 Structure of the Thesis

This thesis consists of seven chapters, including this introduction. The remaining chapters are as follows:

Chapter 2 reviews previous studies of gas permeation, diffusion and sorption in polymers, from theoretical, experimental and modelling perspectives.

Chapter 3 describes the materials and the appratus employed in this work, and addresses the experimental design and the methods used.

Chapter 4 presents the results of single-step transient permeation measurements, and introduces a graphical method for modelling, based on a free volume theory.

Chapter 5 presents the methods for estimating the free-volume parameters in the model, from the results of experiments, which consist of multiple successive pressure steps.

Chapter 6 presents an analysis of the diffusivity and the solubility data obtained from both the permeation experiments and the SL EOS.

Chapter 7 summarises the conclusions drawn from the previous chapters and provides recommendations for future work.

Chapter 2

Literature Review

2.1 Introduction

In this chapter, a review of literature related to transport mechanisms in gas-polymer systems is presented. The concepts and the theoretical models proposed for the transport properties are described. Various factors, which could affect these properties, are discussed. Finally, the experimental methods and the existing techniques for obtaining the transport coefficients are reviewed.

2.2 Solution-Diffusion *vs.* Pore-Flow

Two models are used to describe the permeation process: the solution-diffusion model and the pore-flow model [77]. In the first model, the permeants dissolve in the membrane and then diffuse through it down a concentration gradient. In the second model, the permeants move through the tiny pores in the membrane by pressure-driven convective flow. The primary difference is that the solution-diffusion model assumes that the chemical potential gradient in the membrane is expressed as a concentration gradient, and the pressure within it is uniform at the high-pressure value, as illustrated in Figure 2.1. This way of transmitting pressure in

solution-diffusion membranes is considered the same as that in liquids [77, 78]. On the other hand, the pore-flow model assumes that the chemical potential gradient in the membrane is expressed as a pressure gradient, and the concentrations of solute and solvent within it are uniform [77].

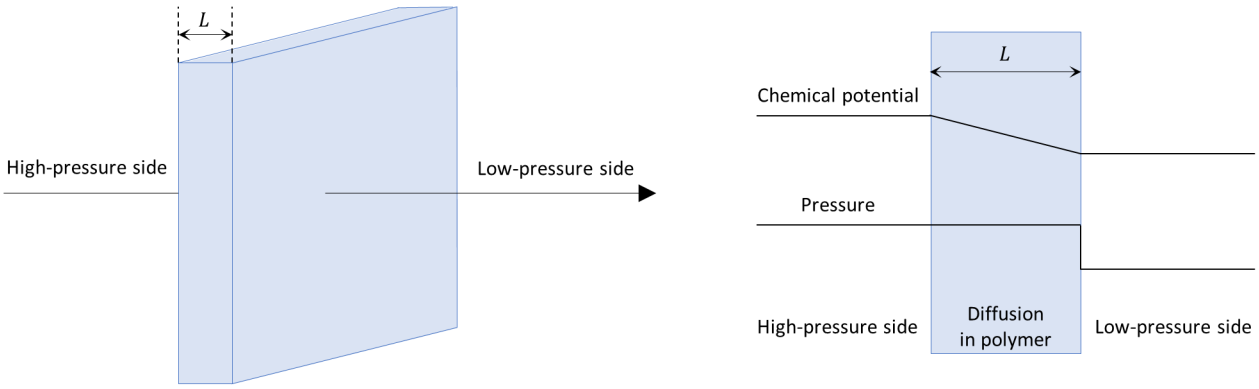


Figure 2.1: Schematic representation of permeation through a polymeric membrane according to solution-diffusion transport model (L denotes the membrane thickness).

Penetrant transport through a polymeric membrane, which is considered as a homogeneous, non-porous material, is normally described by the solution-diffusion model [79]. In this case, as shown in Figure 2.1, the permeation process consists of three steps [80, 81]:

- Sorption of the penetrant at one surface of the polymeric membrane.
- Diffusion of the penetrant, in a condensed liquid form, through the membrane under a driving force of a chemical potential (concentration) gradient.
- Desorption of the penetrant at the side of lower partial pressure into the gaseous state.

Thus, the permeability coefficient, P, depends on both the solubility coefficient, S, which represents the amount of the penetrant molecules dissolved into the membrane, and the diffusivity coefficient, D, which reflects the migration rate of the penetrant molecules through the membrane. These three transport properties, P, D and S, are discussed in the next section.

2.3 Transport Properties

2.3.1 Permeability

The permeability, P, can be related to the steady-state permeation flux, denoted by $F(t = \infty)$, by Eq. (2.1):

$$F(t = \infty) = \frac{P(p_h - p_l)}{L}, \tag{2.1}$$

here, p_h and p_l refer to the high pressure and the low pressure on the two sides of the polymeric membrane, respectively; and L is the thickness of the membrane.

Meanwhile, $F(t = \infty)$ can be expressed as a function of the concentration gradient:

$$F(t = \infty) = \frac{D(C_h - C_l)}{L}, \tag{2.2}$$

where C_h and C_l represent the equilibrium concentrations of the penetrant at the two surfaces of the membrane. Assuming Henry's law holds, *i.e.* a linear relationship exists between the vapour pressure of the penetrant and the corresponding equilibrium concentration of the penetrant at the surfaces of the membrane:

$$C = Sp. \tag{2.3}$$

A relationship, which expresses P as a product of D and S, can then be obtained:

$$P = DS. \tag{2.4}$$

Eq. (2.4) suggests that knowing any two of the three quantities, the third one can be calculated. More specifically, in a permeation experiment, P can be obtained from the steady-state permeation flux with Eq. (2.1). The diffusivity, D, can be derived from a "time lag" of the transient permeation preceding the steady state, as will be described later in Section 2.3.2. Accordingly, S can be calculated by Eq. (2.4).

2.3.2 Diffusivity

Time Lag Method for Determining Diffusivity

Introduced by Daynes and Smith [82] and developed by Barrer [83], the time-lag mothod has been extensively applied to the estimation of diffusivity in membrane studies. During a permeation experiment, after a sufficiently long time, a steady state would be established. The curve of the cumulative amount of diffusing substance, Q_t, against the expermental time, t, would asymptotically approach a straight line, as shown in Figure 2.2:

$$Q_t = \frac{DC_h}{L}\left(t - \frac{L^2}{6D}\right). \tag{2.5}$$

The line has an intercept on the t-axis, Θ, which is referred to as the "time lag":

$$\Theta = \frac{L^2}{6D}. \tag{2.6}$$

From Θ, D can be obtained, since L is known. In addition, C_h can also be estimated from the slope of the line.

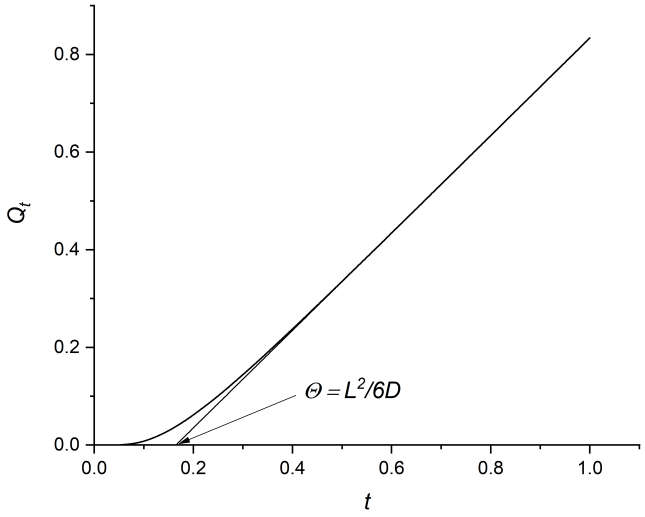


Figure 2.2: Plot of Q_t *vs.* t, showing the "time lag" of a cumulative permeation curve approching steady state.

To apply the time-lag method, the diffusivity, D, has to be assumed constant across the membrane, independent of time or concentration. However, in some systems, such as the diffusion

of vapours in high-molecular-weight polymers, this assumption might be over-simplified, since it is quite typical that the diffusivities are dependent on penetrant concentration [84]. In those cases, models with variable diffusivity, such as free volume models, need to be applied, as will be presented in Section 4.2. Furthermore, the assumption of Henry's law may not hold true, since deviations may occur in the high pressure range, as will be discussed in Section 6.2.2.

Diffusion in Glassy *vs.* Rubbery Polymers

Diffusion of the penetrant in a semicrystalline polymer takes place in the amorphous region, where a reversible transition from a glassy state into a rubbery state may occur, when the temperature is increased above the glass transition temperature, T_g, of the polymer. Below T_g, the glassy-state polymer is rigid and dimensionally stable, since the chain segments can only have limited vibration due to a lack of energy to rotate or change positions. On the other hand, above T_g, the polymer turns into a rubbery state, becoming soft and flexible, owing to a greater rotational freedom [85]. This primary difference in molecular motion leads to their different behaviours. Rubbery polymers tend to respond very quickly to the changes in their conditions, whilst glassy polymers can have time-dependent properties [84].

One essential factor to consider is the viscoelastic stress, which results from a nonlinear memory effect in some polymer systems. This stress is normally related to a term called relaxation time, which corresponds to the time taken for one portion of the entangled polymer network reacting to changes in another portion [86]. There is a certain relaxation time in the glassy region, and the stress is slow to decay after a change in the condition. On the other hand, the memory effect of the stress has a less significant impact on rubbery polymers, owing to their very rapid response.

This important difference in the two types of the polymers leads to distinctive diffusional patterns. Alfrey et al. [87] classified three cases of diffusion: Fickian diffusion, Case II diffusion, and non-Fickian diffusion, which is in the transition region between the first two. Ideal Fickian diffusion is normally applicable to rubbery polymers, in which case Fick's laws of diffusion can be applied. Case II diffusion and non-Fickian diffusion normally occur in glassy polymers.

Case II diffusion is characterised by the velocity of the penentrant's advancing front, which separates the inner glassy core from an outer swollen rubbery shell of the glassy polymer, for specimens of simple geometry, *e.g.* slabs, long cylinders, and spheres. Non-Fickian diffusion is a combination of the two particular patterns of Fickian diffusion and Case II diffusion, in which both the Fickian pattern and the relaxation effects may play a role in the diffusional behaviour.

2.3.3 Solubility

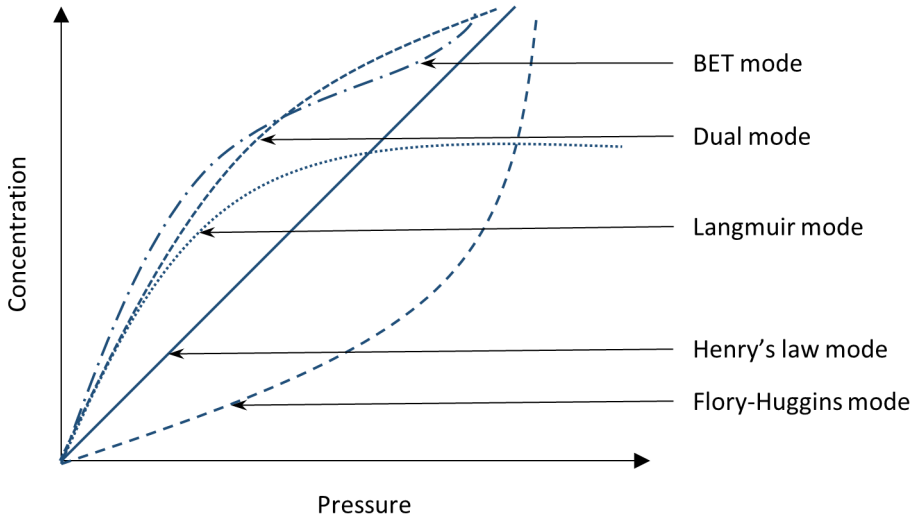


Figure 2.3: Isotherm plots of sorbed concentration *vs.* pressure for the five typical sorption modes (diagram reprodcued from [79]).

The permeation of simple gases, *e.g.* H_2, He and N_2, in rubbery polymers under moderate pressures, tends to possess Fickian diffusion features and follow Henry's law for sorption [79]. However, in the most general case, the solubility coefficient, S, is not a constant, but a function of temperature, pressure, or concentration. There exist various expressions for S, which correspond to the different sorption modes: Henry's law mode, Langmuir mode, Dual mode, Flory-Huggins mode [88–90] and BET mode. Figure 2.3 shows the isotherms for the five sorption modes. The characteristics of these sorption modes are presented in Table 2.1.

Table 2.1: Typical sorption modes, with their respective expressions, dominant interactions, and examples.

Sorption Mode	**Henry's Law**	
Expression	$C = Sp$	(Constant S independent of concentration and temperature, leading to linear relationship between C and p, as shown in Figure 2.3.)
Interaction	Polymer-polymer	(At low pressures, weak penetrant-penetrant and penetrant-polymer interactions.)
Example	Sorption of O_2, N_2 and H_2 in PDMS below 25 atm [28].	
Sorption Mode	**Langmuir**	
Expression	$C = \frac{C'_H bp}{1+bp}$	(C'_H is a "hole saturation" constant, and b is a "hole affinity" constant.)
Interaction	Penetrant-polymer	(Penetrant molecules occupy sites or holes in the polymer, until all sites are occupied, as shown in Figure 2.3.)
Example	Gas adsorption on solid surfaces descibed by the Langmuir model or its extended models [91, 92].	
Sorption Mode	**Dual Mode**	
Expression	$C = Sp + \frac{C'_H bp}{1+bp}$	(Combination of Henry's law mode and Langmuir mode for the glassy polymers, as shown in Figure 2.3.)
Interaction	Polymer-polymer and penetrant-polymer	(One population of molecules dissolved in the polymer following Henry's law and a second population of molecules adsorbed on specific sites under Langmuir mode.)
Example	Sorption of low-activity gases, *e.g.* Ar and N_2, in glassy polymers [93, 94].	

Continuation of Table 2.1		
Sorption Mode	**Flory-Huggins**	
Expression	$\ln a = \ln \phi_1 + (1 - \phi_1) + \chi(1 - \phi_1)^2$	(a is the thermodynamic activity of the gas component; ϕ_1 is the volume fraction of the penetrant in the polymer; and χ is the Flory-Huggins interaction parameter.)
Interaction	Penetrant-penetrant	(Stronger interactions between the penetrant molecules, with increasing solubility coefficient with pressure, as shown in Figure 2.3.)
Example	Sorption of condensable gases of relatively high activities in rubbery polymers under high pressures [95–97].	
Sorption Mode	**BET**	
Expression	$\frac{1}{v[(p_0/p)-1]} = \frac{c_{\mathrm{BET}}-1}{v_m c_{\mathrm{BET}}}\left(\frac{p}{p_0}\right) + \frac{1}{v_m c_{\mathrm{BET}}}$	(v is the adsorbed volumetric quantity of the penetrant; v_m is the monolayer adsorbed quantity; c_{BET} is the BET constant; p and p_0 are the equilibrium and the saturation pressure of the adsorbates, respectively.)
Interaction	Penetrant-polymer and penetrant-penetrant	(Combination of Langmuir and Flory-Huggins modes, as shown in Figure 2.3.)
Example	Sorption of water in highly hydrophilic polymers [98–100].	

Amongst these sorption models, the Flory-Huggins model, which is an activity coefficient model, is most suitable for simulating phase equilibrium and thermodynamic properties for the sorption of high-activity penetrants (*e.g.* CO_2, high-molecular-weight hydrocarbons and vapours) in rubbery polymers under elevated pressures. However, there are two major drawbacks of the Flory-Huggins model: (i) the model relies on a few assumptions, which weaken its ability to successfully describe the experimental data for polymer solutions. For instance, the model poorly describes diluted solution behaviour, with its assumption of a uniform distribution of polymer segments; (ii) to satisfactorily describe the isotherms of polymer solutions with large

values of χ (typically $\chi > 0.8$), the addition of several *ad hoc* empirical parameters is required, considerably limiting the usefulness of the model [101, 102]. In comparison, modern equations of state, such as the Sanchez-Lacombe EOS [103, 104], which will be presented in more detail in Section 6.2.2, are found to be more appropriate for modelling sorption properties in rubbery polymers [105].

2.4 Free Volume Theory

According to free volume theory, diffusing molecules migrate in a polymer by jumping between thermally generated voids or holes in the polymer matrix. The sum of all the voids in the amorphous region of the polymer is called free volume, as compared to the occupied volume by the polymer chains. A fractional free volume, f, can be defined as a ratio between the specific free volume, V_F, and the macroscopic specific volume of the polymer, V [102]:

$$f = \frac{V_F}{V} = \frac{V - V_0}{V}, \tag{2.7}$$

where V_F is regarded as the difference between V and the specific volume occupied by the polymer chains, V_0.

2.4.1 Free Volume in Glassy and Rubbery Polymers

As can be seen in Figure 2.4, above T_g, when the polymer is in its rubbery state, the polymer chains have large freedom to move, resulting in hole free volume. Below T_g, the "frozen" polymer chains can no longer rotate freely, leading to a great reduction of their mobility. The excess free volume arises from a nonequilibrium state, at which the excess free volume is trapped in the polymer matrix. On long time scales of weeks to years, the glassy polymers continuously evolve from the nonequilibrium state towards the equilibrium state, through a relaxation process known as physical aging [106]. During this process, the free volumes redistribute in the polymer, leading to a loss of the excess free volume.

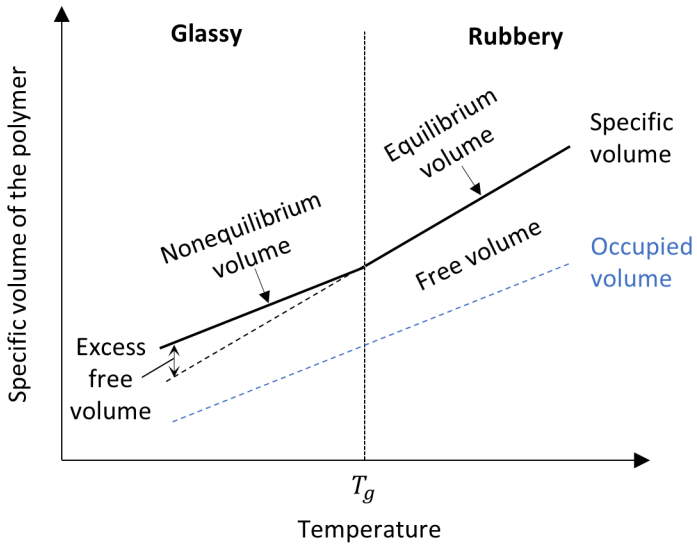


Figure 2.4: The specific volume of a polymer as a function of temperature, with free volume and occupied volume shown in the graph.

2.4.2 Free Volume Models

Various free volume models exist in the literature, including the most widely used models of Fujita [107, 108], and Vrentas-Duda [109–111]. In this section, the two models are reviewed, with a discussion on their primary differences and conditions under which they are applicable.

Fujita's Model

Fujita [107] considered a binary solution consisting of a monodispersed rubbery polymer and a pure solvent. It was assumed that a single solvent molecule and a polymer segment acted as thermal jumping units separated by free volume. On the basis of Doolittle's empirical relation for liquid viscosity [112, 113], Fujita made an *ad hoc* assumption that the relation was applicable to each jumping unit in polymer-solvent systems. Denoting the mobility of the solvent by m_s, expressed in terms of the fractional free volume, f:

$$\ln m_s = C_s - B_d/f, \tag{2.8}$$

where C_s and B_d are parameters, which were assumed to be independent of temperature and concentration. From solution thermodynamics, Fujita and Kishimoto [114] proposed a relation between f and the volume fraction of the solvent, ϕ_s:

$$f(\phi_s) = \overline{f}_p^0 + \beta\phi_s, \tag{2.9}$$

with

$$\beta = \overline{f}_s^* - \overline{f}_p^0, \tag{2.10}$$

where $\overline{f}_p^0$ denotes the fractional free volume of the pure polymer, and $\overline{f}_s^*$ refers to the fractional free volume associated with the solvent at the limit of $\phi_s \to 0$, *i.e.* in a very dilute solution that is close to a pure polymer.

Combining Eq. (2.8) and Eq. (2.9) yields:

$$\ln \frac{m_s(\phi_s)}{m_s(0)} = \frac{B_d\beta\phi_s}{(\overline{f}_p^0)^2 + \beta\overline{f}_p^0\phi_s}, \tag{2.11}$$

The mobility of the solvent, m_s, can be related to the thermodynamic diffusivity, D_T, by:

$$D_T = RTm_s, \tag{2.12}$$

where R is the ideal gas constant, and T is the absolute temperature of the solution. Thus, Eq. (2.11) can be equivalently expressed as:

$$\ln \frac{D_T}{D_T^0} = \frac{B_d\beta\phi_s}{(\overline{f}_p^0)^2 + \beta\overline{f}_p^0\phi_s}, \tag{2.13}$$

where D_T^0 represents the thermodynamic diffusivity at $\phi_s \to 0$. Fujita's free volume model has been successfully applied to a number of penetrant-rubbery polymer systems, particularly when the diffusivity exhibits a strong concentration dependence. However, Fujita [107] considered his model to be not applicable to the diffusion of small molecules, such as water, in polymers, owing to a failure of the model to describe the temperature and concentration dependence of the diffusivity in these cases. Nevertheless, Kulkarni and Stern [115] tested the validity of

Fujita's model for small non-polar molecules in polymers, and concluded that the inconsistency observed in the case of water was due to its hydrogen-bonding nature rather than a failure of the model. On the other hand, Vrentas and Duda [109] claimed that this hydrogen-bonding nature was unlikely to account for the lack of temperature and concentration dependence of diffusivity, given the clearly dominant free-volume effects in water-polymer systems. They claimed that Fujita's model could be derived from a more general free volume model proposed by them, under several further restrictions, which in their opinion were responsible for the failure of Fujita's model for water-polymer systems.

Vrentas-Duda Model

Vrentas and Duda [109] formulated a free volume model, starting from Cohen and Turnbull's theory of self diffusion [116], where an expression for the mobility of a molecule in pure liquids was derived under a so-called hole-volume assumption; this assumption states that the difference between the liquid volume per molecule and the average free volume per molecule gives the critical hole volume per molecule, which represents the minimum volume of a hole that a molecule must find in its neighbour for a thermal jump. Vrentas and Duda [109] extended Cohen and Turnbull's theory [116] to polymer-solvent systems and derived an expression for the mobility of the solvent, m_s:

$$\ln m_s(\phi_s) = C_s - \frac{\gamma'[\overline{v}_s^0\phi_s + \overline{v}_p^0\xi(1-\phi_s)]}{f_s\phi_s + f_p(1-\phi_s)}, \tag{2.14}$$

with

$$\overline{v}_s^0 = v_s^0/v_s, \overline{v}_p^0 = v_p^0/v_p, \tag{2.15}$$

where v_s and v_p denote the specific volumes of the pure solvent and the pure polymer, respectively; v_s^0 and v_p^0 are v_s and v_p at zero absolute temperature, respectively; f_s and f_p are the fractional free volumes of the pure solvent and the pure polymer, respectively; γ' is a numerical factor between 0.5 and 1; and ξ is a dimensionless quantity denoting the molar critical hole volume of the solvent relative to that of the polymer segment. Eq. (2.14) forms the basis of

the Vrentas-Duda free volume model.

Vrentas and Duda [109] derived from Eq. (2.14) an expression for the thermodynamic diffusivity, D_T:

$$\ln \frac{D_T}{D_T^0} = \frac{\overline{B}_d \overline{\beta} V \phi_s}{v_p f_p^2 + \overline{\beta} f_p V \phi_s}, \tag{2.16}$$

with

$$\overline{B}_d \overline{\beta} = \gamma' \left[\frac{\xi v_{hp} f_s}{v_p} - \frac{v_{hs} f_p}{v_s} \right], \tag{2.17}$$

$$\overline{\beta} = f_s - \frac{v_p}{v_s} f_p, \tag{2.18}$$

where v_{hs} and v_{hp} are the specific critical hole volume of a jumping unit of the solvent and that of the polymer segment, respectively.

The change in the liquid volume, V, on mixing can be represented by:

$$\Delta V(\omega_s) = V - \omega_s v_s - \omega_p v_p, \tag{2.19}$$

where ω_s and ω_p are the masses of the jumping units of the solvent and the polymer, respectively. When no volume change upon mixing is assumed, *i.e.* $\Delta V = 0$, Eq. (2.19) becomes:

$$\frac{V}{v_p} = 1 + \frac{(v_s - v_p)\omega_s}{v_p}. \tag{2.20}$$

Under the condition that:

$$\frac{(v_s - v_p)\omega_s}{v_p} \ll 1, \tag{2.21}$$

Eq. (2.16) can be reduced to Eq. (2.22), by replacing V with v_p:

$$\ln \frac{D_T}{D_T^0} = \frac{\overline{B}_d \overline{\beta} \phi_s}{f_p^2 + \overline{\beta} f_p \phi_s}. \tag{2.22}$$

This equation agrees with Eq. (2.13) that Fujita and Kishimoto [114] derived from their free volume formulation, despite that $\overline{B}_d$ and $\overline{\beta}$ differ from B_d and β in the contents. From the formal agreement, Vrentas and Duda [109] claimed that the Fujita's model, Eq. (2.13), was a special case of their more general model, Eq. (2.16), when the value of ω_s is small, *i.e.* polymer

solutions with dilute solvent, as suggested by the condition specified by Eq. (2.21). Futhermore, as illustrated in Vrentas and Duda's original paper [109], in order to guarantee that B_d and β in Fujita's model are equivalent to $\overline{B}_d$ and $\overline{\beta}$ in the Vrentas-Duda model, another condition needs to be met: the molecular weight of the solvent is equal to that of a jumping unit of the polymer segment. However, this condition may not be valid for all polymer-solvent systems. Thus, Vrentas and Duda [109] stated that the usefulness of the Fujita's model is restricted to certain scenarios, whilst the Vrentas-Duda model is applicable to polymer-solvent mixtures regardless of the size of the solvent. In addition, Vrentas and Duda [109] also pointed out that their model, coupled with experimental data for pure liquids, can be used to predict the concentration, molecular weight , and temperature dependence of diffusivities for amorphous polymer-solvent systems, whilst Fujita's model is a correlative one and does not have a predictive capability.

Fujita [117] in a later paper clarified a major difference, that Fujita's theory was based on the free volume per unit volume of solution, whereas the Vrentas-Duda theory was based on the average free volume per jumping unit. Fujita [117] disagreed with the conclusion that his model was a special case of the Vrentas-Duda model, by pointing out that Eq. (2.16) can be transformed into an expression conforming to Eq. (2.13) with $\overline{\beta} = f_s - f_p$ without invoking Eq. (2.21). Nevertheless, Fujita agreed that his theory lacked the predictive capability of the Vrentas-Duda theory. However, in another paper Fujita [118] questioned the predictability of the Vrentas-Duda theory, with respect to its assumptions. He recommended careful examinations of the assumptions used in the Vrentas-Duda theory to give satisfactory predictions and for better agreement with observations.

Applicability of Fujita and Vrentas-Duda Models

Both Fujita's free volume model and the Vrentas-Duda model have been extensively applied to diffusion in penetrant-polymer systems. A selected list of these works are summarised in Table 2.2. As a straightforward correlative model, Fujita's free volume model, which is the basis of many other free volume models, has been modified and applied to model permeation processes of various polymer-diluent systems. Some of these works are also included in Table 2.2.

Table 2.2: A non-exclusive summary of the literature applying the Vrentas-Duda theory and Fujita's theory of free volume.

Vrentas-Duda Theory		
No	Work	References
1	Effects of thermodynamic models on the predictions of the Vrentas-Duda free volume theory for concentrated polymer solutions.	Mossner and Grulke [119]
2	Representation of the behaviour of diffusion coefficients by the Vrentas-Duda free volume theory.	Yoon et al. [120]
3	Predictions of the diffusion behaviour for several polymer/solvent systems using the Vrentas-Duda free volume theory.	Hong [121]
4	Tests of the predictive capability of the Vrentas-Duda free volume model for diffusion of organic solvents in natural rubber.	Guo et al. [122]
5	Predictions of the solvent self-diffusion coefficients in rubbers with the Vrentas-Duda free volume theory.	Hong [123]
6	Tests of the Vrentas-Duda free volume theory for penetrant diffusion in rubbery polyers.	Tonge and Gilbert [124]
7	Evaluation of a multicomponent free volume model based on Vrentas-Duda theory applied to diffusion in liquids.	Mauviel and Favre [125]
8	Correlations of the diffusion coefficients determined from sorption kinetics measurements, with predictions of Vrentas-Duda free volume theory.	Schabel et al. [126]
9	Comparative studies on both Fujita's theory and Vrentas-Duda theory for diffusivity through polymeric membrane in pervaporation process.	Mafi et al. [127]

Continuation of Table 2.2

10	Measurements and correlations of the diffusivity in polymer-solvent systems using Vrentas-Duda free volume theory.	Danner [128]

Fujita's Theory

No	Work	References
1	Comparative investigation of the diffusion and viscosity behaviour of polybutadiene solutions.	Chalykh et al. [129]
2	Sorption and permeation of organic solvent in polypeptide membranes.	Kinoshita et al. [130]
3	Modelling the binary diffusion and solubility coefficients for CO_2, CH_4, C_2H_4, and C_3H_8 in polyethylene at elevated pressures using Fujita's free volume theory.	Kulkarni and Stern [115]
4	An interpretation of the temperature dependence of the self diffusion of polystyrene and polyethylene in the melt with the free volume theory in the form of Doolittle and Fujita.	Fleischer [131]
5	Predictions of separation factor and permeability in the separation of binary mixtures by pervaporation.	Rhim and Huang [132]
6	A study of the gas solubility and permeability of various cured polyalkoxysilylbutadiene films.	Hachisuka et al. [133]
7	Measurements of the transport of CO_2 in linear low-density polyethylene.	Laguna et al. [134]
8	An interpretation of the self-diffusion of water, ethanol and decafluropentane in perfluorosulfonate ionomer by Fujita's free volume theory.	Gong et al. [135]
9	Derivation of the concentration dependency of the diffusivity of a solvent in a polymer solution, on the basis of a modified Fujita-Doolittle free volume equation.	Hsu and Lin [136]

Continuation of Table 2.2		
10	Estimations of the thermodiffusion coefficients in ternary mixtures, using a new proposed model based on Fujita's free volume theory.	Abbasi et al. [137]

Other Free Volume Models

Apart from Fujita's model and the Vrentas-Duda model, which are the two most widely applied free volume models for penetrant-polymer systems, there exist at least 20 more in the literature for specific applications. Amongst these various models, four relatively new ones are presented and discussed in this section. They are Liu et al.'s generalised free volume model [138], Thornton et al.'s relation between diffusion and free volume [139], Ohashi et al.'s shell-like free volume theory [140], and Abbasi et al.'s thermodiffusion model [137].

Liu et al. [138] developed a free volume correlation for the self-diffusion coefficient, D, by considering both the molar free volume, V_f, and the activation energy, E_a:

$$D = f(V_f) \exp\left(-\frac{E_a}{RT}\right). \tag{2.23}$$

This relationship can also be applied to other transport properties, such as viscosity and thermal conductivity. Moreover, Liu et al. [138] investigated the relationship between free volume expressions and equations of state of a van der Waals type. Following a comparison of the effects of density, temperature and molecular shape, some free volume expressions were recommended to represent the transport properties over wide ranges of temperature and pressure.

Thornton et al. [139] modified Doolittle's empirical relation and obtained:

$$D = \alpha' \exp\left(\beta' f\right), \tag{2.24}$$

where α' and β' are constants; and f is the fractional free volume, as defined by Eq. (2.7). This relation has been shown to model the data for gas diffusion through a glassy polymer

well, and agree with a variety of computational simulations. Thornton et al. [139] claimed that it could be used as an efficient tool for predicting transport properties in a wide range of available polymers, on the basis of the fractional free volume. In addition, this relation has been shown to provide an exact solution to the vacancy diffusion equation, which allows accurate and convenient modelling of physical aging of thin films [141].

Ohashi et al. [140] developed the shell-like free volume theory to estimate the self-diffusivity in multicomponent polymeric systems, using only pure component parameters of the constituents. The shell-like free volume is defined as the free space surrounding the penetrant molecule that emerges from molecular collisions. The theory is expressed as follows:

$$D = D_0 \exp\left[-\frac{\hat{V}^*_{\text{pen.}}}{s_{\text{pen.}}/M_{\text{pen.}}} \frac{\sum_i \omega_i (s_i/M_i)}{\sum_i \omega_i (V_{f,i}/\gamma'')}\right], \tag{2.25}$$

where D_0 is the pre-exponential factor; $\hat{V}^*_{\text{pen.}}$ is the molecular core volume of the penetrant; $s_{\text{pen.}}$ is the molar surface area of the penetrant molecules; $M_{\text{pen.}}$ is the molecular weight of the penetrant; ω_i is the weight fraction of component i, which is in contact with the penetrant molecule; s_i, M_i, and $V_{f,i}/\gamma''$ represent the molar surface area, molecular weight and free volume of componoent i, respectively, with γ'' being the free-volume parameter. On the basis of the excellent prediction results, Ohashi et al. [140] concluded that this multicomponent shell-like free volume theory is an appropriate predictive tool for applications such as various polymeric membrane systems, polymer coating-drying processes, and diffusion in polymer solutions.

Abbasi et al. [137] proposed a new model for predicting the thermodiffusion coefficients. They incorporated the size and the concentration of the molecule, on the basis of a Fujita-type model to determine the ratio of evaporation energy to activation energy, τ_k, in ternary hydrocarbon systems:

$$\tau_k = \tau_{k,\text{pure}} \exp\left|1 - \frac{x_k V_k}{x_i V_i}\right|, \tag{2.26}$$

where $\tau_{k,\text{pure}}$ is the ratio of the evaporation energy to the viscous energy in pure limits; x_k and V_k are the mole fraction and the partial molar volume of component k in the mixture; x_i and V_i are the mole fraction and the partial molar volume of largest component in the

mixture. Abbasi et al. [137] showed that this new model resulted in an improvement in the accuracy of thermodiffusion modelling and the diffusivity estimation for the ternary mixtures they investigated.

2.5 Equations of State for Penetrant-Polymer Systems

In modelling polymer systems at high pressures, equations of state have several advantages over activity coefficient models. For instance, activity coefficient models ignore the equation of state properties of the pure components, and thus completely fail to describe the lower critical solution temperature (LCST) behaviour [104]. In contrast, EOS models are able to predict both upper critical solution temperature (UCST) and LCST types of phase behaviour in polymer solutions [142]. Second, the activity coefficient models work well at low reduced temperatures and up to moderate pressures, where the liquid phase is relatively incompressible [143]. Violation of these bounds may lead to serious problems, particularly for supercritical components. In comparison, EOS models are valid from the dilute-gas to the dense-liquid regions, and are not limited to incompressible liquids. Furthermore, in the cases of activity coefficient models, the use of different models for the various phases precludes the correct description of mixture critical points [143], whereas the EOS extended to mixtures provides accurate information for both pure components and mixtures.

2.5.1 Equations of State

The equations of state for polymer systems can be categorised into the following types [144, 145]:

- Cell theory. Many equations of state for P-V-T behaviour of chain molecular systems in the solid and melt states are based on the modifications of cell theory of Lennard-Jones and Devonshire (LJD) [146], which was developed for monomers. The cell models are based on the assumption that each molecule in the liquid is confined to a "cell" by its nearest neighbours, restricting the molecular motion to the small free volume of

the cell [147]. To adapt the cell model formalism to describe polymer liquids, Prigogine et al. [148, 149] proposed internal and external modes of polymer molecules, which are associated with internal motions of the molecules and intermolecular interactions, respectively.

- Lattice theory. In lattice models, each monomer segment, solvent molecule, or void occupies a single lattice site. The Sanchez-Lacombe equation of state [103, 104], which was derived from the lattice fluid theory by introducing vacant sites in the lattice, has been widely used to describe polymer-solvent phase behaviour of molecular fluids of arbitrary size.

- Hole theory. In the hole models, the thermal expansion of liquids is considered to result from holes, *i.e.* the vacant cells, while changes of cell volume are also allowed [150]. The representative Simha and Somcynsky [150] hole model has been successfully used to describe the P-V-T behaviour for several polymer liquids. However, the difficulty in solving the model has hindered its wide applications. To overcome its drawback of mathematical complexity, Zhong et al. [151] derived a simplified hole theory EOS, following the approach of Simha and Somcynsky [150]. Through a comparison between the two equations of state, Zhong et al. [151] showed that their EOS was of the same quality as the other, but with much less computing effort.

- Statistical associating fluid theory (SAFT). SAFT [152, 153] is a perturbation-based equation of state solution model for associating fluids, which contain clusters of molecules capable of forming associative complexes. SAFT accounts for the association effects and has been found to be accurate in predicting properties of pure components and mixtures over a wide range of operating conditions.

Amongst the various equations of state, the Sanchez-Lacombe EOS is the most widely used model to correlate the solubility and the swelling effect of CO_2 in polymers [154–156].

2.5.2 Sanchez-Lacombe EOS

The Sanchez-Lacombe (SL) EOS is a lattice-based statistical mechanical theory, which has been proven to be advantegeous for predicting gas and organic vapour solubilities in polymer liquids, as well as in semicrystalline polymer solids above T_g [144]. The penetrant at its limit of solubility is considered to be in thermodynamic equilibrium with the polymer, under the assumption that the polymer, being monodispersed and behaving as a liquid in the state above its T_g, does not dissolve in the dense phase of the penetrant. The SL EOS models the polymer solution as a lattice consisting of occupied and empty sites [103]. The vacancies or "holes" in the lattice account for the compressibility of a solution, related to the "free volume" [157]. These empty sites are introduced to illustrate the extra entropy change in the system, as a function of volume and temperature of the system [158].

Sanchez and Lacombe [103] expressed the total number of lattice sites, N_r, for a binary mixture of N $m-$mers and N_0 empty sites as:

$$N_r = N_0 + mN, \tag{2.27}$$

where N is the number of molecules in the system; each of the molecule occupies m sites (an $m-$mer); and N_0 is the number of vacant lattice sites. The total volume of the system is:

$$V = (N_0 + mN)v^*, \tag{2.28}$$

where v^* refers to the volume of a lattice site. Sanchez and Lacombe [103] defined a reduced density, $\tilde{\rho}$, as the fraction of the occupied sites:

$$\tilde{\rho} = \frac{\rho}{\rho^*} = \frac{mN}{N_0 + mN}, \tag{2.29}$$

with

$$\rho^* = \frac{M_W}{mv^*}, \tag{2.30}$$

$$\rho = \frac{NM_W}{V}, \tag{2.31}$$

where ρ^* is a characteristic parameter of the pure fluid, representing the scale factor for density; ρ is the mass density of the fluid; and M_W is its molecular weight. In particular, for polymer components, M_W refers to the number average molecular weight.

In addition to ρ^*, the SL EOS introduced two more characteristic parameters for pure components, *i.e.* the characteristic temperature, T^*, which is associated to the potential energy; and the characteristic pressure, p^*, which is related to the cohesive energy density of the component in the close-packed state, *i.e.* that of a liquid at 0 K [159]. The main equations of the SL EOS for the pure fluids and the mixtures will be elaborated in Section 6.2.2, where a solubility analysis is conducted based on the SL EOS.

2.6 Factors Affecting the Transport Properties

The transport properties can be affected by a number of factors: temperature, pressure, crystallinity, penetrant properties, polymer properties, *etc.* The effects of temperature, pressure and crystallinity are discussed in the following sections.

2.6.1 Effects of Temperature

The transport coefficients, namely permeability P, diffusivity D, and solubility coefficient S, depend on temperature according to Arrhenius laws:

$$P = P_{00} \exp\left(-\frac{E_P}{RT}\right), \tag{2.32}$$

$$D = D_{00} \exp\left(-\frac{E_D}{RT}\right), \tag{2.33}$$

$$S = S_{00} \exp\left(-\frac{\Delta H_S}{RT}\right). \tag{2.34}$$

The pre-exponential constants represent the limits of the coefficients when $T \to \infty$; E_P and E_D are the activation energies of permeability and diffusivity; and ΔH_S is the apparent heat

of solution [79, 160]. A relation exists for E_P, E_D and ΔH_S:

$$E_P = E_D + \Delta H_S. \tag{2.35}$$

These parameters depend on the morphology (*i.e.* amorphous or semicrystalline structure) of the polymer, as well as the temperature relative to the characteristic temperature (*e.g.* T_g) [79].

In a study of the transport of CH_4 in various polyethylenes at temperatures up to 80 °C and pressures up to 10 MPa, Flaconnèche et al. [161] reported that trends were evident in P and D, increasing with increasing temperature, whilst S appeared to be less sensitive to temperature. In addition, Clarizia et al. [162] reported in their study of gas transport in a polydimenthylsiloxane (PDMS) membrane in the temperature range of 15 °C - 65 °C, that permeability increased with temperature for all species considered (CO_2, CH_4, O_2, He, and N_2). Nevertheless, compared with the other gases, the gas which most readily permeated through the polymer, CO_2, was less affected by temperature. Meanwhile, the diffusivity for CO_2, CH_4 and O_2 increased with increasing temperature, whilst solubility decreased. In a study of the sorption of CO_2 and N_2 in molten polypropylene (PP) and high density polyethylene (HDPE) at 433.2 K, 453.2 K, and 473.2 K and pressures up to 17 MPa, Sato et al. [163] found that the solubilities of CO_2 decreased with increasing temperature, while those of N_2 increased within the range of temperatures investigated.

Regarding diffusivity, as can be seen from the above results, D is an increasing function of the temperature. This is due to the activation energy, E_D, which represents physically the energy level that a molecule needs to reach for a jump between one position and another [79], always being positive. The higher temperature promotes the diffusion process, in such a way that an increase in the free volume is caused by the increased segmental motions of the polymer.

Park and Paul [164] related the permeability, P, to the fractional free volume of the polymer

matrix, f, which is added to the Arrhenius formulation for P, *i.e.* Eq. (2.32) [165]:

$$P(T) = P_{00} \exp\left(-\frac{E_P}{RT}\right) \exp\left[-\frac{B_P}{f(T)}\right]. \tag{2.36}$$

Similarly, for D and S:

$$D(T) = D_{00} \exp\left(-\frac{E_D}{RT}\right) \exp\left[-\frac{B_D}{f(T)}\right], \tag{2.37}$$

$$S(T) = S_{00} \exp\left(-\frac{\Delta H_S}{RT}\right) \exp\left[-\frac{B_S}{f(T)}\right]. \tag{2.38}$$

In these equations, B_P, B_D and B_S are the penetrant-free volume interaction parameters, which are practically independent of temperature.

2.6.2 Effects of Pressure

A number of studies reported insignificant pressure effect on the gas transport coefficients in polyethylene. Flaconnèche et al. [161] found that the values of permeability, diffusivity and solubility for He and CH_4 in polyethylene hardly exhibited variations with pressure in the investigated range of 4 to 10 MPa. In a study of the diffusion of methane in linear polyethylene under various temperatures and pressures, Lundberg [166] found that at 104.04 °C, the diffusivity is approximately independent of pressure. However, at 162.78 °C and 188.31 °C, the diffusivity exhibited a decreasing trend with increasing pressure. Naito et al. [167] analysed the effect of pressure on permeation of 10 gases through semicrystalline polyethylene and polypropylene, in the pressure range of 1 - 130 atm at 25 °C, which is above T_g. They found that the permeability decreased with increasing pressure for slightly soluble gases (He, Ne, H_2, N_2, O_2, and Ar), whilst the permeability increased with increasing pressure for highly soluble gases (CH_4, Kr, CO_2, and N_2O). Accordingly, they attributed the pressure effect on permeability to two aspects: a decrease of diffusivity due to hydrostatic pressure, which compressed the polymer matrix and led to a reduction in the free volume; and an increase of solubility due to increased concentration at the higher pressure. Naito et al. [168] proposed a diffusivity model

to describe the two opposite effects:

$$D = D'_0 \exp\left(-\beta_h p + \alpha_c C\right), \tag{2.39}$$

where D'_0 is the diffusion coefficient at $p = 0$ and $C = 0$; β_h is a constant expressing the drop of diffusivity due to hydrostatic pressure effect; α_c is a constant characterising the increase of dissolved penetrant in the polymer. Naito et al. [168] also derived an equation for permeability:

$$P = D'_0 k_D \exp\left[-\beta_h p + \left(\sigma + \frac{\alpha_c}{2}\right) k_D p\right], \tag{2.40}$$

where k_D is the Henry's law coefficient, which is equivalent to S, the solubility coefficient independent of concentration; and σ is a constant related to polymer-penetrant interaction.

For slightly condensable gases, *e.g.* H_2, O_2, and N_2, under pressures lower than 10 MPa, Henry's law is likely to be obeyed, in which case the solubility coefficient seems to be only dependent on temperature, but neither hydrostatic pressure nor gas concentration [28, 168]. For more condensable gases, *e.g.* CO_2, N_2O, and C_2H_4, under significantly higher pressures, strong deviations from Henry's law behaviour, including non-linear sorption isotherms, which are convex to the pressure axis, can be observed for rubbery polymers [97]. In such cases, the solubility coefficient increases with increasing pressure, as a result of the swelling effect due to high penetrant concentration.

2.6.3 Effects of Crystallinity

Michaels and Parker Jr. [169] pointed out that for semicrystalline polymers, the crystalline phase was an effectively impermeable dispersed phase to penetrants, whilst the permeation process took place almost exclusively in the amorphous region. The dispersed crystalline phase impedes the penetrant transport under two effects: first, the penentrant molecules are constrained to move through irregular intercrystallite passages, adding extra path length for diffusion; and second, the polymer chain-segment mobility might be reduced in the interstitial amorphous phase, raising the energy barrier for diffusion. To account for these two effects, Michaels

and Parker Jr. [169] introduced "tortuosity factor", ς, and "chain immobilisation factor", ψ, obtaining the expressions for the transport coefficients:

$$S = S^* \phi_a, \tag{2.41}$$

$$D = \frac{D^*}{\varsigma \psi}, \tag{2.42}$$

$$P = \frac{P^* \phi_a}{\varsigma \psi}, \tag{2.43}$$

where S^*, D^* and P^* are the solubility coefficient, the diffusivity and the permeability of the penetrant in completely amorphous polymer; and ϕ_a is the volume fraction of the amorphous phase in the polymer. Michaels and Bixler [20] pointed out that the existence of the crystalline regions hardly changes the nature of the amorphous phase, so that the transport coefficients in completely amorphous polymer (*i.e.* S^*, D^* and P^*) are equivalent to those in the amorphous phase of a semicrystalline polymer (denoted by S_a, D_a and P_a). That is to say:

$$S^* = S_a, D^* = D_a, P^* = P_a. \tag{2.44}$$

Peterlin [170] proposed different expressions for the diffusivity and permeability, by considering the amorphous phase as a complex network of tortuous thin flat channels, with the mobility of the amorphous chains restrained by their ends fixed in the adjacent crystals:

$$D = \frac{\Psi}{\zeta} D_a, \tag{2.45}$$

$$P = \frac{\Psi \phi_a}{\zeta} P_a, \tag{2.46}$$

with Klute's "detour ratio" Ψ between 0 and 1, describing the detour required to avoid the impermeable crystalline zone [171]; and Michaels and Parker's "blocking factor" ζ greater than 1, suggesting narrow amorphous regions between two crystalline zones [169].

Practically, understanding of the transport mechanisms in semicrystalline polymers is limited by the facts that it is not possible to directly measure S^*, D^* or P^*, and that it is not common to

measure the properties for a completely amorphous polymer (S_a, D_a or P_a). Budzien et al. [172] showed that the crystalline phase could affect the nature of the amorphous phase. Budzien et al. [172] criticised Michaels and Parker's oversimplified treatment of neglecting the contribution of the crystalline phase for sorption. Instead, they proposed a method to predict the gas solubilities in completely amorphous polyethylene, by extrapolating alkane behaviour to the long chain limit with Flory-Huggins theory. Their predictions were approximately a factor of two higher than those found from Michaels and Bixler's extrapolation of solubilities in semicrystalline polyethylenes [173].

2.7 Experimental Techniques

There are three categories of experimental methods for penetrant permeability in polymers [174]:

(1) Sorption-desorption method, which measures the uptake of the penetrant by a known amount of polymer. The solubility coefficient can be directly obtained from the amount of the absorbed gas, which is typically very small and thus requires sensitive measurements.

(2) Isovolumetric permeation method, which determines the amount of the gas permeating into a closed chamber by gravimetric or manometric measurements.

(3) Isobaric permeation method, in which case the permeated gas is swept away by a flowing gas towards a device, which measures the concentration of the permeated gas in the flow.

2.7.1 Sorption-Desorption

Determinations of the transport coefficients can be achieved by direct measurement of the rate of uptake or loss of a penetrant by a polymer sample, via gravimetric, pressure-decay, or volumetric methods. There are several advantages of the sorption approach, compared with the permeation approach. First, it is suitable for lengthy experiments on materials in which the

diffusion coefficients are low [175]. Second, it reduces uncertainties in the sample surface area exposed to permeation. Moreover, visual inspection of the penetration process in the sample is allowed in some cases.

Gravimetric Method

The weight variation of a polymer sample after absorbing the penetrant can be quantified with gravimetric approaches. For instance, Kamiya et al. [176] determined precisely the solubilities of gases (*e.g.* N_2, CH_4, C_2H_6, and CO_2) in polymers, such as low density polyethylene (LDPE), polycarbonate (PC), and polysulfone (PSUL), at pressures up to 50 atm, using an electromicrobalance. Chaudhary and Johns [177] used a novel magnetic suspension balance with good mass sensitivity, for measuring gas solubilities in polymers. With this device, the balance can be separated from the saturation system and thus be protected from aggressive gases. The needs for accurate determination of the initial pressure (or volume), and conversions of pressure (or volume) to mass with fugacity, are avoided by using the gravimetric approach, in comparison with the other approaches.

Pressure-Decay or Volumetric Method

Being simple in its principle and mechanics, the pressure-decay method has been adopted in a number of studies [178–185] to measure the penetrant solubilities in polymers at high pressures. With the pressure-decay method, the solubility is obtained by measuring the reduction in pressure due to sorption in a constant-volume vessel containing a polymer sample. To overcome the problem caused by Joule heating of the gas, so as to obtain accurate gas density from pressure data at the beginning of an experiment, Koros and Paul [180] developed a dual-chamber method, in which the gas was expanded into the sample chamber from a second vessel of known pressure, volume and temperature. This dual-chamber method significantly improved the reliability and accuracy of the pressure-decay method, and thus has been the standard method of pressure-decay experiments for decades [184]. On that basis, Davis et al. [184] developed two new volumetric sorption techniques, in which the initial density was measured

by simple extrapolation of the mass uptake curve or was measured gravimetrically using a small titanium capsule. With the solubility and diffusion data collected for carbon dioxide, ethylene, and nitrogen in LDPE, it was shown that the simpler extrapolation method produced the same results as the more complicated dual-chamber method.

2.7.2 Permeation

Isovolumetric Permeation

The amount of the gas crossing a polymeric membrane and accumulating in a closed receiving chamber of a constant volume, is determined as a function of time, by gravimetric or manometric measurements. With the manometric methods, which are widely used for determining permeability, the pressure change due to the gas accumulated in the receiving chamber, is continuously recorded [167, 168, 186]. For instance, with the manometric measurements, Naito et al. [167] determined the permeabilities for 10 gases through semicrystalline polymers above T_g, in the pressure range of 1-130 atm.

Apart from the manometric methods, there are also analytical methods, in which the quantity of permeated gas is determined indirectly from parameters that are proportional to it. These analytical techniques include infrared spectroscopy, ultraviolet (UV) spectroscopy, mass spectroscopy, radio tracers and thermal conductivity [174].

Isobaric Permeation

In the cases of isobaric permeation, the permeated gas is swept away by a flowing gas stream (*e.g.* N_2), towards a measuring device. The concentration of the permeated gas in the stream can be measured by analytical techniques that are able to measure relatively low concentrations with a high accuracy [187–189].

There are several advantages of this method. It is able to quantify the permeation of each species in a gas mixture by using gas chromatography or mass spectrometry. Moreover, it is possible

to determine the intrinsic transport coefficients of each species, and to detect the presence of particular affinities of a polymer for a gas [174]. Therefore, this technique has been extensively applied to selective membranes for binary mixtures (*e.g.* CO_2-CH_4) [187, 188, 190–192].

2.8 Concluding Remarks

This chapter has reviewed the two models that describe the common permeation processes: the solution-diffusion model and the pore-flow model. The former is most applicable to the cases of penetrant transport through polymeric materials considered in this work. The theories related to the transport properties and the methods for determining their values were presented. The time-lag method, which has been extensively applied since it was introduced, provides a convenient approach for simultaneous determinations of the transport properties from a single permeation experiment. However, this method can be over-simplified for scenarios where the diffusivity is concentration-dependent or where Henry's law is not obeyed.

Free volume theories offer an interpretation of the concentration-dependent diffusivity in a free-volume context. Two commonly applied free volume models, Fujita's model and the Vrentas-Duda model, have been discussed and compared. It was concluded that the Vrentas-Duda model had a predictive capability that the Fujita's model lacked, whilst many other free volume models, including the one derived in this work, were developed on the basis of the straightforward formula of Fujita's. Amongst the various equations of state, Sanchez-Lacombe EOS is considered to be an appropriate one for estimating the thermodynamic properties of CO_2-polymer systems. Therefore, it is aimed in this work to apply both the free volume theory and the Sanchez-Lacombe EOS to elucidate the diffusion and sorption mechanisms for systems under various conditions.

The effects of temperature, pressure and crystallinity on the transport properties have been described with examples and the accompanying theories. Various experimental techniques for permeation studies have been reviewed. In this study, the isobaric permeation method was adopted, owing to its superiority in accurate measurements of relatively low concentrations

of the permeated species. Furthermore, despite that pure CO_2 was investigated in this work, the isobaric permeation method is advantageous to future permeation studies for gas mixtures through polymers, since the permeation of each component could be accurately quantified by the method. In addition to permeation experiments, which were conducted in this work by applying the isobaric permeation method, sorption experiments using the sorption-desorption method were also designed, as described in the following chapter. The sorption experiments will be carried out in the future to supplement the current permeation study and verify the results obtained in this work.

Chapter 3

Experimental

3.1 Introduction

In this chapter the properties of the materials, including the gases and the polymers employed in this work, are specified. A detailed description of the design of the experimental setup is provided, with safety aspects taken into consideration. The apparatus used for the experiment is introduced. The experimental procedure is given, so that other researchers are able to reproduce the experiments. Finally, this chapter ends with a discussion of the repeatability and uncertainty of the experiment.

3.2 Materials

3.2.1 Gas Specifications

Three gases were used in this study: carbon dioxide, nitrogen, and argon. Information and specifications for them are presented in Table 3.1.

Table 3.1: Purchase information and specifications for the gases used in this work.

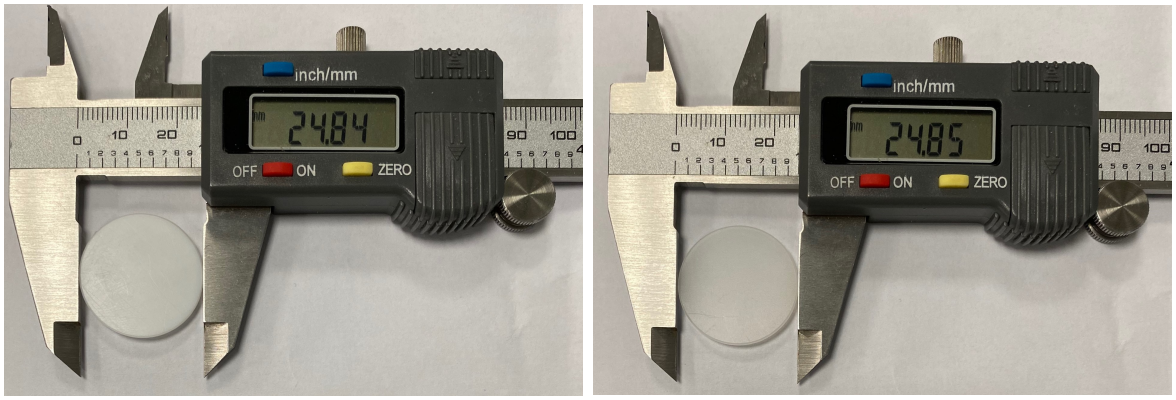
	Carbon Dioxide*	Nitrogen	Argon
Process	Permeating fluid	Sweep gas	Purge gas
Supplier	BOC	BOC	BOC
Grade	CP grade	Oxygen free	Zero grade
Purity (mol%)	> 99.995	> 99.95	> 99.999
Pressure** (bar)	55 - 65	300	200
Temperature** (°C)	20	20	20

* of a dip tube for liquid withdrawal.

** At purchase.

3.2.2 Polymer Characterisation

Two semicrystalline polymers were used in this study: polytetrafluoroethylene (PTFE) and high density polyethelene (HDPE). All the polymer samples were cut into round pieces from the plain sheets supplied by Direct Plastics (Figure 3.1). The characteristics of the two polymers are summarised in Table 3.2.



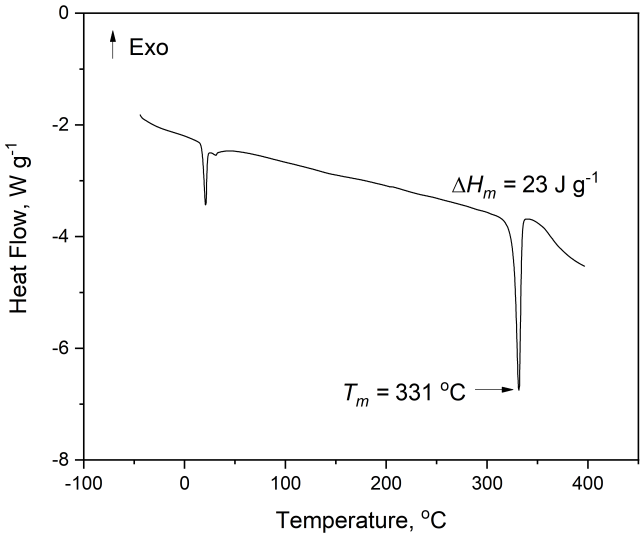
(a) (b)

Figure 3.1: (a) PTFE sample; (b) HDPE sample.

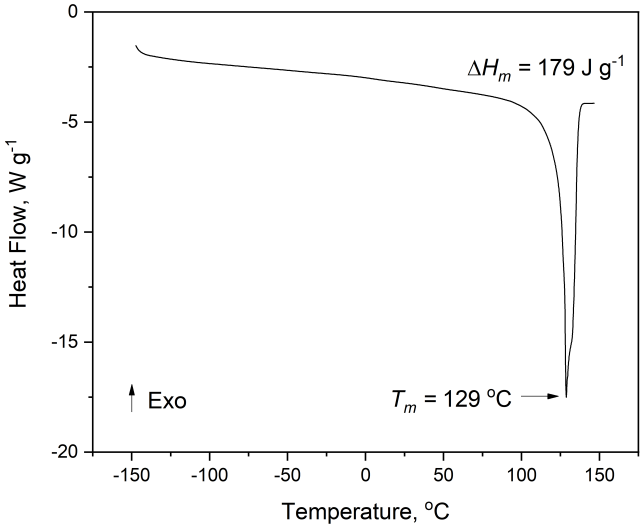
Table 3.2: Characteristics of the polymer samples.

Sample	Thickness, L (mm)	Diameter, d (mm)	Density, ρ (g cm^{-3})	Amorphous Fraction, ϕ_a	Glass Transition, T_g (°C)
PTFE	1.05 ± 0.01	24.78 ± 0.18	2.18 ± 0.03	0.73 ± 0.03	-20 [193]
HDPE	0.92 ± 0.01	24.82 ± 0.19	0.94 ± 0.01	0.39 ± 0.02	-95 [194]

Differential Scanning Calorimety (DSC) Measurements



(a) PTFE



(b) HDPE

Figure 3.2: DSC curves of the samples.

The degree of crystallinity, X_c, which specifies the percentage of the crystalline volume of the semicrystalline polymer, can be obtained from DSC measurements [195]. The PTFE and the HDPE samples were analysed in duplicate on a TA Instrument Q2000 DSC (10 °C min^{-1}, -50 to 400 °C for PTFE; and 10 °C min^{-1}, -150 to 150 °C for HDPE). The degree of crystallinity,X_c, is calculated by:

$$X_c = \Delta H_m / \Delta H_m^0, \tag{3.1}$$

where ΔH_m is the enthalpy of fusion, *i.e.* the heat absorbed by the polymer sample during the heating process; ΔH_m^0 is the enthalpy of fusion of the 100% crystalline poymer. The enthalpy of fusion, ΔH_m, was estimated by integration of the melting endotherm.

Figure 3.2a and Figure 3.2b show the heat flows measured by DSC for the two polymer samples. For PTFE, the melting temperature of the sample, T_m, was found to be 331 °C. From the DSC measurement, it was found that ΔH_m was 23 J g^{-1}. Typically, ΔH_m^0 is 85 J g^{-1} for PTFE [196]. Therefore, X_c was 0.27. The amorphous volume fraction of the sample, ϕ_a, obtained by subtracting X_c from 1, was 0.73. For HDPE, T_m, was found to be 129 °C, and ΔH_m was 179 J g^{-1}. For 100% crystalline HDPE, ΔH_m^0 is typically 293 J g^{-1} [197]. Therefore, X_c was 0.61, and accordingly ϕ_a was 0.39.

It was noticed in Figure 3.2a that there was a smaller peak at around 21 °C for PTFE sample, whilst such peak was not observed in Figure 3.2b for HDPE sample. For PTFE, the peak may indicate a glass transition at the temperature of 21 °C. For HDPE, this glass transition was not detected from the DSC measurement. Three reasons might account for it. First, the glass transition temperature of the particular grade of HDPE used was outside the applied temperature range (*i.e.* below -150 °C). Nevertheless, this hypothesis seems unlikely, given the glass transition temperature of -95 °C suggested in the supplier's material datasheet for HDPE [194]. Second, T_g was within the experimental temperature range, but the heating rate could affect the measuring result. This hypothesis was tested by conducting the measurements with different heating rates at up to 40 °C min^{-1}. However, the smaller peak that associated with glass transition temperature was not observed in all cases. Third, the DSC measurement was not sensitive enough to capture the glass transition of the HDPE sample. In fact, apart from

DSC, dynamic mechanical analysis (DMA), which measures the response of a sample to an applied oscillatory strain, is considered to be the most sensitive technique for T_g analysis. For reference, the glass transition temperatures given in the supplier's material data sheets for the PTFE and the HDPE samples are shown in Table 3.2. It is noted that these temperatures are well below those at which all the permeation experiments were conducted in this work.

3.3 Experimental Design

3.3.1 Permeation Setup

As shown in Figure 3.3, the setup for permeation experiments can be divided into four sections: feeding, first-stage pressurisation, second-stage pressurisation, and permeation. For pressures in a range of 1 - 500 barg, an ISCO 260D syringe pump, P-1, was used to raise the pressure. For pressures in a range of 500 - 1000 barg, P-1 and P-2, the latter of which is an ISCO 65D syringe pump, were used for the high pressure. Prior to each experiment, argon was used to purge the system and also for leak testing. To start a measurement, the three-way valve (V-1) was open to the C-1 (CO_2) side and closed to the C-2 (Ar) side. Liquid CO_2 at around 57 bar, which is the equilibrium pressure of CO_2 at room temperature, was drawn out from C-1 and flowed to the system through V-1. No pressure regulator was attached to C-1. Instead, a pressure indicator was used for reading the outlet pressure of CO_2 from C-1. A pressure relief valve (PRV-1) was set at 65 barg and relieved higher pressure in line 01001 in case of failure of the non return valves.

Despite that permeation experiments under pressures up to 600 bar are the focus of this project, the experimental setup was designed and constructed with greater capacities, so that it can be conveniently extended for experiments conducted under higher pressures up to 1400 bar (20000 psi) and adapted for separate sorption experiments as follow-ups for future projects. The process flow diagram for permeation experiment is presented (in landscape) on the following pages, whilst information on the sorption experimental design is included in Appendix A.

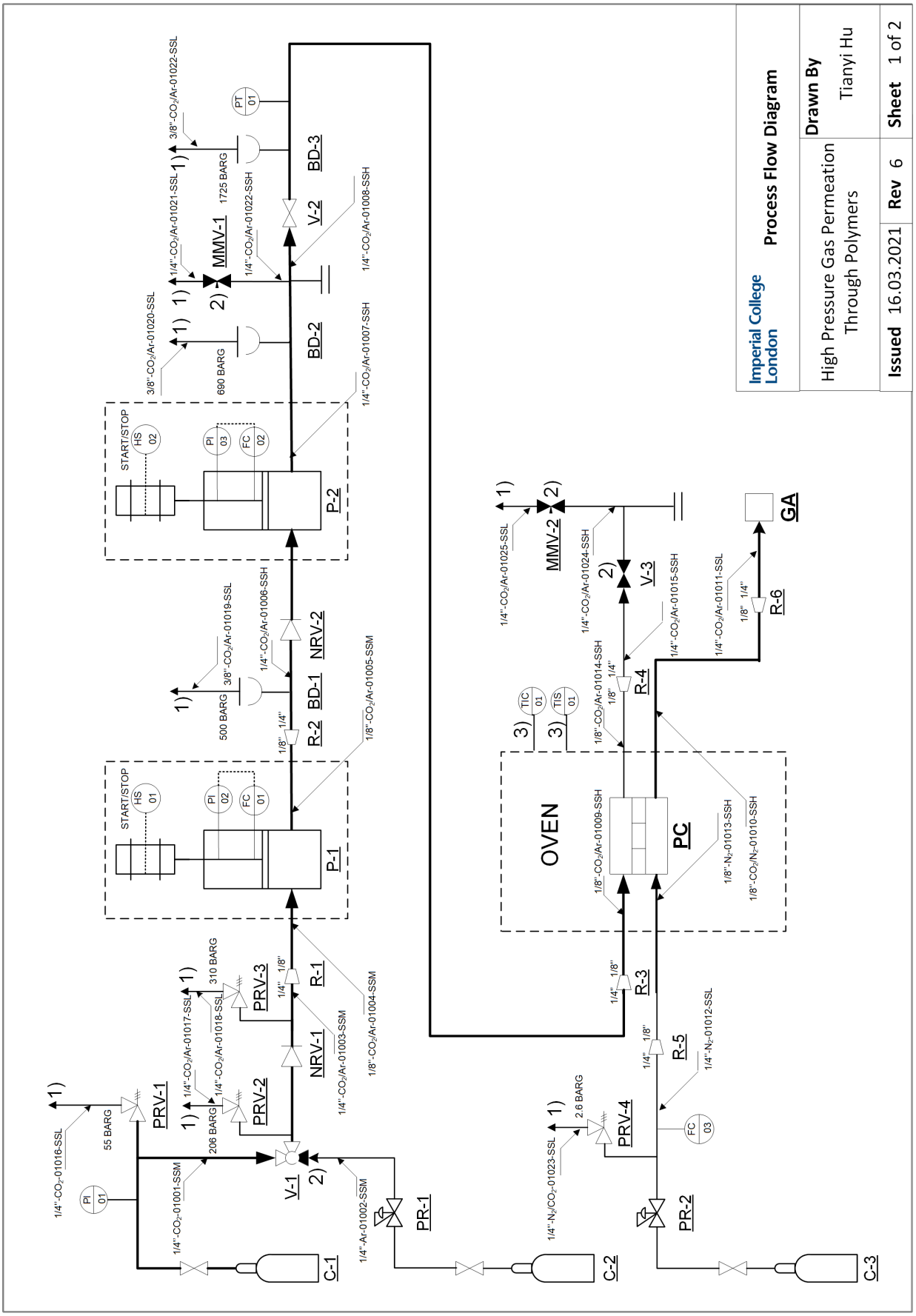
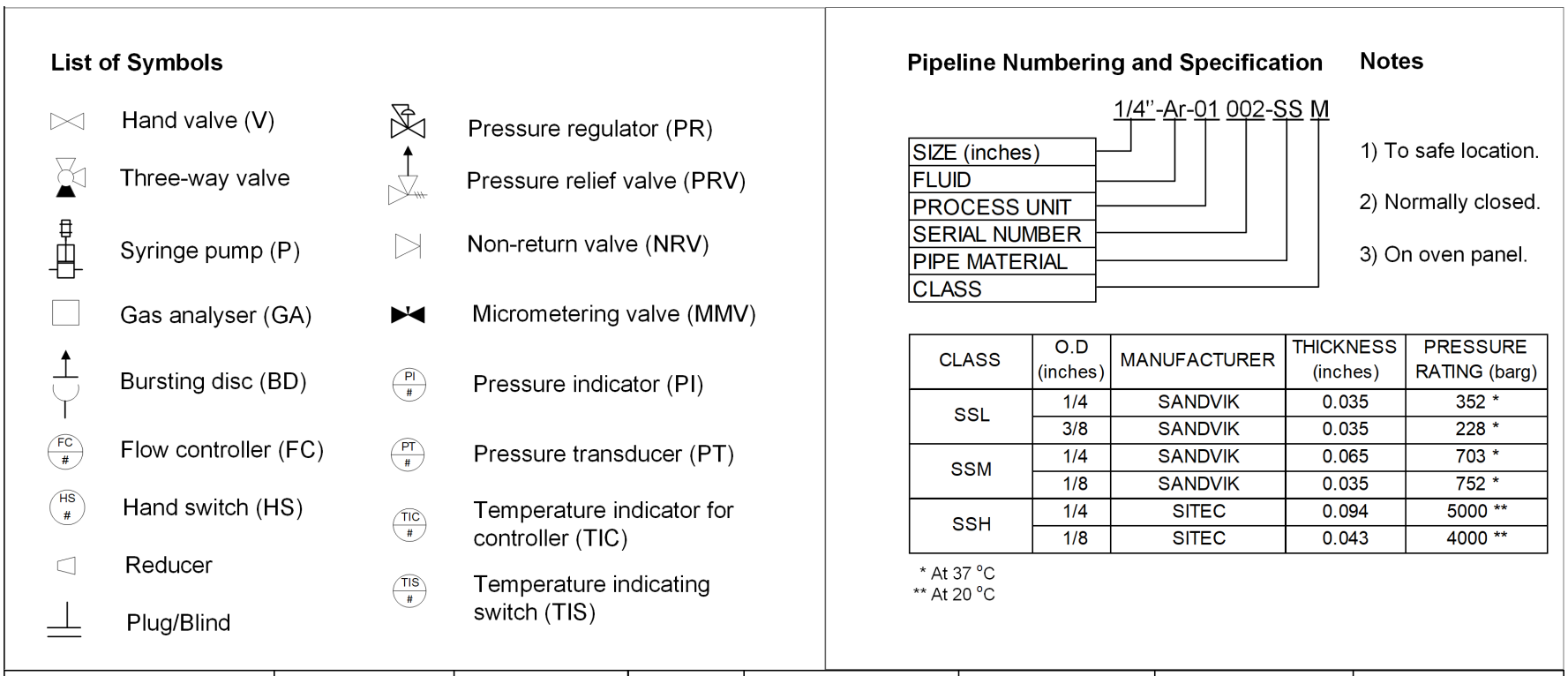


Figure 3.3: Process flow diagram for permeation experiments (1 of 2).



Equipment Tag	C-1	C-2	C-3	P-1	P-2	PC	GA
Description	CO_2 Cylinder	Ar Cylinder	N_2 Cylinder	Syringe Pump	Syringe Pump	Permeation Cell	Gas analyser
Material of Construction	Carbon Steel (CS)	Carbon Steel (CS)	Composite	Stainless Steel (SS)	Stainless Steel (SS)	Stainless Steel (SS)	Composite and metal
Operating pressure (barg)	180 - 200	200	2	up to 517	up to 1379	up to1725	Ambient
Operating Temperature (°C)	20	20	20	5 - 40 (Ambient)	5 - 40 (Ambient)	up to 300	51.4
Fluid	CO_2	Ar	N_2	CO_2 or Ar	CO_2 or Ar	CO_2 or Ar	CO_2
Capacity	5 kg	88 kg	20 L	266 mL or 107 mL/min	68 mL or 25 mL/min	2 mL	1 L/min

Items	SWAGELOK (barg)			VALCO (barg)		PT-1,2 (barg)	FC-3 (psig)	SITEC (barg)	
	V-1	Tee	NRV-1	R-1	R-2			Tee (1/4HP-DN3)	NPT Adapter
Pressure Ratings	689	1379	414	1379	689	1600	150	4000	1500

Items	SITEC (barg)							
	BD-1	BD-2	BD-3	NRV-2	MMV-1,2	V-2 to 5	R-3 to 6	Tee (1/4HP-G1/2"-DN3)
Pressure Ratings	500 +/- 10%	690 +/- 10%	1725 +/- 5%	4000	2000	2000	4000	2500

Imperial College London — **Process Flow Diagram**

High Pressure Gas Permeation Through Polymers

Drawn By Tianyi Hu

Issued 16.03.2021 **Rev** 6 **Sheet** 2 of 2

Figure 3.3: Process flow diagram for permeation experiments (2 of 2).

In the permeation section of the setup, the inert nitrogen, which was used as a sweeping gas, was discharged from C-3 at room temperature and at a pressure of 2 barg, which was controlled using a pressure regulator (PR-3). A pressure relief valve (PRV-3) was set at 230 barg. The nitrogen stream with a flowrate of 10 cm^3 min^{-1}, which was controlled by a mass flow controller from MKS Instruments (FC-3), flowed into the downstream compartment of the permeation cell (PC) through line 01012. It carried the permeated CO_2 into a gas analyser (GA) through line 01011. The concentration of CO_2 was measured by an infrared (IR) gas analyser (LI-COR LI-850). The permeation cell (PC) was placed in an oven. The cell was comprised of a top plug and a bottom plug, with the sample disc inserted in between, forming the high-pressure upstream compartment and the low-pressure downstream compartment. Apart from the permeated portion of the CO_2 stream, the rest of the stream was discharged to a safe location through a micrometering valve (MMV-2). At the end of the experiment, the valves on the gas cylinders were closed, and the fluids in the system were vented to a fume cupboard.

3.3.2 Safety Aspects

The major hazard of the experiment was the high pressure in the system. In a case of over-pressure, serious consequences could result, when the pressure exceeds the equipment design pressure. As a result, several layers of protection were implemented to minimise the risk of overpressure and to ensure a safe working environment.

Bursting Discs (BD)

BD-1 was used between P-1 and the non-return valve (NRV-2) to protect P-1. The pump design pressure, which was the shear key breaking pressure, was 683 bar. Beyond this pressure, the pump could be damaged. The design pressure of P-1 was 646 bar, with a maximum operating pressure of 517 bar (646 bar $\times$ 0.8 =517 bar). A bursting disc with a nominal bursting pressure of 646 bar ($\pm$ 10%) could potentially burst at 711 bar (646 bar $\times$ 1.1 = 711 bar), which was above the shear key breaking pressure of 683 bar, leading to potential damage to the pump.

Thus, it was recommended to operate P-1 at pressures not higher than 400 bar, and use a bursting disc of a nominal bursting pressure of 500 bar (± 10%).

BD-2 was used between P-2 and the valve (V-2) to protect P-2. A nominal bursting pressure of 690 bar (± 10%) was chosen for BD-2. The lowest possible bursting pressure was 621 bar (690 bar × 0.9 = 621 bar). The highest possible bursting pressure was 759 bar (690 bar × 1.1 = 759 bar), which was well below the pump design pressure of 1986 bar.

The bursting disc BD-3 was used between P-2 and PC to protect the pump and the cell. The design pressure of the cell was 1725 bar, which was also the maximum operating pressure of P-2 (1379 bar / 0.8 = 1725 bar) and the nominal bursting pressure of BD-3 (1725 bar ± 5%). The bursting disc could burst at 1811 bar (1725 × 1.05 = 1811 bar), which was below the shear key breaking pressure of P-2 of 1986 bar and the pump would be protected. However, this highest possible bursting pressure of 1811 bar was above the design pressure of PC. Therefore, it was recommended to conduct experiments at pressures lower than 1725 bar. For follow-up projects, the maximum pressure of the experiments has been determined to be 1400 bar, which is the maximum operating pressure of P-2.

Pressure Relief Valves (PRV)

PRV-1, set at 65 barg, was attached to the CO_2 cylinder (C-1). It was used to protect C-1 from the potential reverse flow of the high-pressure gas, in a case of V-1 failure, introducing high-pressure gas from the Ar cylinder (C-2), or a failure of NRV-1, introducing high pressure gas from downstream and damaging C-1. PRV-2, set at 206 barg, was used to protect both C-1 and C-2 from the failure of NRV-1. PRV-3, set at 310 barg, was used to protect NRV-1, whose pressure rating is 414 barg.

Regarding the low-pressure N_2 lines, the pressure relief valve (PRV-4), set at 2.6 barg, was used to protect the tubing, the N_2 cylinder (C-3), the mass flow controller (FC-3) whose maximum allowable pressure is 10 bar, and the gas analyser (GA) with a maximum allowable flowrate of 1 L min^{-1} at atmospheric conditions.

3.3.3 Apparatus

Pumps



(a) (b)

Figure 3.4: (a) ISCO 260D pump (P-1); (b) ISCO 65D pump (P-2).

Teledyne ISCO 260D syringe pump, as shown in Figure 3.4a, P-1, was used for first-stage pressurisation of CO_2. It offered pressure control to 517 bar, with high-precision pressure transducers of 0.1% linear accuracy. The applicable flowrate of the pump ranged from 0.001 to 107 cm^3 min^{-1}, with a cylinder capacity of 266 cm^3. Teledyne ISCO 65D syringe pump, as shown in Figure 3.4b, P-2, was used to assist the second-stage pressurisation of CO_2. It offered precise control for high-pressure applications conducted at up to 1379 bar. The applicable flowrate of this pump ranged from 0.00001 to 25 cm^3 min^{-1}, with a cylinder capacity of 68 cm^3. The two pumps can be operated at ambient temperatures of 5 to 40 °C, with pump cylinder heated up to 200 °C.

Permeation Cell

The permeation cell has a design pressure of 1725 bar (25000 psi) and a maximum operating pressure of 1400 bar (20000 psi). The cell passed a hydro test of 2475 bar (35880 psi) and can be operated in a temperature range of 0 - 250 °C, with a design temperature of 300 °C. The cell was CE-marked, indicating that it complies with Category IV, Module G of the Pressure Equipment Directive (PED).



Figure 3.5: Permeation cell (PC): (1) circlip; (2) cap; (3) sleeve; (4) top plug; (5) dowel; (6) dip tube; (7) bottom plug.

As can be seen from Figure 3.5, the permeation cell is comprised of a top plug (4) and a bottom plug (7). They are clamped together in a sleeve (3) by two locking caps (2). When the two plugs are assembled together, a removable sealing ring clamps up on a sample disc. The sealing ring is placed into the inside face of the top plug and seals against the top plug using an O-ring and a back-up ring. Any leakage between the sample disc and the sealing ring can be detected by a 1/8" NPT leakage detection port in the sleeve. In the bottom plug, the sample disc sits

on top of a porous sintered stainless steel disc, which is 2 mm thick with a nominal pore size of 1 µm, supplied by Aegis Advanced Metals Ltd. The part of the sample disc exposed to CO_2 is 10 mm diameter.

Two 1/8" Sitec ports in the top plug are used to introduce and vent the upstream high-pressure gas through the gas chamber by a 1/8" dip tube (6), which was intended to enable gas to be bubbled through liquid in future experiments involving water or hydrocarbons. Similarly, the bottom plug has two 1/8" Sitec ports for the N_2 stream through the porous support and carrying the permeated gas. Two circlips (1) are used to retain the two caps (2) on the plugs. These plugs have been treated with PTFE based electroless Nickle to prevent galling. Two threaded holes on the sleeve help fix the permeation cell on a support frame, which is placed inside an oven.

Gas Analyser



Figure 3.6: The infrared (IR) gas analyser (LI-COR LI-850) gas analyser used in this work.

Figure 3.6 shows a LI-850 CO_2/H_2O gas analyser (GA) from LI-COR, which is based on non-dispersive infrared absorption, was used to quantify the concentration of CO_2 in the sweep gas. This analyser was considered to be suitable for the work, owing to its several advantages. First, it has a thermostatically controlled IR detection system, which provides excellent stability and high accuracy of measurement. Specifically, for CO_2 and H_2O concentrations, a narrow band

optical filter, which only allows the wavebands of interest to illuminate the detectors, is applied to eliminate the influence of other infrared absorbing gases. Second, liquid nitrogen is not required by the analyser, since it does not use mercury cadmium telluride (MCT) detectors. Thus, the LI-850 analyser has a lower expense and a smaller size, making it convenient to use. Third, the volume of the sample cell is only 14.5 cm^3, leading to a relatively quick response of the system.

The analyser used in this work was calibrated using a gas of known concentration (CK Special Gases, 500 ± 5 ppm carbon dioxide mixed with nitrogen). A magnitude of 500 ppm for the molar fraction of CO_2 in the sweeping stream was typical in a permeation experiment. By conducting a step-change measurement, where the time lag of the concentration change measured by the analyser was recorded after a step change in the flowrate of the sweeping stream, *e.g.* from 20 $cm^3\ min^{-1}$ to 10 $cm^3\ min^{-1}$, a dead time of two minutes was determined for the permeated CO_2 travelling from the cell to the analyser, under the flowrate of 10 $cm^3\ min^{-1}$ for the sweeping stream. This dead time was substracted from the measured permeation time to obtain the real permeation time, resulting in a shift of the time axis by this amount in a flux-versus-time plot. In addition, the random noise of the concentration measurement was found to be less than 1 ppm, when the calibration gas flowed through the analyser, at an average CO_2 concentration of 500 ppm.

Other Apparatus

The flowrate of the sweeping N_2 stream was 10 $cm^3\ min^{-1}$, referred to standard temperature and pressure, STP, of 273.15 K and 1 atm. The flowrate was controlled by a mass flow controller (FC-3) supplied by MKS Instruments, as shown in Figure 3.7a, which can be operated in a temperature range of 0 - 50 °C, with a maximum inlet pressure of 150 psig (10 barg). The flowrate measured by the mass flow controller was calibrated with N_2 using a bubble column, resulting in measured flowrates of 10.00 ± 0.01 $cm^3\ min^{-1}$.

A pressure transmitter (PT-1) from WIKA, as shown in Figure 3.7b, was used to measure the CO_2 pressure in the upper compartment of the cell. It is suitable for high-pressure applications

with pressure ranging from 0 to 1600 bar (0 to 20000 psi), and temperature in a range of -30 to 100 °C. The pressure transmitter was calibrated using a gas pressure controller (DHI model PPCH-G-70M), in a pressure range of 0 - 600 bar. The pressure transmitter measured pressure with a random noise of less than 0.5 bar.



(a) (b) (c)

Figure 3.7: (a) Mass flow controller (MKS Instruments); (b) pressure transmitter (WIKA); (c) Thermocouple (TC Ltd).

A Type K thermocouple, as shown in Figure 3.7c, was used for measuring the temperature of the permeation system. This thermocouple was suitable for temperature measurement below 250 °C. It measured the temperature with a random noise of less than 0.01 °C. The thermocouple was inserted through a hole on the top plug of the cell, with its tip located within 3 mm of the sample disc. The thermocouple measured the temperature of the cell when it reached thermal equilibrium with the inside of the oven. It was assumed that the temperature measured by this thermocouple was the same as that of the fluid inside the cell, and thus represented the system temperature at the thermal-equilibrium state.

3.4 Experimental Procedure

The operating procedure for the permeation experiment is detailed here, to enable the permeation measurements to be understood, so that the experiment can be conveniently and consistently reproduced.

1) Leak test.

   (a) Check the pressure of each cylinder, and the condition of each apparatus with each connection port.

   (b) Test leaks for the system, by introducing gases at certain pressures to the closed system, *e.g.* Ar at 20 bar to the upper compartment of the cell, and N_2 at 2 bar to the lower compartment. If the pressures could be maintained for a certain period of time, *e.g.* 10 minutes, the system passes the leak test. Otherwise, test leaks for each connection port, until the leaks are found and the problem is solved.

2) Preparation.

   (a) Prepare a 1 mm thick sample disc of 10 mm diameter.

   (b) Place the sample disc into the permeation cell.

   (c) Tighten the permeation cell and all fittings.

3) Evacuation.

   (a) Close the valves attached to the CO_2 cylinder (C-1) and the Ar cylinder (C-2). Open the three-way valve (V-1) towards the C-1 end during the first evacuation run, and towards the C-2 end during the second evacuation run. Close MMV-1 and V-2.

   (b) Connect the vacuum pump to MMV-1. Switch on the vacuum pump and slowly open MMV-1. Evacuate this section for 15 minutes for each of the two evacuation runs.

   (c) After the 30-minute evacuation, close MMV-1, switch off the vacuum pump, and disconnect it from MMV-1. Close MMV-2 and open V-3.

   (d) Connect the vacuum pump to MMV-2. Switch on the vacuum pump and slowly open MMV-2. Evacuate this section for 30 minutes.

   (e) After the 30-minute evacuation, close MMV-2, switch off the vacuum pump, and disconnect it from MMV-2.

(f) Close the cylinder valve and the pressure regulator attached to the N_2 cylinder (C-3). Connect the vacuum pump to the outlet port of the gas analyser.

(g) Switch on the vacuum pump. Evacuate this section for 30 minutes.

(h) After the 30-minute evacuation, switch off the vacuum pump and disconnect it from the gas analyser.

4) Permeation.

(a) Open the valve of the N_2 cylinder (C-3). Set the outlet pressure to 2 barg using the pressure regulator.

(b) Open V-1 towards the CO_2 cylinder (C-1) side. Open V-2, and close MMV-1, MMV-2, and V-3.

(c) Open the valve of C-1. Switch on P-1 and P-2.

(d) Switch on the oven, and heat up the system to the required temperature.

(e) If the required system pressure is between 50 and 300 barg, then use P-2. Refill P-2 to a "full" position, but keep P-1 at an "empty" position. Run P-2 at the constant pressure (CP) mode and specify the desired pressure.

(f) If the required system pressure is between 300 barg and 600 barg, then use both P-1 and P-2. Refill both pumps to "full". Run P-1 at the constant flow (CF) mode and specify the flowrate to be 90 $cm^3\ min^{-1}$, which is the maximum flowrate of P-1. Once P-1 cylinder becomes empty, run P-2 at the constant pressure (CP) mode and specify the desired pressure.

5) Depressurisation.

(a) After the permeation experiment is finished, close all cylinder valves. Close V-2 and open V-3.

(b) Switch off all electrical devices.

(c) Slowly open MMV-1 and MMV-2, and vent the gas until atmospheric pressure is reached.

3.5 Experimental Methodology

As mentioned earlier, an isobaric permeation method was adoped in this work, whereby the permeated CO_2 was swept away by a flow of N_2, towards the gas analyser. Denoting the molar fraction of CO_2 in the sweeping N_2 stream by y_{CO_2}, the flowrate of the sweeping stream by q, and the surface area of the sample disc exposed to CO_2 in the upper compartment of the cell by A, the permeation flux of CO_2, F_m, can then be expressed by:

$$F_m = \frac{q y_{CO_2}}{A}, \tag{3.2}$$

where q is in $cm^3\ s^{-1}$, and A is in cm^2. Therefore, F_m is in $cm^3(STP)\ cm^{-2}\ s^{-1}$. The uncertainty of F_m was obtained as a combined result of the uncertainties of the measurements for q, y_{CO_2} and A, which were repeated for multiple times for the same measurements. To be specific, taking a run conducted with a PTFE sample disc as an example, the permeation area, A, was measured for several times. The measurements led to a mean value of 0.79 cm^2, with a standard deviation (SD) of 0.01 cm^2. The uncertainty of A was taken to be twice the value of SD, *i.e.* $\pm$ 0.02 cm^2, which included about 95% of the measurements. Therefore, the value for A was expressed as 0.79 $cm^2 \pm 0.02\ cm^2$. Similarly for q and y_{CO_2}, mean values were determined from a number of measurements, and twice the standard deviations were used as the uncertainties. That is to say, q was 10.00 $cm^3\ min^{-1} \pm 0.01\ cm^3\ min^{-1}$, and y_{CO_2} was 393 ppm $\pm$ 1 ppm. By applying Eq. (3.2), the mean value of F_m was calculated from the mean values of q, y_{CO_2} and A. The uncertainty of F_m was obtained in such a way that its upper bound, which represented its largest possible value, was calculated from the maximum values of q and y_{CO_2}, as well as the minimum value of A; and vice versa. As a result, the mean value and the uncertainty range of F_m were 8.33×10^{-5} $cm^3(STP)\ cm^{-2}\ s^{-1} \pm 0.16\times10^{-5}$ $cm^3(STP)\ cm^{-2}\ s^{-1}$, as shown in Table 4.4 for Run-P-1. The other fluxes shown in the table were obtained in a similar way.

In order to analyse the permeation data obtained from measurements, by using Fick's laws of diffusion, together with free volume theory and Sanchez-Lacombe EOS, the following assumptions were made: (1) At the start of an experiment, the sample disc was initially free of the

penerant CO_2. (2) During the experiment, the top surface of the sample disc was considered to be saturated with CO_2 at the system temperature and pressure. (3) The concentration or the volumetric fraction of CO_2 in the penetrant-polymer system was assumed to be zero at the lower face of the sample disc. These assumptions were considered to be reasonable for this work, and they will be discussed in greater detail in Chapter 4.

3.6 Systematic and Random Errors

There are two main types of measurement errors: systematic errors and random errors. Systematic errors normally arise from poor calibration of the instruments, errors in observation, or interference from the environment. Therefore, systematic errors are predictable in a way that they affect the measurements with the same amount or by the same proportion. Primarily, systematic errors influence a measurement's accuracy, which indicates how close the measurement is to the true value. On the other hand, random errors normally result from instrumental limitations, or dynamic changes in conditions. Random errors are unpredictable and often exhibit a Gaussian normal distribution. Random errors affect a measurement's precision, which represents how consistent a series of repeated measurements are with each other.

In an experiment, the quantities of interest may be directly measured, or calculated from other measured quantities. The uncertainty of each quantity can be analysed, from the point of view of the systematic errors or the random errors. Once the contributing factors to the uncertainty are identified, error mitigating measures can be taken to obtain more accurate results. Here, an example is given for the analysis of the experimental uncertainty.

The flowrate q was controlled by the mass flow controller (FC-3), whose control range was 1 - 50 cm^3 min^{-1}. Within this range, five flowrates were tested with N_2 and a bubble column, to compare with the specified values. Regarding the random errors introduced by reading the volumetric flask and the stopwatch, each specified flowrate was tested for five times, and an average value was taken as the measured flowrate.

To reduce the offset error and the scale factor errors, which are two common types of the

systematic errors, the zero and span of the gas analyser were checked and reset, by using the calibration gas mixture of carbon dioxide and nitrogen (CK Special Gases). Typically, a permeation experiment lasts for about 10 hours, after which drift in the zero and span may occur. As a result, it is recommended to conduct calibration before each experimental run to increase the accuracy of y_{CO_2}.

Inside the permeation cell, a removable sealing ring seals against the the top plug and the sample disc, which sits on top of a porous sintered disc in the bottom plug. The area for permeation, A, was determined by the area of the porous sintered disc, through which the permeated CO_2 was swept by the N_2 flow. Since the same sintered disc was used for all experimental runs, the random error associated with A can be effectively minimised by repeating the measurement of the size of the sintered disc for several times.

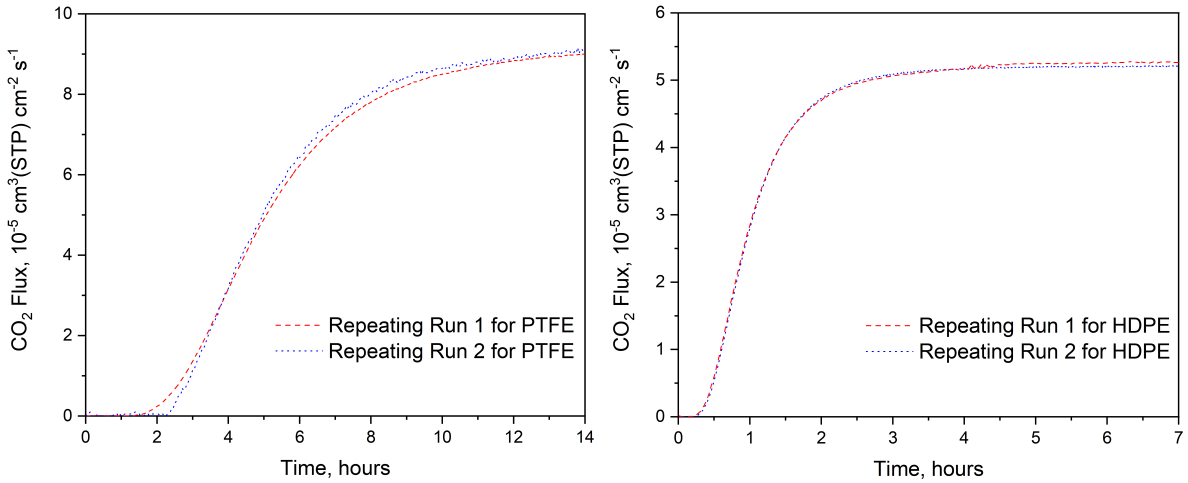
In fact, the systematic error might be the major factor contributing to the uncertainty, owing to the assumptions made for calculation. Firstly, variations of the permeation area due to the extrusion of the polymer sample into the tiny pores of the sintered disc were neglected. Secondly, only axial diffusion was considered, whereas radial diffusion was neglected. In addition, for the calculation of diffusivities with Fick's diffusion laws in the following chapters, the swelling effect of CO_2 on the polymer sample was neglected, meaning that the thickness of the sample disc was assumed to remain unchanged. The errors introduced by these assumptions existed in all experimental runs and they were due to simplifications of the diffusion process. Therefore, these were considered as systematic errors rather than random errors.

These errors cannot be minimised by repeating the experiments. Nevertheless, there seem to be appropriate reasons for neglecting each of them: (i) there has been no evidence of polymer extrusion, upon removing the sample from the permeation cell after the measurements; (ii) the polymer disc is relatively thin, comparing its thickness of about 1 mm with the diameter of around 25 mm, so that axial diffusion is considered to be more significant than radial diffusion; (iii) at pressures up to 200 bar, measurements of CO_2 sorption in polyethylene conducted by Sarrasin et al. [198] indicated approximately 5% swelling, which seemed to be a reasonably small degree for swelling. Although the systematic errors due to these assumptions are not quantified

in this work, for future's investigation to obtain more accurate results, it is recommended that the effects of the assumptions on the results should be evaluated, and appropriate methods should be adopted to take these effects into account.

The systematic measurement errors can be minimised by routinely calibrating the equipment, whereas the random errors cannot be predicted or eliminated. However, it is helpful to take an average value of multiple data points to be close to the true value. For the flowrate of N_2 stream, the obtained data points for q were within the range of 10.00 cm^3 min^{-1} $\pm$ 0.01 cm^3 min^{-1}. For y_{CO_2}, the data points clustered around the average value within 1 ppm. For A, the uncertainty primarily came from the systematic errors. It was considered to be equal to the area of the porous sintered disc, whose dimensions can be precisely measured by taking the measurements for multiple times at various positions of the sintered disc.

3.7 Repeatability



(a) PTFE, 56 bar, 28 °C (b) HDPE, 52 bar, 35 °C

Figure 3.8: Breakthrough curves of CO_2 flux against time, obtained from repeating runs of CO_2 through PTFE and HDPE.

Owing to the relatively low permeabilities of CO_2 in the two polymers, it normally took around 10 hours to finish each experimental run at a specific temperature and pressure. In the cases with multiple pressure steps, a typical experimental time of more than 80 hours for one run

would be expected. To achieve the objectives of the project, as specified in Section 1.4, within the constrained time, the measurement was not repeated for each run. However, representatively, the repeatability of the experimental results was examined with two repeating runs at 56 bar and 28 °C with two initially penetrant-free PTFE samples, and with two repeating runs at 52 bar and 35 °C with two HDPE samples. As can be seen from Figure 3.8, although the curves in the two cases do not entirely overlap, the differences between the curves are comparable to the 2% uncertainty obtained from the flux error analysis. Given that the sample discs used in the two repeating runs may have slightly different properties, the repeatability presented in Figure 3.8a and Figure 3.8b was considered acceptable.

In this study, the uncertainties for the quantities of interest were considered based on three categories: (i) those of the measured quantities, *e.g.* N_2 flowrate q, CO_2 molar fraction in N_2 stream y_{CO_2}, and permeation area A, *etc.* As mentioned in Section 3.5, the uncertainty ranges for these quantities were obtained by repeating the measurements for multiple times, and taking twice the values of the standard deviations around the mean values, covering about 95% of the measurements. (ii) The quantities calculated from measured ones, such as permeation flux F_m, and penetrant concentration in the mixture C. The upper and lower bounds of these quantities, *i.e.* their largest and smallest possible values, were calcualted from the uncertainty bounds of the measured quantities appeared in the equations. (iii) The modelling parameters estimated from the slope or the intercept of linear regression, *e.g.* c and $|k|$ estimated by early approximation, solubilty coefficient S estimated from the linear part of the C *vs.* p curves, and binary interaction parameters k_{ij} and η_{ij} from SL EOS modelling, *etc.* The uncertainties of these estimates were obtained with 95% confidence intervals. In the following chapters, the uncertainty bounds were shown for all quantities presented in the tables.

Chapter 4

Transient Permeation Following a Single Pressure Step

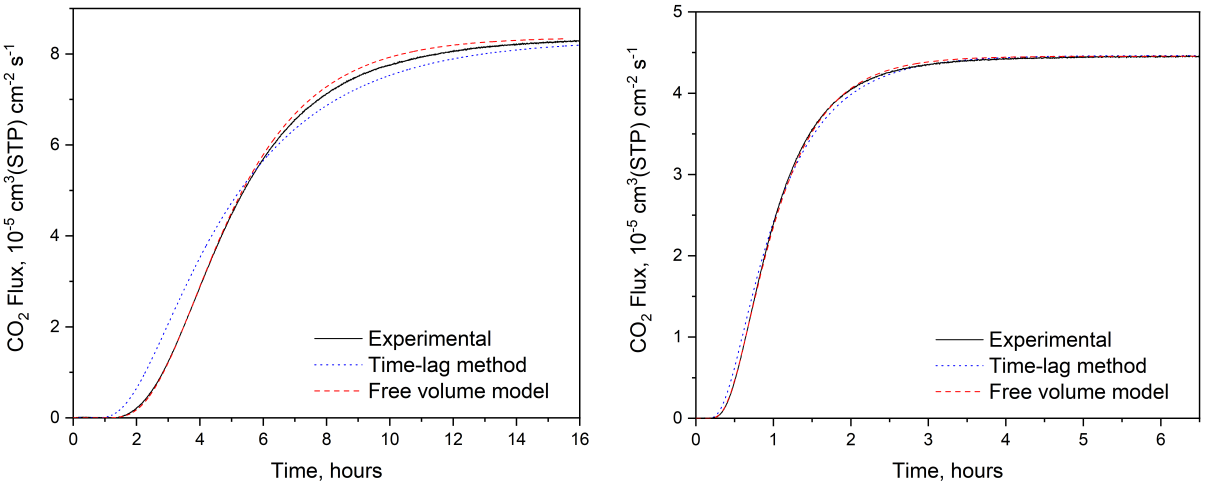
4.1 Introduction

This chapter focuses on transient measurements of the permeation of CO_2 through PTFE and HDPE on a single pressure step under elevated pressures. This chapter consists of two parts: Part I develops a simplified, nondimensionalised free volume model and proposes a method of graphical analysis; and Part II applies this method to the analysis of the experimental results, from which the transport properties and lumped free-volume parameters are determined.

4.1.1 Background

A fundamental understanding of the permeation process of a fluid through a polymer is important in a wide range of applications [49, 199–201]. Many of these processes take place at elevated temperature and pressure, under which conditions the diffusivity can exhibit a strong dependence on penetrant concentration. The permeation of CO_2 in the two polymers investigated in this study is such an example. Figure 4.1 shows the results, which provided the motivation for developing the new framework. As can be seen, in both cases, the breakthrough

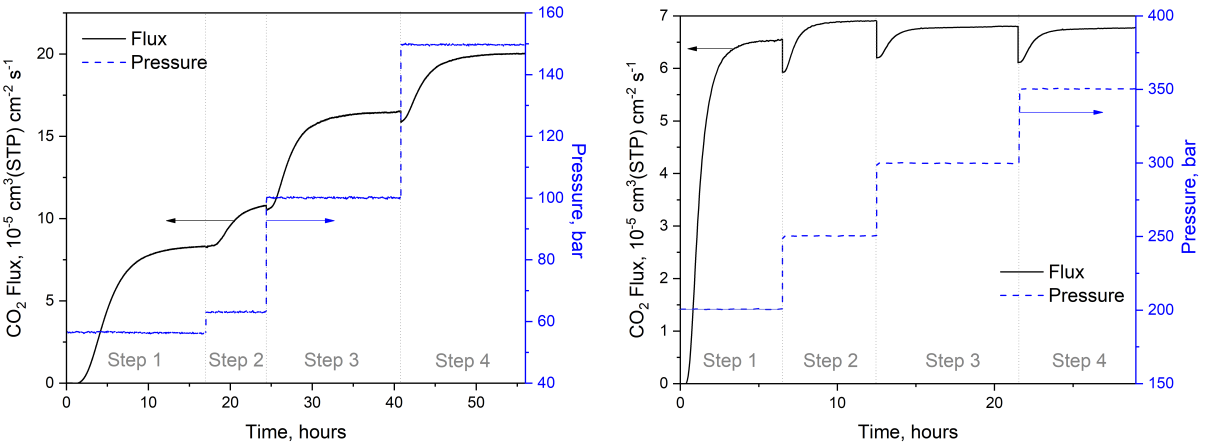
curves obtained by applying the time-lag method where a constant diffusivity was assumed (see Section 2.3.2), were not as close as those obtained by using the free volume model with a thermodynamic diffusivity (see Section 4.2), to the experimental curves.



(a) PTFE, 55 bar, 28 °C (b) HDPE, 55 bar, 35 °C

Figure 4.1: Comparisons of the breakthrough curves of CO_2 flux against time, obtained from the permeation experiments, by applying the time-lag method with a constant diffusivity, or by using the free volume model with a thermodynamic diffusivity, for the two polymers.

In addition, it was observed that during a successive permeation experiment which involved multiple pressure steps (see Chapter 5), when the upstream pressure was suddenly increased, there was an immediate drop in the flux, as can be seen in Figure 4.2.



(a) PTFE, 28 °C (b) HDPE, 35 °C

Figure 4.2: Plots of flux and pressure against time in a successive permeation experiment for PTFE and HDPE.

This drop of the flux upon pressure increase also seems to be observed in the transient perme-

ation measurements made by Craster and Jones [202]. It was speculated in this work that the compaction caused by the higher hydrostatic pressure acting upon the polymer matrix led to a decrease of the free volume in the polymer, giving rise to a decrease of the diffusivity and accordingly a drop in the flux. Following the near-instantaneous drop, the permeation flux would gradually increase, owing to the increase in solubility at the higher pressure, also leading to an increase of the thermodynamic diffusivity, until a new steady state is established.

4.1.2 Aims

There is a lack of experimental data in literature, regarding the concentration-dependent transport properties for penetrant-polymer systems at elevated pressures. Therefore, through the work presented in this chapter, it is aimed to further develop the practical and theoretical understanding of the topic. Specifically, the following objectives are set out for this chapter:

1) to conduct measurements of the transient permeation of CO_2 in PTFE and HDPE at various temperatures and pressures;

2) to report the experimental results and interprete the data using a free volume model;

3) to nondimensionalise the free volume model, so as to reduce the number of the parameters;

4) to further simplify the free volume model and propose a straightforward method, which can eliminate the requirements for advanced computational tools for data analysis and parameter estimation;

5) to examine and discuss the applicability of the proposed method to new and existing measurements of transient permeation, with the permeation systems investigated in this work as examples.

Part I: Theoretical

4.2 Model Development

4.2.1 Constant Diffusivity

The permeation flux, F, *i.e.* the rate at which the penetrant emerges from unit area of the bottom face of the polymer, $x = L$, is given by:

$$F = -D\left(\frac{\partial C}{\partial x}\right)_{x=L}, \tag{4.1}$$

where C is the concentration of the penetrant; x is the space coordinate normal to the polymer section; and L is the initial thickness of the polymer disc. L may be considered a nominal thickness, since the increase in L due to the absorption of the penetrant in the polymer is not considered in this work. However, it was found from literature that swelling may increase with pressure under low to moderate pressures, and then barely change or even decrease under high pressures, owing to the effect of hydrostatic pressure [36, 198]. For CO_2 sorption in polyethylene, Sarrasin et al. [198] reported approximately 5% swelling at pressures up to 200 bar.

A typical unit of the concentration is mol cm^{-3}, and the unit of diffusivity is normally $cm^2\ s^{-1}$. The corresponding unit of the flux is mol $cm^{-1}\ s^{-1}$. In permeation studies, it is also common to express the gas volume at STP. That is to say, the amount of the penetrant is expressed in *e.g.* cm^3 (STP), instead of mol. Nevertheless, in either case, as long as consistent units are used for F and C, the unit of D is always $cm^2\ s^{-1}$.

Fick's second law for non-steady state diffusion with constant diffusivity is written:

$$\frac{\partial C}{\partial t} = D\frac{\partial^2 C}{\partial x^2}. \tag{4.2}$$

For the experiments carried out in this study, the initial and boundary conditions for the above

diffusion equation are:

$$t = 0, \quad 0 < x < L, \quad C = 0, \tag{4.3}$$

$$t \geq 0, \qquad x = 0, \quad C = C(x = 0), \tag{4.4}$$

$$t \geq 0, \qquad x = L, \quad C = 0, \tag{4.5}$$

where $C(x = 0)$ denotes the concentration of the penetrant at the top surface of the polymer disc. At $t = 0$, the polymer disc was initially free of the penetrant. The top surface was considered to be saturated with CO_2 at the system temperature and pressure. At the lower face of the polymer $x = L$, the diffusing CO_2 was swept away with the N_2 carrier gas. Given the low pressure of the sweeping stream, and that the measured concentration of CO_2 in the sweeping stream was typically no more than 500 ppm, it was reasonable to assume that $C \approx 0$ at the bottom surface.

4.2.2 Free Volume Model

Fujita's free volume model [107] was modified by Kreituss and Frisch [203] for semicrystalline polymers, by introducing the amorphous volume fraction of the polymer, ϕ_a, into the expression:

$$D_T = RTA_d \exp\left[-\frac{B_d}{\phi_a v_f(T, p, \nu)}\right]. \tag{4.6}$$

Here, D_T is the thermodynamic diffusion coefficient of the penetrant [204]. The pre-exponential constant, A_d, correlates the mobility of a diffusing molecule in the polymer, with the probability of the molecule finding a large enough hole nearby to displace into. The parameter, B_d, characterises the minimum size of the hole necessary for such a displacement. The fractional free volume of the system, $v_f(T, p, \nu)$, is a function of T, p and ν, where p is the pressure applied to the polymer, and ν is the volume fraction of the penetrant in the polymer mixture. Eq. (4.6) can also be derived from the Vrentas-Duda model, under simplifying assumptions, which are considered reasonable for typical diluent-polymer systems [109]. The fractional free

volume, $v_f(T, p, \nu)$, can be expressed as:

$$v_f(T, p, \nu) = v_f^*(T, p, 0) + \gamma\nu, \tag{4.7}$$

where $v_f^*(T, p, 0)$ is the fractional free volume of the pure polymer at p and T, and γ is the coefficient of concentration dependence. The volume fraction, ν, can be related to the volumetric concentration of the penentrant in the mixture at the standard conditions, C_{STP}:

$$C_{STP} = \frac{\nu}{V'}, \tag{4.8}$$

where V' is the ratio of the specific volume of the penetrant at the experimental conditions, $V_{T,p}$, to that at the standard conditions, $V_{273\text{K},1\text{atm}}$:

$$V' = \frac{V_{T,p}}{V_{273\text{K},1\text{atm}}}. \tag{4.9}$$

At specific T and p, $V_{T,p}$ is a constant, leading to a constant value for V'. Thus, C_{STP} is proportional to ν. Fick's second law of diffusion is written:

$$\frac{\partial C}{\partial t} = \frac{\partial}{\partial x}\left(D_M \frac{\partial C}{\partial x}\right). \tag{4.10}$$

Here, D_M is the mutual diffusion coefficient of the two-component system. D_M is related to the thermodynamic diffusivity, D_T, by [107, 115]:

$$\frac{D_M}{1-\nu} = D_T \tag{4.11}$$

Combining Eq. (4.8) to Eq. (4.11), the following equation is obtained:

$$\frac{\partial \nu}{\partial t} = \frac{\partial}{\partial x}\left(D_T \frac{\partial \nu}{\partial x}\right). \tag{4.12}$$

Similar to the constant diffusivity case, the initial and boundary conditions are:

$$t = 0, \quad 0 < x < L, \quad \nu = 0, \tag{4.13}$$

$$t \geq 0, \qquad x = 0, \quad \nu = \nu(x = 0), \tag{4.14}$$

$$t \geq 0, \qquad x = L, \quad \nu = 0, \tag{4.15}$$

where $\nu(x = 0)$ refers to the volume fraction of the penentrant at the top surface of the polymer. An equation for the flux, F, expressed in terms of D_T and ν, can be derived [205, 206]. In a binary mixture, the penetrant is denoted by component 1 with a subscript "1", and the polymer is denoted by component 2 with a subscript "2". The mass flux of the penetrant, F_1^m can be written:

$$F_1^m = \omega_1 \left(F_1^m + F_2^m\right) - \rho D_M \nabla \omega_1. \tag{4.16}$$

Here, F_i^m is the mass flux of component i; ρ is the density of the system; ω_1 is the mass fraction of the penetrant. When the mobility of the polymer is negligible, *i.e.* $F_2^m \ll F_1^m$, and when the area of the polymer sheet is sufficiently large, *i.e.* radial diffusion can be neglected, Eqn. (4.16) can be rearranged into the following form:

$$F_1^m = \frac{-\rho D_M}{1 - \omega_1} \frac{\mathrm{d}\omega_1}{\mathrm{d}x}. \tag{4.17}$$

Also, ρ can be expressed by Eqn. (4.18), with an assumption of zero excess volume of mixing:

$$\frac{1}{\rho} = \omega_1 V_1 + \omega_2 V_2. \tag{4.18}$$

Here, V_i is the specific volume occupied by component i in the system. The volume fraction of the penetrant, ν, can be expressed by:

$$\nu = \frac{\omega_1 V_1}{\omega_1 V_1 + \omega_2 V_2}. \tag{4.19}$$

Multiplying both sides of Eqn. (4.17) by V_1, the equation can be reformulated as:

$$V_1 F_1^m = \frac{-D_M}{1-\nu}\frac{\mathrm{d}\nu}{\mathrm{d}x}. \tag{4.20}$$

It can be noted that $V_1 F_1^m$ is equivalent to the flux, F, which represents the local flux relative to stationary coordinates. Combining Eqn. (4.8), Eqn. (4.11) and Eqn. (4.20), F can be expressed in terms of D_T and ν by:

$$F = -\frac{D_T}{V'}\left(\frac{\partial \nu}{\partial x}\right)_{x=L}. \tag{4.21}$$

4.2.3 Nondimensionalised Model

It is difficult to explicitly solve the diffusion equations, Eq. (4.12) and Eq. (4.21), without resorting to advanced numerical tools, since D_T has a complex relationship to the penetrant volume fraction ν, as suggested by Eq. (4.6) and Eq. (4.7). Nevertheless, efforts can be made to nondimensionalise D_T and thus transform the intricate diffusion equations into more straightforward ones. By introducing $D_T(T, p, 0)$, which is the thermodynamic diffusivity for infinite dilution of the penetrant, *i.e.* $\nu \to 0$, at the experimental temperature T and pressure p, D_T can be nondimensionalised:

$$D_T(T, p, 0) = RTA_d \exp\left[-\frac{B_d}{\phi_a v_f^*(T, p, 0)}\right]. \tag{4.22}$$

The dimensionless diffusivity, D', is then:

$$D' = \frac{D_T}{D_T(T, p, 0)} = \exp\left\{\frac{B_d \gamma \nu}{\phi_a \left[v_f^*(T, p, 0) + \gamma\nu\right] v_f^*(T, p, 0)}\right\}. \tag{4.23}$$

In this case, dimensionless time and length are defined as:

$$\tau = \frac{D_T(T, p, 0)t}{L^2}, \tag{4.24}$$

$$X = \frac{x}{L}. \tag{4.25}$$

Defining dimensionless parameters, U and W:

$$U = \frac{v_f^*(T,p,0)}{\gamma}, and \tag{4.26}$$

$$W = \frac{B_d}{\phi_a v_f^*(T,p,0)}, \tag{4.27}$$

Eq. (4.23) can be written in a simple form:

$$D' = \exp\left(\frac{W\nu}{U+\nu}\right). \tag{4.28}$$

Or equivalently,

$$\nu = \frac{U \ln D'}{W - \ln D'}. \tag{4.29}$$

Given the relationship between ν and D', Fick's second law of diffusion, as shown by Eq. (4.12), can be formulated in terms of D', so that ν is eliminated from the expression:

$$\frac{\partial D'}{\partial \tau} = D' \left(W - \ln D'\right)^2 \frac{\partial}{\partial X}\left[\frac{1}{\left(W - \ln D'\right)^2}\frac{\partial D'}{\partial X}\right]. \tag{4.30}$$

In this case, the initial and boundary conditions can be written as:

$$\tau = 0, \quad 0 < X < 1, \quad D' = 1, \tag{4.31}$$

$$\tau \geq 0, \qquad X = 0, \quad D' = D'(X=0), \tag{4.32}$$

$$\tau \geq 0, \qquad X = 1, \quad D' = 1. \tag{4.33}$$

Therefore, the diffusion equation is now expressed in terms of a single variable D'. The permeation flux, F, can be similarly expressed in a dimensionless form, F':

$$F' = \frac{FL}{D_T(T,p,0)}. \tag{4.34}$$

Combining Eq. (4.21) and Eq. (4.34), transforming ν to D' and nondimensionalising x:

$$F' = -\frac{U}{V'W}\left(\frac{\partial D'}{\partial X}\right)_{X=1}. \tag{4.35}$$

Normalising F' with its steady-state value:

$$F'/F'(\tau=\infty) = \frac{(-\partial D'/\partial X)_{X=1}}{(-\partial D'/\partial X)_{X=1,\tau=\infty}}. \tag{4.36}$$

It should be noted that the various forms of the normalised flux, *i.e.* $F/F(t=\infty)$, $F'/F'(\tau=\infty)$ and $F_m/F_m(t=\infty)$, all ranging from 0 to 1, are exactly equivalent. In addition, by combining Eq. (4.34) and Eq. (4.35), a relationship between U and F can be derived, which will be used for the steady-state analysis in Section 4.7:

$$U = \frac{FLV'W}{D_T(T,p,0)(-\partial D'/\partial X)_{X=1}} \tag{4.37}$$

4.3 Full Model *vs.* Simplified Model

Conditions may be identified, under which the diffusion model can be further simplified. When the value of W is much larger than that of $\ln D'$, W can be eliminated from Eq. (4.30). In that case, a simplified form of Eq. (4.30) is obtained:

$$\frac{\partial D'}{\partial \tau} = D'\frac{\partial^2 D'}{\partial X^2}. \tag{4.38}$$

At steady state, when the time derivative is zero, D' decreases linearly from $D'(X=0)$ to 1 across the polymer disc. Thus, at steady state and at $X=1$, $(-\partial D'/\partial X) = D'(X=0) - 1$.

So far, the three models and the number of the parameters required for solving them can be summarised:

1) Original model, Eq. (4.12) and Eq. (4.21), 7 parameters are required - A_d, B_d, ϕ_a, $v_f^*(T,p,0)$, γ, $\nu(x=0)$ and V'.

2) Full nondimensionalised model, Eq. (4.30) and Eq. (4.35), 5 parameters are required - $D_T(T,p,0)$, $D'(X=0)$, W, U and V'.

3) Simplified nondimensionalised model, Eq. (4.38) and Eq. (4.35), 3 parameters including a lumped one are required - $D_T(T, p, 0)$, $D'(X = 0)$ and $U/(V'W)$.

By nondimensionalising and simplifying the free volume model, the number of the key parameters or groups has been significantly reduced, so that it is not necessary to determine the value of each free-volume parameter. Instead, estimates of the groups of these parameters, *i.e.* $D_T(T, p, 0), D'(X = 0)$ and $U/(V'W)$ suffice to characterise the transient permeation measurements.

4.3.1 Dimensionless Diffusivity D'

Regarding the nondimensionalised free volume models, the differences between the results obtained from the full model, and those obtained from the simplified one, will now be discussed. In the first place, with the specified initial and boundary conditions, the full model can be solved numerically by applying the finite difference method in computational software, such as gPROMS. Thus, the distribution of D' relative to the position, X, in the polymer disc and its evolution relative to time, τ, was obtained, as shown in Figure 4.3.

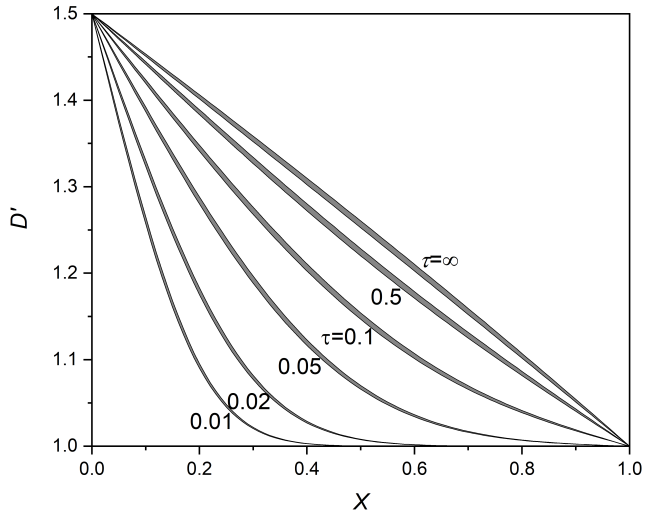


Figure 4.3: Dimensionless diffusivity D' as a function of the dimensionless time τ, and the dimensionless distance X, with $D'(X = 0) = 1.5$, which was used for illustration. For each value of τ, the upper curve is the one obtained using the full nondimensionalised model, Eq. (4.30), with $W = 5$; and the lower curve is the one obtained using the simplified nondimenisionalised model, Eq. (4.38).

The value of W can be estimated from its definition of $W = B_d/\left[\phi_a v_f^*(T,p,0)\right]$, where the free-volume parameters B_d and $v_f^*(T,p,0)$ can be experimentally determined or empirically correlated [107, 109, 110, 115, 187]. For example, using the values of the parameters obtained in Kulkarni and Stern's work for the diffusion of CO_2 in polyethylene at 35 °C [115], the values of W are 10.3 at 52 bar, 10.7 at 125 bar and 11.1 at 200 bar. Although the exact values of the free-volume parameters may differ under specific conditions, the magnitude of the lumped parameter, W, appeared to be around 10, whilst the values of $\ln D'$ were generally smaller than 1. As the value of W increases, the difference between W and $\ln D'$ increases, thus it can be seen from Eq. (4.30) and Eq. (4.38), the full model may be increasingly well approximated by the simplified model. In order to investigate the effect of W in a physically relevant range, as presented in Figure 4.3, two cases are considered: the full nondimensionalised model of Eq. (4.30), solved with $W = 5$, and the simplfied nondimensionalised model of Eq. (4.38), which does not depend on W. The results obtained from the full model with $W = 5$ may represent a typical worst case for deviation of the full model from the simplified model. It can be seen in Figure 4.3 that for each τ, the curves obtained from the two models are reasonably close. When $\ln D'$ is negligibly small compared with W, the model reduces to the simplified case.

4.3.2 Dimensionless Flux F'

After the profiles of the dimensionless diffusivity, D', as a function of X and τ, are solved numerically, the dimensionless flux, F', and the normalised dimensionless flux, $F'/F'(\tau = \infty)$, can be obtained using Eq. (4.35) and Eq. (4.36), respectively. Since the constant $U/(V'W)$ is cancelled from the expression of the normalised flux, the only determinant factor for $F'/F'(\tau = \infty)$ is $(\partial D'/\partial X)_{X=1}$. Figure 4.4 shows the normalised fluxes with four different values of $D'(X = 0)$ for the nondimensionalised model with $W = 5$ and the simplified model. The constant diffusivity case, modelled using Eq. (4.1) and Eq. (4.2), is also included in Figure 4.4, referred to as $D'(X = 0) = 1$. Specifically, when the diffusivity is independent of the penetrant concentration, the diffusivity would accordingly be constant regardless of the time and the position in the sheet. In this case, D_T is always equal to $D_T(T,p,0)$, and thus D' is 1.

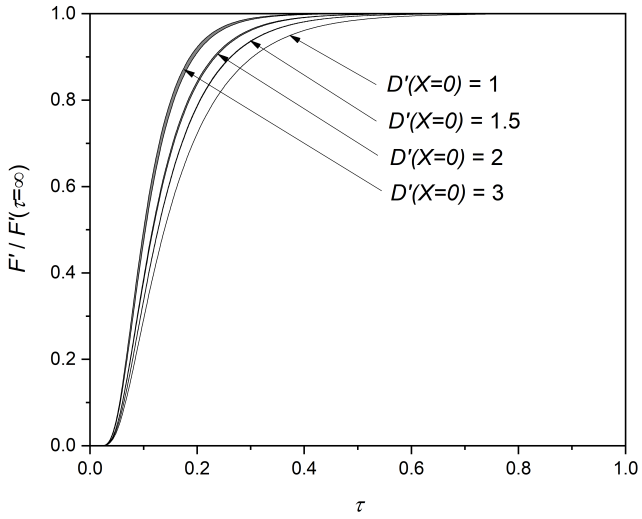


Figure 4.4: Plot of the normalised dimensionless flux, as a function of the dimensionless time τ. For each value of $D'(X = 0)$, the upper curve is the one obtained using the full nondimensionalised model, Eq. (4.30) and Eq. (4.36), with $W = 5$; and the lower curve is the one obtained using the simplified nondimensionalised model, Eq. (4.38) and Eq. (4.36).

It can be seen in Figure 4.4 that the shapes of the normalised flux curves are very insensitive to the magnitude of W. There are two implications for this: (1) the magnitude of W cannot be estimated with confidence by fitting the full model to the transient permeation measurements; and (2) the simplified model, represented by Eq. (4.35), Eq. (4.36), Eq. (4.38), together with the relevant initial and boundary conditions, can be used without introducing significant error. On the other hand, the magnitude of $D'(X = 0)$ has a clearly distinguishable effect on the shape of the normalised breakthrough curve. Consequently, unlike W, the magnitude of $D'(X = 0)$ can be estimated with confidence from the shape of a normalised curve.

4.4 Early Approximation Method

Numerical tools, such as Matlab, Maple, Mathematica, gPROMS, *etc.*, could be used to fit the experimental data to the free volume model, to achieve a minimum difference between the experimental and modelled permeation curves, by optimising the values of the parameters in the model. An example is provided in Appendix B to illustrate how this was done in gPROMS. However, such computational tools may not always be accessible to all researchers and require a certain level of knowledge in numerical methods and skills in the associated software. To

overcome these barriers, it would be beneficial to develop a simple method, which requires no advanced tools, to fit an experimental flux curve to one of the generic flux curves in Figure 4.4, and to determine the transport properties and the lumped free-volume parameters in the model accordingly.

In this work, a graphical approach based on a method of early approximation, which is described in the following context, was proposed to simultaneously estimate the values of $D_T(T, p, 0)$ and $D'(X = 0)$ from the experimental data. This approach originates from Rogers et al.'s formulation of the flux [207], which is the analytical solution to the Fick's diffusion equations for a constant diffusivity, as shown by Eq. (4.1) and Eq. (4.2):

$$F = 2\sum_{m=0}^{\infty}\left(\frac{D}{\pi t}\right)^{1/2}\exp\left[-\frac{(2m+1)^2L^2}{4Dt}\right]. \tag{4.39}$$

For small values of t, by taking only the leading term of the series of exponentials:

$$\ln\left(t^{1/2}F\right) = \ln\left[2C(x=0)\left(\frac{D}{\pi}\right)^{1/2}\right] - \frac{L^2}{4Dt}. \tag{4.40}$$

Eq. (4.40), known as the early approximation, approximates the early breakthrough for small times. From the slope and intercept of the line, experimental data can yield D and $C(x = 0)$. To nondimensionalise the equation, dimensionless quantities, which are of similar forms to Eq. (4.24), Eq. (4.25) and Eq. (4.34), can be defined with the constant diffusivity:

$$\tau = \frac{Dt}{L^2}, \tag{4.41}$$

$$X = \frac{x}{L}, \tag{4.42}$$

$$F' = \frac{FL}{D}. \tag{4.43}$$

Accordingly, Eq. (4.39) and Eq. (4.40) can be reformulated in terms of $F'/F'(\tau = \infty)$ and τ:

$$F'/F'(\tau=\infty) = 2\sum_{m=0}^{\infty}\left(\frac{1}{\pi\tau}\right)^{1/2}\exp\left[-\frac{(2m+1)^2}{4\tau}\right], \tag{4.44}$$

$$\ln\left[\tau^{1/2}F'/F'(\tau=\infty)\right] = \frac{1}{2}\ln\left(\frac{4}{\pi}\right) - \frac{1}{4\tau}. \tag{4.45}$$

In this case, the absolute value of the slope of the line, $|k|$, is 0.25, and the $y-$intercept, c, is $(1/2)\ln(4/\pi)$. Intuitively, it was considered to be worth investigating whether this relationship could be applied to the case of concentration-dependent diffusivity. Unfortunately, as expected, there was a significant deviation between the early breakthrough curve predicted by Eq. (4.45) and the ones obtained from the solutions to the full and the simplified models with the thermodynamic diffusivity. For the latter, the slope of the line deviated from -0.25, and the $y-$intercept did not equal $(1/2)\ln(4/\pi)$. Nevertheless, it was found that by modifying Eq. (4.45) with two constants, λ and μ, whose values only depend on W and $D'(X=0)$, the approximation could be forced to match the solution to the thermodynamic diffusivity model:

$$\ln\left[\tau^{1/2}F'/F'(\tau=\infty)\right] = \frac{1}{2}\ln\left(\frac{\lambda}{\pi}\right) - \frac{\mu}{\tau}. \tag{4.46}$$

Taking the full nondimensionalised model with $W=5$ and $D'(X=0)=1.5$ as an example, it was found that the plot of $\ln\left[\tau^{1/2}F'/F'(\tau=\infty)\right]$ against $1/\tau$, during early times of τ ranging from 0.05 to 0.3, was a straight line, as shown in Figure 4.5, with a slope of $|k|=0.2415$, which was equal to μ, and an intercept of $c=0.1623$, which was equal to $(1/2)\ln(\lambda/\pi)$. Thus, it was deduced that $\mu=0.2415$ and $\lambda=4.3463$.

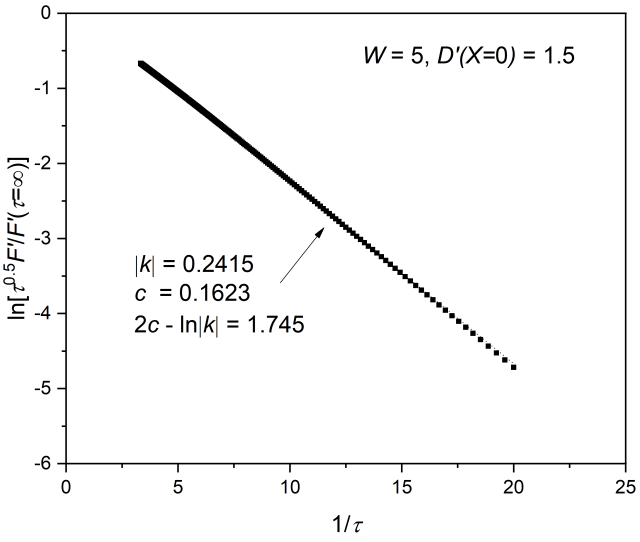


Figure 4.5: Plot of $\ln\left[\tau^{1/2}F'/F'(\tau=\infty)\right]$ against $1/\tau$ for the early breakthrough obtained from the full nondimensionalised model, Eq. (4.30) and Eq. (4.36), with $W=5$ and $D'(X=0)=1.5$.

A number of early approximation plots are included in Appendix C, showing slopes and intercepts of the lines obtained with flux data from $\tau = 0.05$ to $\tau = 0.3$, by using both the simplified model and the full model with $W = 5$, for a series of $D'(X = 0)$ values ranging from 1 to 5.

Regarding a permeation experiment, a straight line of $\ln\left[t^{1/2}F_m/F_m(t=\infty)\right]$ against $1/t$ can also be plotted, once the data for F_m and t are obtained from the measurement. Given the definition of $\tau = D_T(T,p,0)t/L^2$, Eq. (4.46) can be equivalently written in terms of t and $F_m/F_m(t=\infty)$:

$$\ln\left[t^{1/2}F_m/F_m(t=\infty)\right] = \frac{1}{2}\ln\left[\frac{\lambda}{\pi}\frac{L^2}{D_T(T,p,0)}\right] - \frac{\mu L^2}{D_T(T,p,0)t}. \tag{4.47}$$

In this case, $|k|$ is $\mu L^2/D_T(T,p,0)$, and c is $(1/2)\ln\{\lambda L^2/[\pi D_T(T,p,0)]\}$. By computing $2c - \ln|k|$,which is equal to $\ln[\lambda/(\pi\mu)]$, $D_T(T,p,0)$ can be cancelled from the expression. This value characterises the shape of the normalised flux curve, which is strongly dependent on $D'(X=0)$ but weakly dependent on W. Therefore, $2c - \ln|k|$, whose value can be found from the experimental data, can be used to estimate the value of $D'(X=0)$.

Nevertheless, there remains a question. Since the exact values of λ and μ are dependent on W, in order to apply the early approximation to deduce the values of $D'(X=0)$ and $D_T(T,p,0)$, the value of W needs to be specified *a priori*. However, the values of the parameters in the definition of W are rarely known for the specific polymer under test. As a result, the influence of the magnitude of W on the early approximation plot must be evaluated.

Corresponding to different values of $D'(X=0)$, a series of values of λ and μ can be found from the numerical solutions to the simplified model and the full model. These values are summarised in Table 4.1, for $D'(X=0)$ ranging from 1 to 5. In the table, the constant diffusivity case, referring to $D'(X=0)=1$, is included for reference. The values in the columns headed "Simplified" refer to the values obtained from the simplified model. To demonstrate the effect of W on the results, in the columns headed "$W = 5$", the values are those obtained from the full model with $W = 5$. Thus, the agreement can be seen between the simplified model and the full model, in a plausible worst case of $W = 5$. Moreover, correlations are found between

$D'(X=0)$ and $2c - \ln|k|$, and between $|k|$ and $D'(X=0)$, as shown in Figure 4.6 and Figure 4.7, respectively.

Table 4.1: Values of the parameters used for early approximation, for the simplified model, and the full model with $W = 5$, and the relative difference between the two.

$D'(X=0)$	$2c - \ln\|k\|$			μ		
1	1.628			0.25		
	Simplified	$W=5$	Difference	Simplified	$W=5$	Difference
1.05	1.642	1.642	+ 0.012%	0.2493	0.2493	0
1.1	1.655	1.656	+ 0.012%	0.2485	0.2485	0
1.2	1.679	1.681	+ 0.072%	0.2470	0.2469	− 0.040%
1.3	1.702	1.704	+ 0.107%	0.2454	0.2452	− 0.081%
1.4	1.722	1.725	+ 0.188%	0.2438	0.2434	− 0.164%
1.5	1.741	1.745	+ 0.270%	0.2422	0.2415	− 0.289%
1.6	1.758	1.764	+ 0.316%	0.2405	0.2396	− 0.374%
1.7	1.774	1.780	+ 0.363%	0.2388	0.2376	− 0.503%
1.8	1.788	1.795	+ 0.401%	0.2371	0.2355	− 0.675%
1.9	1.801	1.809	+ 0.417%	0.2353	0.2334	− 0.807%
2	1.813	1.821	+ 0.459%	0.2336	0.2312	− 1.027%
2.5	1.867	1.880	+ 0.687%	0.2252	0.2206	− 2.043%
3	1.922	1.940	+ 0.944%	0.2179	0.2105	− 3.396%
3.5	1.974	1.994	+ 1.023%	0.2112	0.2009	− 4.877%
4	2.015	2.038	+ 1.108%	0.2045	0.1913	− 6.455%
4.5	2.056	2.082	+ 1.266%	0.1984	0.1823	− 8.115%
5	2.091	2.122	+ 1.463%	0.1925	0.1738	− 9.714%

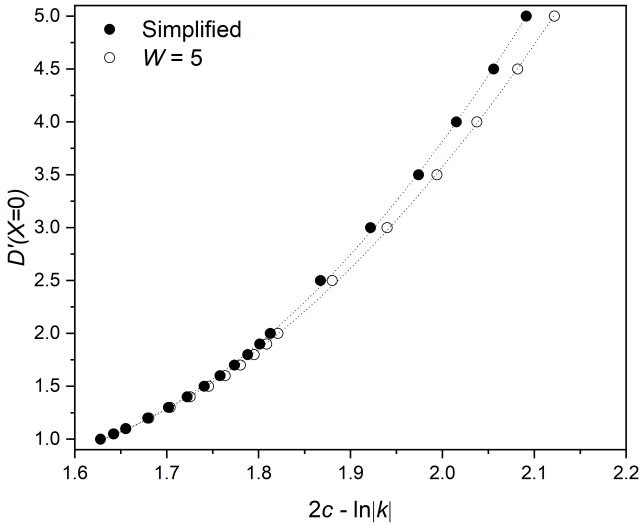


Figure 4.6: Plot of $D'(X = 0)$ *vs.* $2c - \ln|k|$. For the simplified model: $D'(X = 0) = 11.5(2c - \ln|k|)^2 - 34.0(2c - \ln|k|) + 26.0$. For the full model with $W = 5$: $D'(X = 0) = 9.8(2c - \ln|k|)^2 - 28.5(2c - \ln|k|) + 21.5$.

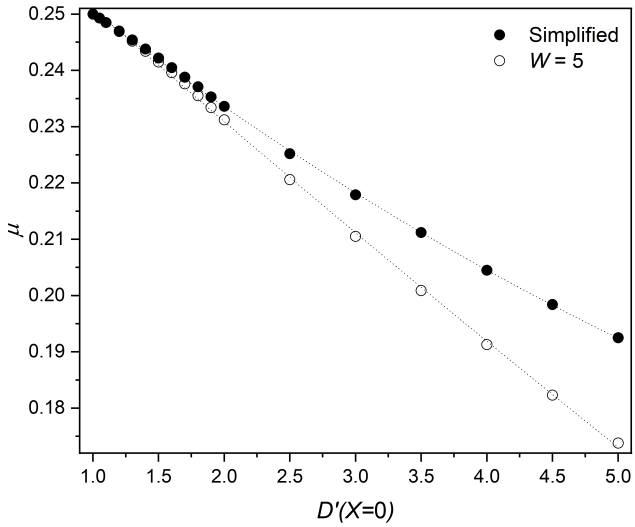


Figure 4.7: Plot of μ *vs.* $D'(X = 0)$. For the simplified model: $\mu = 8.0 \times 10^{-4}[D'(X = 0)]^2 - 1.9 \times 10^{-2} D'(X = 0) + 2.7 \times 10^{-1}$. For the full model with $W = 5$: $\mu = 2.2 \times 10^{-4}[D'(X = 0)]^2 - 2.1 \times 10^{-2} D'(X = 0) + 2.7 \times 10^{-1}$.

As can be seen from the two graphs, the differences in the parameters obtained for the simplified and the full models become larger as $D'(X = 0)$ increases. When applying the early approximation method with the deduced correlations to estimate $D'(X = 0)$ and $D_T(T, p, 0)$ for a permeation run, the uncertainty of estimation needs to be considered, especially when large values of $D'(X = 0)$, *i.e.* high volume fraction of penetrant and strong concentration dependence of diffusivity, are involved.

4.5 Procedure for Graphical Analysis

Figure 4.8 is a flow chart detailing a procedure for estimating the values of $D_T(T, p, 0)$ and $D'(X = 0)$ during a permeation experiment. The first step is to determine whether the constant diffusivity model or the free volume model is more appropriate for characterising the experimental flux curve. Then, the steps for the time-lag method or the early approximation method can be followed, respectively.

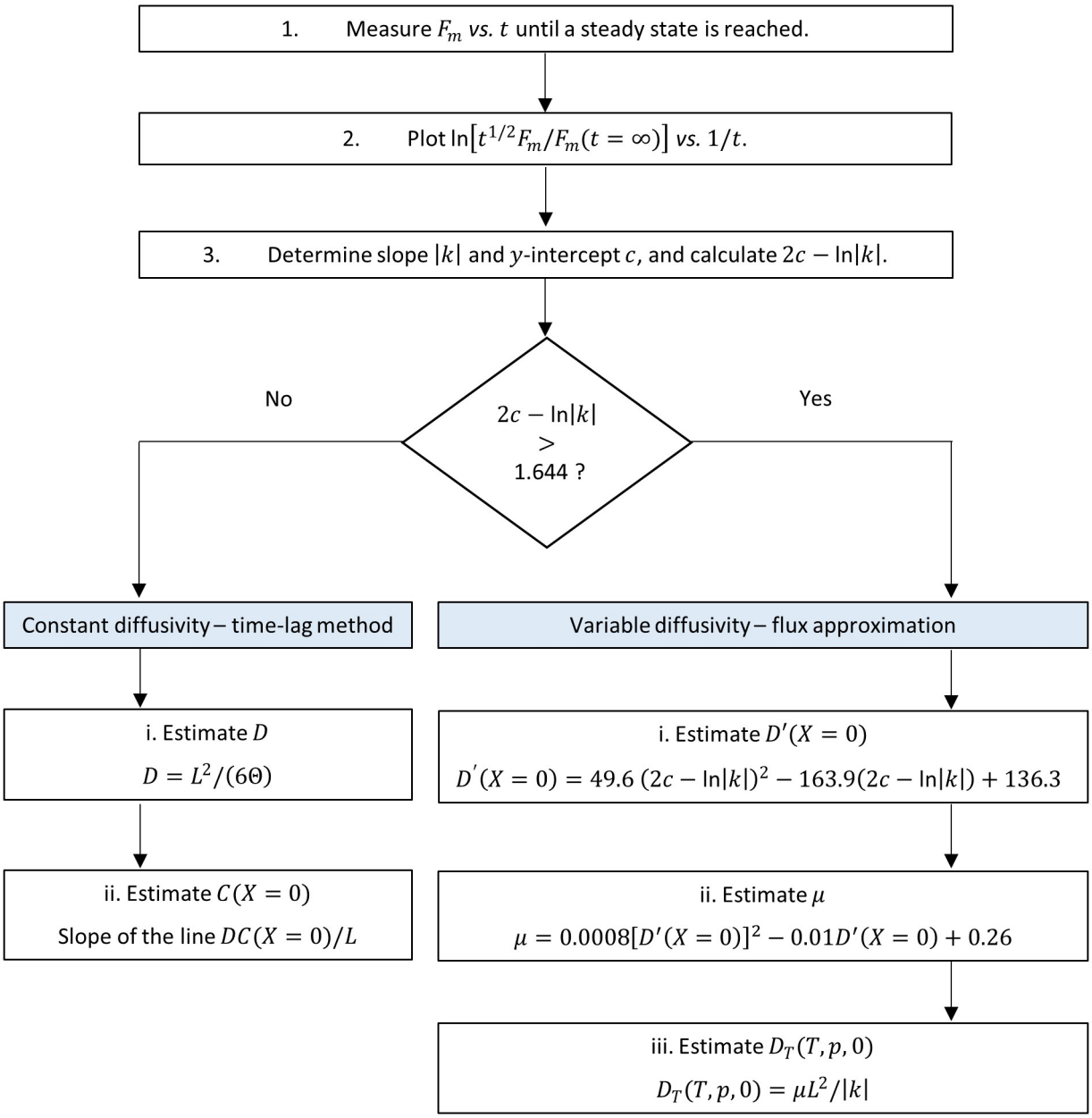


Figure 4.8: A diagram showing the procedure for estimating the values of transport properties, which can characterise a permeation process.

The procedure shown in Figure 4.8 is exemplified by the experimental results, as illustrated in the next section. Although W is not known *a priori*, the sensitivity of the estimated parameters will be discussed.

Part II: Experimental

4.6 Transient Flux Measurements

Nine experimental runs, which are numbered for clarification, were conducted at various pressures and temperatures with the two polymers. For reference, the conditions for the runs are tabulated in Table 4.2.

Table 4.2: 9 experimental runs of transient permeation, with the experimental conditions specified.

Runs	Polymer	Temperature, °C	Pressure, bar
Run-P-1	PTFE	28	55
Run-P-2	PTFE	40	50
Run-P-3	PTFE	50	50
Run-H-4	HDPE	28	55
Run-H-5	HDPE	35	5
Run-H-6	HDPE	35	55
Run-H-7	HDPE	35	125
Run-H-8	HDPE	35	200
Run-H-9	HDPE	50	5

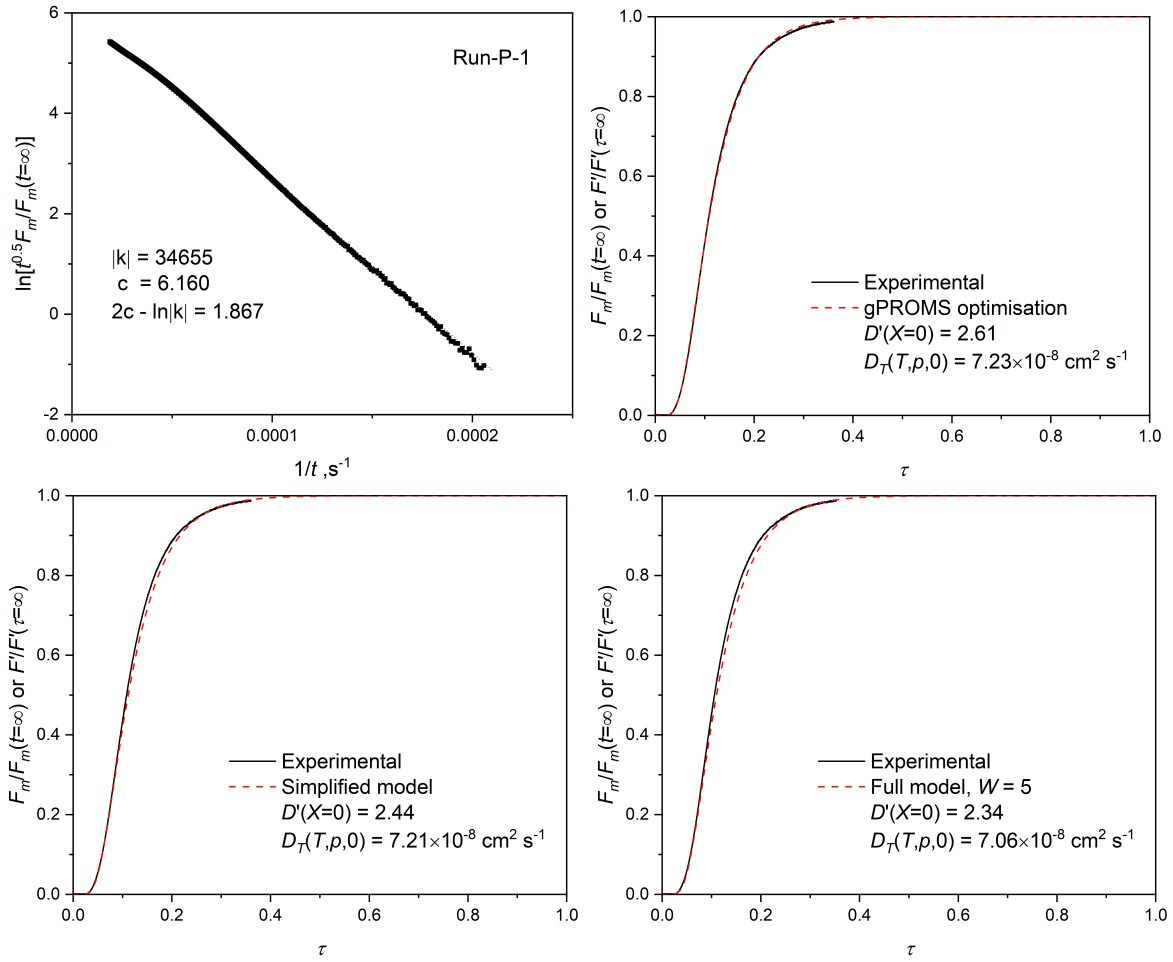
In Table 4.2, "P" in the names for the runs stands for "PTFE", and "H" refers to "HDPE". Except for Run-H-7, which was conducted only at 125 bar, the others were successive runs with multiple pressure steps. Detailed analysis of the multi-step permeation results will be presented

in Chapter 5. Here, the pressures shown in Table 4.2 refer to the pressures applied during the first steps for the runs. Analysis on the transient permeation during the first step is the focus of this chapter.

The choice of conditions shown in Table 4.2 evolved as the concentration-dependent behaviour became apparent, and were not decided as a coherent set *a priori*. The practical experience gained during the implementation of the experiments has been summarised in Appendix D, which can be reviewed for future improvements on the planning and the scheduling of experiments. Overall, the experimental data gathered from these runs suffice for useful analysis of the transient permeation.

Following the procedure outlined in Figure 4.8, transient CO_2 fluxes were measured and analysed. The early approximation plots and the fits of the experimental flux curves to the modelled curves for these runs are shown in Figure 4.9 on the following pages. It should be pointed out that the early approximation plots were made using a portion of the data with the normalised flux ranging from 0.01 to 0.98. As can be seen from the various flux curves shown in Figure 4.4, this range for the normalised flux corresponds to an approximate range of 0.05 to 0.3 for τ, over which the early approximation method was developed. The intercept and slope of the line could be obtained from the linear regression of the early approximation plot. The estimation uncertainties were obtained with a confidence level of 95% for the linear regression. The modelled flux curves were obtained using both the simplied model and the full model with $W = 5$. Correspondingly, for each run, the estimated values of $D'(X = 0)$ and $D_T(T, p, 0)$, with the estimation uncertainties, were displayed in Table 4.3 following the figures.

In addition, optimisations of $D'(X = 0)$ and $D_T(T, p, 0)$ were also performed using gPROMS, by which the values of the two parameters were adjusted to minimise the objective function, which was the mean squared difference between the modelled flux and the experimental flux. Since the results were relatively insensitive to W, the simplified model, *i.e.* Eq. (4.36) together with Eq. (4.38), was used for the optimisation with gPROMS. The obtained modelled flux curves were also shown in Figure 4.9. The optimised values of $D'(X = 0)$ and $D_T(T, p, 0)$ and their uncertainties, estimated with 95% confidence intervals, were also included in Table 4.3.



(a) Run-P-1.

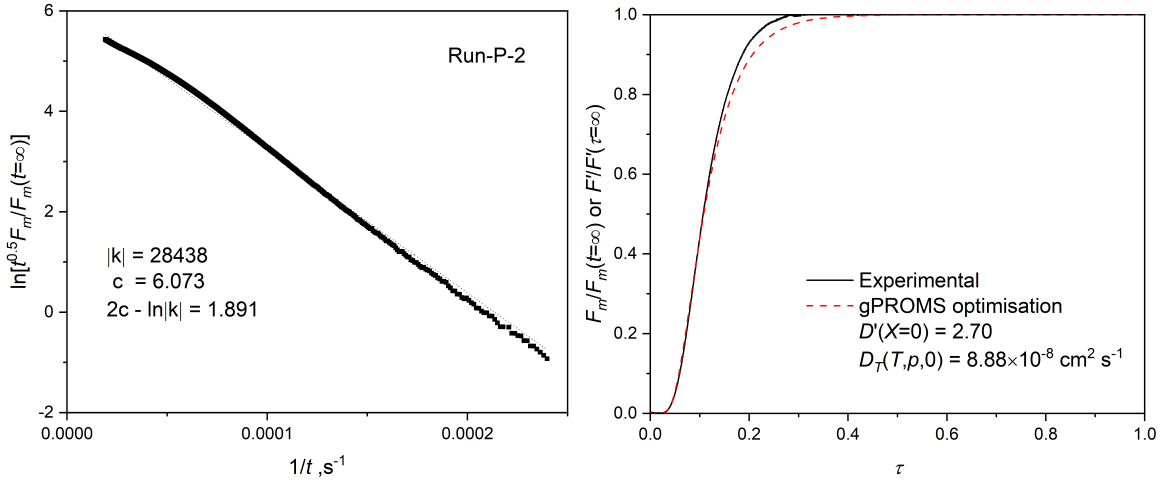
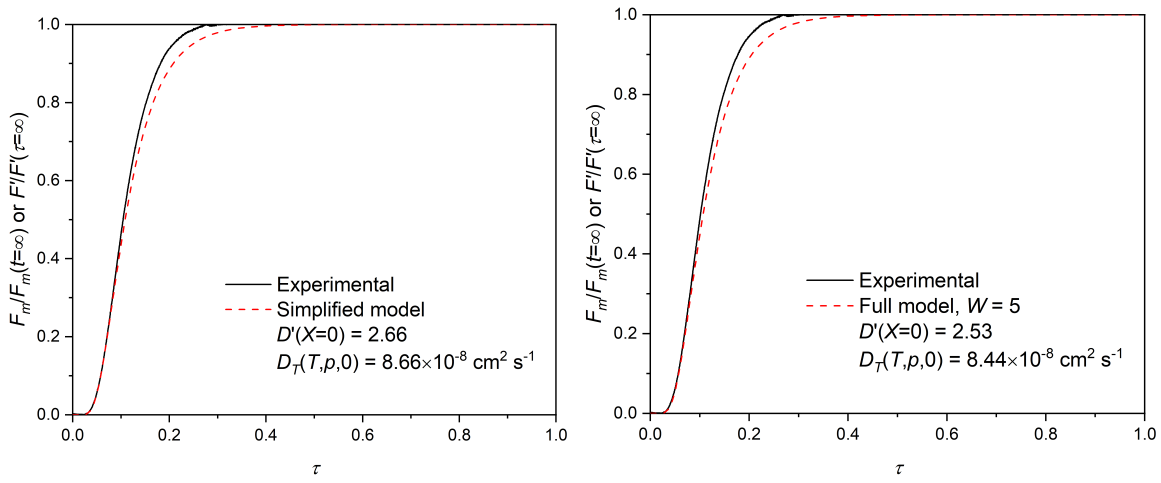
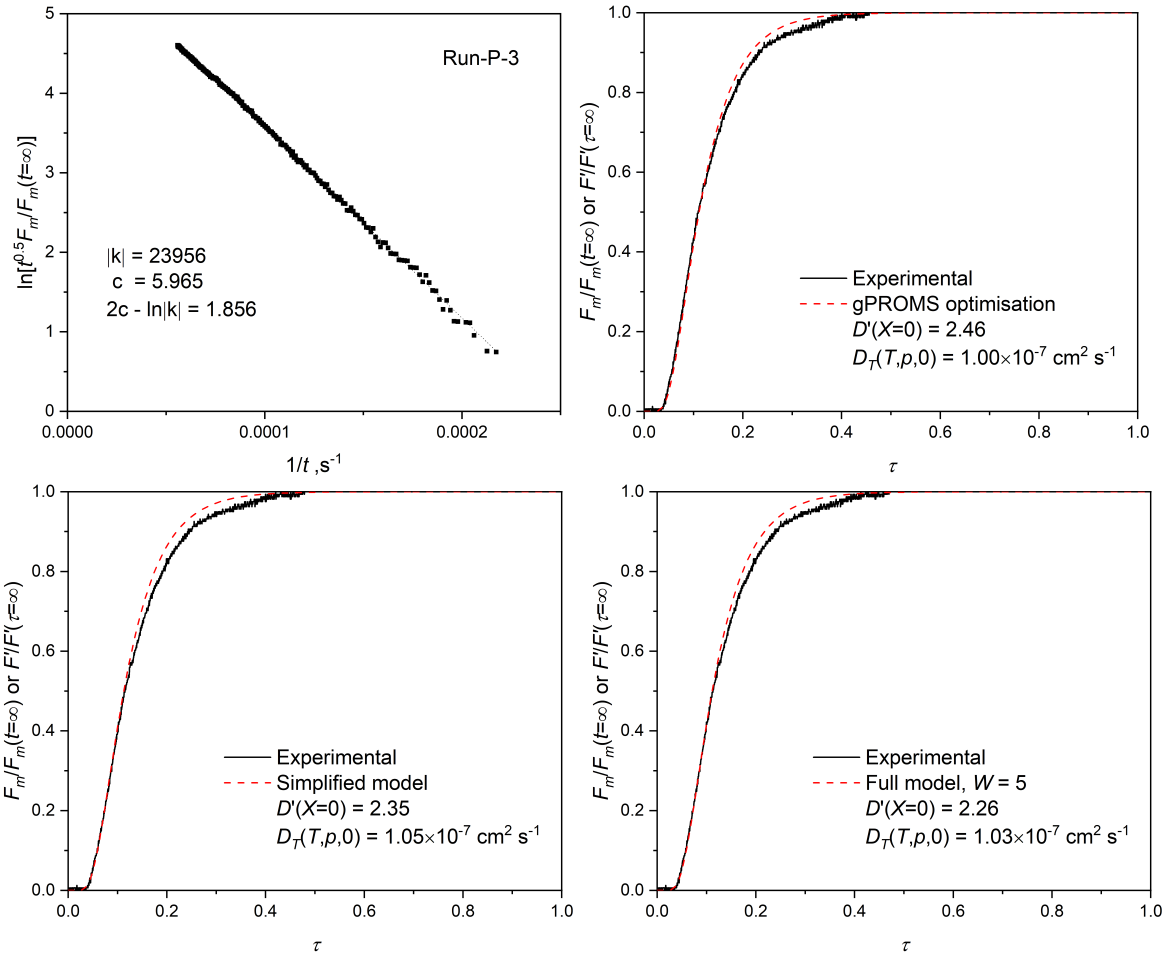


Figure 4.9: Early approximation plots and fitting of modelling results to experimental data for the runs.

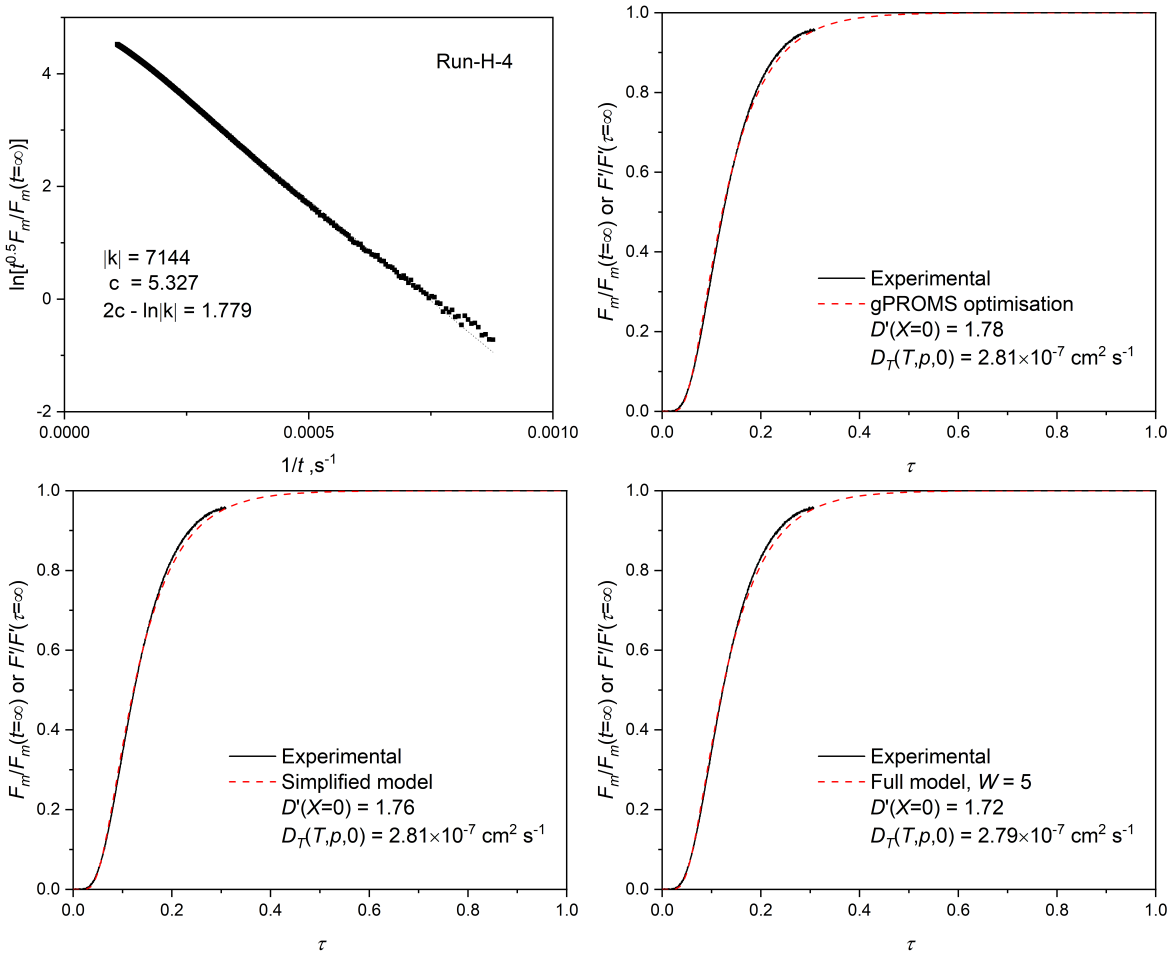


(b) Run-P-2.



(c) Run-P-3.

Figure 4.9: Early approximation plots and fitting of modelling results to experimental data for the runs (cont.).



(d) Run-H-4.

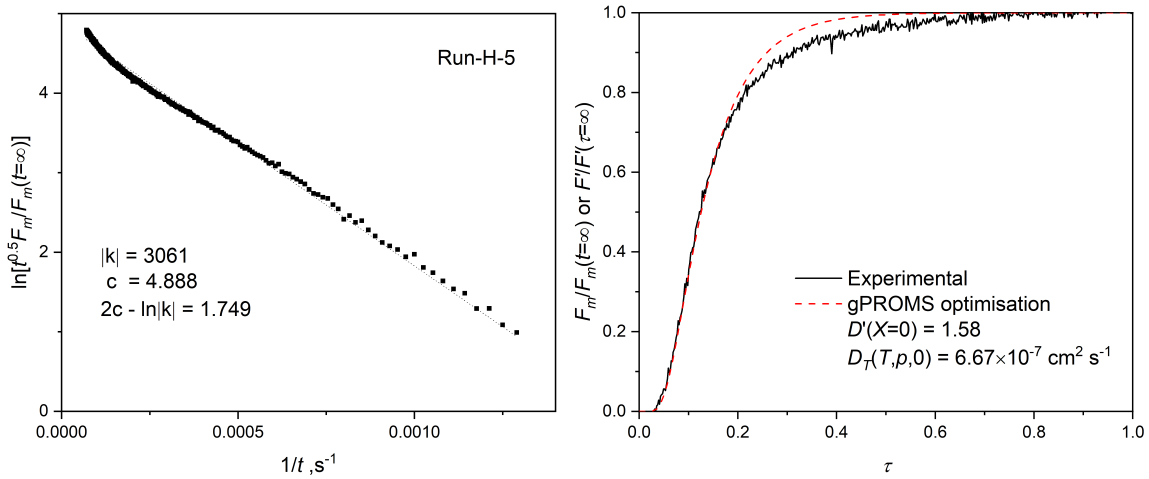
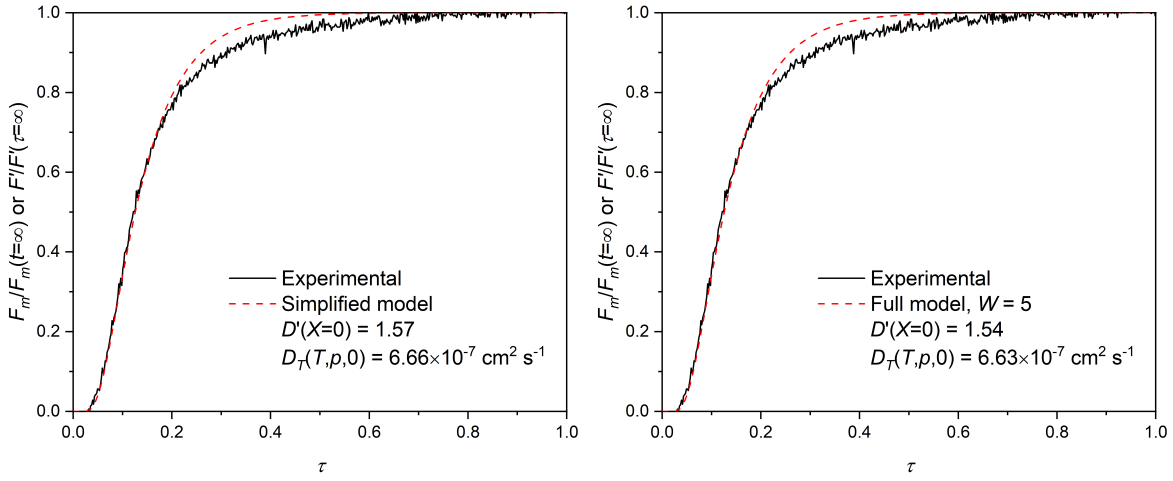
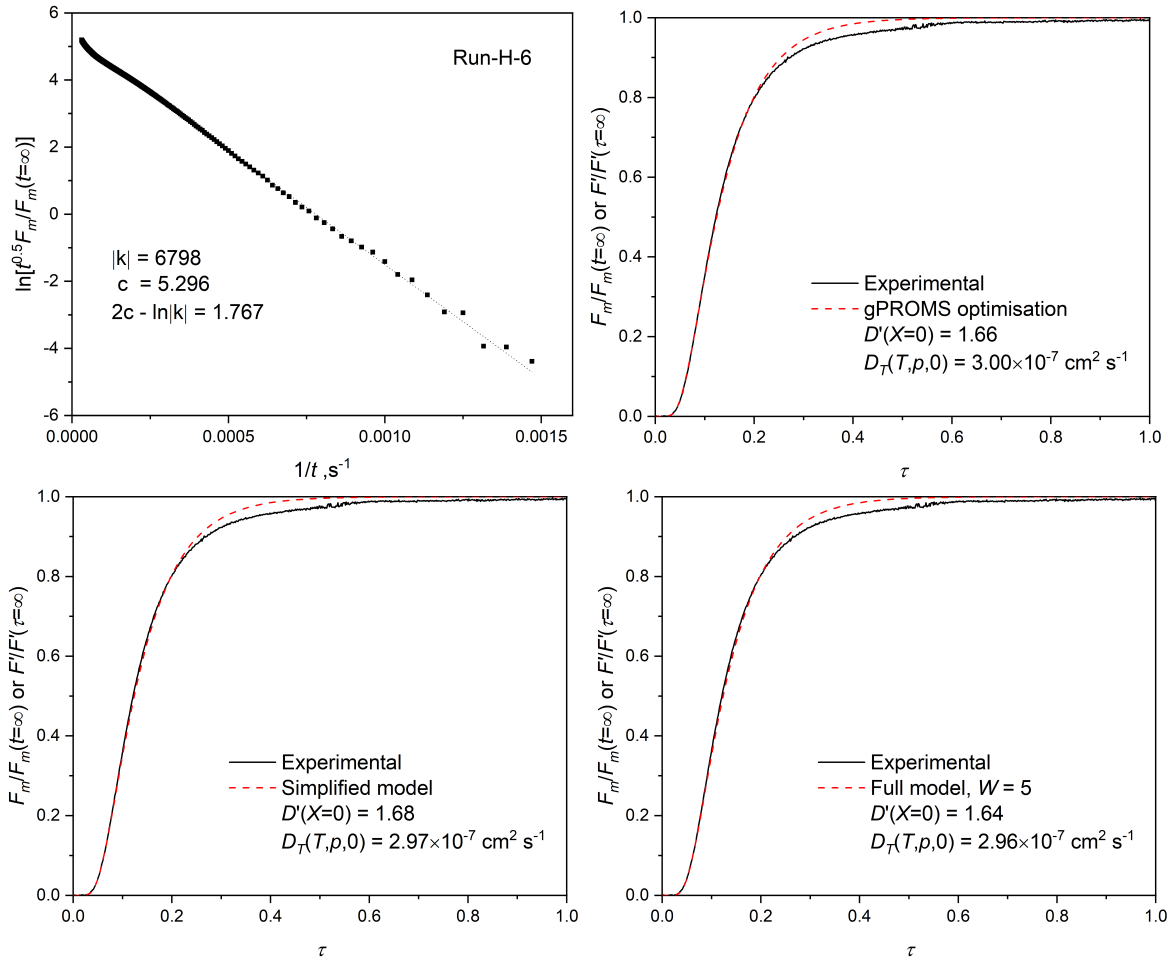


Figure 4.9: Early approximation plots and fitting of modelling results to experimental data for the runs (cont.).

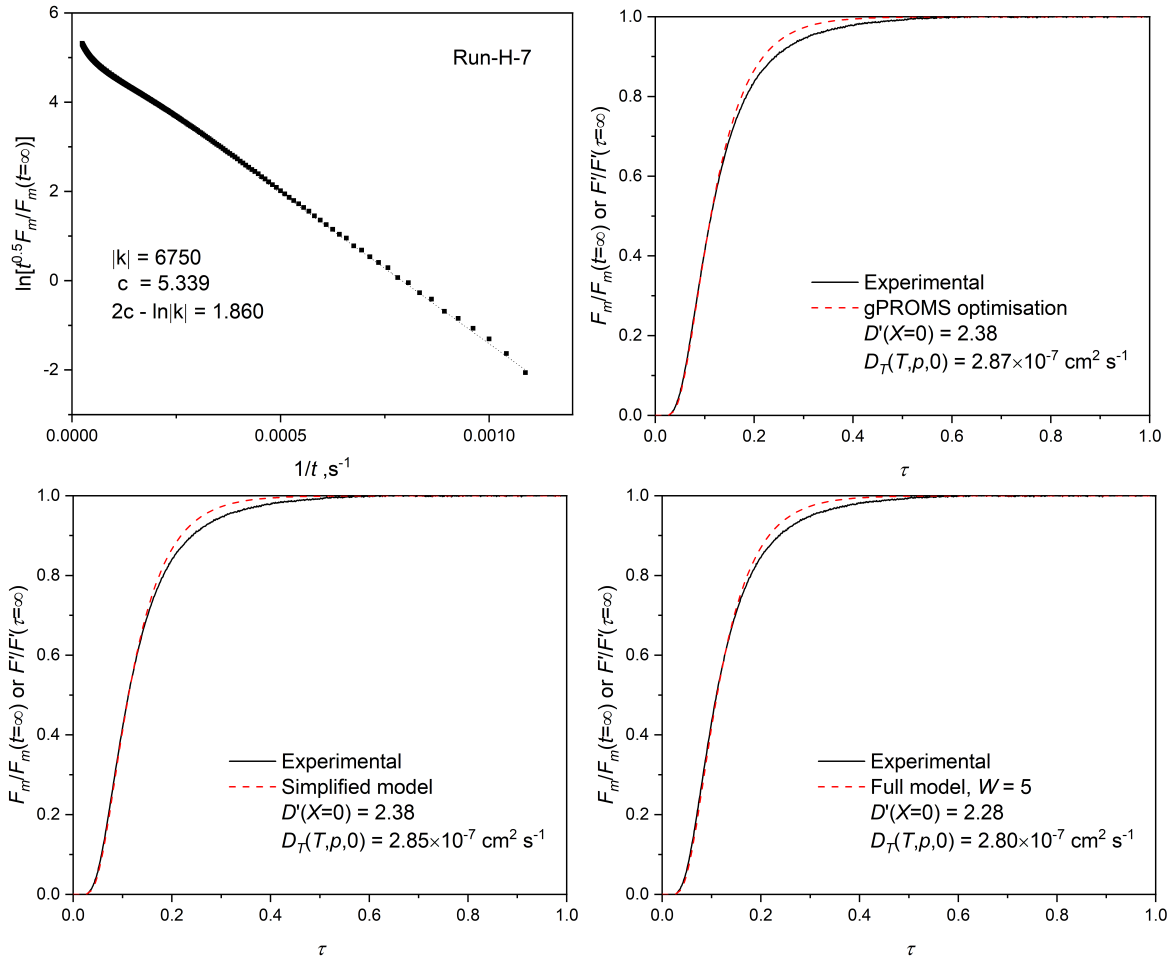


(e) Run-H-5.



(f) Run-H-6.

Figure 4.9: Early approximation plots and fitting of modelling results to experimental data for the runs (cont.).



(g) Run-H-7.

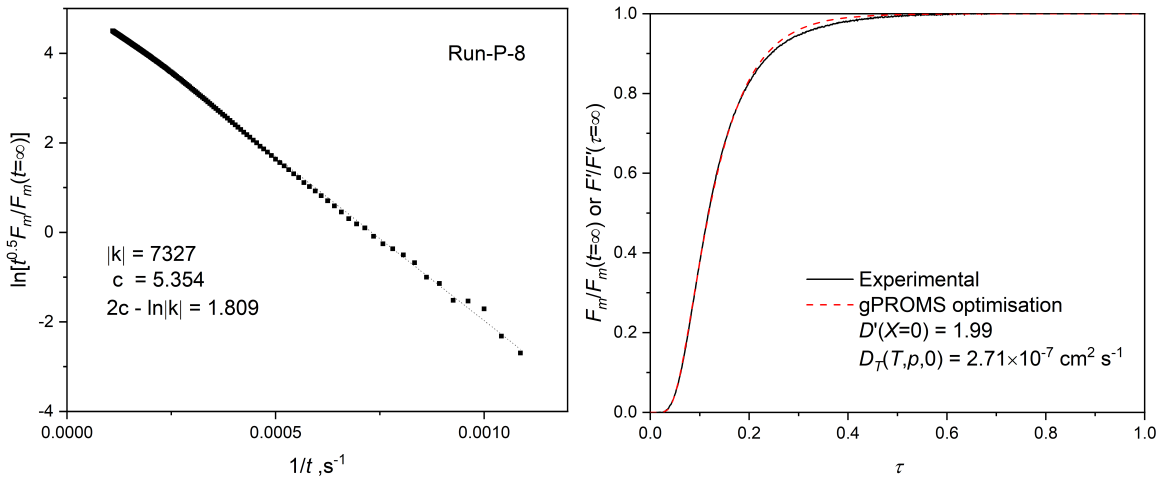
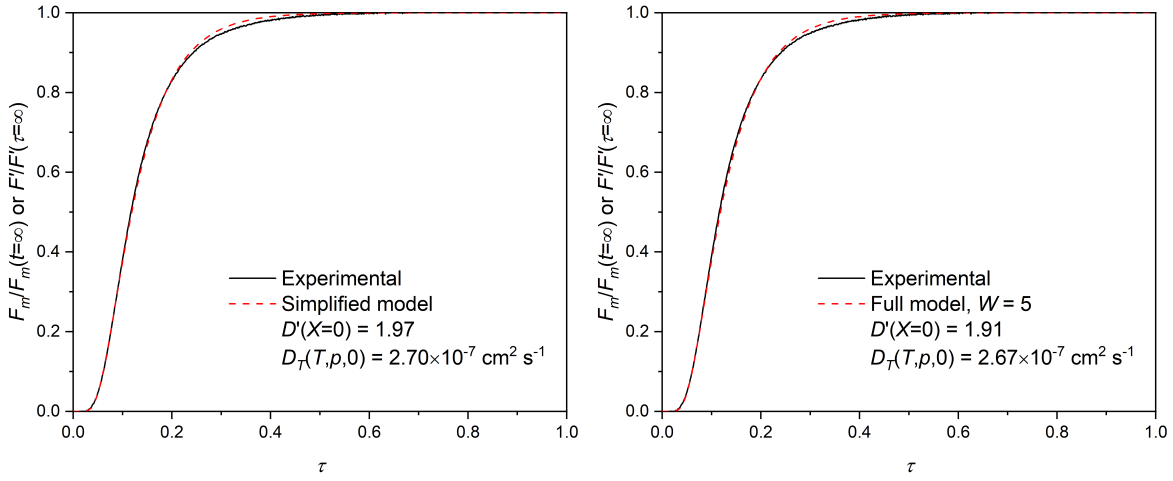
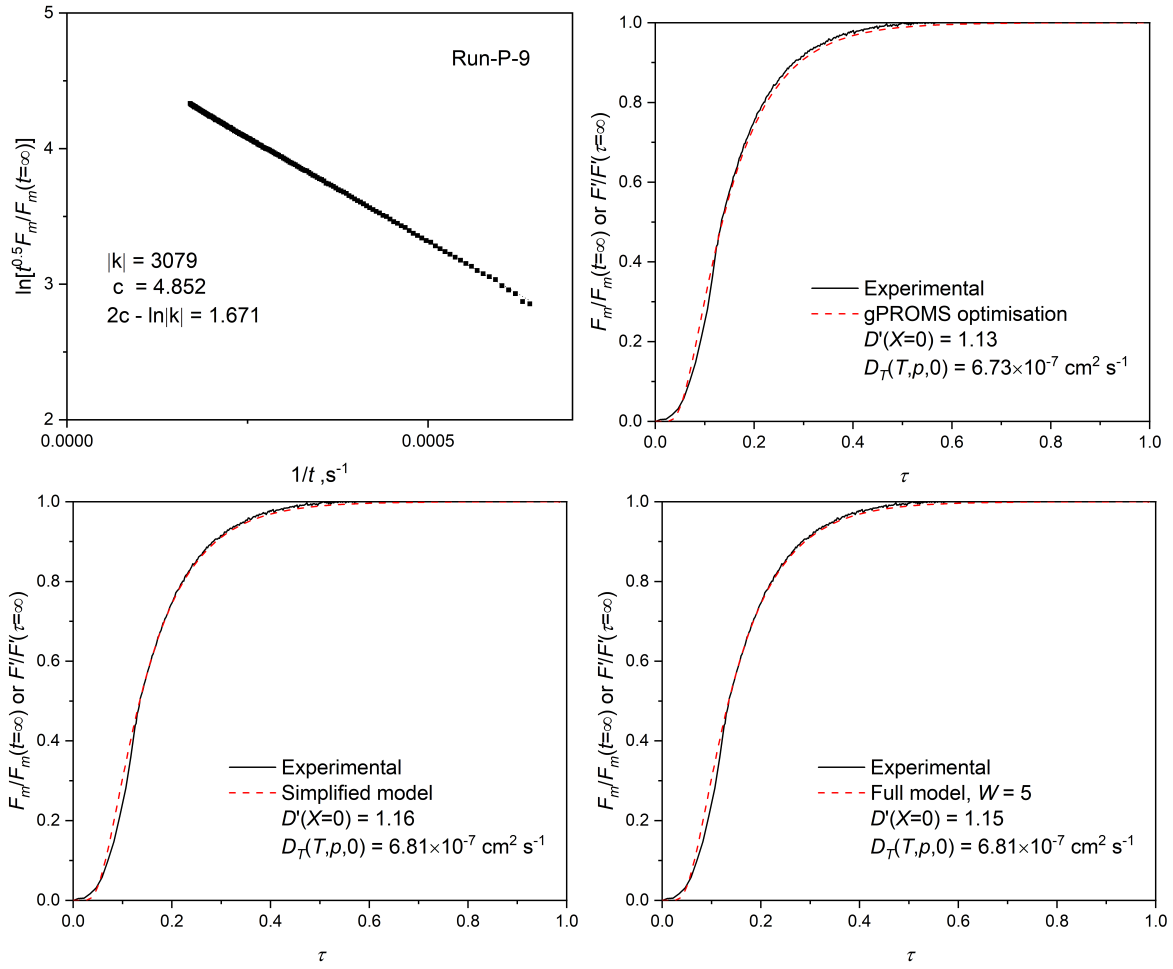


Figure 4.9: Early approximation plots and fitting of modelling results to experimental data for the runs (cont.).



(h) Run-H-8.



(i) Run-H-9.

Figure 4.9: Early approximation plots and fitting of modelling results to experimental data for the runs (cont.).

Table 4.3: Values of the parameters estimated for the permeation runs, by applying the early approximation method with the simplified model, and the full model with $W = 5$; and the optimised values obtained using gPROMS.

Runs	Early Approximation		Parameters	Simplified	$W = 5$	gPROMS
Run-P-1	c	6.160±0.005	$D'(X = 0)$	2.44±0.11	2.34±0.10	2.61±0.01
	$\lvert k\rvert$	34655±82	$D_T(T, p, 0)$,			
	$2c - \ln\lvert k\rvert$	1.867±0.012	$\times 10^{-8}$ cm^2 s^{-1}	7.21±0.04	7.06±0.06	7.23±0.01
Run-P-2	c	6.073±0.006	$D'(X = 0)$	2.66±0.15	2.53±0.14	2.70±0.01
	$\lvert k\rvert$	28438±94	$D_T(T, p, 0)$,			
	$2c - \ln\lvert k\rvert$	1.891±0.016	$\times 10^{-8}$ cm^2 s^{-1}	8.66±0.09	8.44±0.11	8.88±0.01
Run-P-3	c	5.965±0.010	$D'(X = 0)$	2.35±0.27	2.26±0.24	2.46±0.01
	$\lvert k\rvert$	23956±88	$D_T(T, p, 0)$,			
	$2c - \ln\lvert k\rvert$	1.846±0.023	$\times 10^{-7}$ cm^2 s^{-1}	1.05±0.02	1.03±0.02	1.00±0.01
Run-H-4	c	5.288±0.005	$D'(X = 0)$	1.76±0.08	1.72±0.08	1.78±0.02
	$\lvert k\rvert$	7144±16	$D_T(T, p, 0)$,			
	$2c - \ln\lvert k\rvert$	1.779±0.012	$\times 10^{-7}$ cm^2 s^{-1}	2.81±0.01	2.79±0.01	2.81±0.01
Run-H-5	c	4.888±0.008	$D'(X = 0)$	1.57±0.15	1.54±0.14	1.58±0.02
	$\lvert k\rvert$	3061±25	$D_T(T, p, 0)$,			
	$2c - \ln\lvert k\rvert$	1.749±0.023	$\times 10^{-7}$ cm^2 s^{-1}	6.66±0.01	6.63±0.03	6.67±0.01

Continuation of Table 4.3

Runs	Early Approximation		Parameters	Simplified	$W = 5$	gPROMS
Run-H-6	c	5.296±0.005	$D'(X = 0)$	1.68±0.09	1.64±0.08	1.66±0.02
	$\lvert k\rvert$	6798±22	$D_T(T, p, 0)$,	2.97±0.01	2.96±0.01	3.00±0.01
	$2c - \ln\lvert k\rvert$	1.767±0.013	$\times 10^{-7}$ cm^2 s^{-1}			
Run-H-7	c	5.339±0.005	$D'(X = 0)$	2.38±0.14	2.28±0.13	2.38±0.02
	$\lvert k\rvert$	6750±33	$D_T(T, p, 0)$,	2.85±0.01	2.80±0.02	2.87±0.01
	$2c - \ln\lvert k\rvert$	1.860±0.016	$\times 10^{-7}$ cm^2 s^{-1}			
Run-H-8	c	5.354±0.011	$D'(X = 0)$	1.97±0.20	1.91±0.18	1.99±0.01
	$\lvert k\rvert$	7327±30	$D_T(T, p, 0)$,	2.70±0.03	2.67±0.03	2.71±0.01
	$2c - \ln\lvert k\rvert$	1.809±0.025	$\times 10^{-7}$ cm^2 s^{-1}			
Run-H-9	c	4.852±0.002	$D'(X = 0)$	1.16±0.03	1.15±0.03	1.13±0.03
	$\lvert k\rvert$	3079±6	$D_T(T, p, 0)$,	6.81±0.01	6.81±0.01	6.73±0.03
	$2c - \ln\lvert k\rvert$	1.671±0.006	$\times 10^{-7}$ cm^2 s^{-1}			

Figure 4.9 and Table 4.3 present the results of early approximation and parameter estimations for the runs. Several pieces of important information, extracted from the graphs and the tabulated data, are discussed here.

Early Approximation and Fits

In general, regarding the fits to the permeation flux and the parameter estimations, the results obtained with the early approximation method, were close to those obtained from gPROMS

optimisation. It can be seen in Figure 4.9 that for the runs with excellent agreements between the experimental flux curve and the modelled fits, such as Run-P-1 (Figure 4.9a), Run-H-4 (Figure 4.9d), and Run-H-8 (Figure 4.9h), the early approximation curves exhibited excellent linearity. On the other hand, in some other cases, such as Run-P-2 (Figure 4.9b), Run-H-5 (Figure 4.9e), Run-H-6 (Figure 4.9f), and Run-H-7 (Figure 4.9g), there was good agreement between the experimental and the modelled flux curves during the early times when τ was smaller than 0.3, but there was poor agreement during the later times. This was also featured by the early approximation curves, which deviated from the lines during the late times when t was large (*i.e.* $1/t$ was small on the graph). There was no clear clue why excellent fits during the late times were achieved for some runs, but not for the others. For future work, it is worth repeating these experiments under the same conditions, and check whether good fits would be obtained for all runs, by applying the derived models and the proposed methods.

Comparison of the Three Approaches

In terms of the fits shown in Figure 4.9, the three cases of gPROMS optimisation, early approximation with the simplified model, and early approximation with the full model ($W = 5$), were almost indistinguishable. Estimates of $D'(X = 0)$ and $D_T(T, p, 0)$ for the nine runs with each approach are compared in Table 4.3. As can be seen, overall, consistent results were obtained within the uncertainty bounds. Particularly, the parameter estimations in Run-H-4, Run-H-5, and Run-H-6 using the three approaches were very close. This could support the application of the proposed graphical method to the analysis of the transient permeation, without the requirement for advanced computational tools.

It was noticed that for the early approximation with the two models, the uncertainty of estimation seemed to increase with the estimated $D'(X = 0)$. Comparing the results obtained with the simplified model and the full model ($W = 5$), it was noticed that the differences between the estimations also increased with the estimated $D'(X = 0)$. These may be explained by the correlations between $D'(X = 0)$ and $2c - \ln|k|$ shown in Figure 4.6, where it can be seen that the slopes of the curves increased with $D'(X = 0)$. This indicated greater variations of $D'(X = 0)$ with the changes in $2c - \ln|k|$ for larger values of $D'(X = 0)$, leading to larger uncertainties

for the estimation. In addition, as can be seen in Figure 4.6, as $D'(X = 0)$ became larger, the difference between the correlated values with the simplified and the full model became greater, resulting in greater differences between the estimation results.

Estimated Parameters

The estimated values of $D_T(T, p, 0)$ for the runs conducted with HDPE were of approximately one order of magnitude higher than those with PTFE, suggesting a faster permeation in HDPE than that in PTFE. This can also be seen from the experimental breakthrough curves for the two polymers, as shown in Figure 4.1, which showed a shorter duration for the measurement with HDPE than that with PTFE. With the same polymer type, despite the different pieces of polymer discs used in the runs, the estimated $D_T(T, p, 0)$ seemed to decrease with the increasing pressure at the same temperature, as can be seen from Run-H-5 to Run-H-8, whilst it increased with the increasing temperature at the same pressure, as can be seen from Run-H-4 and Run-H-6, or Run-H-5 and Run-H-9. On the basis of these estimated parameters, the values of a few more parameters, such as the transport coefficients, and the lumped group, $U/V'W$, can be estimated with the flux data obtained at the steady state, as described in the following section.

4.7 Analysis of Steady-State Flux

4.7.1 Derivation for $U/(WV')$

During an experiment, after sufficiently long time, a steady-state flux, $F_m(t = \infty)$, was obtained. Replacing F by $F_m(t = \infty)$ in Eq. (4.37), and substituting this expression into Eq. (4.8) and Eq. (4.29), an expression for the penetrant concentration at the top surface of the polymer, $C(X = 0)$, expressed in cm^3(STP) cm^{-3}(mixture), can be written:

$$C(X = 0) = \frac{\Omega_W L F_m(t = \infty)}{D_T(T, p, 0)}, \tag{4.48}$$

where

$$\Omega_W = \frac{W \ln [D'(X=0)]}{\{W - \ln [D'(X=0)]\}(-\partial D'/\partial X)_{X=1,\tau=\infty}}. \tag{4.49}$$

It is clear from Eq. (4.49) that Ω_W is dependent on W. On the other hand, when $W \gg \ln D'$ (*i.e.* the assumption of the simplified model), Eq. (4.29) can be reduced to $\nu(X=0) = U/W \ln [D'(X=0)]$. In this case, the relationship between $C(X=0)$ and $F_m(t=\infty)$ becomes:

$$C(X=0) = \frac{\Omega_s L F_m(t=\infty)}{D_T(T,p,0)}, \tag{4.50}$$

where

$$\Omega_s = \frac{\ln [D'(X=0)]}{(-\partial D'/\partial X)_{X=1,\tau=\infty}} = \frac{\ln [D'(X=0)]}{D'(X=0)-1}. \tag{4.51}$$

Given the value of $D'(X=0)$, which can be determined using the correlation between $D'(X=0)$ and $2c - \ln|k|$ (Figure 4.6) by applying the early approximation method, the values of Ω_s and Ω_W can thus be obtained from the numerical solution to the simplified model, and the full model with the assumed $W=5$, respectively. Figure 4.10 shows the relationship between Ω_s or Ω_W, and $2c - \ln|k|$. It can be seen that given same values of $2c - \ln|k|$, the differences between the values of Ω_s from the simplified model and those of Ω_W from the full model with $W=5$, are very small, particularly for small values of $2c - \ln|k|$.

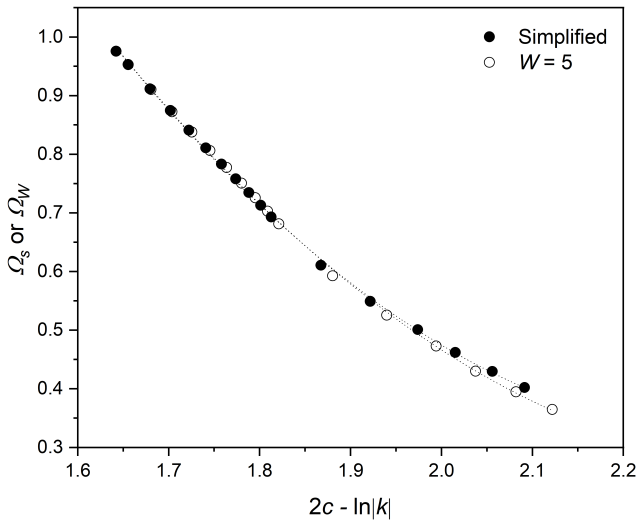


Figure 4.10: Plot of Ω_s (Ω_W) *vs.* $2c - \ln|k|$. For the simplified model: $\Omega_s = 1.38(2c - \ln|k|)^2 - 6.44(2c - \ln|k|) + 7.83$. For the full model with $W=5$: $\Omega_W = 1.24(2c - \ln|k|)^2 - 5.94(2c - \ln|k|) + 7.41$.

As can be seen from Eq. (4.48) and Eq. (4.49), or Eq. (4.50) and Eq. (4.51), V' was eliminated from the equations, and $C(X = 0)$ was directly related to $F_m(t = \infty)$. This means that the top-surface concentration, $C(X = 0)$, can be calculated from the measured steady-state flux, $F_m(t = \infty)$, without knowing the value of V', which is normally estimated using an appropriate equation of state for the mixture. By rearranging Eq. (4.37), at the steady state, the lumped parameter $U/(WV')$ is:

$$\frac{U}{WV'} = \frac{LF_m(t = \infty)}{D_T(T, p, 0)(-\partial D'/\partial X)_{X=1,\tau=\infty}}. \tag{4.52}$$

As discussed in Section 4.3, for the simplified model, under the assumption that $W \gg \ln D'$, it can be shown that $(-\partial D'/\partial X)_{X=1,\tau=\infty} = D'(X = 0) - 1$. Thus, the lumped parameter $U/(WV')$ can be conveniently estimated from Eq. (4.52) in the case of the simplified model. For the full model, the determination of $(-\partial D'/\partial X)_{X=1,\tau=\infty}$ is not straightforward. As a result, correlations between $(-\partial D'/\partial X)_{X=1,\tau=\infty}$ and $D'(X = 0)$ are obtained, as shown in Figure 4.11, for both the simplified model, and the full model with $W = 5$.

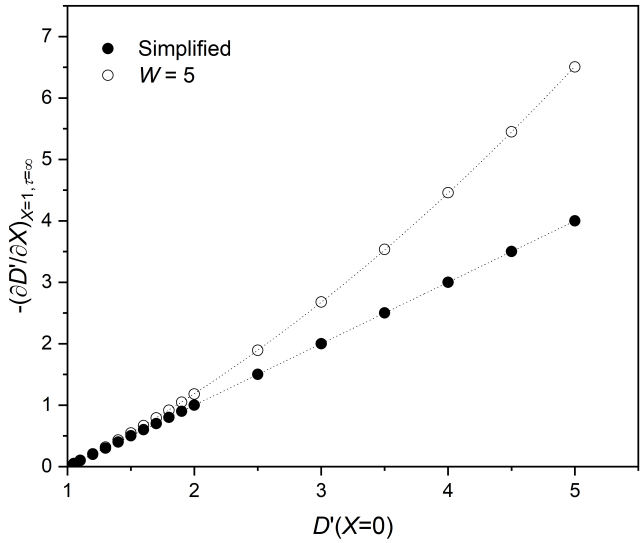


Figure 4.11: Plot of $(-\partial D'/\partial X)_{X=1,\tau=\infty}$ *vs.* $D'(X = 0)$. For the simplified model: $(-\partial D'/\partial X)_{X=1,\tau=\infty} = D'(X = 0) - 1$. For the full model with $W = 5$: $(-\partial D'/\partial X)_{X=1,\tau=\infty} = 0.14[D'(X = 0)]^2 + 0.77[D'(X = 0)] - 0.92$.

With the derived correlations for $(-\partial D'/\partial X)_{X=1,\tau=\infty}$ for the two models, $U/(WV')$ can be estimated from Eq. (4.52). In fact, as shown by Eq. (4.53), this lumped parameter is a quantity related to the free-volume parameters, given the definitions of U [Eq. (4.26)] and W

[Eq. (4.27)]. Estimations of the free-volume parameters from the lumped parameter will be discussed in Chapter 5, where the results from successive measurements are presented.

$$\frac{U}{WV'} = \frac{\phi_a \left[v_f^*(T,p,0)\right]^2}{V'\gamma B_d} \tag{4.53}$$

On the basis of the equations derived here, the values of the transport coefficients, and the lumped parameter $U/(WV')$, can be estimated for each run, with the experimentally determined $F_m(t=\infty)$, and the values of $D'(X=0)$ and $D_T(T,p,0)$, which were estimated with the early approximation method or gPROMS optimisation, as described in Section 4.6. Correspondingly, the results obtained with each approach are summarised and compared in Table 4.4. In addition, parameter estimations by the time-lag method assuming constant diffusivity are also included.

4.7.2 Estimation of Parameter Values

Table 4.4: Summary and comparison of the estimated transport coefficients and the lumped parameter for the runs, with the approaches of the time-lag method, graphical method with the simplified model and the full model with $W = 5$, and gPROMS optimisation.

	Run-P-1	**Run-P-2**	**Run-P-3**
	(28°C,55bar)	**(40°C,50bar)**	**(50°C,50bar)**
$F_m(t=\infty)$, $\times 10^{-5}$ cm^3(STP) cm^{-2} s^{-1}	8.33 ± 0.16	9.23 ± 0.18	9.52 ± 0.18
P, barrer	21.6 ± 0.2	26.4 ± 0.3	27.2 ± 0.3
	Constant diffusivity, time-lag method		
D, $\times 10^{-7}$ cm^2 s^{-1}	1.02 ± 0.02	1.30 ± 0.03	1.32 ± 0.03
$C(X=0)$, cm^3(STP) cm^{-3}(mixture)	83.4 ± 2.5	74.3 ± 2.4	74.5 ± 2.2
	Variable diffusivity, simplified model		
$D_T(T,p,0)$, $\times 10^{-8}$ cm^2 s^{-1}	7.21 ± 0.04	8.66 ± 0.09	10.50 ± 0.15
$D'(X=0)$	2.44 ± 0.11	2.66 ± 0.15	2.35 ± 0.27

Continuation of Table 4.4

$D_T\,[T,p,\nu(X=0)]$, $\times 10^{-7}$ cm^2 s^{-1}	1.76 ± 0.07	2.29 ± 0.14	2.46 ± 0.25
$C(X=0)$, cm^3(STP) cm^{-3}(mixture)	75.1 ± 0.8	66.2 ± 3.1	60.3 ± 2.7
$U/\,(WV')$	84.2 ± 5.6	67.4 ± 5.5	70.5 ± 15.4
	Variable diffusivity, full model ($W=5$)		
$D_T(T,p,0)$, $\times 10^{-8}$ cm^2 s^{-1}	7.06 ± 0.06	8.44 ± 0.11	10.31 ± 0.21
$D'(X=0)$	2.34 ± 0.10	2.53 ± 0.14	2.26 ± 0.24
$D_T\,[T,p,\nu(X=0)]$, $\times 10^{-7}$ cm^2 s^{-1}	1.65 ± 0.06	2.13 ± 0.10	2.32 ± 0.21
$C(X=0)$, cm^3(STP) cm^{-3}(mixture)	77.0 ± 0.8	67.9 ± 1.2	61.6 ± 2.5
$U/\,(WV')$	74.6 ± 5.5	59.1 ± 5.2	63.0 ± 15.2
	Variable diffusivity, gPROMS optimisation		
$D_T(T,p,0)$, $\times 10^{-8}$ cm^2 s^{-1}	7.23 ± 0.01	8.88 ± 0.01	10.00 ± 0.10
$D'(X=0)$	2.61 ± 0.01	2.70 ± 0.01	2.46 ± 0.01
$D_T\,[T,p,\nu(X=0)]$, $\times 10^{-7}$ cm^2 s^{-1}	1.89 ± 0.01	2.40 ± 0.01	2.46 ± 0.03
$C(X=0)$, cm^3(STP) cm^{-3}(mixture)	72.1 ± 0.4	63.7 ± 0.4	61.6 ± 0.2
$U/\,(WV')$	75.1 ± 0.2	64.2 ± 0.2	68.4 ± 0.5
	Run-H-4 (28°C,55bar)	**Run-H-5 (35°C,5bar)**	**Run-H-6 (35°C,55bar)**
$F_m(t=\infty)$, $\times 10^{-5}$ cm^3(STP) cm^{-2} s^{-1}	3.56 ± 0.08	0.55 ± 0.01	4.47 ± 0.10
P, barrer	8.1 ± 0.1	16.9 ± 0.2	10.1 ± 0.1
	Constant diffusivity, time-lag method		
D, $\times 10^{-7}$ cm^2 s^{-1}	3.67 ± 0.09	6.84 ± 0.20	3.44 ± 0.07
$C(X=0)$, cm^3(STP) cm^{-3}(mixture)	8.5 ± 0.3	0.8 ± 0.1	11.8 ± 0.4
	Variable diffusivity, simplified model		
$D_T(T,p,0)$, $\times 10^{-7}$ cm^2 s^{-1}	2.81 ± 0.01	6.66 ± 0.01	2.97 ± 0.01

Continuation of Table 4.4

$D'(X=0)$	1.76 ± 0.08	1.57 ± 0.15	1.68 ± 0.09
$D_T\,[T,p,\nu(X=0)]$, $\times 10^{-7}$ cm^2 s^{-1}	4.95 ± 0.22	10.43 ± 0.97	4.99 ± 0.24
$C(X=0)$, cm^3(STP) cm^{-3}(mixture)	8.7 ± 0.1	0.6 ± 0.1	10.5 ± 0.1
$U/\,(WV')$	15.3 ± 3.0	1.3 ± 0.4	20.4 ± 2.5
	Variable diffusivity, full model ($W=5$)		
$D_T(T,p,0)$, $\times 10^{-7}$ cm^2 s^{-1}	2.81 ± 0.01	6.63 ± 0.03	2.96 ± 0.01
$D'(X=0)$	1.72 ± 0.08	1.54 ± 0.14	1.64 ± 0.08
$D_T\,[T,p,\nu(X=0)]$, $\times 10^{-7}$ cm^2 s^{-1}	4.79 ± 0.19	10.20 ± 0.87	4.85 ± 0.21
$C(X=0)$, cm^3(STP) cm^{-3}(mixture)	8.8 ± 0.1	0.6 ± 0.1	10.6 ± 0.1
$U/\,(WV')$	14.4 ± 1.6	1.3 ± 0.4	19.2 ± 2.5
	Variable diffusivity, gPROMS optimisation		
$D_T(T,p,0)$, $\times 10^{-7}$ cm^2 s^{-1}	2.81 ± 0.01	6.67 ± 0.01	3.00 ± 0.01
$D'(X=0)$	1.78 ± 0.02	1.58 ± 0.02	1.66 ± 0.02
$D_T\,[T,p,\nu(X=0)]$, $\times 10^{-7}$ cm^2 s^{-1}	5.00 ± 0.07	10.54 ± 0.15	4.98 ± 0.08
$C(X=0)$, cm^3(STP) cm^{-3}(mixture)	8.6 ± 0.1	0.6 ± 0.1	10.5 ± 0.1
$U/\,(WV')$	15.0 ± 0.3	1.3 ± 0.1	20.7 ± 0.5
	Run-H-7	**Run-H-8**	**Run-H-9**
	(35°C,125bar)	**(35°C,200bar)**	**(50°C,5bar)**
$F_m(t=\infty)$, $\times 10^{-5}$ cm^3(STP) cm^{-2} s^{-1}	6.52 ± 0.14	6.55 ± 0.14	2.22 ± 0.05
P, barrer	6.5 ± 0.1	4.0 ± 0.1	68.1 ± 0.7
	Constant diffusivity, time-lag method		
D, $\times 10^{-7}$ cm^2 s^{-1}	3.58 ± 0.08	3.31 ± 0.07	7.29 ± 0.20
$C(X=0)$, cm^3(STP) cm^{-3}(mixture)	16.7 ± 0.6	18.1 ± 0.6	2.8 ± 0.1
	Variable diffusivity, simplified model		

Continuation of Table 4.4

$D_T(T,p,0)$, $\times 10^{-7}$ cm^2 s^{-1}	2.85 ± 0.01	2.70 ± 0.03	6.81 ± 0.01
$D'(X=0)$	2.38 ± 0.14	1.97 ± 0.20	1.16 ± 0.03
$D_T\left[T,p,\nu(X=0)\right]$, $\times 10^{-7}$ cm^2 s^{-1}	6.79 ± 0.37	5.32 ± 0.47	7.88 ± 0.18
$C(X=0)$, cm^3(STP) cm^{-3}(mixture)	13.2 ± 0.2	15.6 ± 0.5	2.8 ± 0.1
$U/\left(WV'\right)$	15.2 ± 1.4	23.0 ± 4.8	19.1 ± 3.5
	Variable diffusivity, full model ($W=5$)		
$D_T(T,p,0)$, $\times 10^{-7}$ cm^2 s^{-1}	2.80 ± 0.02	2.67 ± 0.03	6.81 ± 0.01
$D'(X=0)$	2.28 ± 0.13	1.91 ± 0.18	1.15 ± 0.03
$D_T\left[T,p,\nu(X=0)\right]$, $\times 10^{-7}$ cm^2 s^{-1}	6.39 ± 0.31	5.11 ± 0.41	7.86 ± 0.17
$C(X=0)$, cm^3(STP) cm^{-3}(mixture)	13.5 ± 0.2	15.8 ± 0.5	2.8 ± 0.1
$U/\left(WV'\right)$	13.6 ± 1.4	21.1 ± 4.8	19.7 ± 4.0
	Variable diffusivity, gPROMS optimisation		
$D_T(T,p,0)$, $\times 10^{-7}$ cm^2 s^{-1}	2.87 ± 0.01	2.71 ± 0.01	6.73 ± 0.03
$D'(X=0)$	2.38 ± 0.02	1.99 ± 0.01	1.13 ± 0.03
$D_T\left[T,p,\nu(X=0)\right]$, $\times 10^{-7}$ cm^2 s^{-1}	6.83 ± 0.08	5.39 ± 0.05	7.60 ± 0.24
$C(X=0)$, cm^3(STP) cm^{-3}(mixture)	13.1 ± 0.1	15.4 ± 0.1	2.9 ± 0.1
$U/\left(WV'\right)$	15.1 ± 0.1	22.5 ± 0.1	23.3 ± 6.8

In the table, $F_m(t=\infty)$ was calculated from Eq. (3.2); P was calculated from Eq. (2.1), in a unit of barrer, which is equal to 10^{-10}cm^3(STP)cm^{-3}(mixture)s^{-1}cmHg^{-1}. For the constant diffusivity cases, D was obtained from the "time lag" with Eq. (2.6), and $C(X=0)$ was calculated from the slope of the approaching line with Eq. (2.5). For the variable diffusivity cases, the product of $D_T(T,p,0)$ and $D'(X=0)$ results in $D_T\left[T,p,\nu(X=0)\right]$, representing the thermodynamic diffusivity at the top surface of the polymer disc at T and p; $C(X=0)$ was calculated with Eq. (4.48) or Eq. (4.50); and $U/\left(WV'\right)$ was obtained from Eq. (4.52).

4.7.3 Discussion on the Estimated Parameters

Results of Constant Diffusivity *vs.* Variable Diffusivity

The constant diffusivity, D, obtained using the time-lag method, may be regarded as a mean diffusivity across the polymer disc throughout the measurement. As can be seen in Table 4.4, the values of D obtained for the runs were of the same order of magnitude as those of the thermodynamic diffusivity, whose values were bounded by $D_T(T, p, 0)$ and $D_T[T, p, \nu(X = 0)]$. As for the penetrant concentration at the top surface of the polymer disc, $C(X = 0)$, consistent values seemed to be obtained, comparing the results of the constant diffusivity and the variable diffusivity cases. However, the time-lag method primarily features the permeation process at the steady state, regardless of the factors that may affect the diffusion behaviour. On the other hand, the free volume formulations incorporating the thermodynamic diffusivity, which characterises the pressure and temperature dependence of diffusion, could provide satisfactory modelling for not only the steady-state but also the transient permeation.

Comparisons of the Approaches for Variable Diffusivity

Considering the application of the graphical method with early approximation, the results obtained using the simplified model and those obtained using the full model with $W = 5$ will now be compared. For the nine runs, it was found that the differences between the estimates were less than 2% for $D_T(T, p, 0)$, 5% for $D'(X = 0)$, 7% for $D_T[T, p, \nu(X = 0)]$, and 3% for $C(X = 0)$, which were within the uncertainty bounds for each quantity. For $U/(WV')$, there were around 10% differences between the estimates from the simplified and the full models. This relatively larger difference was likely due to the deviation of the value of $(-\partial D'/\partial X)_{X=1,\tau=\infty}$, which is a term in Eq. (4.52), for the simplified model, from that for the full model ($W = 5$), when there is a relatively large estimate of $D'(X = 0)$, as shown in Figure 4.11. Nevertheless, overall, the estimates of these parameters for the nine runs with the the simplified model were reasonably close to those obtained from the full model with $W = 5$, confirming that the modelling results were insentive to the magnitude of W, as previously stated in Section 4.3.2 and Section 4.6.

With the simplified model, the parameter estimations using the graphical method can also be compared with those obtained by gPROMS optimisation. For the nine runs, the differences between the estimates were approximately 1% for $D_T(T, p, 0)$, 2% for $D'(X = 0)$, 4% for $D_T[T, p, \nu(X = 0)]$, 2% for $C(X = 0)$, and 3% for $U/(WV')$ (except for Run-H-9, in which case the difference for $U/(WV')$ was about 20%). This comparatively large deviation may result from the considerably low estimates for $D'(X = 0)$ in Run-H-9 in both approaches. Since the term of $D'(X = 0)$ appears in the denominator in Eq. (4.52), minor variations of this small quantity would significantly affect the estimates for $U/(WV')$. In fact, for the same reason, there was a relatively high uncertainty (around 20%) related to the estimation of $U/(WV')$ for Run-H-9. Overall, the estimates of these parameters with the graphical method and gPROMS optimisation were reasonably close and were effectively within the uncertainty bounds for each quantity. Hence, the graphical method, without the requirement for modelling software, can be used for convenient modelling of the transient diffusion and for accurate estimations of the key transport properties.

Trends in Estimated Parameters with Varying Conditions

Considering the pressure effect on the parameters, as can be seen from the results of Run-P-5 to Run-P-8 in table 4.4, permeability at the steady state, P, decreased with increasing pressure, whilst the concentration of the penetrant in the system at the top surface of the polymer, $C(X = 0)$, estimated with all approaches, increased with pressure. However, $C(X = 0)$ did not increase linearly with pressure, demonstrating that Henry's law does not apply at the elevated pressures. In fact, with respect to these runs, the increase in $C(X = 0)$ became less significant from 55 bar to higher pressures. The deviation from Henry's law at higher pressures will be further addressed in Chapter 5.

The system pressure affects the thermodynamic diffusivity in two opposing ways. On one hand, increasing the pressure would increase the penetrant concentration in the mixture, contributing to an increase of the free volume in the polymer and thus an increase of the thermodynamic diffusivity. This could be suggested by the increasing $D'(X = 0)$ with the increasing pressure from Run-P-5 to Run-P-8, as shown in Table 4.4. On the other hand, increasing the pressure

leads to a decrease of the free volume, owing to the mechanical compaction of the polymer. Consequently, the thermodynamic diffusivity might be reduced, as can be seen from the decreasing $D_T(T, p, 0)$ with the increasing pressure. On the basis of the results obtained in this chapter, it is speculated that as pressure increases, the increase of the penetrant concentration may dominate over the compaction effect in the lower pressure range (possibly below a certain pressure between 55 bar and 125 bar), resulting in an overall increase of the diffusivity with the increasing pressure. When the pressure is elevated to a higher range, the mechanic compaction effect may dominate over any increase in the penetrant concentration, leading to a decrease of the free volume and the overall diffusivity with the increasing pressure.

Regarding the temperature effect on the parameters when the pressure is constant, results for Run-P-1 to Run-P-3, or Run-H-4 and Run-H-6, or Run-H-5 and Run-H-9, can be compared respectively. In general, the values of $F_m(t = \infty)$, P, $D_T(T, p, 0)$, $D'(X = 0)$, and $D_T\left[T, p, \nu(X = 0)\right]$, increased with the increasing temperature. However, $C(X = 0)$ seemed to decrease with the increasing temperature. This could be explained by the decreasing solubility of CO_2 in polymers with the increasing temperature, as reported in many other studies [208–211].

4.8 Concluding Remarks

In this chapter, methods and results were reported for the transient permeation properties of CO_2-PTFE and CO_2-HDPE systems under various temperatures and pressures. The key conclusions are: (1) Diffusion equations incorporating a free volume model were used to interprete the transient diffusion of the penetrant through the polymers. It was shown that the model with a variable diffusivity could better describe the diffusional behaviour of the system, than the one with the commonly used time-lag method, which assumes that diffusivity is constant. (2) The diffusion equations, expressed in terms of a thermodynamic diffusivity, were nondimensionalised and simplified to enable a more straightforward analysis. By doing so, the number of parameters contained in the model was significantly reduced from 7 to 3. It was shown that

the simplified model offered accuarate and reliable estimation results for the parameters, as well as reasonably good fits to the experimental flux data. (3) A graphical method based on early approximation for estimating the optimal values of the key transport properties has been proposed. The straightforward procedure proposed in this chapter can be applied to new and existing measurements of transient permeation, without the requirement of advanced numerical software for parameter optimisation. (4) The influence of pressure and temperature on the estimated parameters were discussed. It was found that the pressure has two opposing effects on the thermodynamic diffusivity. As the pressure increased, the increasing penetrant concentration appears to dominate the diffusion process and accelerate the diffusion in the lower pressure range, but this effect was outweighed by the compaction effect, which inhibited the diffusion in the higher pressure range. It was possible to estimate the concentration of CO_2 on the upper surface of the HDPE sheet, without knowledge of the specific volume of the penetrant. It was also found that Henry's law was not obeyed as the pressure increased. On the basis of the work presented in this chapter, further investigation of the diffusion characteristics and the free-volume parameters, subject to varied pressures in a successive permeation measurement, will be presented in the following chapter.

Chapter 5

Transient Permeation Following Successive Pressure Steps

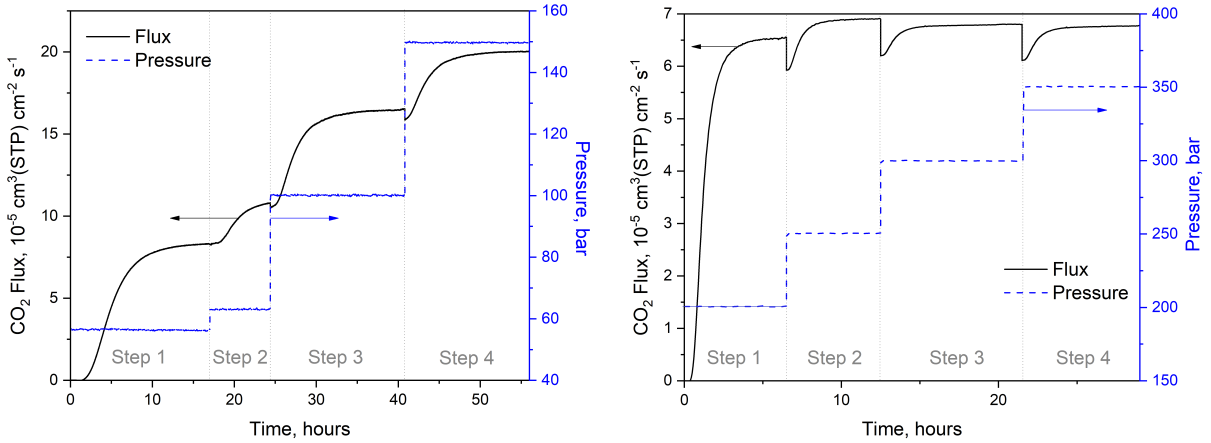
5.1 Introduction

This chapter focuses on transient permeation experiments consisting of multiple successive pressure steps, in a wide pressure range from tens to hundreds of bars. There are two parts in this chapter: Part I introduces the theoretical model, based on the simplified, nondimensionalised free volume model and the graphical method developed in the previous chapter, for the analysis of the successive measurements; and Part II discusses the application of the developed model with the proposed method, to the analysis of the experimental results, the estimation of the transport properties at each pressure step, and the determination of the values of the free-volume parameters in the model.

5.1.1 Background

It was found that during a successive permeation experiment, after a steady state was reached, abruptly increasing the penetrant pressure would cause a near-instananeous drop of the flux, as can be seen in Figure 5.1 (previously exhibited in Figure 4.2). It was postulated that this

immediate change in the flux, subject to the pressure change, was caused by a decrease in the free volume, leading to a decrease of the thermodynamic diffusivity at the bottom surface of the polymer disc. Specifically, when there was an increase of the hydrostatic pressure acting upon the polymer disc, the pressure term would have an immediate effect on reducing the free volume, before the penetrant volume fraction in the system started to increase with the increasing pressure. Following this immediate drop, the permeation flux would gradually increase, as a result of the increasing penetrant volume fraction in the system, until a new steady state was established. By varying the hydrostatic pressure during a transient permeation experiment with successive steps and analysing the fall in permeation flux at each step, free-volume parameters can be estimated. Furthermore, the effects of pressure on the diffusivity and the solubility of the penetrant-polymer system can also be investigated.



(a) PTFE, 28 °C (b) HDPE, 35 °C

Figure 5.1: Plots of flux and pressure against time in a successive permeation experiment for PTFE and HDPE.

5.1.2 Aims

In this chapter, the diffusion equations incorporating the nondimensionalised free volume model, are further developed for the modelling of permeation experiments with multiple pressure steps. The aims of the work in this chapter are to:

1) make meaurements of the permeation flux of CO_2 in PTFE and HDPE with multiple pressure steps;

2) interprete the experimental data using the nondimensionalised free volume model, which is developed for continuous permeation with successive steps;

3) propose a straightforward method for estimating the free-volume parameters, and the transport properties at each pressure step;

4) investigate the effects of the pressure on thermodynamic diffusivity and solubility;

5) compare the obtained results with literature data, and to examine the applicability of the proposed model and method to similar penetrant-polymer systems under a wide range of conditions.

Part I: Theoretical

5.2 Stepwise Model Development

5.2.1 Diffusion Equations

In Chapter 4, $v_f^*(T,p,0)$, which represents the fractional free volume of the pure polymer at p and T, was introduced in Eq. (4.7). In this chapter, the effect of pressure on $v_f^*(T,p,0)$ is accounted for in the relationship:

$$v_f^*(T,p,0) = v_f(T,0,0) - \beta_p p, \tag{5.1}$$

where $v_f(T,0,0)$ is the fractional free volume of the pure polymer ($\nu = 0$) at T and $p = 0$, and β_p is the coefficient of pressure dependence.

For the i^{th} step, $D_{T,i}(T,p_i,0)$, which is the thermodynamic diffusivity at infinite dilution of the penetrant, *i.e.* $\nu \to 0$, at T and p_i, can be defined to nondimensionalise the model:

$$D_{T,i}(T,p_i,0) = RTA_d \exp\left\{-\frac{B_d}{\phi_a[v_f(T,0,0) - \beta_p p_i]}\right\}. \tag{5.2}$$

The dimensionless diffusivity at the i^{th} step, D'_i, is:

$$D'_i = \frac{D_T}{D_{T,i}(T, p_i, 0)} = \exp\left\{\frac{B_d \gamma \nu}{\phi_a \left[v_f(T,0,0) - \beta_p p_i\right]\left[v_f(T,0,0) - \beta_p p_i + \gamma\nu\right]}\right\}. \tag{5.3}$$

The definitions of U_i and W_i are consistent with those previously defined for single pressure step in chapter 4:

$$U_i = \frac{v_f(T,0,0) - \beta_p p_i}{\gamma}, \tag{5.4}$$

$$W_i = \frac{B_d}{\phi_a \left[v_f(T,0,0) - \beta_p p_i\right]}. \tag{5.5}$$

Thus, Eq. (5.3) can be written in an equivalent form:

$$D'_i = \exp\left(\frac{W_i \nu}{U_i + \nu}\right). \tag{5.6}$$

Dimensionless time and length are re-defined:

$$\tau_i = \frac{D_{T,i}(T, p_i, 0) t_i}{L^2}, \tag{5.7}$$

$$X = \frac{x}{L}. \tag{5.8}$$

Given the above relationships, Fick's second law of diffusion can be formulated in terms of D'_i, τ_i and X:

$$\frac{\partial D'_i}{\partial \tau_i} = D'_i \left(W_i - \ln D'_i\right)^2 \frac{\partial}{\partial X}\left[\frac{1}{\left(W_i - \ln D'_i\right)^2}\frac{\partial D'_i}{\partial X}\right], \tag{5.9}$$

The initial and boundary conditions are given:

$$\tau_i = 0, \quad 0 < X < 1, \quad D'_i = 1, \tag{5.10}$$

$$\tau_i \geq 0, \qquad X = 0, \quad D'_i = D'_i(X = 0), \tag{5.11}$$

$$\tau_i \geq 0, \qquad X = 1, \quad D'_i = 1. \tag{5.12}$$

When the value of W_i is much larger than that of $\ln D'_i$, Eq. (5.9) can be simplified to:

$$\frac{\partial D'_i}{\partial \tau_i} = D'_i \frac{\partial^2 D'_i}{\partial X^2}. \tag{5.13}$$

At steady state and $X = 1$, $(-\partial D'_i/\partial X)_{X=1} = D'_i(X = 0) - 1$. This can be seen by setting the time derivative in Eq. (5.13) to zero, thus it is clear that D'_i decreases linearly from $D'_i(X = 0)$ to 1 across the disc.

5.2.2 Permeation Flux

The flux, F_i, can also be expressed in terms of D'_i and X:

$$F_i = \frac{U_i}{V' W_i} \frac{D_{T,i}(T, p_i, 0)}{L} \left(-\frac{\partial D'_i}{\partial X} \right)_{X=1} = \frac{U_i}{V' W_i} \frac{D_{T,i}(T, p_i, 0)}{L} \left[D'_i(X = 0) - 1 \right]. \tag{5.14}$$

It is assumed that V', as defined by Eq. (4.9), is a constant, regardless of p_i. This assumption is equivalent to V_{T,p_i}, *i.e.* the specific volume of the penetrant dissolved in the polymer mixture at T and p_i, being assumed constant regardless of p_i. In reality, V_{T,p_i} may decrease as the pressure increases. However, given the relatively low concentration and the low compressibility of the dissolved penetrant in the mixture [212, 213], changes of V_{T,p_i} and hence V' may be considered negligible as the pressure changes. This assumption is considered in more detail in Chapter 6.

The steady-state flux for the i^{th} step is denoted by $F(t_i = \infty)$, and $t_i = \infty$ represents the time, which is sufficiently long for a steady state of permeation to be reached for the i^{th} step. Upon the change in hydrostatic pressure from p_i to p_{i+1} at the moment of $t_{i+1} = 0$, the flux changes correspondingly from $F(t_i = \infty)$ to $F(t_{i+1} = 0)$. From Eqn. (4.21), taking the ratio of $F(t_{i+1} = 0)$ to $F(t_i = \infty)$, which is equivalent to the ratio of $F_m(t_{i+1} = 0)$ to $F_m(t_i = \infty)$, the ratio denoted by F'_{i+1} can be expressed as:

$$F'_{i+1} = \frac{F_m(t_{i+1} = 0)}{F_m(t_i = \infty)} = \frac{F(t_{i+1} = 0)}{F(t_i = \infty)} = \frac{D_{T,i+1}(T, p_{i+1}, 0)}{D_{T,i}(T, p_i, 0)} \frac{(-\partial \nu_{i+1}/\partial x)_{x=L, t_{i+1}=0}}{(-\partial \nu_i/\partial x)_{x=L, t_i=\infty}}, \tag{5.15}$$

where V', assumed to be constant, has been cancelled from the expression. Compared with the

decrease of free volume in the mixture, the decrease of the occupied volumes of the penetrant and the polymer molecules may be considered insignificant [214]. Therefore, it is reasonable to assume that the distribution of $\nu(X)$, the volume fration of the penetrant in the mixture, remains unchanged, at the instant the pressure is increased. That is to say, the difference between $(-\partial\nu_{i+1}/\partial x)_{x=L,t_{i+1}=0}$ and $(-\partial\nu_i/\partial x)_{x=L,t_i=\infty}$ was considered insignificant for the drop of the flux. As a result, the expression for F'_{i+1} can be simplified to:

$$F'_{i+1} = \frac{D_{T,i+1}(T, p_{i+1}, 0)}{D_{T,i}(T, p_i, 0)}. \tag{5.16}$$

Eq. (5.16) indicates that when the pressure is increased, the decrease in flux mainly results from a decrease of the thermodynamic diffusivity at infinite dilution, *i.e.* its value at the bottom surface of the polymer disc. Furthermore, Eq. (5.16) suggests that $D_{T,i}(T, p_i, 0)$ corresponding to each pressure p_i, can be estimated from the drop of the measured flux observed at the beginning of each step, once $D_{T,1}(T, p_1, 0)$ is known.

5.3 Constants $\tilde{a}$, $\tilde{b}$ and $\tilde{c}$

Three constants, $\tilde{a}$, $\tilde{b}$ and $\tilde{c}$, can be defined:

$$\tilde{a} = RTA_d, \tag{5.17}$$

$$\tilde{b} = \frac{B_d}{\phi_a \beta_p}, \tag{5.18}$$

$$\tilde{c} = \frac{v_f(T, 0, 0)}{\beta_p}. \tag{5.19}$$

Thus, from Eq. (5.2), $D_{T,i}(T, p_i, 0)$ can be expressed as:

$$D_{T,i}(T, p_i, 0) = \tilde{a} \exp\left(-\frac{\tilde{b}}{\tilde{c} - p_i}\right). \tag{5.20}$$

As suggested by Eq. (5.20), the relationship between $D_{T,i}(T, p_i, 0)$ and p_i can be described by $\tilde{a}$, $\tilde{b}$ and $\tilde{c}$, which are lumped constants of free-volume parameters. The values of $\tilde{a}$, $\tilde{b}$ and

$\tilde{c}$ can be optimised using the method of least squares, by minimising the sum of the squared differences between the experimentally obtained values of $D_{T,i}(T, p_i, 0)$ and those calculated from Eq. (5.20). The optimisation could be conducted using numerical software, *e.g.* Matlab and gPROMS. Alternatively, Excel Solver can also be used to optimise $\tilde{a}$, $\tilde{b}$ and $\tilde{c}$, using a nonlinear least squares method, which involves minimising the sum of the squared differences, Q, by taking its partial differentials with respect to $\tilde{a}$, $\tilde{b}$ and $\tilde{c}$:

$$Q = \sum \left(\ln D_{T,i}^{\text{exp}} - \ln D_{T,i}^{\text{cal}}\right)^2 = \sum \left[\ln D_{T,i}^{\text{exp}} - \left(\ln \tilde{a} - \frac{\tilde{b}}{\tilde{c} - p_i}\right)\right]^2, \tag{5.21}$$

with

$$\frac{\partial Q}{\partial \tilde{a}} = 0, \frac{\partial Q}{\partial \tilde{b}} = 0, \frac{\partial Q}{\partial \tilde{c}} = 0, \tag{5.22}$$

where $\ln D_{T,i}^{\text{exp}}$ and $\ln D_{T,i}^{\text{cal}}$ represent the experimental and the calculated values of $D_{T,i}(T, p_i, 0)$, respectively. The partial differentials, calculated from Eq. (5.22), lead to linear equations, from which the varables, $\tilde{a}$ and $\tilde{b}$, can be expressed by $\tilde{c}$:

$$\tilde{a} = \exp\left[\frac{\sum \ln D_{T,i}^{\text{exp}} + \tilde{b} \sum \left(\frac{1}{\tilde{c} - p_i}\right)}{n}\right], \tag{5.23}$$

and

$$\tilde{b} = \frac{\sum \ln D_{T,i}^{\text{exp}} \cdot \sum \left(\frac{1}{\tilde{c} - p_i}\right) - n \sum \left(\frac{\ln D_{T,i}^{\text{exp}}}{\tilde{c} - p_i}\right)}{n \sum \left(\frac{1}{\tilde{c} - p_i}\right)^2 - \left[\sum \left(\frac{1}{\tilde{c} - p_i}\right)\right]^2}, \tag{5.24}$$

where n refers to the total number of steps in a measurement. The minimisation can then be computed with only one adjustable parameter, $\tilde{c}$, which can be optimised with Excel Solver to minimise the squared difference, Q.

5.4 Estimation of $D_i'(X=0)$

The values of $D_i'(X=0)$ can be estimated sequentially from $D_1'(X=0)$, which can be estimated using the graphical method previously described for a single pressure step in Chapter 4, with a relationship derived from Eq. (5.14) and Eq. (5.16). Taking the ratio of the steady-state flux

at the i^{th} step, $F_i(\tau_i = \infty)$, to that at the $(i+1)^{\text{th}}$ step, $F_{i+1}(\tau_{i+1} = \infty)$, is:

$$\frac{F_i(\tau_i = \infty)}{F_{i+1}(\tau_{i+1} = \infty)} = \frac{1}{F'_{i+1}} \frac{(\partial D'_i/\partial X)_{X=1,t_i=\infty}}{(\partial D'_{i+1}/\partial X)_{X=1,t_{i+1}=\infty}}. \tag{5.25}$$

As discussed in Section 5.2.1, at the steady state, D'_i decreases linearly from $D'_i(X = 0)$ to 1 across the disc, so that $(-\partial D'_i/\partial X) = D'_i(X = 0) - 1$. Substituting this relationship into Eq. (5.25) and rearranging the equation:

$$D'_{i+1}(X = 0) = \frac{U_i/(W_i V')F_{i+1}(\tau_{i+1} = \infty)[D'_i(X = 0) - 1]}{U_{i+1}/(W_{i+1}V')F_i(\tau_i = \infty)F'_{i+1}} + 1. \tag{5.26}$$

From the definitions of U_i and W_i, *i.e.* Eq. (5.4) and Eq. (5.5), the following relationship is obtained:

$$\frac{U_i/(W_i V')}{U_{i+1}/(W_{i+1}V')} = \left[\frac{v_f(T, 0, 0) - \beta_p p_i}{v_f(T, 0, 0) - \beta_p p_{i+1}}\right]^2. \tag{5.27}$$

By combining Eq. (4.8) and Eq. (5.6), $C_i(X = 0)$, which is the volumetric concentration of the penetrant, corresponding to STP, at the top surface of the disc for the i^{th} step, can be derived from $D_{T,i}(T, p_i, 0)$ and $D'_i(X = 0)$. This will be presented in Chapter 6, together with the modelling using Sanchez-Lacombe equation of state.

Part II: Experimental

5.5 Measurements of Steady-State Flux for Step i

Most of the single-step measurements presented in Chapter 4, except for Run-H-7, were in fact the first steps of successive pressure step experiments. The results of these eight runs are presented in Table 5.1, where F'_{i+1}, as defined by Eq. (5.15), is the ratio of $F_m(t_{i+1} = 0)$ to $F_m(t_i = \infty)$. Also, $D_{T,i+1}(T, p_{i+1}, 0)$ was obtained by multiplying $D_{T,i}(T, p_i, 0)$ by F'_{i+1}.

Table 5.1: Experimental results for the continuous runs: $F_m(t_i = 0)$ and $F_m(t_i = \infty)$ obtained using Eq. (3.2), F'_{i+1} obtained using Eq. (5.15), and $D_{T,i}(T, p_i, 0)$ obtained using Eq. (5.16).

Step i	p_i, bar	$F_m(t_i = 0)$, $\times 10^{-5}$ cm^3 (STP) cm^{-2} s^{-1}	$F_m(t_i = \infty)$, $\times 10^{-5}$ cm^3 (STP) cm^{-2} s^{-1}	F'_{i+1},	$D_{T,i}(T, p_i, 0)$, $\times 10^{-7}$ cm^2 s^{-1}
			Run-P-1, PTFE, 28 ˚C		
1	55	0	8.32 ± 0.16	1	0.72 ± 0.01
2	63	8.27 ± 0.16	10.79 ± 0.21	0.99 ± 0.01	0.72 ± 0.01
3	100	10.47 ± 0.20	16.53 ± 0.32	0.97 ± 0.01	0.70 ± 0.01
4	150	15.86 ± 0.31	20.04 ± 0.38	0.96 ± 0.01	0.67 ± 0.01
			Run-P-2, PTFE, 40 ˚C		
1	50	0	9.23 ± 0.18	1	0.87 ± 0.01
2	100	8.46 ± 0.16	29.10 ± 0.56	0.92 ± 0.01	0.79 ± 0.01
3	150	27.11 ± 0.52	20.26 ± 0.39	0.93 ± 0.01	0.74 ± 0.01
4	200	18.75 ± 0.36	33.46 ± 0.65	0.93 ± 0.01	0.68 ± 0.01
5	250	31.08 ± 0.60	28.38 ± 0.55	0.93 ± 0.01	0.64 ± 0.01
6	300	26.25 ± 0.51	37.47 ± 0.72	0.92 ± 0.01	0.59 ± 0.01
7	350	34.57 ± 0.67	33.90 ± 0.66	0.92 ± 0.01	0.54 ± 0.01
8	400	31.19 ± 0.60	40.38 ± 0.78	0.92 ± 0.01	0.50 ± 0.01
9	450	37.09 ± 0.72	37.07 ± 0.72	0.92 ± 0.01	0.46 ± 0.01
10	500	33.95 ± 0.66	41.79 ± 0.81	0.92 ± 0.01	0.42 ± 0.01
			Run-P-3, PTFE, 50 ˚C		
1	50	0	9.52 ± 0.18	1	1.05 ± 0.02
2	100	8.93 ± 0.17	25.53 ± 0.48	0.94 ± 0.01	0.99 ± 0.01
3	150	23.98 ± 0.45	24.66 ± 0.46	0.94 ± 0.01	0.93 ± 0.01
4	200	23.04 ± 0.43	34.98 ± 0.66	0.93 ± 0.01	0.86 ± 0.01

Continuation of Table 5.1

Step i	p_i, bar	$F_m(t_i = 0)$, $\times 10^{-5}$ cm^3 (STP) cm^{-2} s^{-1}	$F_m(t_i = \infty)$, $\times 10^{-5}$ cm^3 (STP) cm^{-2} s^{-1}	F'_{i+1},	$D_{T,i}(T, p_i, 0)$, $\times 10^{-7}$ cm^2 s^{-1}
5	250	32.89 ± 0.62	35.36 ± 0.66	0.94 ± 0.01	0.81 ± 0.01
6	300	32.94 ± 0.62	42.87 ± 0.81	0.93 ± 0.01	0.76 ± 0.01
7	350	40.03 ± 0.75	40.50 ± 0.76	0.93 ± 0.01	0.71 ± 0.01
		Run-H-4, HDPE, 28 °C			
1	55	0	3.56 ± 0.07	1	2.81 ± 0.01
2	72	3.49 ± 0.07	4.21 ± 0.08	0.98 ± 0.01	2.75 ± 0.01
3	88	4.12 ± 0.08	4.64 ± 0.09	0.98 ± 0.01	2.70 ± 0.01
4	100	4.53 ± 0.08	4.60 ± 0.09	0.98 ± 0.01	2.64 ± 0.01
5	125	4.43 ± 0.09	4.70 ± 0.09	0.96 ± 0.01	2.54 ± 0.01
6	150	4.55 ± 0.09	4.78 ± 0.09	0.97 ± 0.01	2.46 ± 0.01
7	175	4.58 ± 0.09	4.88 ± 0.09	0.96 ± 0.01	2.35 ± 0.01
8	200	4.73 ± 0.09	4.96 ± 0.09	0.97 ± 0.01	2.28 ± 0.01
9	250	4.62 ± 0.09	4.88 ± 0.09	0.93 ± 0.01	2.12 ± 0.01
10	300	4.47 ± 0.09	4.98 ± 0.09	0.92 ± 0.01	1.95 ± 0.01
11	350	4.69 ± 0.09	4.90 ± 0.09	0.94 ± 0.01	1.83 ± 0.01
12	400	4.52 ± 0.08	5.00 ± 0.09	0.92 ± 0.01	1.69 ± 0.01
13	450	4.57 ± 0.09	5.01 ± 0.09	0.91 ± 0.01	1.55 ± 0.01
14	500	4.64 ± 0.09	4.80 ± 0.09	0.93 ± 0.01	1.43 ± 0.01
15	550	4.42 ± 0.08	4.79 ± 0.09	0.92 ± 0.01	1.32 ± 0.01
16	600	4.35 ± 0.08	4.56 ± 0.09	0.91 ± 0.01	1.20 ± 0.01
		Run-H-5, HDPE, 35 °C			
1	5	0	0.55 ± 0.01	1	6.66 ± 0.01

Continuation of Table 5.1

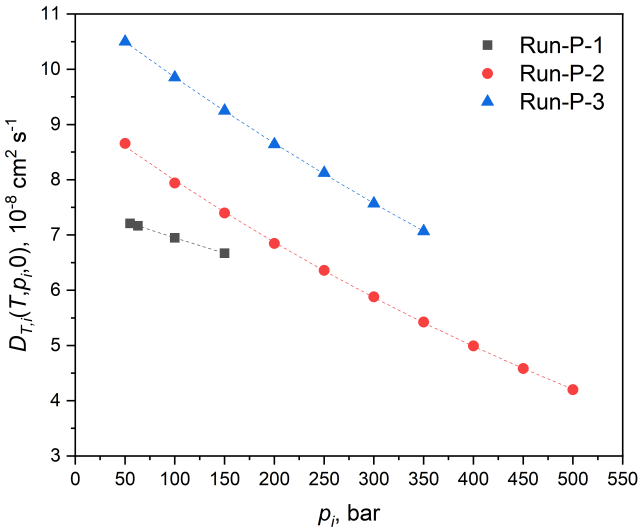
Step i	p_i, bar	$F_m(t_i = 0)$, $\times 10^{-5}$ cm^3 (STP) cm^{-2} s^{-1}	$F_m(t_i = \infty)$, $\times 10^{-5}$ cm^3 (STP) cm^{-2} s^{-1}	F'_{i+1},	$D_{T,i}(T, p_i, 0)$, $\times 10^{-7}$ cm^2 s^{-1}
2	10	0.55 ± 0.01	1.27 ± 0.02	0.99 ± 0.01	6.59 ± 0.01
3	20	1.25 ± 0.02	1.99 ± 0.04	0.99 ± 0.01	6.50 ± 0.01
4	30	1.97 ± 0.04	2.78 ± 0.05	0.99 ± 0.01	6.43 ± 0.01
5	40	2.74 ± 0.05	3.43 ± 0.06	0.98 ± 0.01	6.33 ± 0.01
6	55	3.35 ± 0.06	4.62 ± 0.09	0.98 ± 0.01	6.19 ± 0.01
7	75	4.49 ± 0.08	5.90 ± 0.11	0.97 ± 0.01	6.01 ± 0.01
8	100	5.67 ± 0.11	6.24 ± 0.12	0.96 ± 0.01	5.78 ± 0.01
9	125	5.99 ± 0.11	6.51 ± 0.12	0.96 ± 0.01	5.54 ± 0.01
10	150	6.24 ± 0.12	6.64 ± 0.12	0.96 ± 0.01	5.32 ± 0.01
11	175	6.38 ± 0.12	6.67 ± 0.13	0.96 ± 0.01	5.10 ± 0.01
12	200	6.36 ± 0.12	6.62 ± 0.12	0.95 ± 0.01	4.87 ± 0.01
13	250	6.10 ± 0.12	6.54 ± 0.12	0.92 ± 0.01	4.49 ± 0.01
14	300	6.01 ± 0.11	6.44 ± 0.12	0.92 ± 0.01	4.12 ± 0.01
15	350	5.94 ± 0.11	6.29 ± 0.12	0.92 ± 0.01	3.79 ± 0.01
		Run-H-6, HDPE, 35 °C			
1	55	0	4.47 ± 0.08	1	2.97 ± 0.01
2	100	4.11 ± 0.08	6.21 ± 0.12	0.92 ± 0.01	2.74 ± 0.01
3	150	5.69 ± 0.11	6.47 ± 0.12	0.92 ± 0.01	2.51 ± 0.01
4	200	5.87 ± 0.11	6.78 ± 0.13	0.91 ± 0.01	2.27 ± 0.01
5	250	6.11 ± 0.11	6.88 ± 0.13	0.90 ± 0.01	2.05 ± 0.01
6	300	6.24 ± 0.12	6.74 ± 0.13	0.91 ± 0.01	1.86 ± 0.01
7	400	5.48 ± 0.10	6.32 ± 0.12	0.81 ± 0.01	1.51 ± 0.01

Continuation of Table 5.1

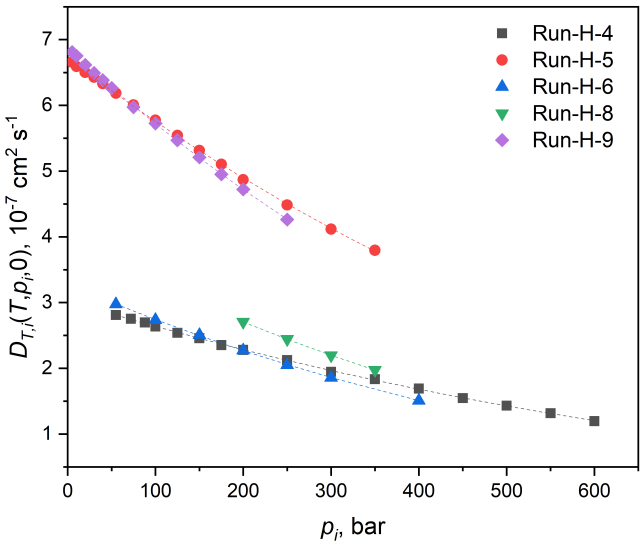
Step i	p_i, bar	$F_m(t_i = 0)$, $\times 10^{-5}$ cm^3 (STP) cm^{-2} s^{-1}	$F_m(t_i = \infty)$, $\times 10^{-5}$ cm^3 (STP) cm^{-2} s^{-1}	F'_{i+1},	$D_{T,i}(T, p_i, 0)$, $\times 10^{-7}$ cm^2 s^{-1}
			Run-H-8, HDPE, 35 °C		
1	200	0	6.55 ± 0.12	1	2.70 ± 0.02
2	250	5.92 ± 0.11	6.90 ± 0.13	0.90 ± 0.01	2.44 ± 0.02
3	300	6.20 ± 0.12	6.80 ± 0.13	0.90 ± 0.01	2.20 ± 0.02
4	350	6.11 ± 0.11	6.78 ± 0.13	0.90 ± 0.01	1.97 ± 0.02
			Run-H-9, HDPE, 50 °C		
1	5	0	2.22 ± 0.04	1	6.81 ± 0.01
2	10	2.20 ± 0.04	4.84 ± 0.09	0.99 ± 0.01	6.75 ± 0.01
3	20	4.75 ± 0.09	8.95 ± 0.17	0.98 ± 0.01	6.61 ± 0.01
4	30	8.79 ± 0.17	13.40 ± 0.25	0.98 ± 0.01	6.49 ± 0.01
5	40	13.17 ± 0.25	17.39 ± 0.33	0.98 ± 0.01	6.38 ± 0.01
6	50	17.07 ± 0.32	20.24 ± 0.38	0.98 ± 0.01	6.26 ± 0.01
7	75	19.30 ± 0.36	28.97 ± 0.54	0.95 ± 0.01	5.97 ± 0.01
8	100	27.77 ± 0.52	33.06 ± 0.62	0.96 ± 0.01	5.73 ± 0.01
9	125	31.58 ± 0.59	37.28 ± 0.70	0.96 ± 0.01	5.47 ± 0.01
10	150	35.52 ± 0.67	40.87 ± 0.77	0.95 ± 0.01	5.21 ± 0.01
11	175	38.85 ± 0.73	41.81 ± 0.79	0.95 ± 0.01	4.95 ± 0.01
12	200	39.86 ± 0.75	43.03 ± 0.81	0.95 ± 0.01	4.72 ± 0.01
13	250	38.85 ± 0.73	42.45 ± 0.80	0.90 ± 0.01	4.26 ± 0.01

5.6 Determination of $\tilde{a}$, $\tilde{b}$ and $\tilde{c}$

These experimentally determined values of $D_{T,i}(T, p_i, 0)$ shown in Table 5.1, were plotted against the corresponding pressure p_i in Figure 5.2, as represented by the symbols in the figures. In comparison, the dash lines in the figures show the modelled results of $D_{T,i}(T, p_i, 0)$ as a function of p_i, which were obtained using Eq. (5.20), with the optimised values of $\tilde{c}$, from which the values of $\tilde{a}$ and $\tilde{b}$ were derived using Eq. (5.23) and Eq. (5.24), respectively.



(a) PTFE runs



(b) HDPE runs

Figure 5.2: Comparison of the modelled $D_{T,i}(T, p_i, 0)$ by optimisation (dashed) and the experimentally obtained $D_{T,i}(T, p_i, 0)$ (symbols) for the eight runs.

As can be seen from Figure 5.2, despite the exponential formulation of $D_{T,i}(T, p_i, 0)$ shown by Eq. (5.20), the curves for the eight runs appeared to be rather linear. Comparing the experimentally obtained $D_{T,i}(T, p_i, 0)$ with those modelled with the optimised values of $\tilde{a}$, $\tilde{b}$ and $\tilde{c}$, excellent agreement between model and experiment was achieved using the optimisation method described in Section 5.3. For the three runs conducted with PTFE, the curves seemed to have similar gradients, which may account for the consistent estimations of $\tilde{c}$ for these runs.

For the five runs conducted with HDPE, as can be seen in Figure 5.2b, the curves seemed to be differentiated into two groups, one being Run-H-5 and Run-H-9, and the other being Run-H-4, Run-H-6 and Run-H-8. The primary difference between the two groups resulted from the different values of $D_{T,1}(T, p_1, 0)$ at p_1. In fact, p_1 for Run-H-5 and Run-H-9 was 5 bar, whilst that for Run-H-4 and Run-H-6 was 55 bar, and that for Run-H-8 was 200 bar. This might indicate that in a successive measurement, the different initial pressures, especially in the low pressure range, could lead to different diffusional characteristics. It would be helpful in the future to carry out more experiments with various initial pressures, to investigate the repeatability of these experiments, and to identify the effects of the initial pressures on the diffusional behaviour.

5.7 Estimations of Free-Volume Parameters

With the estimated values of $\tilde{a}$, $\tilde{b}$ and $\tilde{c}$, free-volume parameters, A_d, β_p and B_d were estimated using Eq. (5.17), Eq. (5.18) and Eq. (5.19). These estimates of $\tilde{a}$, $\tilde{b}$, $\tilde{c}$, and the free-volume parameters for each run were presented in Table 5.2.

5.7.1 Estimating A_d

From the definition of $\tilde{a}$, *i.e.* Eq. (5.17), the proportionality factor in the free volume model, A_d, was estimated. As mentioned in Section 4.2.2, this parameter correlates the mobility of the penetrant with the probability of the molecule finding a hole large enough in its neighbour for

a displacement. It has been considered to be dependent on mainly the size and the shape of the penetrant [107], but independent of temperature and penetrant concentration.

Table 5.2: The values of $\tilde{a}$, $\tilde{b}$ and $\tilde{c}$, estimated by the optimisation method described in Section 5.3; and the free-volume parameters obtained as described in Section 5.7.

	Run-P-1 *28 ˚C*	*Run-P-2* *40 ˚C*	*Run-P-3* *50 ˚C*	*Run-H-4* *28 ˚C*
$\tilde{a}$, $\times 10^{-4}$ cm^2 s^{-1}	2.87 ± 0.03	3.24 ± 0.07	1.11 ± 0.02	2.64 ± 0.02
$\tilde{b}$, $\times 10^{4}$ bar	8.43 ± 0.01	4.64 ± 0.04	3.89 ± 0.01	3.39 ± 0.01
$\tilde{c}$, $\times 10^{3}$ bar	10.23 ± 0.01	5.68 ± 0.02	5.64 ± 0.01	5.00 ± 0.01
A_d, $\times 10^{-7}$ cm^2 mol s^{-1} J^{-1}	1.15 ± 0.01	1.24 ± 0.02	0.41 ± 0.01	1.06 ± 0.01
B_d	0.31 ± 0.03	0.35 ± 0.03	0.32 ± 0.03	0.47 ± 0.05
β_p, $\times 10^{-5}$ bar^{-1}	0.51 ± 0.04	1.04 ± 0.09	1.14 ± 0.10	1.91 ± 0.24
	Run-H-5 *35 ˚C*	*Run-H-6* *35 ˚C*	*Run-H-8* *35 ˚C*	*Run-H-9* *50 ˚C*
$\tilde{a}$, $\times 10^{-4}$ cm^2 s^{-1}	4.83 ± 0.08	4.42 ± 0.05	4.27 ± 0.05	2.94 ± 0.02
$\tilde{b}$, $\times 10^{4}$ bar	2.86 ± 0.01	2.96 ± 0.01	2.69 ± 0.01	2.09 ± 0.01
$\tilde{c}$, $\times 10^{3}$ bar	4.35 ± 0.01	4.11 ± 0.01	3.85 ± 0.01	3.44 ± 0.01
A_d, $\times 10^{-7}$ cm^2 mol s^{-1} J^{-1}	1.88 ± 0.04	1.73 ± 0.01	1.67 ± 0.03	1.09 ± 0.01
B_d	0.48 ± 0.06	0.52 ± 0.06	0.51 ± 0.06	0.48 ± 0.06
β_p, $\times 10^{-5}$ bar^{-1}	2.29 ± 0.28	2.43 ± 0.29	2.59 ± 0.31	3.12 ± 0.36

As shown in Table 5.2, the calculated values of A_d for the diffusion of CO_2 in both PTFE and HDPE in this work were $\sim 1\times 10^{-7}$ cm^2 mol s^{-1} J^{-1}. The values of A_d for CO_2-PTFE and CO_2-HDPE systems could not be found in literature, but the obtained values were of the same order of magnitude as similar systems, for which values of A_d have been reported [115, 215–220]. For instance, in Kulkarni and Stern's study of the CO_2-polyethylene system at 35 °C and pressures up to 40 bar, they obtained a value of 3.1×10^{-7} cm^2 mol s^{-1} J^{-1} for A_d [115]. Sato et al. [215]

measured the solubility and diffusion coefficient of CO_2 in poly(butylene succinate) (PBS) and poly(butylene succinate-co-adipate (PBSA) at temperatures from 50 to 180 °C and pressures up to 200 bar. They used A_d as a fitting parameter to represent the experimental diffusion coefficient, and they determined its value as 2.41×10^{-7} cm^2 mol s^{-1} J^{-1} for CO_2-PBS and 3.55×10^{-7} cm^2 mol s^{-1} J^{-1} for CO_2-PBSA. In Chen et al. [216]'s work of solubility and diffusivity of CO_2 in polypropylene(PP)/Micro-calcium carbonate (Micro$CaCO_3$) composites at 200 and 220 °C and CO_2 pressures up to 220 bar, A_d was also used as a fitting paramter for diffusion coefficients. Values of A_d were determined as follows: 4.90×10^{-8} cm^2 mol s^{-1} J^{-1} for PP & PP composites without compatibiliser, and 3.98×10^{-8} cm^2 mol s^{-1} J^{-1} for PP & PP composites with compatibiliser.

Ushiki et al. [217] studied the solubilities and diffusion coefficients of CO_2 in poly(methyl methacrylate) (PMMA) at temperatures of 100 - 200 °C and pressures of up to 200 bar, and they obtained a value of 1.25×10^{-6} cm^2 mol s^{-1} J^{-1} for A_d. Meanwhile, they found that the A_d values were similar for CO_2 and N_2, the latter of which was 2.20×10^{-6} cm^2 mol s^{-1} J^{-1}. They attributed the similarity to the similar molecular size for CO_2 and N_2. In another study of the solubilities and diffusion coefficients of CO_2 in poly(ethylene-co-acrylic acid) (PEAA) over temperatures of 100 - 200 °C and pressures of up to 200 bar, Ushiki et al. [218] obtained a value of 1.85×10^{-7} cm^2 mol s^{-1} J^{-1} for A_d, using both A_d and B_d as fitting parameters. Moreover, to improve the correlation accuracy, they used A_d as a polymer-dependent fitting parameter, whilst using B_d as a universal parameter, which remained a constant for every polymer. As a result, they derived a relationship between the value of A_d and the mass fraction of arcylic acid (AA) in PEAA polymers, obtaining values of A_d in the range of 1.67×10^{-7} - 2.49×10^{-7} cm^2 mol s^{-1} J^{-1}, with mass fractions of AA ranging from 0 to 20%, respectively.

In addition to CO_2, there are a number of diffusion studies for various penetrants in polymers. For example, Guo and de Kee [219] investigated the diffusion of 11 different organic liquids, *e.g.* chloroform, toluene and acetone, in polyethylene within a temperature range of 10 - 60 °C, and they obtained the values of A_d, ranging from 7.58×10^{-8} cm^2 mol s^{-1} J^{-1} to 2.07×10^{-7} cm^2 mol s^{-1} J^{-1}. They claimed that a common value of 1.14×10^{-7} cm^2 mol s^{-1} J^{-1} could be assumed for these different organic liquids, since the obtained values of A_d for these liquids do not differ

considerably from each other. On the other hand, Guo and de Kee [219] obtained a higher A_d value for benzene, compared with the other investigated organic liquids. This seems to agree with the result obtained in Yeom and Huang [220]'s work, where the diffusion of benzene in polyethylene at 25 - 45 °C was studied, and a value of 4.9×10^{-7} cm^2 s^{-1} for A_d was obtained. The higher values of A_d for benzene than those for CO_2 and the other organic liquids might result from a larger molecular size of benzene than the molecular sizes of the others. Indeed, this hypothesis could be supported by a semiempirical correlation of A_d proposed by Kulkarni and Stern [115], who found that A_d was proportional to the penetrant size, and showed that the value of A_d for benzene was higher than that for CO_2, using the correlation they obtained.

5.7.2 Estimating β_p

The extraction of β_p from $\tilde{c}$ by applying Eq. (5.19), and the following B_d from $\tilde{b}$ by applying Eq. (5.18), was precluded by a lack of measurements of the free volume of the polymer under test. Specifically, the value of $v_f(T, 0, 0)$, which is the fractional free volume of the pure polymer at T and $p = 0$ bar, needs to be determined. In this section, it will be demonstrated how knowledge of the polymer free volume polymer free volume, combined with the transient permeation experiments, could be used to derive all the parameters in the free volume model.

For a wide variety of polymers or polymer solutions, the value of $v_f(T, 0, 0)$ can be calculated using WLF expression [221]:

$$v_f(T, 0, 0) = 0.025 + 4.82 \times 10^{-4}(T - T_g), \tag{5.28}$$

where T_g is the glass transition temperature of the pure polymer. This expression is valid for temperatures in the range $T_g < T < T_g + 100$ [221]. According to the datasheets attached to the PTFE [193] and HDPE [194] polymers from the provider, T_g for PTFE is -20 °C and that for HDPE is -95 °C. Thus, the temperatures investigated in this study from 28 °C to 50 °C are within the applicable range of WLF expression for the PTFE samples, but above that for the HDPE samples. The values of $v_f(T, 0, 0)$ calculated with Eq. (5.28) for PTFE and HDPE

under various temperatures were summarised in Table 5.3.

Table 5.3: The values of $v_f(T, 0, 0)$ calculated based on formulations and data from various sources.

$v_f(T, 0, 0)$ - PTFE			
Data Source	28 °C	40 °C	50 °C
Eq. (5.28) [221]	0.048	0.054	0.059
Eq. (5.29) [115, 222]	0.057	0.064	0.070
This work*	0.053 ± 0.005	0.059 ± 0.005	0.065 ± 0.006
$v_f(T, 0, 0)$ - HDPE			
Data Source	28 °C	35 °C	50 °C
Eq. (5.28) [221]	0.084	0.088	0.095
Eq. (5.29) [115, 222, 223]**	0.107	0.111	0.120
Eq. (5.29) [115, 224]***	0.095	0.100	0.108
This work*	0.095 ± 0.012	0.100 ± 0.012	0.108 ± 0.013

* Average value of $v_f(T, 0, 0)$ shown with mean absolute deviation.

** Data of α_r and α_g for PE.

*** Data of α_r and α_g for LPE.

Moreover, Kulkarni and Stern [115] modified Eq. (5.28) for a wider temperature range:

$$v_f(T, 0, 0) = \frac{0.025 + \int_{T_g}^{T} (\alpha_r - 0.975\alpha_g)\, \mathrm{d}T}{1 + \int_{T_g}^{T} \alpha_r\, \mathrm{d}T}, \tag{5.29}$$

where α_r and α_g are the volume expansion coefficients of the polymer at rubbery state ($T > T_g$) and glassy state ($T < T_g$), respectively. However, the data of α_r and α_g for polyethylene (PE) are more readily available than those for HDPE, which could not be found in literature. Thus, the data of α_r and α_g for PE were used to calculate $v_f(T, 0, 0)$ for HDPE, by using Eq. (5.29). According to Simha and Boyer [222]'s estimates of α_r and α_g, which were originated

from Quinn and Mandelkern [223]'s raw data, the values of $v_f(T,0,0)$ were calculated for HDPE under various temperatures, as summarised in Table 5.3. In addition, Simha and Boyer [222] also estimated α_r and α_g for PTFE, based on which the values of $v_f(T,0,0)$ were also calculated with Eq. (5.29). Furthermore, Stehling and Mandelkern [224] obtained α_r and α_g for linear polyethylene (LPE). Applying these data to the calculation of $v_f(T,0,0)$ for HDPE, the obtained values were also included in Table 5.3.

In this work, the average values of $v_f(T,0,0)$, obtained with formulations and data from various sources for PTFE and HDPE under each temperature, were adopted, and the mean absolute deviations were considered as uncertainties, as shown in Table 5.3. With the obtained estimates of $v_f(T,0,0)$ and $\tilde{c}$, the values of the compressibility, β_p, were calculated, which are shown in Table 5.2. Intuitively, two pieces of information could be extracted from the results for β_p. Firstly, the values of β_p for all runs were of the same order of magnitude, *i.e.* around 2×10^{-5} bar^{-1}. The uncertainty in the estimation resulted mainly from that of $v_f(T,0,0)$, and increased with the magnitude of β_p. Secondly, the values of β_p were found to increase with the increasing temperature. Although it is difficult to find compressibility data for PTFE and HDPE in literature, relevant compressibility data are readily available for polyethylene [115, 225–227] and crystalline PTFE and HDPE [228, 229]. The results reported in these works showed great consistency with those obtained here.

For instance, Ito [228] reported a value of 1.89×10^{-5} bar^{-1} for the isothermal compressibility of crystalline PTFE, and 1.56×10^{-5} bar^{-1} for crystalline HDPE. Lorenzen et al. [229] reported a decreasing bulk compressibility of crystalline PTFE as pressure increases, with different values obtained for different crystalline structures of PTFE in various phases, *e.g.* 1.57×10^{-5} bar^{-1} in form II, 5.1×10^{-6} bar^{-1} in form III (orthorhombic), and 3.8×10^{-6} bar^{-1} in form III (monoclinic). In addition, in Tsujita et al.'s work of the P-V-T relations measured for linear polyethylene, the compressibility of polyetheylene increased from about 3×10^{-5} bar^{-1} at 20 °C, to around 4×10^{-5} bar^{-1} at 50 °C [225]. Isăcescu et al. [226] published data on the compressibility of polyethylenes of differing molecular weights at temperatures between 23 °C and 300 °C, and pressures between 1 atm and 1800 atm. They investigated both the pressure and the temperature dependences of the isothermal compressibility coefficient, and noticed that it

decreased with increasing pressure but increased at higher temperatures. For example, at 23 °C, they reported a decrease of compressibility from 4.8×10^{-5} atm^{-1} at 100 atm, to 3.2×10^{-5} atm^{-1} at 1800 atm; at 100 atm, they reported an increase of compressibility from 4.8×10^{-5} atm^{-1} at 23 °C, to 25.6×10^{-5} atm^{-1} at 300 °C. They explained this temperature dependence of compressibility by pointing out that at higher temperature, there would be larger free space, apart from the molecular volume itself, for compression. Hatakeyama et al. [227] also observed a decreasing trend of the compressibility of polyethylene with the increasing pressures up to around 4900 bar. Nevertheless, the obtained values were slightly lower than those obtained by Isăcescu et al. [226]. The discrepancy might result from the highly crystalline samples Hatakeyama et al. [227] used, of which the compressibility could be much lower than that of highly amorphous ones. Despite the fact that the pressure dependence of β_p was not obtained in this work, since a constant compressibility was assumed when analysing the successive pressure step experiments, regardless of the varied pressure, the orders of magnitude of the obtained compressibility, as well as the temperature effects, were in agreement with the findings in these referenced works.

5.7.3 Estimating B_d

Given the values of $\tilde{b}$, ϕ_a and β_p, from Eq.(5.18), the values of B_d can be estimated. The amorphous volume fraction of the polymer, ϕ_a, measured by DSC (see Table 3.2 in Section 3.2.2), was assumed to be constant in the ranges of temperatures, pressures and penetrant concentrations under which the experiments were conducted. This same assumption was applied in Sato et al.'s study, and verified by their crystallinity observations of before and after the solubility experiments with X-ray diffraction [215]. As can be seen from Table 5.2, there were minor variations in the values of B_d determined from each run. For PTFE, the values of B_d were in a range of 0.31 - 0.35; for HDPE, they were in a range of 0.47 - 0.52.

Fujita [107] considered B_d as the parameter, which characterises the minimum hole size required for a penetrant molecule to displace into. Thus, B_d may be considered to be related to the penetrant size and shape. Similar to A_d, the obtained values of B_d were comparable to the ones

existing in literature. For instance, Kulkarni and Stern [115] estimated B_d to be 0.38, 0.39 and 0.39, for diffusion of CO_2 in polyethylene (PE) at 5 °C, 20 °C and 35 °C, respectively. In Sato et al. [215]'s work of CO_2 diffusion in polymers, the values of B_d obtained were 0.42 in PBS, and 0.51 in PBSA. Apart from CO_2, diffusion studies of a number of other penetrants in various polymers reported similar values of B_d. For the 13 organic liquids that Guo and de Kee [219] investigated for the diffusion in polyethylene at 30 °C, estimations of B_d in a range of 0.37 - 0.60 were obtained. In addition, Yeom and Huang [220] determined values of B_d to be 0.38, 0.40, 0.50 and 0.54 for the diffusion of benzene, toluene, n-hexane and n-heptane in polyethylene, respectively, in a temperature range of 25 - 45 °C. Thus the values of B_d determined in this work were highly consistent with those reported in other pertinent studies.

5.8 Estimation of W_i, $U_i/(W_iV')$ and $D_i'(X=0)$

The analysis presented in the previous sections, on the basis of *e.g.* Eq. (5.14) for F_i, was conducted under the assumption that the values of W_i were much greater than those of $\ln[D_i'(X=0)]$, so that the simplified model could be applied. After obtaining the estimates of B_d, $v_f(T,0,0)$ and β_p, as described in Section 5.7, values of W_i could be determined using Eq. (5.5); these were shown in Table 5.4.

Table 5.4: Estimated values of W_i, $U_i/(W_iV')$, and $D_i'(X=0)$, obtained from Eq. (5.5), Eq. (5.27), and Eq. (5.26), respectively, for the eight runs.

	Run-P-1, PTFE, 28 °C				*Run-P-2, PTFE, 40 °C*			
i	p_i, bar	W_i	$U_i/(W_iV')$	$D_i'(X=0)$	p_i, bar	W_i	$U_i/(W_iV')$	$D_i'(X=0)$
1	55	8.29±0.36	84.17±5.64	2.44±0.11	50	8.23±0.35	67.39±5.49	2.66±0.15
2	63	8.29±0.36	84.04±5.64	2.88±0.14	100	8.31±0.36	66.20±5.39	6.81±0.53
3	100	8.32±0.36	83.43±5.59	3.30±0.18	150	8.38±0.36	65.02±5.30	2.38±0.12
4	150	8.37±0.36	82.61±5.54	2.91±0.15	200	8.46±0.36	63.85±5.20	4.53±0.32
5					250	8.54±0.37	62.69±5.11	2.95±0.18

Continuation of Table 5.4

6				300	8.62±0.37	61.54±5.01	4.29±0.30
7				350	8.70±0.37	60.40±4.92	3.44±0.22
8				400	8.78±0.38	59.27±4.83	4.50±0.32
9				450	8.86±0.38	58.15±4.74	3.93±0.27
10				500	8.95±0.38	57.05±4.65	4.93±0.36
	Run-P-3, PTFE, 50 ˚C				*Run-H-4, HDPE, 28 ˚C*		
i	p_i, bar	W_i	$U_i/(W_iV')$	$D'_i(X=0)$	p_i, bar	W_i	$U_i/(W_iV')$	$D'_i(X=0)$
1	50	7.07±0.30	70.52±15.42	2.35±0.27	55	13.10±1.35	15.34±2.96	1.76±0.08
2	100	7.44±0.32	63.76±13.94	5.27±0.85	72	13.18±1.36	15.24±2.94	1.92±0.10
3	150	7.48±0.32	63.01±13.78	2.50±0.30	88	13.23±1.36	15.14±2.92	1.88±0.09
4	200	7.73±0.33	58.96±12.89	3.49±0.49	100	13.23±1.36	15.07±2.91	1.81±0.09
5	250	7.77±0.33	58.40±12.77	2.78±0.35	125	13.24±1.36	14.91±2.88	1.87±0.09
6	300	8.01±0.34	54.95±12.01	3.41±0.48	150	13.25±1.36	14.76±2.85	1.89±0.10
7	350	8.03±0.34	54.62±11.94	2.91±0.38	175	13.26±1.36	14.61±2.82	1.94±0.10
8					200	13.27±1.36	14.46±2.79	1.96±0.10
9					250	13.26±1.36	14.16±2.73	2.01±0.11
10					300	13.27±1.36	13.86±2.68	2.14±0.12
11					350	13.26±1.36	13.57±2.62	2.17±0.13
12					400	13.28±1.37	13.28±2.56	2.32±0.14
13					450	13.28±1.37	12.99±2.51	2.42±0.15
14					500	13.25±1.36	12.71±2.45	2.46±0.16
15					550	13.25±1.36	12.43±2.40	2.65±0.18
16					600	13.22±1.36	12.15±2.35	2.74±0.19

Continuation of Table 5.4

	Run-H-5, HDPE, 35 ˚C				*Run-H-6, HDPE, 35 ˚C*			
i	p_i, bar	W_i	$U_i/(W_iV')$	$D_i'(X=0)$	p_i, bar	W_i	$U_i/(W_iV')$	$D_i'(X=0)$
1	5	12.38±0.67	1.34±0.41	1.57±0.15	55	14.26±0.77	20.40±2.53	1.68±0.09
2	10	12.48±0.67	1.34±0.41	2.32±0.35	100	14.57±0.79	19.95±2.48	2.05±0.13
3	20	12.58±0.68	1.33±0.41	1.91±0.24	150	14.62±0.79	19.46±2.42	1.86±0.11
4	30	12.69±0.69	1.33±0.40	1.82±0.22	200	14.67±0.79	18.97±2.35	1.95±0.12
5	40	12.78±0.69	1.32±0.40	1.74±0.19	250	14.69±0.79	18.48±2.29	2.02±0.13
6	55	12.96±0.70	1.31±0.40	1.83±0.22	300	14.67±0.79	18.01±2.24	2.09±0.14
7	75	13.15±0.71	1.30±0.40	1.81±0.21	400	14.59±0.79	17.07±2.12	2.32±0.17
8	100	13.20±0.71	1.29±0.39	1.70±0.18				
9	125	13.24±0.72	1.27±0.39	1.72±0.19				
10	150	13.26±0.72	1.26±0.38	1.73±0.19				
11	175	13.26±0.72	1.24±0.38	1.75±0.20				
12	200	13.26±0.72	1.23±0.37	1.78±0.20				
13	250	13.24±0.72	1.20±0.36	1.85±0.22				
14	300	13.23±0.72	1.17±0.36	1.92±0.24				
15	350	13.21±0.71	1.14±0.35	2.00±0.26				
	Run-H-8, HDPE, 35 ˚C				*Run-H-9, HDPE, 50 ˚C*			
i	p_i, bar	W_i	$U_i/(W_iV')$	$D_i'(X=0)$	p_i, bar	W_i	$U_i/(W_iV')$	$D_i'(X=0)$
1	200	14.23±0.77	23.00±4.83	1.97±0.20	5	11.64±0.63	19.05±3.53	1.16±0.03
2	250	14.30±0.77	22.37±4.70	2.16±0.23	10	12.00±0.65	18.99±3.52	1.35±0.06
3	300	14.28±0.77	21.75±4.57	2.21±0.24	20	12.63±0.68	18.88±3.50	1.30±0.05
4	350	14.27±0.77	21.15±4.44	2.36±0.27	30	13.38±0.72	18.77±3.48	1.25±0.04

Continuation of Table 5.4

i	p_i, bar	W_i	$U_i/(W_iV')$	$D'_i(X=0)$
5	40	14.14±0.76	18.66±3.46	1.22±0.04
6	50	14.73±0.80	18.55±3.44	1.20±0.03
7	75	16.92±0.91	18.28±3.39	1.26±0.04
8	100	18.18±0.98	18.01±3.34	1.22±0.04
9	125	19.69±1.06	17.74±3.29	1.22±0.04
10	150	21.20±1.15	17.47±3.24	1.23±0.04
11	175	21.63±1.17	17.21±3.19	1.23±0.04
12	200	22.21±1.20	16.95±3.14	1.24±0.04
13	250	21.93±1.19	16.43±3.05	1.26±0.04

It can be seen in Table 5.4 that in general, the values of W_i ranged approximately from 7 to 22, whilst the values of $\ln[D'_i(X=0)]$ were less than 1. These values of W_i were greater than $W=5$, which was the worst case scenatio used to test the sensitivity of the simplified model to the assumption of $W_i \gg \ln[D'_i(X=0)]$.

It might be observed from the table that the estimates of W_i were approximately the same in a single run for all runs but Run-H-9, in which case W_i increased roughly from 12 to 22 with increasing pressure. This was likely due to the comparatively larger value of the compressibility, β_p, obtained for Run-H-9.

In addition to W_i, the lumped parameter, $U_i/(W_iV')$, can also be estimated. As described in Section 4.52, for the initial step, the value of $U_1/(W_1V')$ can be calculated from Eq. (4.52), given the obtained values of F_1, $D_{T,1}(T,p_1,0)$ and $D'_1(X=0)$. The subsequent values of $U_i/(W_iV')$ for the i^{th} step can be calculated using Eq. (5.27), with the obtained free-volume parameters, *i.e.* $v_f(T,0,0)$ and β_p. Finally, the values of $D'_i(X=0)$ can be estimated from Eq. (5.26). The obtained values are summarised in Table 5.4.

The uncertainties in the estimates of $U_i/(W_iV')$ were relatively significant, arising from the accumulation of uncertainties, when estimating $U_i/(W_iV')$ from $U_{i-1}/(W_{i-1}V')$. In this case, a small uncertainty in $D'_i(X=0)$ led to a considerably increased uncertainty in the estimated $U_i/(W_iV')$. Compared with the other runs, Run-H-5, which was conducted at 35 °C, starting from a low pressure of 5 bar, seemed to have lower estimates of $U_i/(W_iV')$. This was due to a comparatively low starting value during the first step for $U_1/(W_1V')$, which was estimated with Eq. (4.52), from the obtained values for $F_m(t_1=\infty)$, $D_{T,1}(T,p_1,0)$, and $D'_1(X=0)$.

By comparing Run-H-5 with the other runs that were also conducted under 35 °C but with higher initial pressures, *i.e.* Run-H-4, Run-H-6, and Run-H-8, it can be seen from Table 4.4 that the value of $F_m(t_1=\infty)$, which appears in the numerator of Eq. (4.52), for Run-H-5 was on average an order of magnitude less than that for the other runs; and the value of $D_{T,1}(T,p_1,0)$, which appears in the denominator of Eq. (4.52), for Run-H-5 was on average twice as that for the other runs; whilst the values of $D'_1(X=0)$ were comparable among these runs. As a result, the estimates of $U_i/(W_iV')$ for Run-H-5 were about 0.06 - 0.08 of those for Run-H-4,6,8.

By comparing Run-H-5 with Run-H-9, which was conducted under a higher temperature of 50 °C starting from the same pressure of 5 bar as that for Run-H-5, it can be seen from Table 4.4 that the value of $F_m(t_1=\infty)$ for Run-H-5 was about a quarter of that for Run-H-9, possibly owing to the lower temperature applied to Run-H-5; the value of $D'_1(X=0)$, which is in the denominator of Eq. (4.52), for Run-H-5 was about 1.3 times as that for Run-H-9, whilst the values of $D_{T,1}(T,p_1,0)$ were similar in the two cases. Consequently, the estimates of $U_i/(W_iV')$ for Run-H-5 were approximately 0.07 of those for Run-H-9.

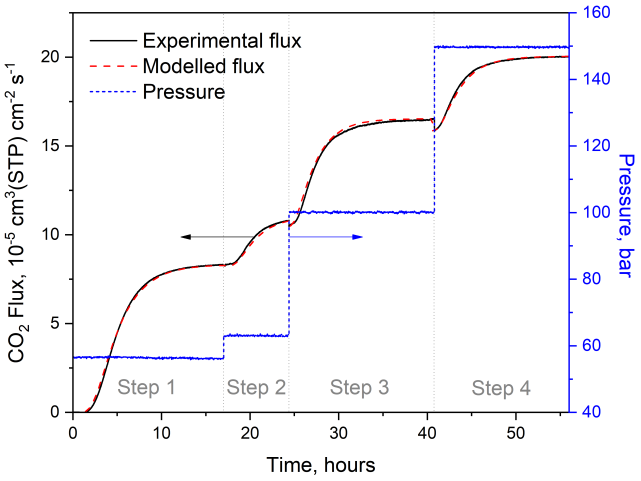
Although the value of $F_m(t_1=\infty)$ for Run-H-5 was smaller than that for the other runs, when comparing the values of $F_m(t_i=\infty)$ under the same pressure and temperature, *e.g.* $F_m(t_{i=6}=\infty)$ for Run-H-5 and $F_m(t_1=\infty)$ for Run-H-6 at 55 bar, $F_m(t_{i=8}=\infty)$ for Run-H-5 and $F_m(t_{i=2}=\infty)$ for Run-H-6 at 100 bar, and $F_m(t_{i=10}=\infty)$ for Run-H-5 and $F_m(t_3=\infty)$ for Run-H-6 at 150 bar, as can be seen from Table 5.1, it was found that these steady-state fluxes were close under the same pressure for the two runs, regardless of the initial pressure or pressure steps. This raised a question on how the successive measurements with multiple pressure steps,

may differ from the single-step measurements, regarding the estimation of transport properties and free-volume parameters in the model.

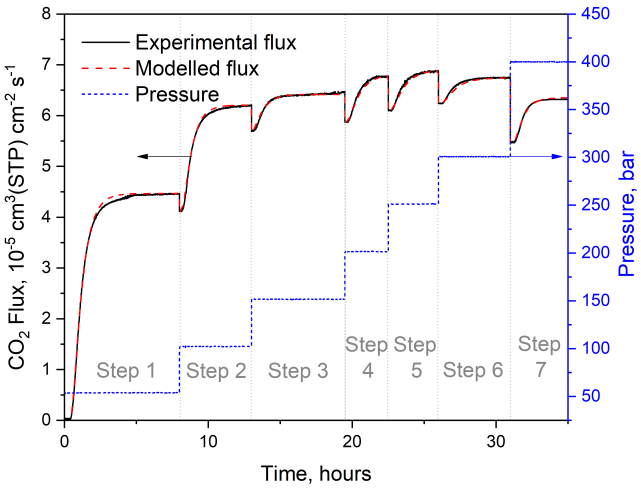
In fact, it was speculated that less consistent results might be obtained from successive measurements in a low pressure range, since the effects of concentration and pressure on diffusion are more significant under higher pressures. For Run-H-5, the estimation results were built on those obtained under low pressures, in which case there was likely to be higher estimation uncertainty, by applying the diffusion model developed with free volume theory. Supplementary experiments may be conducted in future projects. For example, Run-H-5 could be repeated under the same conditions, with the same initial pressure and pressure steps, to verify the flux obtained at each step. Furthermore, a series of single-step measurements may be conducted under the corresponding pressures to those in the successive measurements, to compare the estimations obtained by applying the methodologies for the single-step measurements and the successive measurements. These experiments could help explain the reason for the lower estimates of $U_i/(W_i V')$ for Run-H-5, and also verify the validity of the experimental and modelling method for successive measurements.

5.9 Comparison of Measured *vs.* Modelled Fluxes

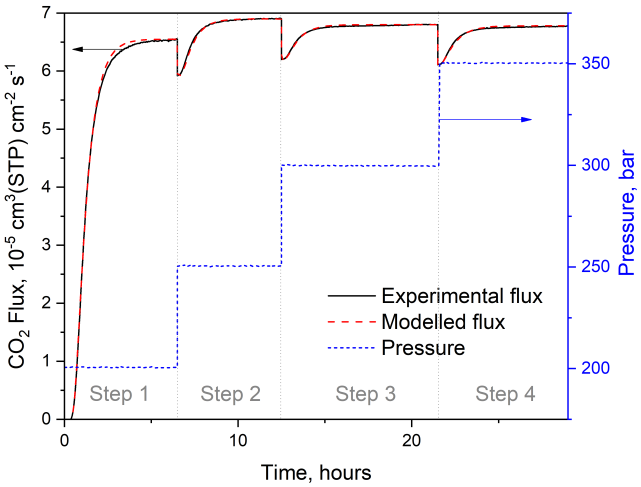
The flux curves can be modelled using Eq. (5.10) to Eq. (5.14), with the parameters determined from the experimental measurements, using the methods described above. Figure 5.3 presents the modelled flux curves, compared with the experimental ones, for three three examples: Run-P-1, Run-H-6 and Run-H-8. In Figure 5.3, the dimensionless time used in the model, τ_i, was converted to real time with Eq. (5.7), and was presented consecutively from the previous step. It can be seen that there was an excellent agreement between the experimental flux curves and the modelled ones. This showed that the parameters determined using the methods described above did indeed give excellent fits to the experimental measurements, during both the transient and the steady-state periods.



(a) Run-P-1



(b) Run-H-6



(c) Run-H-8

Figure 5.3: Comparison of the experimental flux curves and the modelled flux curves, with three runs as examples.

5.10 Concluding Remarks

In this chapter, the results of continuous permeation experiments, which involved multiple successive pressure steps, were presented and analysed. The effects of pressure on the transport properties were studied, with key conclusions as follows: (1) An instantaneous drop of the measured permeation flux was observed, when the system pressure was increased. This phenomenon was most likely caused by a compaction of the polymer matrix at the higher pressure. Consequently, diffusion was inhibited, as a result of the decrease in diffusivity caused by a decrease in free volume subject to the pressure increase. (2) Building on the nondimensionalised diffusion model developed for transient permeation in Chapter 4, a model was developed to analyse permeation experiments with successive pressure steps. Excellent agreement between measured and modelled flux curves were obtained, with the values of the key dimensionless parameters determined for each pressure step, *e.g.* $D_{T,i}(T, p_i, 0)$, $D_i'(X = 0)$, and $U_i/(W_i V')$, by applying the methods developed in this chapter. (3) By quantifying the flux drop and the decrease of the thermodynamic diffusivity, when the pressure was increased, the values of the free-volume parameters, *i.e.* A_d, β_p, and B_d, were estimated. The obtained values for each run were in agreement with values reported in the literature for similar systems. It should be pointed out that correlations for $v_f(T, 0, 0)$ were used to determine the values of β_p and subsequently those of B_d. Ideally, it would be desirable to experimentally measure $v_f(T, 0, 0)$ for the polymers. Nevertheless, the work presented in this chapter primarily demonstrated how to estimate all the paramters in the free volume model, once the free volume of the specific polymer under test was known. Moreover, considerations on the validity of the estimation results obtained from successive permeation experiments in a low pressure range by applying the proposed method were discussed, and recommendations on future investigation to address the inconsistency issue were provided. On the basis of the results obtained in this chapter, the work could be further developed for solubility analysis, which will be focused in the next chapter.

Chapter 6

Solubility Analysis

6.1 Introduction

This chapter further develops the analysis by modelling the concentration of CO_2 at the top surface of the polymer, $C(X = 0)$, assumed to be in equilibrium with the PTFE and HDPE samples, as determined using the methods described in Chapters 4 and 5. As described in the previous chapters, nine experimental runs, amongst which eight were continuous runs with successive pressure steps, were carried out under various conditions. The pressure dependence of the free volume were characterised, by applying a simplified, nondimensionalised free volume model with Fick's laws of diffusion. However, the individual parameter, γ, which characterises the dependence of the diffusivity on the penetrant volume fraction, could not be determined independently, since it was contained in the lumped group, $U_i/(W_i V_i')$. In this chapter, an equation of state was introduced to investigate V_i', which was defined by Eq. (4.9), *i.e.* $V_i' = V_{T,p_i}/V_{273\mathrm{K},1\mathrm{atm}}$, as a ratio of the penetrant specific volumes at the two specified conditions.

The relationship between equilibrium solubility and pressure will be described using Sanchez-Lacombe (SL) equation of state (EOS) [103, 104, 157], by optimising the CO_2-polymer interaction parameters in the model. As mentioned in Chapter 2, the SL EOS, which treats the polymer chains as a set of interacting beads in a lattice, has been extensively applied to model phase equilibrium in polymer solutions and predict thermodynamic properties for penetrant-

polymer systems [105, 154–156, 230–232]. The binary interaction parameters, which have been found to be temperature-dependent in some studies [159, 163, 185, 231–233], are typically optimised to fit the experimental equilibrium solubility data with the SL EOS.

In this chapter, the theoretical framework presented in Chapter 5 was further developed to enable the estimation of the experimental CO_2 solubility, which was considered to be equivalent to $C(X = 0)$, as well as the modelled CO_2 solubility obtained by applying the SL EOS. Furthermore, these experimental and modelled results will be presented and compared. Finally, an analysis on the key results is conducted, with recommendations to make direct measurements of solubility, to validate the indirect measurements made in this work.

6.2 Theoretical

6.2.1 Equilibrium Solubility

Estimates of $D_{T,i}(T, p_i, 0)$ and $D'_i(X = 0)$ were obtained in Chapter 5 by applying Eq. (5.16) and Eq. (5.26), respectively. The volumetric concentration of the penetrant at the top surface of the disc for the i^{th} step, $C_i(X = 0)$, which was assumed to be the equilibrium solubility of CO_2 in the mixture, can be obtained by combining Eq. (4.8) and Eq. (5.6):

$$C_i(X = 0) = \frac{LF_m(t_i = \infty) \ln [D'_i(X = 0)]}{D_{T,i}(T, p_i, 0)[D'_i(X = 0) - 1]}. \tag{6.1}$$

6.2.2 Sanchez-Lacombe (SL) EOS

By minimising the Gibbs free energy of a chain fluid on a lattice, Sanchez and Lacombe [103] derived the SL EOS:

$$\tilde{\rho}^2 + \tilde{p} + \tilde{T} \left[\ln(1 - \tilde{\rho}) + \left(1 - \frac{1}{r}\right) \tilde{\rho} \right] = 0, \tag{6.2}$$

where $\tilde{p}$, $\tilde{T}$ and $\tilde{\rho}$ are the reduced pressure, temperature and density, respectively. They are defined by:

$$\tilde{p} = \frac{p}{p^*}, \tilde{T} = \frac{T}{T^*}, \tilde{\rho} = \frac{\rho}{\rho^*}, r = \frac{M_W p^*}{RT^* \rho^*}, \tag{6.3}$$

where p^*, T^* and ρ^* are the characteristic parameters of the pure penetrant and polymer; r is the size parameter representing the number of lattice sites occupied by a polymer molecule; and M_W is the molecular weight. The characteristic parameters are related to the Boltzmann's constant, k_B, and the lattice variables, ϵ^*, v^* and m by:

$$p^* = \frac{\epsilon^*}{v^*}, T^* = \frac{\epsilon^*}{k_B}, \rho^* = \frac{M_W}{m v^*}. \tag{6.4}$$

For mixtures, the SL EOS is identical to the pure-component equation, *i.e.* Eq. (6.2). However, mixing rules are applied to the parameters:

$$\epsilon^*_{\text{mix}} = \frac{\sum_i \sum_j \phi_i \phi_j \epsilon^*_{ij} v^*_{ij}}{v^*_{\text{mix}}}, \tag{6.5}$$

$$v^*_{\text{mix}} = \sum_i \sum_j \phi_i \phi_j v^*_{ij}, \tag{6.6}$$

$$\frac{1}{m_{\text{mix}}} = \sum_i \frac{\phi_i}{m_i}, \tag{6.7}$$

$$\phi_i = \frac{\frac{\omega_i}{\rho^*_i v^*_i}}{\sum_j \left(\frac{\omega_j}{\rho^*_j v^*_j} \right)}, \tag{6.8}$$

where ϕ_i and ω_i are the volume fraction and the mass fraction of component i, respectively. The cross parameters, ϵ^*_{ij} and v^*_{ij}, are:

$$\epsilon^*_{ij} = \sqrt{\epsilon^*_{ii} \epsilon^*_{jj}} (1 - k_{ij}), \tag{6.9}$$

$$v^*_{ij} = \frac{1}{2} (v^*_{ii} + v^*_{jj}) (1 - \eta_{ij}). \tag{6.10}$$

In the above expressions, k_{ij} and η_{ij} are binary interaction parameters. Through pure-component and binary interaction parameters of the SL EOS, thermodynamic properties of multicomponent mixtures can be predicted.

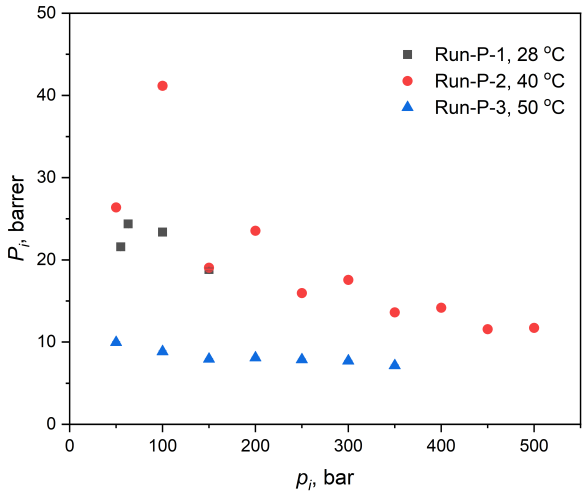
6.3 Results and Discussion

6.3.1 Solubility Measurements

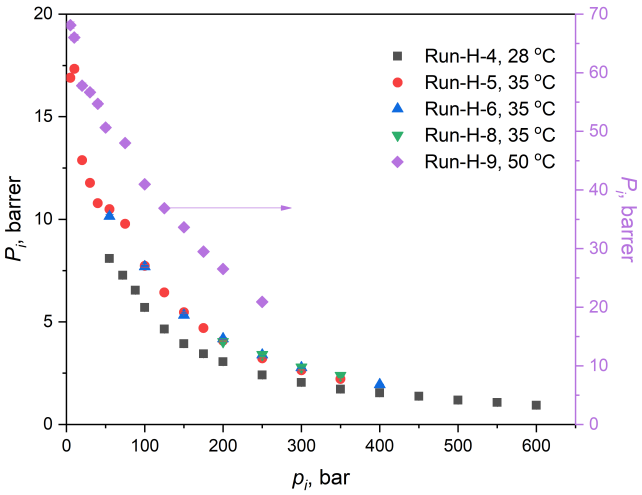
Figure 6.1a - 6.1d are plots of permeability, diffusivity, and solubility obtained from the successive pressure step permeation experiments for CO_2-PTFE and CO_2-HDPE systems. The permeability, P_i, was calculated by Eq. (2.1) from the measured flux. The thermodynamic diffusivity at the top surface of the polymer disc, $D_{T,i}(X = 0)$, was obtained by taking the product of $D_{T,i}(T, p_i, 0)$ and $D_i'(X = 0)$. The concentration of the penetrant at the top surface of the disc, $C_i(X = 0)$, assumed to be the equilibrium solubility of the penetrant in the mixture, was obtained by Eq. (6.1). To test the agreement with Henry's law, *i.e.* $C = Sp$, where the solubility coefficient S is considered as the Henry's law constant, linear fits of the data points for $C_i(X = 0)$ are also shown in the figure.

Pressure Dependences of Transport Properties

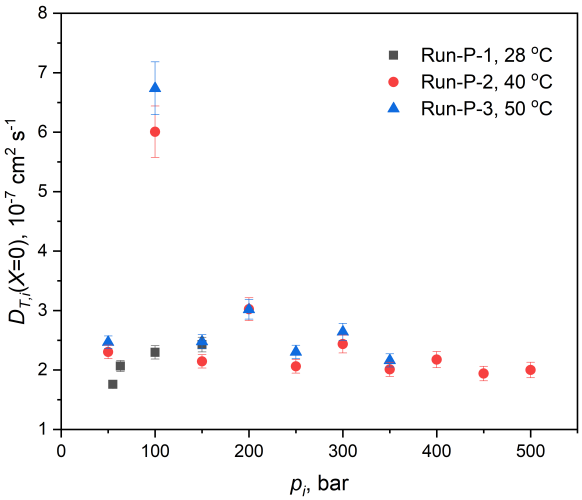
Figure 6.1a and 6.1b show the permeability obtained from the experiments with PTFE and HDPE, respectively. The uncertainty for P_i was relatively low, the error bars were not visible on the plots. There was a clear trend of decreasing permeability with increasing pressure for CO_2-HDPE system, whereas the trend for CO_2-PTFE system was less obvious. A decreasing permeability with increasing pressure, in a wide range of pressures at up to hundreds of bars for CO_2-polymer systems, has also been reported in other works [202, 234]. Since the permeability is a property determined by a combined effect of the diffusivity and the solubility, this trend arises from the decreasing diffusivity, as pressure increases. It can be seen from Figure 6.1d that $D_{T,i}(X = 0)$ decreases with increasing p_i, as a result of the decreasing free volume for diffusion, due to the compaction effect by the increasing pressure.



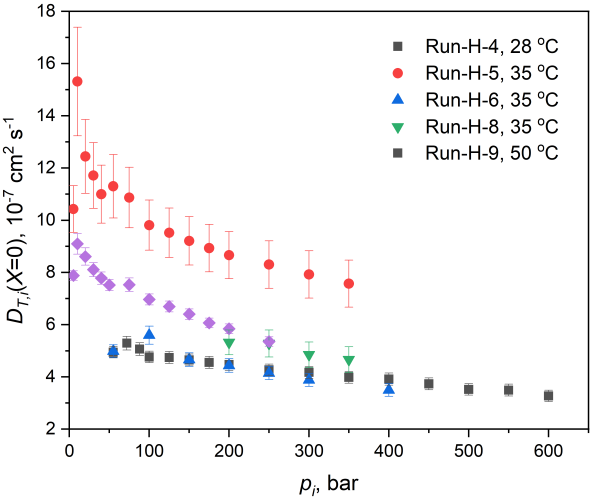
(a) PTFE, P_i *vs.* p_i



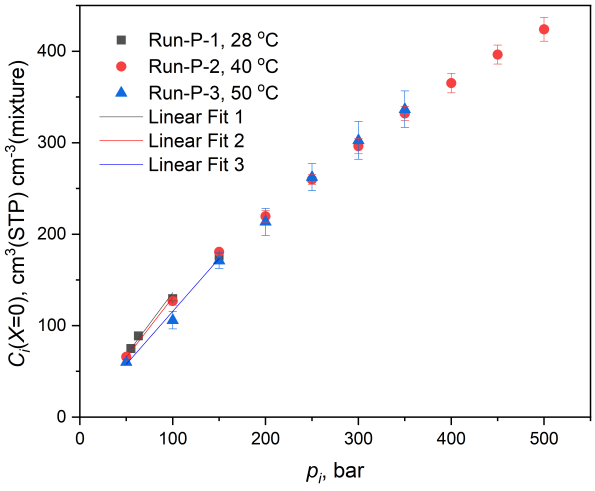
(b) HDPE, P_i *vs.* p_i



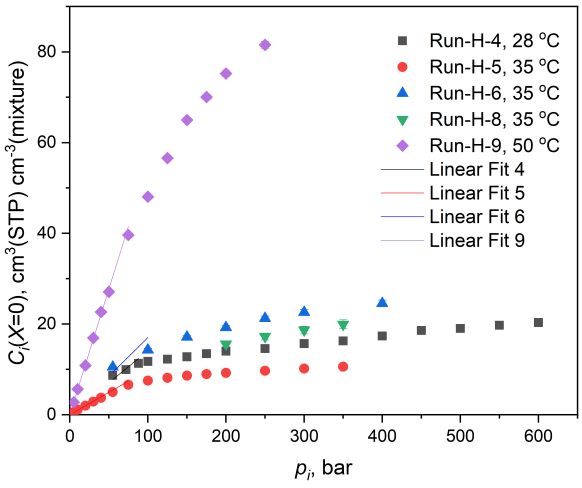
(c) PTFE, $D_{T,i}(X=0)$ *vs.* p_i



(d) HDPE, $D_{T,i}(X=0)$ *vs.* p_i



(e) PTFE, $C_i(X=0)$ *vs.* p_i



(f) HDPE, $C_i(X=0)$ *vs.* p_i

Figure 6.1: Pressure dependences of P_i, $D_{T,i}(X=0)$ and $C_i(X=0)$ for the eight runs, with uncertainties shown by the error bars on the plots. Linear fits for the data points of $C_i(X=0)$ are shown, with slopes presented in Table 6.1.

Intriguingly, by taking a close look at the data points shown in Figure 6.1d, a leap was noticed in the values of $D_{T,i}(X = 0)$ for $i = 2$ from $D_{T,1}(X = 0)$, which was obtained from the transient measurement during the first step. This leap at $D_{T,2}(X = 0)$ was then followed by a decrease in $D_{T,i}(X = 0)$ for the rest of the steps. This phenomenon was observed in all runs with HDPE, regardless of pressure or temperature. By examining the derivation of $D_{T,i}(X = 0)$, it was found that the determining term for its value is the ratio of $F_m(t_i = \infty)$ to $F_m(t_i = 0)$. It can be seen in Table 5.1 that for almost all runs with HDPE, this ratio of $F_m(t_i = \infty)$ to $F_m(t_i = 0)$ for $i \geqslant 2$ was in its maximum after the second step (*i.e.* $i = 2$), subsequently decreasing after further steps.

It can also be seen from Figure 6.1b that P_i had a positive dependence on temperature for the runs with HDPE. It may be hypothesised that this was due to the increasing solubility with increasing temperature. In particular, compared with the other runs, Run-H-9, which was conducted at 50 °C, seemed to have much higher permeability, referring to the secondary y-axis of Figure 6.1b. This high permeability was consistent with the high solubility obtained for Run-H-9, as can be seen in Figure 6.1f.

Figure 6.1f illustrates the pressure dependence of $C_i(X = 0)$, obtained by applying Eq. (6.1), for the HDPE runs. To test the agreement with Henry's law, linear fits of the data points for the runs were also shown in the figure. It can be seen that the data points did not strictly follow Henry's law. There seemed to be a "transition" point between 75 bar and 100 bar. For Run-H-4, 5, 6, and 9, the linear fits were obtained with the data points below 100 bar, but not with those above 100 bar, owing to the significant deviations from Henry's law at higher pressures. In particular, for Run-H-8, which was conducted at pressures higher than 200 bar, the four data points shown in Figure 6.1b appeared not to follow the pattern for Henry's law. As a result, a linear fit was not obtained for Run-H-8. The "transition" point appeared to be in the vicinity of the critical pressure of the penetrant CO_2, *i.e.* 74 bar. Above the "transition" point, CO_2 is in a supercritical state, behaving as a supercritical fluid, with a much higher density than that in the gaseous phase. Solubility curves with similar characteristics were also reported in Nalawade et al. [35]'s work, where CO_2 solubilities in polyester resins were measured at temperatures ranging from 60 to 147 °C and pressures up to 300 bar. At the temperature of

around 60 °C, which is higher than 35 °C applied in this work, they reported that the solubility isotherm was not linear at high pressures. On the other hand, this nonliear behaviour was absent at higher temperatures. They postulated that this deviation in the high pressure range while at 60 °C, might result from the reduced free volume available in the polymer, when the polymer was compressed. Nalawade et al. [35] observed the same trend at 60 °C but not at higher temperatures, postulating that the deviation from Henry's law might be the result of reduced polymer free volume.

For the PTFE runs shown in Figures 6.1a, 6.1c and 6.1e, there seemed to be a few anormalies that obscured the effects of pressure and temperature on permeability, diffusivity and solubility. Specifically, regarding the permeability, P_i seemed to decrease with p_i for Run-P-1 and Run-P-2, but remain almost constant with p_i for Run-P-3. As for $D_{T,i}(X = 0)$, there was an increasing trend of $D_{T,i}(X = 0)$ with increasing p_i for the three runs at pressures below 100 bar. This may result from the increasing volumetric fraction of the penetrant in the mixture, giving rise to more free volume for diffusion, as the pressure increases up to 100 bar. In that case, this positive effect on $D_{T,i}(X = 0)$ appeared to outweigh the compaction effect due to higher pressure, reducing the free volume and hindering the diffusion process. Similarly to the cases for HDPE, leaps in the values of $D_{T,2}(X = 0)$ for $i = 2$ were also observed, as a result of the large value of the ratio of $F_m(t_i = \infty)$ to $F_m(t_i = 0)$ for $i = 2$. At higher pressures, there was a general trend of decreasing $D_{T,i}(X = 0)$ for all the runs. Nevertheless, the temperature dependence of $D_{T,i}(X = 0)$, which was expected to be positive, was not evident. In order to validate the results obtained for the PTFE runs, it is worth repeating these experiments to check whether similar results could be obtained, and carrying out a few more experiments under various conditions for more convincing elucidation on the effects of pressure and temperature on the transport properties of the CO_2-PTFE system.

Considering the obtained solubilities for all runs, except for Run-P-2 and Run-P-3, the uncertainties of $C_i(X = 0)$ seemed to be well below 5%, resulting in almost "invisible" error bars in Figures 6.1e and 6.1f. On the other hand, for Run-P-2 and Run-P-3, there seemed to be higher estimation uncertainties, which increased with increasing p_i or $C_i(X = 0)$. Two reasons may account for it. Firstly, when applying Eq. (6.1) to calculate $C_i(X = 0)$, the major source

of the uncertainty was $D_i'(X = 0)$, which was obtained based on $D'(X = 0)$ in the first step, estimated using the graphical method described in Chapter 4. As shown in Table 4.4, the estimation uncertainties of $D'(X = 0)$ were comparatively larger for Run-P-2 and Run-P-3, than those for the other runs. Secondly, with the accumulative uncertainty of $D_i'(X = 0)$ as step i increased, the estimation uncertainty for $C_i(X = 0)$ increased with increasing pressure. Nevertheless, taking all estimates of $C_i(X = 0)$ for the runs into account, the highest uncertainty was effectively below 10%, which seemed to be acceptable for estimation accuracy, given that these solubilities were indirectly obtained from permeation experiments. Analysis on the solublity and its agreement with Henry's law will be conducted in the following section.

Comparison of Solubility with Literature Data

Comparing the solubility, $C_i(X = 0)$, obtained for the CO_2-PTFE and the CO_2-HDPE systems, it can be seen from Figures 6.1e and 6.1f that the former was about 10 times larger than the latter under similar temperatures and pressures. Overall, these values were comparable to those existing in literature for the sorption of CO_2 in various polymers including PTFE and HDPE under various conditions [36, 163, 235]. For instance, Sato et al. [163] measured the solubilities of CO_2 in molten HDPE at temperatures 160, 180, and 200 °C and pressures up to 170 bar. They reported a linear increase of solubilities with increasing pressure, *e.g.* at 160 °C, from approximately 39 cm^3(STP) cm^{-3}(mixture) at 69 bar to 126 cm^3(STP) cm^{-3}(mixture) at 175 bar; at 180 °C, from about 34 cm^3(STP) cm^{-3}(mixture) at 70 bar to 115 cm^3(STP) cm^{-3}(mixture) at 180 bar; at 200 °C, from about 30 cm^3(STP) cm^{-3}(mixture) at 66 bar to 99 cm^3(STP) cm^{-3}(mixture) at 170 bar. From these data, Sato et al. [163] also reported that the solubilities of CO_2 in HDPE decreased with increasing temperature. In comparison, the measurements in this work did not show a monotonous trend of solubility with temperature. As can be seen from Figure 6.1f, the values of $C_i(X = 0)$ for Run-H-4, which was conducted at 28 °C, were higher than those for Run-H-5 conducted at 35 °C, but were lower than those for Run-H-6 and Run-H-8, which were also conducted at 35 °C. In addition, the solubilities obtained for Run-H-9 at 50 °C appeared to be much greater than those for the other runs.

The obtained temperature effect on the results fails to meet the expectation that the CO_2 solubility generally decreases with increasing temperature. This could discredit the reliability of the experimental results obtained from the different runs. There might be three possible reasons. Firstly, the exceptionally high solubility obtained in the particular run of Run-H-9 could be a random case. Despite the fact that the random errors have been accounted for in the uncertainty calculation, and that the systematic errors should impact on all runs, it is not entirely impossible that there could be operating mistakes, as far as this particular run is concerned. The solution to this likely cause would be to repeat this run for multiple times in the future, when enough time is given and adequate materials are provided. Secondly, the negative temperature dependence of CO_2 solubility in HDPE in most studies [163, 215, 236–238] was reported for much higher temperatures than the ones applied in this work. In fact, in Lei et al. [239]'s solubility study of CO_2-PP system under a variety of temperatures and pressures, they pointed out that at a constant pressure *e.g.* 50 bar, there was an upward trend of CO_2 solubility in the rubbery state of PP as temperatures approached its melting temperature. It would be beneficial to extend the work presented here to elevated temperatures of hundreds of °C, with safety aspects taken into account, to gain a thorough understanding of the temperature effect under a wider range of conditions. Thirdly, the reliability of this indirect approach of obtaining solubility data from permeation measurements might be questionable. Although one good way of verifying the results is through comparison with literature data, it would be more straightforward to conduct seperate sorption experiments, from which the solubility of CO_2 in the polymer can be directly measured.

Similar sorption findings as those in Sato et al. [163]'s work were obtained for the sorption of CO_2 in PTFE by Bonavoglia et al. [36], who measured the equilibrium sorption of supercritical CO_2 in PTFE at different temperatures from 40 to 80 °C and pressures up to 200 bar. The solubilities they obtained were in an approximate range of 5 cm^3(STP) cm^{-3}(mixture) to 30 cm^3(STP) cm^{-3}(mixture), which were about an order of magnitude smaller than those obtained in this work, as shown in Figure 6.1e. Additionally, in a permeation study of CO_2 through PTFE, Pasternak et al. [235] evaluated the solublity coefficient, S, to be 0.92 bar^{-1} at 25 °C, which is about 35% below the values obtained for the PTFE runs in this work, as shown in Table

6.1, which will be discussed later. Nevertheless, the facts that Pasternak et al. [235] evaluated S from the relationship of $S = P/D$ and that they conducted permeation experiments under near-ambient conditions, may have, to some extent, contributed to the different estimations of S in the two studies. To further investigate the sorption of CO_2 in polymer systems and compare the results with those presented here, solubility data for other CO_2-polymer systems can also be found in literature.

Mukaddam et al. [240] determined the sorption isotherms for CO_2 in Nafion, which is an important class of perfluorinated polymers based on sulphonated ionomers, at 35 °C by barometric techniques. They obtained a linear increase of the solubility from 0 to about 15 cm^3(STP) cm^{-3}(polymer), as the pressure increased to 20 atm, with a constant solubility coefficient of 0.75 bar^{-1}. Merkel et al. [28] determined the solubility of CO_2 in PDMS at 35 °C and at pressures up to 20 atm. They obtained a constant solubility coefficient, S, of 1.29 atm^{-1}, in the investigated pressure range. For the sorption of CO_2 in glassy polymers at 35 °C and at pressures up to 30 atm, the solubilities ranged from 0 to about 55 cm^3(STP) cm^{-3}(polymer) in poly(phenylene oxide) (PPO) within the investigated pressure range [241–243]; from 0 to about 45 cm^3(STP) cm^{-3}(polymer) in PMMA [243]; from 0 to about 30 cm^3(STP) cm^{-3}(polymer) in PC [243]; and from 0 to about 10 cm^3(STP) cm^{-3}(polymer) in cyclic olefin copolymer (COC) [243]. It may not make much sense to directly compare these solubility data with those obtained for the CO_2-PTFE system in this work, given the much higher pressures applied for the latter. However, as shown in Figure 6.1e, extrapolations of the solubility curves to pressures below 50 bar would lead to values comparable to those found in literature. If the sorption results obtained in this work for high pressures could be repeated, and verified by a direct approach of sorption measurements, the data would fill the gap in literature on CO_2 solubility in polymers in the high-perssure range.

Agreement with Henry's Law

The solubility coefficient, S, which depicts the relationship between the equilibrium solubility, $C_i(X = 0)$, and pressure, p_i, can be obtained from the gradient of the $C_i(X = 0)$ *vs.* p_i curves.

Table 6.1: The solubility coefficient, S, obtained from the linear fits of $C_i(X = 0)$ *vs.* p_i in Figure 6.1 for the runs.

	Run-P-1	Run-P-2	Run-P-3	
T	28 °C	40 °C	50 °C	
p_i	55 - 100 bar	50 - 100 bar	50 - 150 bar	
S, bar^{-1}	1.36 ± 0.03	1.31 ± 0.02	1.16 ± 0.04	
	Run-H-4	Run-H-5	Run-H-6	Run-H-9
T	28 °C	35 °C	35 °C	50 °C
p_i	55 - 88 bar	100 - 600 bar	5 - 75 bar	5 - 75 bar
S, bar^{-1}	0.14 ± 0.01	0.10 ± 0.01	0.17 ± 0.02	0.55 ± 0.01

As shown in Figure 6.1e and Figure 6.1f for the PTFE and HDPE runs, as the pressure increased above a certain point, the curves seemed to gradually deviate from the lines. In order to test the agreement between the data points and Henry's law, the linear fits for all runs were forced to have zero intercept, with the slopes shown in Table 6.1. Specifically, the data points for the runs were separated into two segments. A line, which fits the data points and intersects at the origin, was obtained below 100 bar for each run (below 150 bar for Run-P-3 particularly).These linear fits appeared to agree with Henry's law. The slopes of these lines, corresponding to the values of S, were summarised in Table 6.1. In particular, the solubility data for Run-H-8, which was conducted at pressures above 200 bar, seem not to obey the Henry's law. Thus, the linear fit for Run-H-8 was not shown in the figure, and S was not obtained for this run.

It has been reported in some studies [185, 238, 239, 244, 245] for molten polymers that at CO_2 pressures below 100 bar, the solubility of CO_2 increased almost linearly with CO_2 pressure; whilst at pressures above 100 bar, the sorption isotherm curves appeared to bend towards the p_i axis. Lei et al. [239] attributed this change in curvature of the sorption curve at pressures higher than 100 bar to the swelling effect, which they considered to be significant at high pressures. With the swelling correction taken into account, they obtained a corrected solubility isotherm curve, which was above the one without correction and exhibited an upward bend at

high pressures.

Regardless of the changing curvature of the sorption isotherm, Sato et al. [215] calculated Henry's constant, denoted by K_P, as the limit of the ratio of gas pressure to solubility, when solubility approaches 0. It is noteworthy that K_P is equivalent to the reciprocal of the solubility coefficient, S, defined in this work. Similar approach was taken to obtain S from the gradients of the linear fits for the sorption curves of the HDPE runs at pressures below 100 bar, as can be seen in Figure 6.1f. These segments of the curves were fitted into lines of zero intercepts. The values of S, presented in Table 6.1, were estimated from the slopes of these linear fits, with a confidence level of 95%.

The obtained values of S shown in Table 6.1 for the PTFE and HDPE runs can be compared with those of $1/K_P$ for CO_2-polymer systems in literature [163, 215, 235, 246]. By analysing these data from literature, two pieces of primary information can be extracted. Firstly, there exists a relationship between $1/K_P$ and $1/T$, demonstrating that $1/K_P$ increases with increasing $1/T$. Second, the values of $1/K_P$ seem to be dependent on polymer type, which may have distinct characteristics regarding glassy and melting temperatures, crystallinity, and chemical bonds, *etc.* For instance, Sato et al. [215] obtained comparable Henry's constants for the CO_2-PBS and CO_2-PBSA systems they studied. The values of $1/K_P$ they obtained for the two systems ranged from 0.24 bar^{-1} to 0.64 bar^{-1}, as the temperature decreased from 180 to 120 °C. Moreover, Sato et al. [163] reported $1/K_P$, whose values were between 0.22 and 0.33 bar^{-1}, for CO_2 in PP and HDPE at temperatures of 200, 180, and 160 °C and pressures up to 170 bar. In addition, Liu and Prausnitz [246] studied the solubilities of CO_2 in LDPE in a temperature range of 125 - 225 °C, and $1/K_P$ obtained from their measurements were in a range of 0.30 - 0.43 bar^{-1}. Larger values of the constant were obtained in Pasternak et al. [235]'s work of the permeation of CO_2 through PTFE, where the solublity coefficient, S, was evaluated to be 0.92 bar^{-1} at 25 °C.

As can be seen from Table 6.1, the values of S obtained for the PTFE runs in this work showed consistent temperature dependence compared to those found in the literature. That is to say, the values of S decreased with increasing temperature. However, these values were larger than

most data found in literauture, including the one obtained for CO_2-PTFE system [235], as mentioned above. As for the HDPE runs, the decreasing trend of S with increasing T was not obvious, owing to the larger value obtained for Run-H-9, which was carried out at the highest temperature among the runs. Nevertheless, the values of S for the HDPE runs seemed to have similar magnitudes as those found in literature. This comparison could be meaningful, since in these instances the values for S or $1/K_P$ were derived using the data points at comparatively low pressures, where the sorption behaviours appeared to obey Henry's law.

The experimental solubility data will now be correlated using the SL EOS. The deviation between the experimental and the modelled solubility was minimised by optimising the binary interaction parameters in the SL EOS model. From the modelling results, not only the binary parameters, k_{ij} and η_{ij}, but also the specific volume of the penetrant at the experimental conditions, $V_{T,p}$, and the ratio, V', defined by Eq. (4.9), can be estimated. On the basis of these quantities, the concentration coefficient, γ, in the free volume model, *i.e.* Eq. (4.6) and Eq. (4.7), could also be estimated. Discussion on the topic is presented in the following section.

6.3.2 Modelling Solubility Using the SL EOS

To model the solubility using the SL EOS, the pure-component characteristic parameters are required, which are tabulated in Table 6.2. These parameters were evaluated from the P-V-T experimental data of each component. Given these parameters, the solubilities of CO_2 in PTFE and HDPE may be calculated using the SL EOS. In this case the ASPEN Polymer Plus software was used; details of the ASPEN modelling procedure are referred to Appendix E.

Table 6.2: Pure-component parameters (p^*, characteristic pressure; ρ^*, characteristic density; T^*, characteristic temperature) for CO_2, PTFE and HDPE in the SL EOS.

	p^*, bar	ρ^*, kg m^{-3}	T^*, K	Ref
CO_2	7436	1629	277	ASPEN [142]
PTFE	3572	2215	630	Rodgers [144]
HDPE	4250	904	649	Sanchez and Lacombe [104]

A value of 277 K for T^* for CO_2, evaluated from vapour-pressure and liquid-density data regression, is provided in the ASPEN mannual [142]. However, it should be pointed out that instead of 277 K, a value of 258 K was used in this work for ASPEN simulation. The reason was that with the value of 277 K specified in the programme for T^* of CO_2, simulation errors occurred and no sorption data were generated, when simulation pressure was above the "transition" pressure, which was around the critical pressure of CO_2, *i.e.* 74 bar, as mentioned in Section 6.3.1.

By varying the value of T^* for CO_2, it was found that when the specified value was between 207 K and 266 K, no errors occurred and the simulation results agreed well with the experimental results above the "transition" pressure; and when the specified value was out of the range of 207 - 266 K, the errors occurred in the high pressure range, regardless of the values of the other characteristic parameters.

Intuitively, T^* was set to be an adjustable parameter, in addition to the two binary interaction parameters, k_{ij} and η_{ij}, so that their values were optimised, and the sum of squared differences between the experimentally determined and the modelled solubilities was minimised. For the sake of consistency in the modelling of solubility and estimations of binary interaction parameters for all runs, an average value of the optimised T^* for CO_2, 258 K, was used to replace the suggested value of 277 K for simulation. The fits of the modelled solubilities to the experimental ones are shown in Figure 6.2, and the optimised values of k_{ij} and η_{ij} are presented in Table 6.3.

In fact, different estimations of T^* for CO_2 were reported in various studies [35, 233, 244, 247–249], ranging from 269.5 to 341.2 K, using the P-V-T experimental data obtained in their respective work. Ideally, it would be beneficial to determine the characteristic parameters from experimental P-V-T data for the components investigated in this tudy, *i.e.* CO_2, PTFE, and HDPE, under the specific conditions applied to the experiments. Although such work was not conducted, with the parameter values taken from literature, as shown in Table 6.2, together with the one obtained by optimisation, excellent fits were obtained between the modelled solubilities and the experimentally determined ones for the eight runs, which are shown in Figure 6.2.

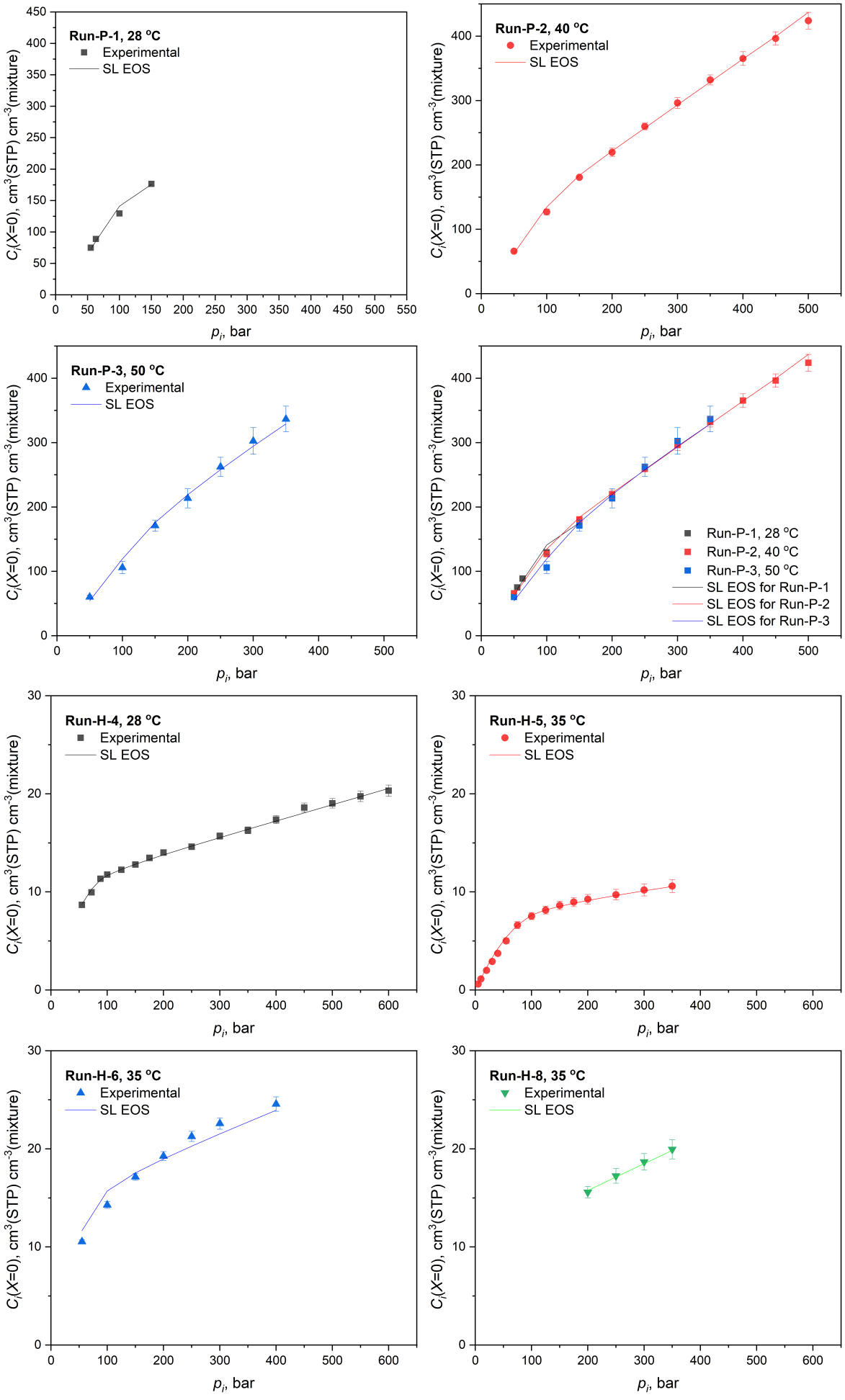


Figure 6.2: Comparison of the experimental solubility and the modelled solubility with SL EOS for PTFE and HDPE.

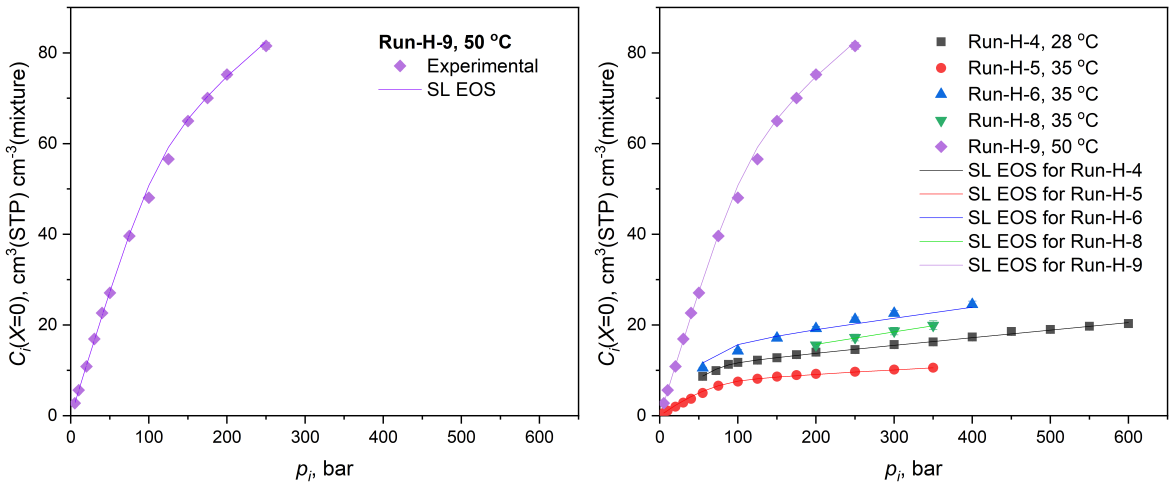


Figure 6.2: Comparison of the experimental solubility and the modelled solubility with SL EOS for PTFE and HDPE (cont.).

Table 6.3: Optimised binary interaction parameters, k_{ij} and η_{ij}, obtained by minimising the sum of the squared differences between the experimental solubilities and those modelled with SL EOS.

	Run-P-1 28 °C, 55 - 150 bar	Run-P-2 40 °C, 50 - 500 bar	Run-P-3 50 °C, 50 - 350 bar
k_{ij}	0.188 ± 0.001	0.171 ± 0.001	0.161 ± 0.001
η_{ij}	0.002 ± 0.001	0.010 ± 0.002	0.001 ± 0.001
	Run-H-4 28 °C, 55 - 600 bar	Run-H-5 35 °C, 5 - 350 bar	Run-H-6 35 °C, 55 - 400 bar
k_{ij}	0.432 ± 0.021	0.365 ± 0.006	0.465 ± 0.013
η_{ij}	0.157 ± 0.020	0.061 ± 0.010	0.217 ± 0.019
	Run-H-8 35 °C, 200 - 350 bar	Run-H-9 50 °C, 5 - 250 bar	
k_{ij}	1.250 ± 0.033	0.185 ± 0.001	
η_{ij}	0.560 ± 0.038	0.003 ± 0.001	

Binary Interaction Parameters k_{ij} and η_{ij}

As can be seen from Figure 6.2, the SL EOS could correlate the solubility data to within 5% average relative deviation for all runs, by optimising the two binary interaction parameters,

k_{ij} and η_{ij}, the values of which are shown in Table 6.3. Overall, the values of η_{ij} obtained for the PTFE runs were two orders of magnitude less than those for the HDPE runs. However, there seemed to be a lack of consistency in the values of this parameter among the runs. In comparison, the obtained values of k_{ij} exhibited a decreasing trend with increasing temperature. The temperature dependence of k_{ij} has been reported in a number of studies for various penetrant-polymer systems. For instance, for the sorption of CO_2 in PP at pressures up to 250 bar, k_{ij} was found to decrease with temperature from 40 to 210 °C [239]. Similar trends for k_{ij} could also be found for CO_2-PBS and CO_2-PBSA systems [215], and for the sorption of butane and isobutane in molten PP and PS [250].

In addition, concentration-dependent k_{ij} was reported in Sato et al. [163]'s work, where they correlated the solubilities of CO_2 and N_2 in molten PP ad HDPE with SL EOS, at temperatures of 160, 180 and 200 °C and pressures up to 170 bar. For N_2, they obtained satisfactory agreements between the experimental and the modelled solubilities, with fixed k_{ij} at a certain temperature, regardless of the variations in pressure or concentration. However, for CO_2, fixed k_{ij} led to large deviations between the experimental and the correlated data. The deviations could be minimised by introducing a relationship for k_{ij}, as a function of the penetrant concentration in the system. In this work, k_{ij} was assumed constant at a specific temperature, and was independent of pressure or concentration variations. This appeared to be a reasonable assumption, as can be seen from the excellent agreement between the experimentally measured and the modelled solubility data shown in Figure 6.2.

The optimised values of k_{ij} and η_{ij} seemed to be positively related. Through an investigation of the relationship between the two quantities, by assigning specific values to one of them and optimising the other one, it was found that in each run, as the value specified for the fixed parameter increased, the optimised value of the other one also increased. Nevertheless, the resulting solubility fits, obtained by optimising one parameter while fixing the other, were not as good as the fits shown in Figure 6.2. The positive relationship between k_{ij} and η_{ij} may also be seen from the optimised values of the two parameters for Run-H-5,6,8, which were conducted at 35 °C with HDPE. As can be seen from the results obtained for the three runs shown in Table 6.3, larger optimised values of k_{ij} were accompanied by larger values of η_{ij}.

Estimating V_i', U_i and γ_i

The volume fraction of CO_2 in the polymer mixture at the top surface of the sample disc, $\nu_i(X = 0)$, assumed to be in equilibrium with the polymer at a given pressure and temperature, can be obtained from the SL EOS. On the basis of this quantitiy and several others derived previously, *i.e.* $C_i(X = 0)$, W_i, $U_i/(W_iV_i')$, $v_f(T, 0, 0)$, and β_p, the values of V_i', U_i, and γ_i could be estimated for each step of the runs. Figure 6.3 is a flow diagram showing the relationships of these quantities and demonstrating the estimating procedures. The results obtained are summarised in Table 6.4.

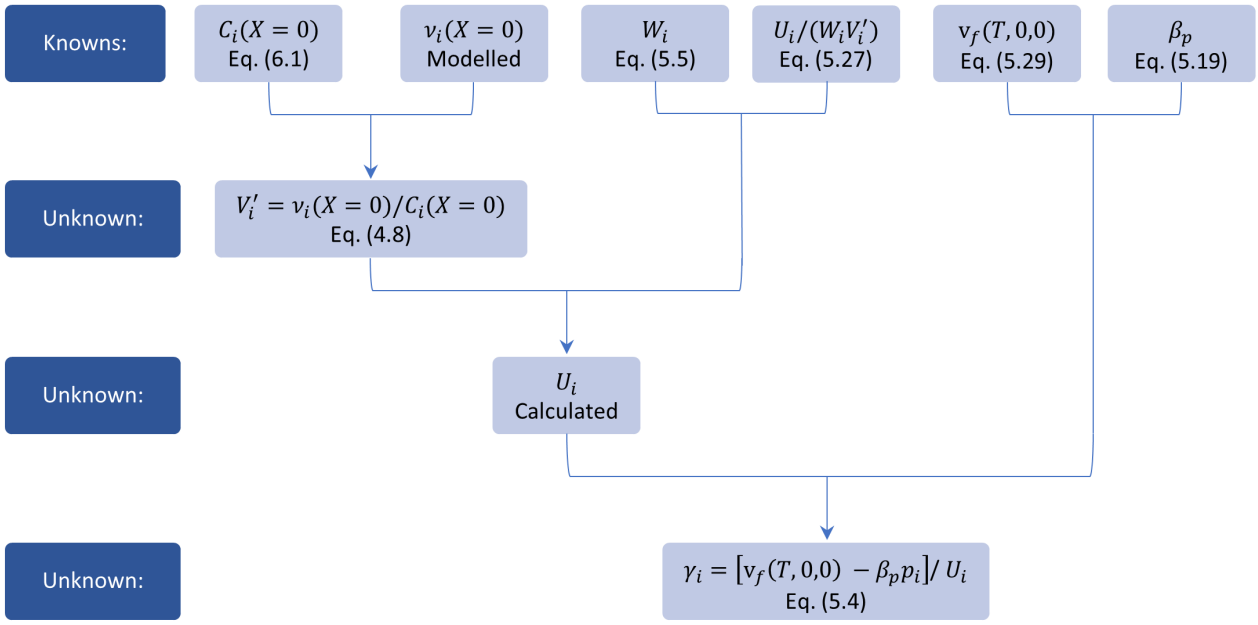


Figure 6.3: Flow diagram showing the procedure for estimating V_i', U_i and γ_i.

Table 6.4: Estimated values of V_i', U_i, and γ_i for the runs, determined using the procedure shown in Figure 6.3.

Step i	p_i, bar	$\nu_i(X = 0)$	V_i', $\times 10^{-3}$	U_i	γ_i
		Run-P-1, PTFE, 28 °C			
1	55	0.150 ± 0.002	2.003 ± 0.006	1.397 ± 0.136	0.037 ± 0.004
2	63	0.179 ± 0.003	2.009 ± 0.004	1.400 ± 0.135	0.037 ± 0.004
3	100	0.283 ± 0.006	2.189 ± 0.011	1.520 ± 0.151	0.034 ± 0.004

Continuation of Table 6.4

Step i	p_i, bar	$\nu_i(X=0)$	V_i', $\times 10^{-3}$	U_i	γ_i
4	150	0.367 ± 0.008	2.079 ± 0.019	1.437 ± 0.148	0.036 ± 0.004
			Run-P-2, PTFE, 40 °C		
1	50	0.132 ± 0.002	2.000 ± 0.005	1.110 ± 0.116	0.053 ± 0.006
2	100	0.278 ± 0.007	2.186 ± 0.025	1.202 ± 0.118	0.048 ± 0.005
3	150	0.391 ± 0.007	2.160 ± 0.002	1.177 ± 0.128	0.049 ± 0.006
4	200	0.473 ± 0.011	2.155 ± 0.015	1.164 ± 0.119	0.049 ± 0.006
5	250	0.555 ± 0.011	2.136 ± 0.005	1.143 ± 0.122	0.049 ± 0.006
6	300	0.633 ± 0.014	2.138 ± 0.015	1.133 ± 0.116	0.049 ± 0.006
7	350	0.711 ± 0.014	2.142 ± 0.012	1.125 ± 0.117	0.049 ± 0.006
8	400	0.787 ± 0.017	2.154 ± 0.021	1.121 ± 0.112	0.049 ± 0.005
9	450	0.860 ± 0.016	2.171 ± 0.020	1.119 ± 0.112	0.049 ± 0.005
10	500	0.938 ± 0.020	2.212 ± 0.038	1.129 ± 0.112	0.048 ± 0.005
			Run-P-3, PTFE, 50 °C		
1	50	0.123 ± 0.012	2.041 ± 0.106	1.018 ± 0.150	0.062 ± 0.008
2	100	0.250 ± 0.047	2.361 ± 0.209	1.119 ± 0.229	0.056 ± 0.010
3	150	0.387 ± 0.072	2.265 ± 0.292	1.067 ± 0.158	0.058 ± 0.008
4	200	0.486 ± 0.091	2.275 ± 0.249	1.037 ± 0.120	0.060 ± 0.006
5	250	0.584 ± 0.096	2.225 ± 0.228	1.010 ± 0.077	0.061 ± 0.004
6	300	0.671 ± 0.103	2.217 ± 0.176	0.976 ± 0.049	0.062 ± 0.003
7	350	0.750 ± 0.100	2.227 ± 0.157	0.977 ± 0.024	0.061 ± 0.002
			Run-H-4, HDPE, 28 °C		
1	55	0.008 ± 0.001	0.905 ± 0.073	0.182 ± 0.011	0.516 ± 0.035
2	72	0.009 ± 0.001	0.928 ± 0.078	0.186 ± 0.011	0.502 ± 0.032

Continuation of Table 6.4

Step i	p_i, bar	$\nu_i(X=0)$	V_i', $\times 10^{-3}$	U_i	γ_i
3	88	0.010 ± 0.001	0.893 ± 0.075	0.179 ± 0.011	0.522 ± 0.033
4	100	0.011 ± 0.001	0.892 ± 0.073	0.178 ± 0.011	0.524 ± 0.034
5	125	0.011 ± 0.001	0.895 ± 0.075	0.177 ± 0.011	0.524 ± 0.034
6	150	0.011 ± 0.001	0.889 ± 0.074	0.174 ± 0.010	0.530 ± 0.034
7	175	0.012 ± 0.002	0.871 ± 0.073	0.169 ± 0.010	0.543 ± 0.035
8	200	0.012 ± 0.002	0.860 ± 0.072	0.165 ± 0.010	0.553 ± 0.035
9	250	0.013 ± 0.002	0.867 ± 0.073	0.163 ± 0.010	0.554 ± 0.035
10	300	0.013 ± 0.002	0.843 ± 0.072	0.155 ± 0.009	0.576 ± 0.036
11	350	0.014 ± 0.002	0.846 ± 0.072	0.152 ± 0.009	0.580 ± 0.036
12	400	0.014 ± 0.002	0.823 ± 0.071	0.145 ± 0.008	0.602 ± 0.037
13	450	0.015 ± 0.002	0.796 ± 0.069	0.137 ± 0.008	0.629 ± 0.038
14	500	0.015 ± 0.002	0.805 ± 0.069	0.135 ± 0.008	0.631 ± 0.039
15	550	0.016 ± 0.002	0.801 ± 0.070	0.132 ± 0.007	0.641 ± 0.038
16	600	0.016 ± 0.002	0.803 ± 0.070	0.129 ± 0.007	0.648 ± 0.039
			Run-H-5, HDPE, 35 °C		
1	5	0.001 ± 0.001	1.622 ± 0.049	0.027 ± 0.006	3.679 ± 0.921
2	10	0.002 ± 0.001	1.693 ± 0.107	0.028 ± 0.005	3.474 ± 0.777
3	20	0.002 ± 0.001	1.827 ± 0.090	0.031 ± 0.006	3.180 ± 0.748
4	30	0.002 ± 0.001	1.805 ± 0.083	0.030 ± 0.006	3.174 ± 0.755
5	40	0.002 ± 0.001	1.788 ± 0.076	0.030 ± 0.006	3.170 ± 0.763
6	55	0.002 ± 0.001	1.701 ± 0.081	0.029 ± 0.006	3.260 ± 0.772
7	75	0.002 ± 0.001	1.577 ± 0.074	0.027 ± 0.006	3.442 ± 0.816
8	100	0.002 ± 0.001	1.587 ± 0.066	0.027 ± 0.006	3.430 ± 0.828

Continuation of Table 6.4

Step i	p_i, bar	$\nu_i(X=0)$	V_i', $\times 10^{-3}$	U_i	γ_i
9	125	0.002 ± 0.001	1.560 ± 0.066	0.026 ± 0.006	3.509 ± 0.845
10	150	0.002 ± 0.001	1.528 ± 0.064	0.025 ± 0.005	3.612 ± 0.870
11	175	0.002 ± 0.001	1.514 ± 0.064	0.025 ± 0.005	3.687 ± 0.888
12	200	0.002 ± 0.001	1.503 ± 0.064	0.024 ± 0.005	3.762 ± 0.904
13	250	0.001 ± 0.001	1.494 ± 0.066	0.024 ± 0.005	3.886 ± 0.929
14	300	0.002 ± 0.001	1.474 ± 0.068	0.023 ± 0.005	4.047 ± 0.962
15	350	0.002 ± 0.001	1.463 ± 0.069	0.022 ± 0.005	4.196 ± 0.993
			Run-H-6, HDPE, 35 ˚C		
1	55	0.006 ± 0.001	0.598 ± 0.059	0.231 ± 0.040	0.427 ± 0.140
2	100	0.009 ± 0.001	0.614 ± 0.055	0.234 ± 0.040	0.416 ± 0.130
3	150	0.010 ± 0.001	0.568 ± 0.052	0.213 ± 0.036	0.452 ± 0.143
4	200	0.010 ± 0.001	0.540 ± 0.048	0.197 ± 0.033	0.480 ± 0.150
5	250	0.011 ± 0.001	0.517 ± 0.045	0.184 ± 0.031	0.508 ± 0.158
6	300	0.012 ± 0.002	0.511 ± 0.044	0.176 ± 0.030	0.523 ± 0.161
7	400	0.013 ± 0.002	0.510 ± 0.042	0.165 ± 0.028	0.542 ± 0.163
			Run-H-8, HDPE, 35 ˚C		
1	200	0.026 ± 0.007	1.662 ± 0.078	0.544 ± 0.085	0.185 ± 0.034
2	250	0.028 ± 0.008	1.617 ± 0.082	0.517 ± 0.079	0.192 ± 0.035
3	300	0.030 ± 0.008	1.597 ± 0.080	0.496 ± 0.076	0.197 ± 0.036
4	350	0.032 ± 0.009	1.589 ± 0.084	0.480 ± 0.073	0.200 ± 0.036
			Run-H-9, HDPE, 50 ˚C		
1	5	0.005 ± 0.001	1.960 ± 0.021	0.434 ± 0.076	0.246 ± 0.051
2	10	0.011 ± 0.001	1.928 ± 0.001	0.440 ± 0.073	0.243 ± 0.048

Continuation of Table 6.4

Step i	p_i, bar	$\nu_i(X=0)$	V_i', $\times 10^{-3}$	U_i	γ_i
3	20	0.022 ± 0.001	2.005 ± 0.004	0.478 ± 0.080	0.223 ± 0.045
4	30	0.033 ± 0.001	1.926 ± 0.010	0.484 ± 0.082	0.219 ± 0.045
5	40	0.043 ± 0.001	1.912 ± 0.013	0.504 ± 0.087	0.210 ± 0.043
6	50	0.054 ± 0.001	1.987 ± 0.016	0.543 ± 0.094	0.194 ± 0.040
7	75	0.079 ± 0.001	1.982 ± 0.009	0.613 ± 0.104	0.171 ± 0.035
8	100	0.100 ± 0.001	2.077 ± 0.015	0.680 ± 0.117	0.153 ± 0.031
9	125	0.116 ± 0.002	2.052 ± 0.015	0.717 ± 0.123	0.144 ± 0.030
10	150	0.128 ± 0.002	1.968 ± 0.014	0.729 ± 0.125	0.140 ± 0.029
11	175	0.137 ± 0.002	1.957 ± 0.015	0.728 ± 0.125	0.139 ± 0.029
12	200	0.145 ± 0.002	1.926 ± 0.014	0.725 ± 0.124	0.139 ± 0.029
13	250	0.158 ± 0.003	1.940 ± 0.013	0.699 ± 0.119	0.142 ± 0.029

It should be pointed out that in Chapter 5, V_i' was assumed to be a constant denoted by V', regardless of p_i. Consistent with this, the values of V_i' shown in Table 6.4 hardly changed with pressure, with a standard deviation of less than 5% of the average value. As for U_i, the obtained values decreased as p_i increased. This observation agrees with the definition for U_i, *i.e.* Eq. (5.4), from which it can be seen that U_i should decrease with increasing p_i. Furthermore, the coefficient, γ_i, which appears in the free volume expression, *i.e.* Eq. (4.7), and is related to the concentration dependence of diffusivity, could also be obtained. As can be seen, on average, the values of γ_i obtained from the PTFE runs were of an order of magnitude less than those obtained from the HDPE runs. In particular, exceptionally larger estimates of γ_i were obtained for Run-H-5, with values about five times higher than those obtained for the other HDPE runs.

Similarly to the discussion presented in Section 5.8 on the estimates of $U_i/(W_iV')$ obtained for Run-H-5, it was found that the large estimates of γ_i for Run-H-5, as shown in Table 6.4,

resulted from the comparatively much lower flux, $F_m(t_1 = 0)$, measured during the experiment. In comparison, despite the different temperatures applied to Run-H-5 and Run-H-9, which were conducted under the same initial pressure with similar pressure steps, the measured fluxes in the former were at least three times smaller than those in the latter. Meanwhile, by comparing the data of Run-H-5 with those of the other runs, which were conducted at the same temperature but with much higher initial pressures, it was found that the smaller flux obtained from the initial step of Run-H-5 led to smaller estimates of $U_i/(W_i V_i')$, based on which smaller values of U_i and larger values of γ_i were derived for the consecutive steps. As pointed out in Section 5.8, further investigation in future work is required to understand the permeation behaviour with multiple steps and validate the method for result analysis.

Although data on the concentration coefficient γ is scarce in literature for CO_2-PTFE or CO_2-HDPE systems, the values of γ obtained from the HDPE runs in this work seemed to be comparable with those obtained in Kulkarni and Stern [115]'s diffusion work for CO_2-PE systems. The values of γ found in their work were 0.50, 0.39 and 0.27 at 5, 20 and 35 °C, respectively. For comparison, the average values of γ_i were 0.57, 0.48 and 0.18 for Run-H-4 (28 °C), Run-H-6 (35 °C) and Run-H-9 (50 °C), respectively. Due to a lack of data for the CO_2-PTFE system in literature, it is difficult to assess the values of γ_i obtained for the PTFE runs. Nevertheless, if these results could be validated, such data would be valuable for filling the knowledge gap.

Swelling, Plasticisation and Crystallinity

So far, through the work presented in this chapter and in the previous ones, the estimates for all essential parameters and properties, which characterise the permeation features of the CO_2-polymer systems, have been derived in a combined approach involving permeation measurements, diffusion modelling with free volume formulations, and sorption modelling using SL EOS. However, there remain some important aspects to consider, such as swelling, plasticisation, and crystallinity. Assumptions were made to simplify the cases, while developing the theories and models for analysis. Despite the great convenience and simplicity of analysis permitted by making these assumptions, thoughtful consideration is required.

For highly soluble penetrants such as CH_4 and CO_2, sufficiently high concentrations of the dissolved penetrants in the semicrystalline polymer could lead to swelling effects in the amorphous region, resulting in increased polymer chain mobility and diffusion coefficients [79]. The sorption phenomena are complicated by the swelling effect, resulting in non-Fickian behaviour, or so-called case II diffusion. The diffusion model applied in this study was based on Fick's laws for Fickian diffusion, and that the swelling effect was not considered. However, such a treatment could be oversimplified. It was reported in Lei et al. [239]'s work for the sorption of CO_2-PP system that corrections to solubility are required for measurements above 100 bar to allow for swelling, since otherwise large deviations would occur between the measured solubility and the available literature data. In a number of studies [163, 238, 239], swelling corrections are often calculated with the SL EOS . Moreover, Chen et al. [238] pointed out that the polymer swelling could also be directly measured through visual observation by a high-pressure view cell.

Apart from the swelling effect, plasticisation can also increase the chain mobility and promote gas diffusion [236, 251]. Carbon dioxide at high temperature and pressure is not only a strong swelling agent, but also an effective plasticiser [251, 252]. The dissolution of CO_2 may dramatically lower the glass transition temperature, T_g, as a result of the intermolecular interactions between CO_2 and the polymer [253]. In this study, the plasticisation effect was not considered, and it was assumed that the T_g's for the PTFE and the HDPE samples were constant throughout the experiments for all runs. However, under elevated temperatures and pressures, plasticisation of the amorphous region of the polymer by CO_2 may occur and T_g may alter. This would affect the estimations of the free volume parmeters, $v_f(T, 0, 0)$ and β_p, as described in Section 5.7.2. In the scenarios where the plasticisation effect is not negligible, despite the challenges in elaborate controls and baseline stability under elevated pressures [254], high-pressure cells are available for DSCs with a typical pressure limitation of approximately 70 bar, to obtain the plasticised T_g for the polymer [253, 255].

In addition to the swelling and plasticisation effects, carbon dioxide at supercritial conditions may also change the degree of crystallinity of the polymer [256–259], *i.e.* X_c or 1-ϕ_a, with the crystallinity increasing with increasing CO_2 pressure [259]. The degree of crystallinility affects

the permeation of CO_2 in polymers, in a way that above a certain pressure the sorption process is mainly driven by the crystallinility, such that the higher the degree of crystallinity, the lower the CO_2 sorption concentration in the polymer [260]. In this work, the crystallinity of the polymer sample was assumed constant, regardless of the varying temperatures and pressures. Despite the limited methods for measuring the polymer crystallinility in the presence of CO_2 at high pressures, researchers have developed spectroscopy techniques to investigate the morphological changes of polymers in an environment of CO_2 [258, 261, 262]. In addition, it was reported that the group-contribution lattice-fluid equation of state (GCLF EOS) could be used to estimate the change in crystallinility with CO_2 dissolution into the polymer [239].

In permeation studies of high pressure CO_2 in semicrystalline polymers, effects of polymer swelling, plasticisation and changes in crystallinity are likely to exist; strong coupling of the three phenomena can add extra layers of complexity and difficulty to the work. However, elucidation of these topics, which may require further investigation, is important for developing accurate measuring and modelling methods, as well as a better understanding of the permeation process for CO_2-polymer systems under high pressures.

6.4 Concluding Remarks

In this chapter, CO_2 solubility obtained from the continuous multi-step permeation experiment was modelled with SL EOS, by optimising the binary interaction parameters of the model. Furthermore, the concentration coefficient in the free volume model, γ, which characterises the dependence of the diffusivity on the penetrant volume fraction in the mixture, was determined based on the modelling results. The main outcomes can be summarised.

Firstly, the diffusion equations derived from the previous chapters were further developed to estimate the concentration of the dissolved penetrant on the top surface of the polymer disc. It was found that Henry's law seemed to be obeyed when the applied pressure was below a "transition" pressure around 75 bar, above which deviations may occur, leading to smaller solubilities than the predictions by Henry's law. The obtained solubilities and the solubility

coefficients were compared with the data available in literaure, where similar findings regarding the solubility estimations as well as the shapes of the solubility curves could be found.

Secondly, the dependences of permeability, diffusivity and solubility on temperature, pressure and concentration were characterised, and were compared with the findings from literatures. With the majority of the results agreeing with the expectations, a few exceptions were observed, the elucidation of which requires more repeating runs to be conducted under the same experimental conditions.

Thirdly, the relationship of the equilibrium solubility and the pressure was successfully described by SL EOS, by optimising the binary interactive parameters of the model. On the basis of the modelling results, the volume fraction of CO_2 in the polymer mixture, and the concentration coefficient in the free volume model, γ, were estimated under various conditions. At this point, through the work demonstrated in Chapter 4, Chapter 5 and Chapter 6, the values of all essential permeation properties and free-volume parameters have been identified, which can help elucidate the transport mechanisms and characterise the transport features of the investigated penetrant-polymer systems under the elevated pressures.

Last but not least, the effects of swelling, plasticisation and crystallinity, which were not taken into consideration in this study but can be important for increasing the accuracy in measuring and modelling, were briefly discussed in this chapter. These considerations, once being put into efforts in the future work, would help complete the methods and models developed in this study, and could further enrich the permeation studies in the area.

Chapter 7

Conclusions

The primary aim of the work presented in this thesis, as stated in Chapter 1 for introduction, was to meet the industrial needs for the application of polymeric materials in CCS, and to fill the research gaps in the permeation studies of penetrant-polymer systems under elevated pressures, by conducting permeation experiments for understanding the diffusional mechanisms, and by developing appropriate models and methods to accurately describe the diffusional behaviour and estimate the transport properties. In doing so, a number of goals were addressed. Firstly, pertinent research on gas permeation, diffusion and sorption from literature needed to be reviewed. Secondly, high pressure permeation experiments needed to be carefully designed and conducted. Thirdly, a suitable diffusion model, together with a convenient method for modelling, needed to be developed and validated. Fourthly, the parameters in the model needed to be estimated by following a comprehensive approach, and the obtained values needed to be compared with literature data. Fifthly, and last, an equation of state needed to be used for solubility simulation to investigate the thermodynamic equilibrium sorption of the investigated systems under conditions of interest. To achieve these goals, two common semicrystalline polymers, PTFE and HDPE, were chosen for the permeation study with CO_2. The research work was carried out during the project, and the obtained outcomes were presented and discussed throughout the thesis.

7.1 Summary

The first objective was addressed in Chapter 2, wherein the two permeation models, *i.e.* the solution-diffusion model and the pore-flow model, and the two commonly applied free volume models, *i.e.* Fujita's model and the Vrentas-Duda model, were reviewed. It was concluded that the solution-diffusion model was applicable to the CO_2-polymer systems targeted in this study. Compared with the time-lag method, which assumes constant diffusivity, approaches with free volume theory seem to be more suitable for the cases in this work, as the concentration dependence of the diffusivity could be successfully represented by the free volume formulation. Among the various experimental techniques for permeation study, the isobaric permeation method, by which the concentration of the permeating species could be accurately measured, was adopted in this study.

The second objective was addressed in Chapter 3, which included the work of characterising material properties, designing experimental setup for the permeation measurements at high pressures, introducing the experimental methodology, and outlining the experimental procedure for reproducing the measurements. One of the significant achievements of this project was the construction of a reliable high-pressure experimental setup, which was built upon elaborate designs on paper and finally put into operation after dedicated efforts. The high-pressure rig has been used for permeation measurements under various conditions for this project, and has the potential of being used for seperate sorption measurements in future projects. Furthermore, the experimetal uncertainty was discussed, which was taken into account for all result analysis throughout the entire thesis.

The third objective was addressed in Chapter 4, wherein the experimental results of transient measurements of CO_2 permeation through the two polymers were analysed using a diffusion model incorporating Fujita's free volume formulation. This chapter dealt with the nondimensionalisation and the simplification of the complicated diffusion model through a series of mathematical operations, using several dimensionless parameters and lumped groups. By doing so, not only was the model greatly simplified in a way that the number of the parameters in the model was reduced from 7 to 3, but also a straightforward graphical method was able to

be developed for convenient analysis of the data, without the need to use advanced numerical tools. The values of the parameters determined from the nondimensionalised model and the graphical method were compared to those determined by parameter estimation in gPROMS; these were found to be in very good agreement.

The fourth objective was addressed in Chapter 5, wherein the nondimensionalised model was further developed for the analysis of the permeation experiments consisting of multiple successive pressure steps. Moreover, a method was proposed to use the models developed in chapter 4 to estimate the transport properties at each pressure step, and to determine the free-volume parameters in the model. It was observed that when the pressure was increased following a steady state of permeation from the previous step, there was a near-instantaneous flux drop, which was hypothesised to be caused by a decrease of the free volume in the mixture, resulting from a compaction of the polymer matrix at the higher pressure. From the flux drop and the corresponding decrease of the thermodynamic diffusivity, the pressure effect on diffusion could be characterised by the free-volume parameters; the values determined were consistent with those reported in the literature for similar systems.

The fifth objective was addressed in Chapter 6, wherein the permeation results obtained from Chapter 5 were further analysed in terms of the solubility modelling with SL EOS. Excellent fits were obtained between the experimental solubility and the modelled solubility, by the optimisation of two binary interaction parameters. On the basis of the modelling results, the concentration coefficient that characterised the dependence of diffusivity on the penetrant volume fraction in the mixture was determined. Furthermore, it was found that Henry's law appeared to be followed when the applied pressure was below 75 bar, which was considered as a "transition" pressure, above which deviations from the law may occur. In order to obtain more accurate and reliable results, it was recommended to take the effects of swelling, plasticisation and crystallinity into account in future studies.

To sum up the work presented in Chapters 4 to 6, measurements of transient permeation of CO_2 in PTFE and HDPE under various temperatures and pressures have been comprehensively analysed and modelled, using a non-dimensionalised and simplified diffusion model incorporating

Fujita's free volume formulation. A graphical method was proposed to estimate the transport properties under various conditions in an accurate and convenient manner. In addition, the free-volume parameters in the diffusion model were estimated from transient measurements of flux during multiple successive pressure steps, and from the modelling results obtained with SL EOS. The modelling demonstrated that the assumptions used to derive the simplified model were valid. Thus, the experimental methodology, the nondimensionalised model, the graphical method, and the EOS modelling demonstrated in this work can be conveniently applied to various penetrant-polymer systems under a wide range of conditions.

7.2 Outlook

As the limited time allocated to this PhD project comes to an end, it has become increasingly clear that there would always be questions to each solution. The project was initiated almost from scratch: it required rig construction, experimental design, safety control, material characterisation, permeation measurements, derivation and simplification of mathematical models, parameter optimisation, *etc.* Although much work in this project required constant trials and errors, the results obtained and the methods proposed in this thesis could form a solid basis for future investigations in pertinent fields. More importantly, with deeper understanding and more knowledge gained on the topic as the project proceeded, a few inspiring insights arose, as outlined below, which may set out future research directions and could lead to intriguing explorations.

Permeation of Gas Mixtures

In CCS applications, it is common to deal with CO_2 streams containing additional compounds, such as H_2S, SO_x and NO_x, which are impurities that could considerably affect the permeability of the stream and the performance of the polymeric materials, especially in high pressure CO_2. This thesis features only the permeation of pure CO_2 in polymers. It would be beneficial to examine whether the developed techniques, models and methods could be extended to the permeation of multicomponent mixtures in polymers under similar operating conditions. Con-

sidering the likely effects of the impurities on corrosion of metallic pipeline and degradation of polymers, modifications to the current experimental design and model development could be expected. New measures such as selectivity and purity might be introduced for analysing the permeation behaviour and assessing the polymer performance. From a practical point of view, by developing standard measuring techniques and appropriate permeation models for CO_2 permeation with impurities, valuable information could be gained on the service life of polymeric seals and liners, facilitating the design and the evaluation of the infrustructure for CCS.

Various Types of Polymers

Two semicrystalline polymers, PTFE and HDPE, which are relatively well investigated, were studied in this thesis. As discussed in Chapter 6, the sorption of CO_2 may cause swelling, plasticisation and changes in the crystallinity of the polymers. In fact, different types of polymers may react differently to the permeation of CO_2. Their performance could be affected by a number of factors, *e.g.* composition of the composite polymers, content of the amorphous region for semicrystalline polymers, the state being glassy or rubbery for the amorphous polymers or regions, *etc.* Practically, understanding of the permeation characteristics against various types of polymers could help select suitable polymeric seals and liners for CCS applications. In addition, it is of vital research interest to extend both experimental and modelling work conducted in this thesis to a wider range of polymers, so as to elucidate the permeation mechanisms for a variety of polymers. For example, anomalies in diffusion characteristics could occur for glassy polymers, which may lead to interesting research findings.

Independent Sorption Measurements

As mentioned in Chapter 3, in addition to the experimental setup for permeation, the facility was provided to use the rig for manometric measurements of gas sorption in a closed cell, with relatively few changes to the components. It is considered necessary to carry out separate sorption measurements to first verify the solubility data derived indirectly from the permeation measurements in this work, second validate the applicability of the SL EOS or other equations of state to the modelling of the solubility behaviour, and finally investigate the swelling of the polymer matrix induced by the sorbed molecules. The independent sorption measurements

would be important supplements to the current permeation measurements, and could contribute to a comprehensive understanding of the processes.

These are some possible directions for further research. With the undergoing explorations on the topic, there is an expectation of many significant developments in future research as well as practical applications.

Appendices

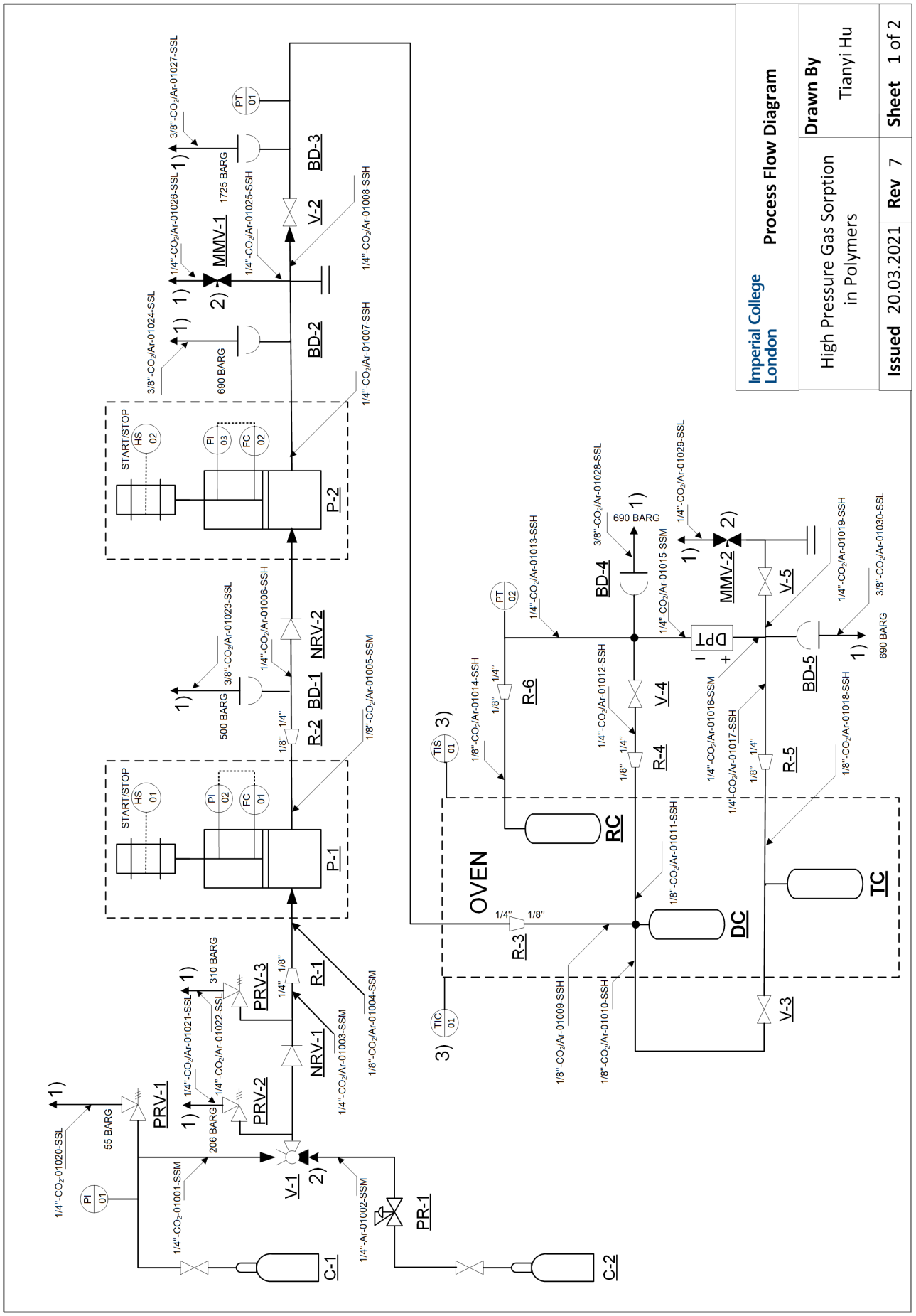
Appendix A

Sorption Experiment

A.1 Process Description

The solubility of high pressure CO_2 in a polymer is the amount of the CO_2 dissolved in the polymer. It is obtained from a measurement of the pressure drops by applying a material balance. A schematic of the experimetal setup (in landscape) is attached on the following pages. The process can be divided into four sections: feeding, first-stage pressurisation, second-stage pressurisation, and sorption. In the pressure range of 1 - 500 barg, P-1 is used for pressurisation; in the range of 500 - 650 barg, P-1 and P-2 are used for the high pressure.

Three cells of the same volume and dimensions are placed in the oven. The cells are dose cell (DC), reference cell (RC), and test cell (TC) containing the polymer sample. The pressure transimitter PT-1 (with an upper limit of 1600 barg), measures the equilibrium pressure inside DC, with the valve (V-2) closed or open. For Ar experiment, RC is not needed and V-3 is closed. Therefore, pressure transducer (PT-2) and differential pressure transducer (DPT) are not used in this case.


Imperial College London
Process Flow Diagram
High Pressure Gas Sorption in Polymers
Drawn By
Tianyi Hu
Issued 20.03.2021
Rev 7
Sheet 1 of 2
OVEN
C-1
C-2
PR-1
V-1
PRV-1
PRV-2
PRV-3
NRV-1
R-1
P-1
P-2
NRV-2
R-2
BD-1
BD-2
BD-3
MMV-1
R-3
R-4
R-5
R-6
RC
DC
TC
V-2
V-3
V-4
V-5
BD-4
BD-5
MMV-2
DPT
PT 01
PT 02
PI 01
PI 02
PI 03
FC 01
FC 02
HS 01
HS 02
START/STOP
TIC 01
TIS 01
55 BARG
206 BARG
310 BARG
500 BARG
690 BARG
1725 BARG
1/4"-CO2-01020-SSL
1/4"-CO2-01001-SSM
1/4"-CO2/Ar-01021-SSL
1/4"-CO2/Ar-01022-SSL
1/4"-CO2/Ar-01003-SSM
1/8"-CO2/Ar-01004-SSM
1/4"-Ar-01002-SSM
3/8"-CO2/Ar-01023-SSL
1/4"-CO2/Ar-01006-SSH
1/8"-CO2/Ar-01005-SSM
3/8"-CO2/Ar-01024-SSL
1/4"-CO2/Ar-01026-SSL
1/4"-CO2/Ar-01025-SSH
3/8"-CO2/Ar-01027-SSL
1/4"-CO2/Ar-01007-SSH
1/4"-CO2/Ar-01008-SSH
1/8"-CO2/Ar-01009-SSH
1/8"-CO2/Ar-01010-SSH
1/8"-CO2/Ar-01011-SSH
1/4"-CO2/Ar-01012-SSH
1/8"-CO2/Ar-01014-SSH
1/4"-CO2/Ar-01013-SSH
3/8"-CO2/Ar-01028-SSL
1/4"-CO2/Ar-01015-SSM
1/4"-CO2/Ar-01029-SSL
1/4"-CO2/Ar-01016-SSM
1/4"-CO2/Ar-01017-SSH
1/8"-CO2/Ar-01018-SSH
1/4"-CO2/Ar-01019-SSH
3/8"-CO2/Ar-01030-SSL

List of Symbols

- Hand valve (V)
- Three-way valve
- Syringe pump (P)
- DPT — Differential pressure transducer (DPT)
- Bursting disc (BD)
- FC # — Flow controller (FC)
- HS # — Hand switch (HS)
- Reducer
- Plug/Blind
- Pressure regulator (PR)
- Pressure relief valve (PRV)
- Non-return valve (NRV)
- Micrometering valve (MMV)
- PI # — Pressure indicator (PI)
- PT # — Pressure transducer (PT)
- TIC # — Temperature indicator for controller (TIC)
- TIS # — Temperature indicating switch (TIS)

Pipeline Numbering and Specification

1/4''-Ar-01 002-SS M

SIZE (inches)
FLUID
PROCESS UNIT
SERIAL NUMBER
PIPE MATERIAL
CLASS

Notes

1) To safe location.

2) Normally closed.

3) On oven panel.

CLASS	O.D (inches)	MANUFACTURER	THICKNESS (inches)	PRESSURE RATING (barg)
SSL	1/4	SANDVIK	0.035	352 *
	3/8	SANDVIK	0.035	228 *
SSM	1/4	SANDVIK	0.065	703 *
	1/8	SANDVIK	0.035	752 *
SSH	1/4	SITEC	0.094	5000 **
	1/8	SITEC	0.043	4000 **

* At 37 °C
** At 20 °C

Equipment Tag	C-1	C-2	P-1	P-2	DC	TC	RC
Description	CO_2 Cylinder	Ar Cylinder	Syringe Pump	Syringe Pump	DOSE CELL	TEST CELL	REFERENCE CELL
Material of Construction	Carbon Steel (CS)	Carbon Steel (CS)	Stainless Steel (SS)	Stainless Steel (SS)	AISI 316 L	AISI 316 L	AISI 316 L
Operating pressure (barg)	180 - 200	200	up to 517	up to 1379	1200	1200	1200
Operating Temperature (°C)	20	20	5 - 40 (Ambient)	5 - 40 (Ambient)	20	20	20
Fluid	CO_2	Ar	CO_2 or Ar	CO_2 or Ar	CO_2 or Ar	CO_2 or Ar	CO_2 or Ar
Capacity	5 kg	88 kg	266 mL or 107 mL/min	68 mL or 25 mL/min	45 mL	45 mL	45 mL

Items	SWAGELOK (barg)			VALCO (barg)		PT-1,2 (barg)	DPT (psig)	SITEC (barg)	
	V-1	Tee	NRV-1	R-1	R-2			Tee (1/4HP-DN3)	NPT Adapter
Pressure Ratings	689	1379	414	1379	689	1600	10000	4000	1500

Items	SITEC (barg)							
	BD-1	BD-2,4,5	BD-3	NRV-2	MMV-1,2	V-2 to 5	R-3 to 6	Tee (1/4HP-G1/2"-DN3)
Pressure Ratings	500 +/- 10%	690 +/- 10%	1725 +/- 5%	4000	2000	2000	4000	2500

Imperial College London — **Process Flow Diagram**

High Pressure Gas Sorption in Polymers

Drawn By Tianyi Hu

Issued 20.03.2021 **Rev** 7 **Sheet** 2 of 2

A.2 Procedure

The operating procedure for the sorption experiment is provided.

1) Leak test.

   (a) Check the pressure of each cylinder, and the condition of each apparatus with each connection port.

   (b) Test leaks in the system.

2) Preparation.

   (a) Weigh a certain amount of the polymer sample and record its weight.

   (b) Place the sample in the glass vial in the test cell (TC).

   (c) Properly tighten the three cells and all fittings.

3) Evacuation.

   (a) Close the valves attached to the CO_2 cylinder (C-1) and the Ar cylinder (C-2). Open the three-way valve (V-1) towards the C-1 end during the first evacuation run, and towards the C-2 end during the second evacuation run. Close MMV-1 and V-2.

   (b) Connect the vacuum pump to MMV-1. Switch on the vacuum pump and slowly open MMV-1. Evacuate this section for 15 minutes during each evacuation run.

   (c) After the 30-minute evacuation, close MMV-1, switch off the vacuum pump, and disconnect it from MMV-1. Close MMV-2 and open V-3, V-4 and V-5.

   (d) Connect the vacuum pump to MMV-2. Switch on the vacuum pump and slowly open MMV-2. Evacuate this section for 30 minutes.

   (e) After the 30-minute evacuation, close MMV-2, switch off the vacuum pump, and disconnect it from MMV-2.

4) Argon experiment.

(a) Open V-1 towards the Ar cylinder (C-2) side. Close MMV-1, MMV-2, V2, V-3, V-4 and V-5.

(b) Record the "zero" pressure, P_0, in the dose cell (DC) by PT-1.

(c) Open the valve of C-2. Switch on the oven, and heat up the system to the required temperature.

(d) Switch on P-1 and P-2. Pressurise the system to the targeted pressure (*e.g.* 30 bar).

(e) Open V-2 and fill Ar in DC to a pressure of about 30 bar. Close V-2.

(f) Wait for a few minutes until the pressure stabilises and record the pressure p_{D1}.

(g) Open V-3 and let Ar expand to TC. Wait for a few minutes until the pressure stabilises, and record the pressure p_1. Close V-3.

(h) Increase pressure to about 60 bar, 90 bar, 120 bar, ..., 550 bar, 600 bar, 650 bar. Repeat the previous two steps, and record the corresponding p_{Dj} and p_j for each pressure.

5) Depressurisation.

(a) Close the cylinder valves. Close V-2, and open V-3 and V-4.

(b) Slowly open MMV-1 and MMV-2, and vent the gas until atmospheric pressure is reached.

6) Carbon dioxide experiment.

(a) Follow the same procedure as above, but replace Ar by CO_2 and add the following step after recording p_j.

(b) Close V-3 and open V-4 to equalise the pressures in RC and DC. Record the pressure change of TC using DPT.

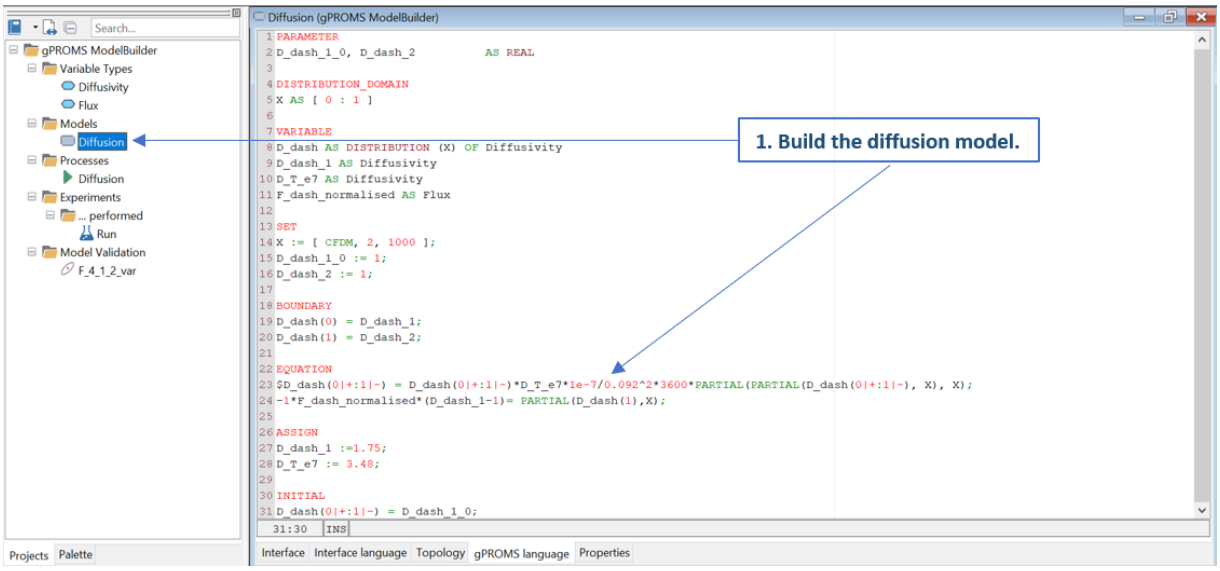
7) Depressurisation.

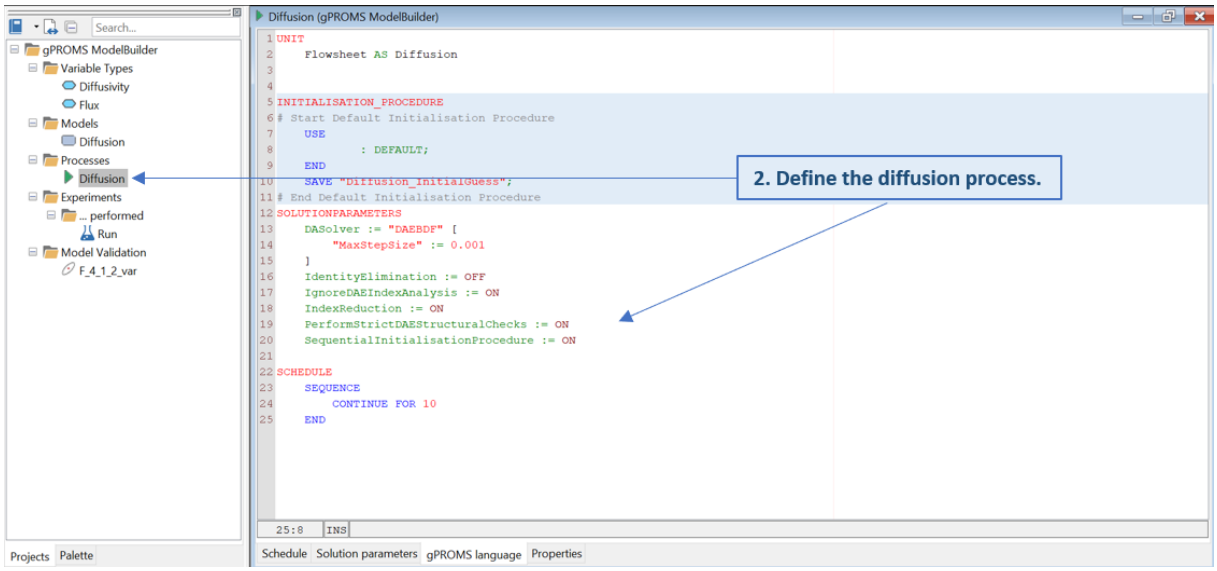
(a) Close the cylinder valves. Close V-2, and open V-3 and V-4.

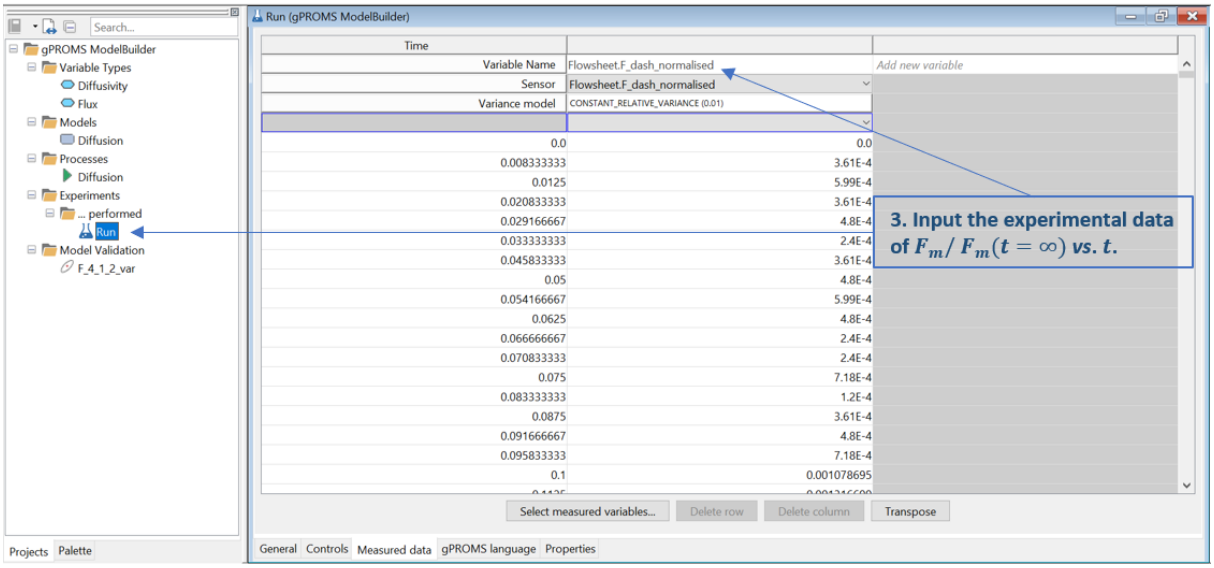
(b) Slowly open MMV-1 and MMV-2, and vent the gas until atmospheric pressure is reached.

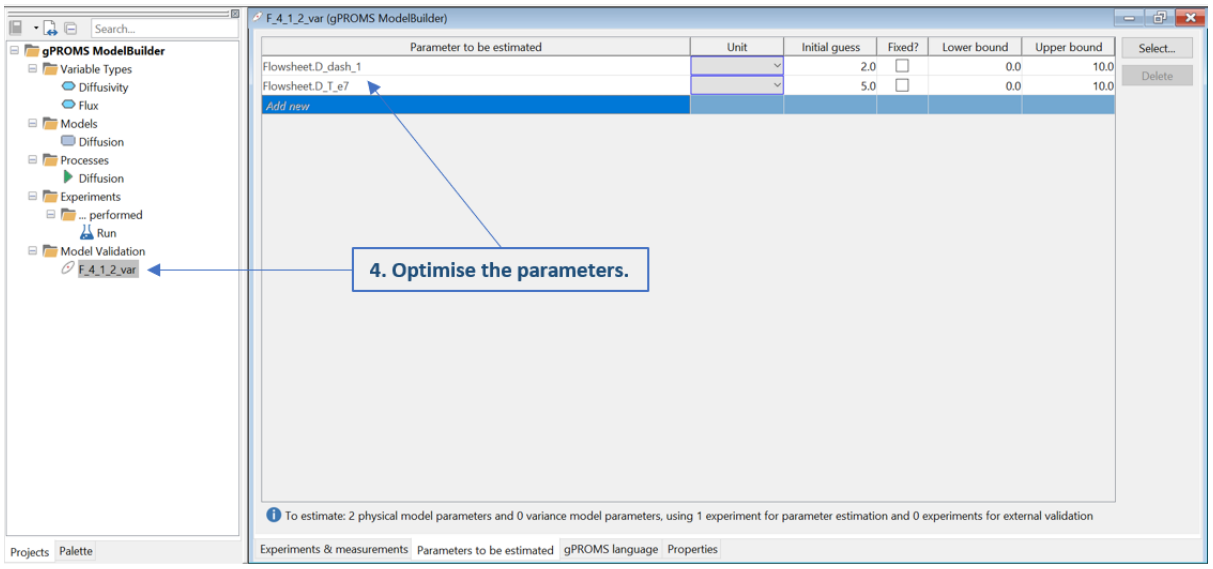
Appendix B

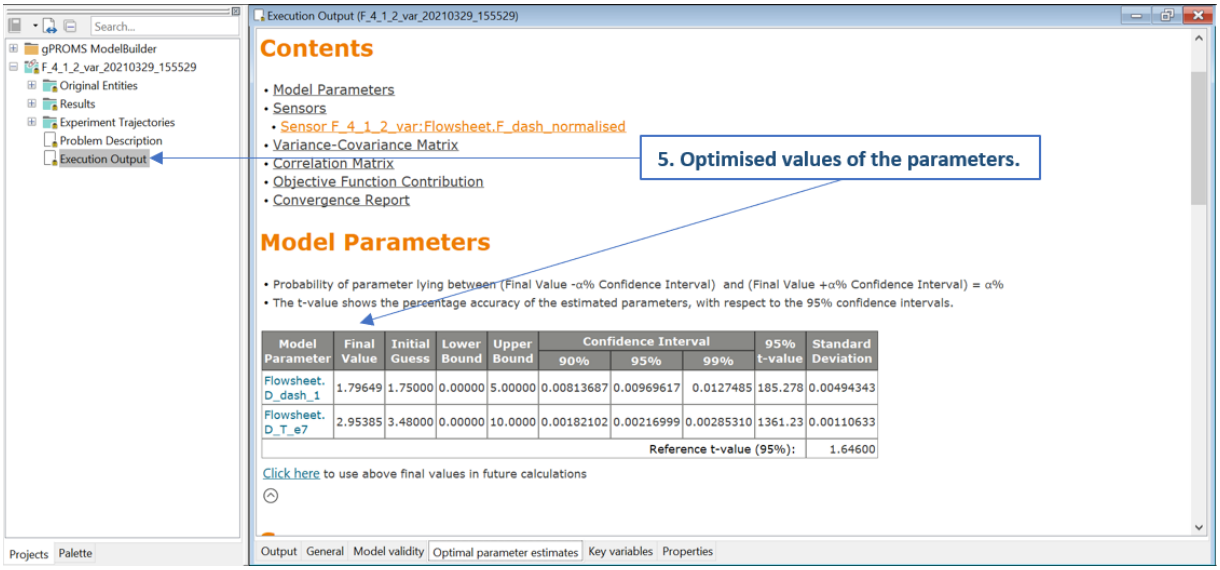
gPROMS Modelling

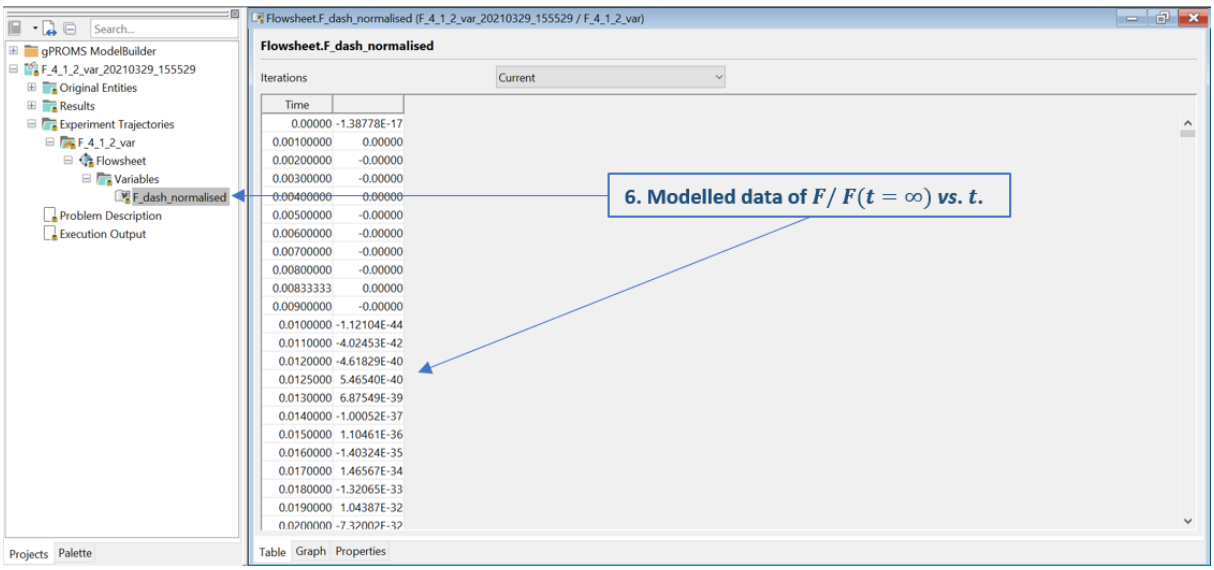


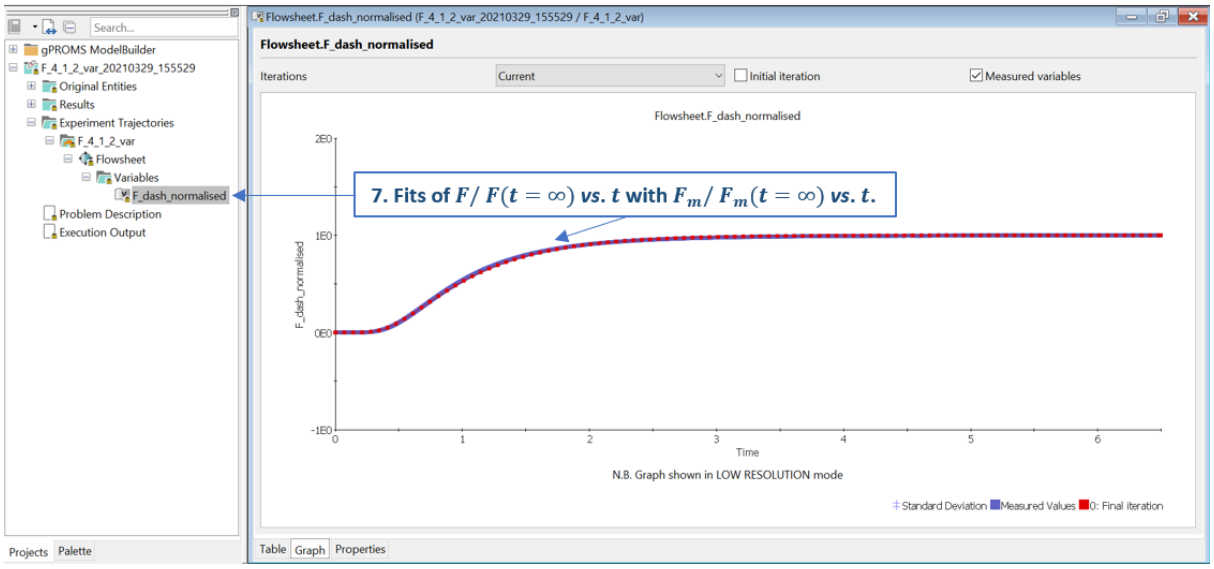



Run (gPROMS ModelBuilder)
gPROMS ModelBuilder
Variable Types
Diffusivity
Flux
Models
Diffusion
Processes
Diffusion
Experiments
... performed
Run
Model Validation
F_4_1_2_var
Time
Variable Name
Flowsheet.F_dash_normalised
Sensor
Flowsheet.F_dash_normalised
Variance model
CONSTANT_RELATIVE_VARIANCE (0.01)
Add new variable
3. Input the experimental data of $F_m/F_m(t=\infty)$ vs. t.
Select measured variables...
Delete row
Delete column
Transpose
General
Controls
Measured data
gPROMS language
Properties
Projects
Palette


F_4_1_2_var (gPROMS ModelBuilder)
gPROMS ModelBuilder
Variable Types
Diffusivity
Flux
Models
Diffusion
Processes
Diffusion
Experiments
... performed
Run
Model Validation
F_4_1_2_var
Parameter to be estimated
Unit
Initial guess
Fixed?
Lower bound
Upper bound
Flowsheet.D_dash_1
2.0
0.0
10.0
Flowsheet.D_T_e7
5.0
0.0
10.0
Add new
Select...
Delete
4. Optimise the parameters.
To estimate: 2 physical model parameters and 0 variance model parameters, using 1 experiment for parameter estimation and 0 experiments for external validation
Experiments & measurements
Parameters to be estimated
gPROMS language
Properties
Projects
Palette


Execution Output (F_4_1_2_var_20210329_155529)
gPROMS ModelBuilder
F_4_1_2_var_20210329_155529
Original Entities
Results
Experiment Trajectories
Problem Description
Execution Output
Contents
Model Parameters
Sensors
Sensor F_4_1_2_var:Flowsheet.F_dash_normalised
Variance-Covariance Matrix
Correlation Matrix
Objective Function Contribution
Convergence Report
5. Optimised values of the parameters.
Model Parameters
Probability of parameter lying between (Final Value -α% Confidence Interval) and (Final Value +α% Confidence Interval) = α%
The t-value shows the percentage accuracy of the estimated parameters, with respect to the 95% confidence intervals.
Model Parameter
Final Value
Initial Guess
Lower Bound
Upper Bound
Confidence Interval
90%
95%
99%
95% t-value
Standard Deviation
Flowsheet.D_dash_1
1.79649
1.75000
0.00000
5.00000
0.00813687
0.00969617
0.0127485
185.278
0.00494343
Flowsheet.D_T_e7
2.95385
3.48000
0.00000
10.0000
0.00182102
0.00216999
0.00285310
1361.23
0.00110633
Reference t-value (95%):
1.64600
Click here to use above final values in future calculations
Output
General
Model validity
Optimal parameter estimates
Key variables
Properties
Projects
Palette

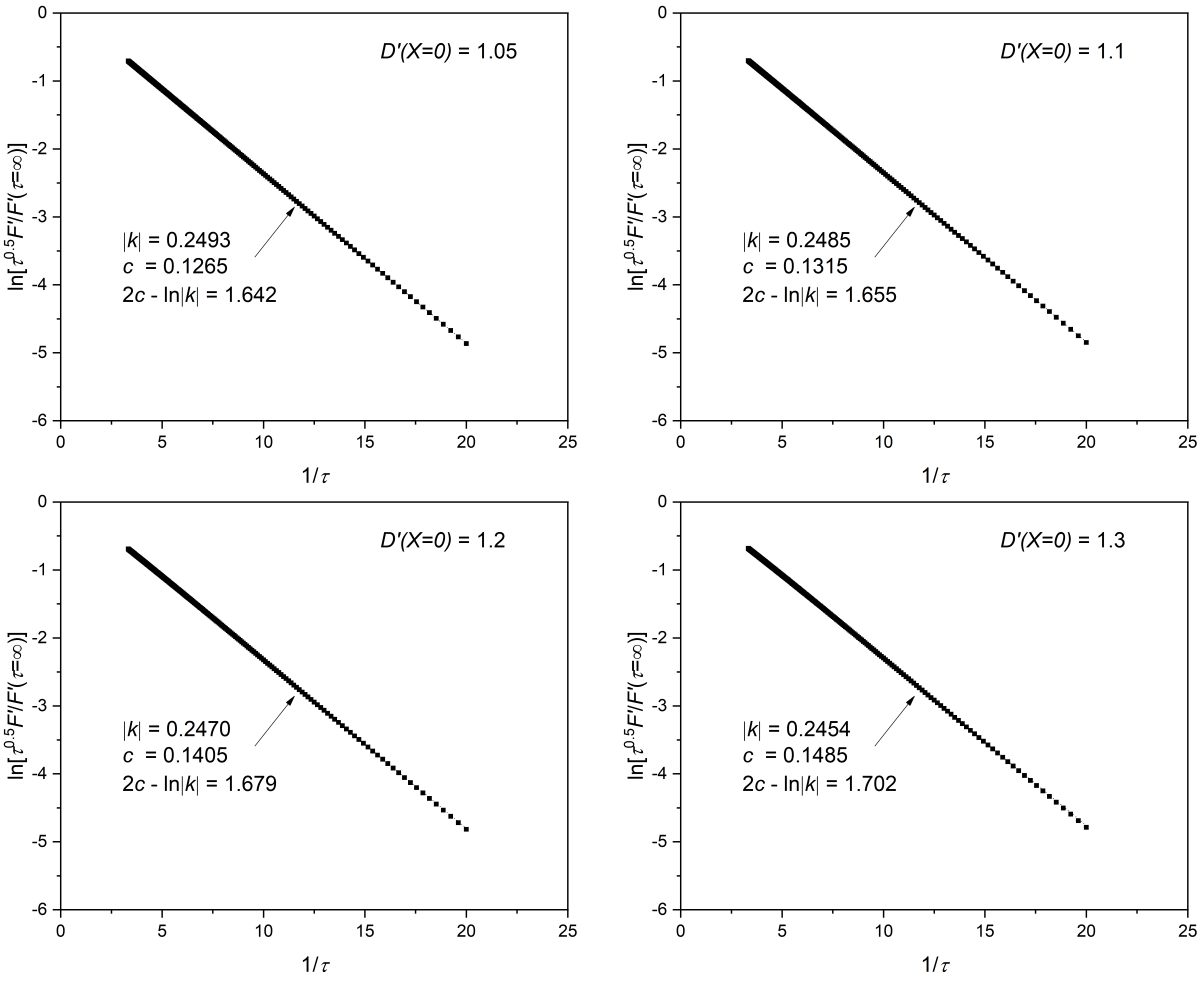

Search...
gPROMS ModelBuilder
F_4_1_2_var_20210329_155529
Original Entities
Results
Experiment Trajectories
F_4_1_2_var
Flowsheet
Variables
F_dash_normalised
Problem Description
Execution Output
Projects
Palette
Flowsheet.F_dash_normalised (F_4_1_2_var_20210329_155529 / F_4_1_2_var)
Flowsheet.F_dash_normalised
Iterations
Current
Time
0.00000 -1.38778E-17
0.00100000 0.00000
0.00200000 -0.00000
0.00300000 -0.00000
0.00400000 0.00000
0.00500000 -0.00000
0.00600000 -0.00000
0.00700000 -0.00000
0.00800000 -0.00000
0.00833333 0.00000
0.00900000 -0.00000
0.0100000 -1.12104E-44
0.0110000 -4.02453E-42
0.0120000 -4.61829E-40
0.0125000 5.46540E-40
0.0130000 6.87549E-39
0.0140000 -1.00052E-37
0.0150000 1.10461E-36
0.0160000 -1.40324E-35
0.0170000 1.46567E-34
0.0180000 -1.32065E-33
0.0190000 1.04387E-32
0.0200000 -7.32002E-32
Table
Graph
Properties
6. Modelled data of $F/F(t=\infty)$ vs. t.

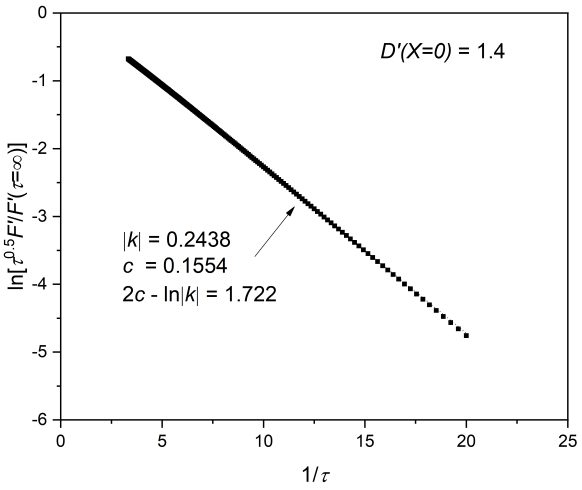

Search...
gPROMS ModelBuilder
F_4_1_2_var_20210329_155529
Original Entities
Results
Experiment Trajectories
F_4_1_2_var
Flowsheet
Variables
F_dash_normalised
Problem Description
Execution Output
Projects
Palette
Flowsheet.F_dash_normalised (F_4_1_2_var_20210329_155529 / F_4_1_2_var)
Flowsheet.F_dash_normalised
Iterations
Current
Initial iteration
Measured variables
Flowsheet.F_dash_normalised
2E0
1E0
0E0
-1E0
F_dash_normalised
0
1
2
3
4
5
6
Time
N.B. Graph shown in LOW RESOLUTION mode
Standard Deviation
Measured Values
0: Final Iteration
Table
Graph
Properties
7. Fits of $F/F(t=\infty)$ vs. t with $F_m/F_m(t=\infty)$ vs. t.

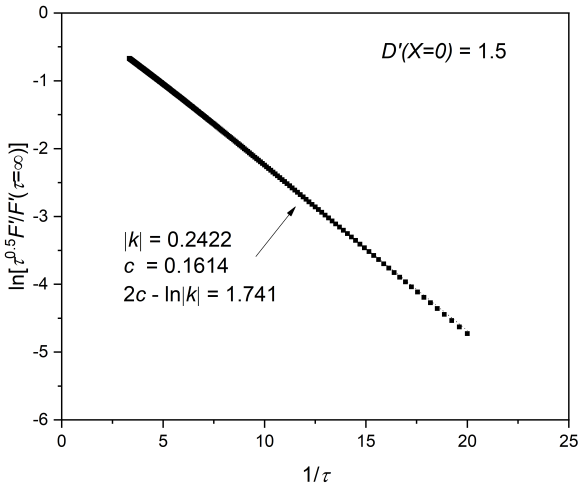
Appendix C

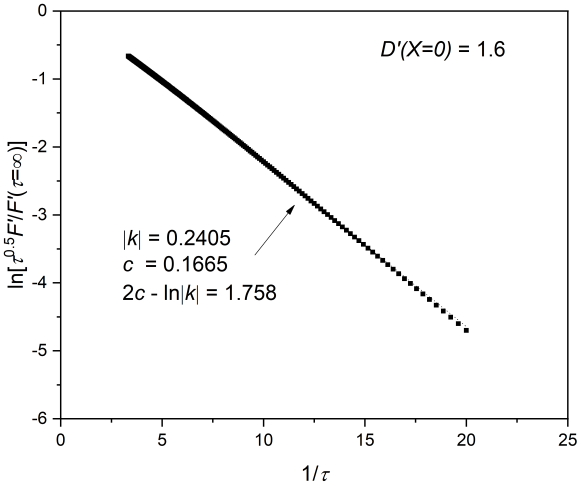
Flux Approximation Plots

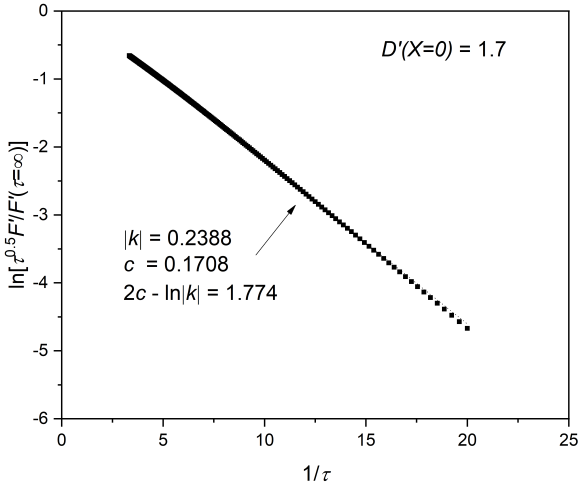
C.1 Simplified Model

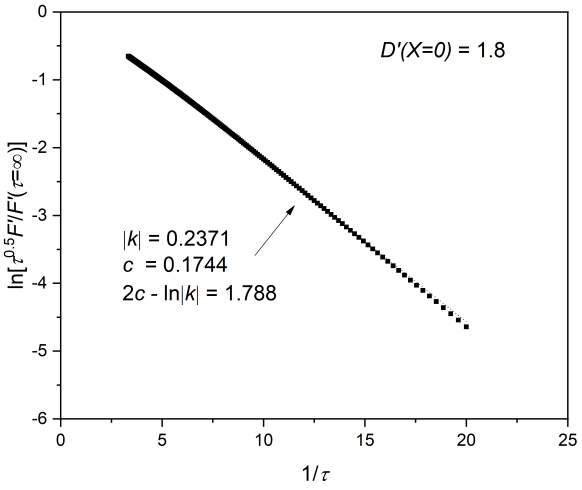


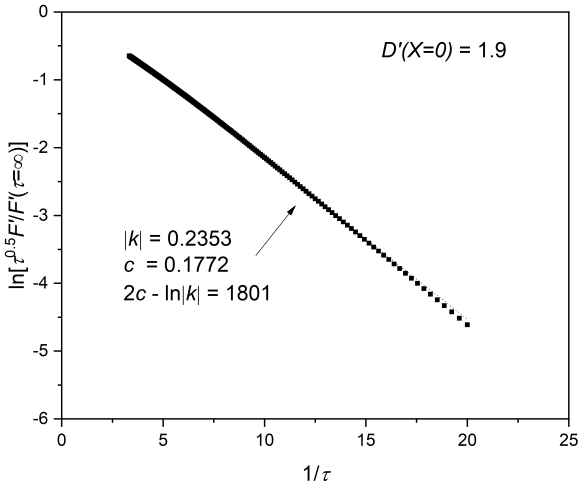

D'(X=0) = 1.4
|k| = 0.2438
c = 0.1554
2c - ln|k| = 1.722
ln[τ^0.5F'/F'(τ=∞)]
1/τ

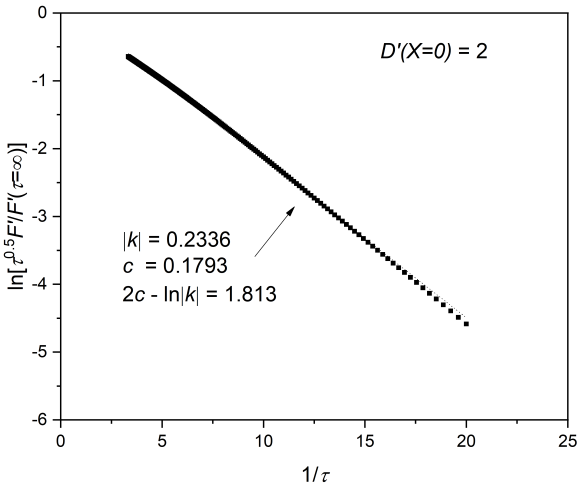

D'(X=0) = 1.5
|k| = 0.2422
c = 0.1614
2c - ln|k| = 1.741
ln[τ^0.5F'/F'(τ=∞)]
1/τ

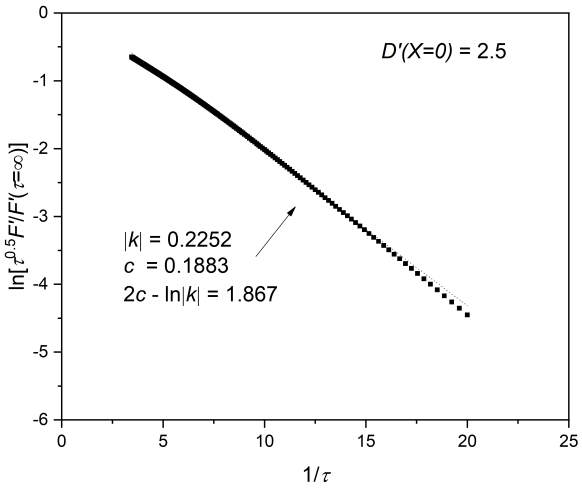

D'(X=0) = 1.6
|k| = 0.2405
c = 0.1665
2c - ln|k| = 1.758
ln[τ^0.5F'/F'(τ=∞)]
1/τ

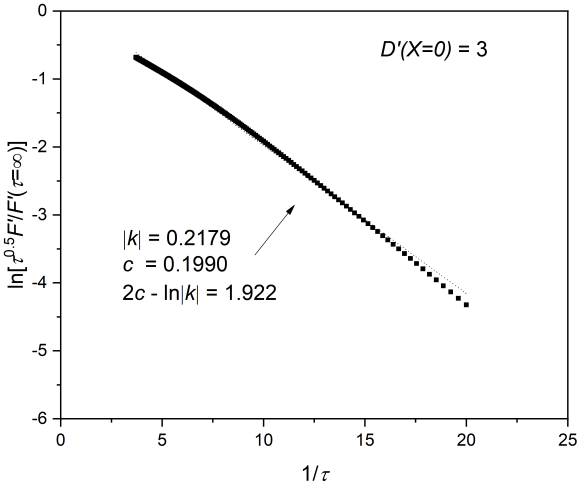

D'(X=0) = 1.7
|k| = 0.2388
c = 0.1708
2c - ln|k| = 1.774
ln[τ^0.5F'/F'(τ=∞)]
1/τ

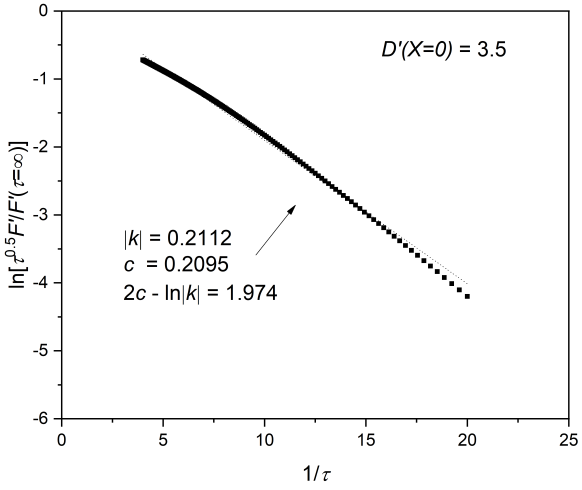

D'(X=0) = 1.8
|k| = 0.2371
c = 0.1744
2c - ln|k| = 1.788
ln[τ^0.5F'/F'(τ=∞)]
1/τ

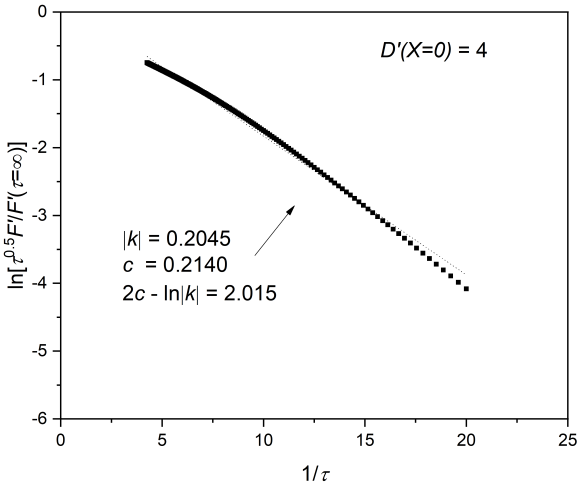

D'(X=0) = 1.9
|k| = 0.2353
c = 0.1772
2c - ln|k| = 1801
ln[τ^0.5F'/F'(τ=∞)]
1/τ

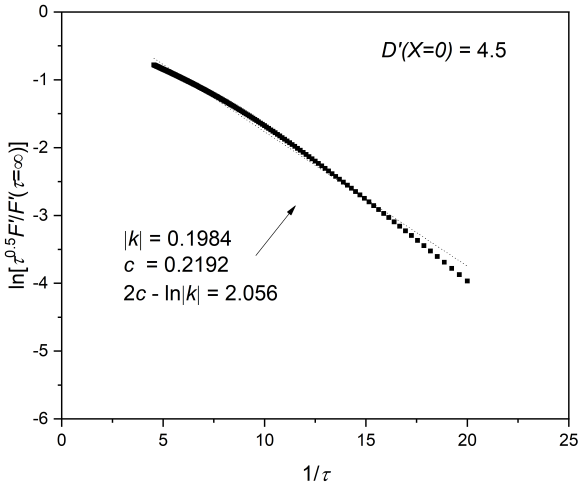

D'(X=0) = 2
|k| = 0.2336
c = 0.1793
2c - ln|k| = 1.813
ln[τ^0.5F'/F'(τ=∞)]
1/τ


D'(X=0) = 2.5
|k| = 0.2252
c = 0.1883
2c - ln|k| = 1.867
ln[τ^0.5F'/F'(τ=∞)]
1/τ

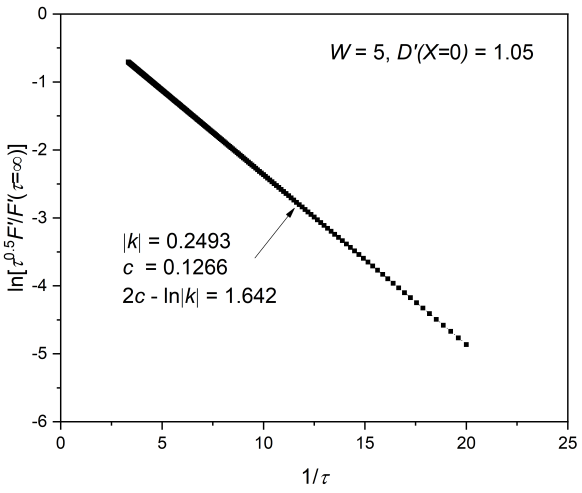

D'(X=0) = 3
|k| = 0.2179
c = 0.1990
2c - ln|k| = 1.922
ln[τ^0.5F'/F'(τ=∞)]
1/τ

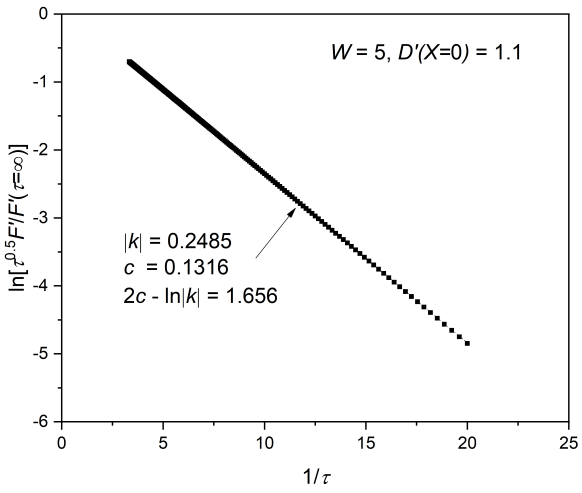

D'(X=0) = 3.5
|k| = 0.2112
c = 0.2095
2c - ln|k| = 1.974
ln[τ^0.5F'/F'(τ=∞)]
1/τ

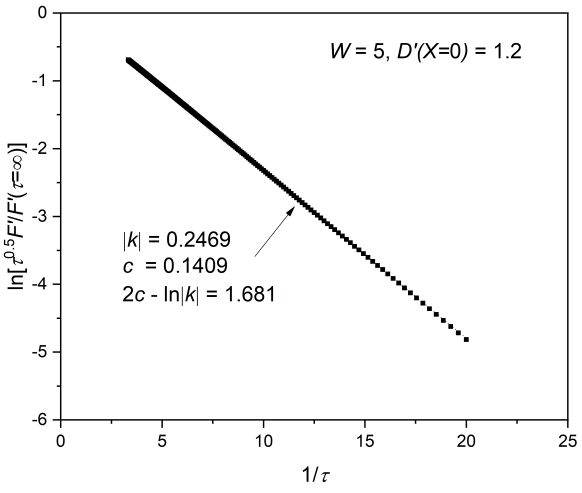

D'(X=0) = 4
|k| = 0.2045
c = 0.2140
2c - ln|k| = 2.015
ln[τ^0.5F'/F'(τ=∞)]
1/τ

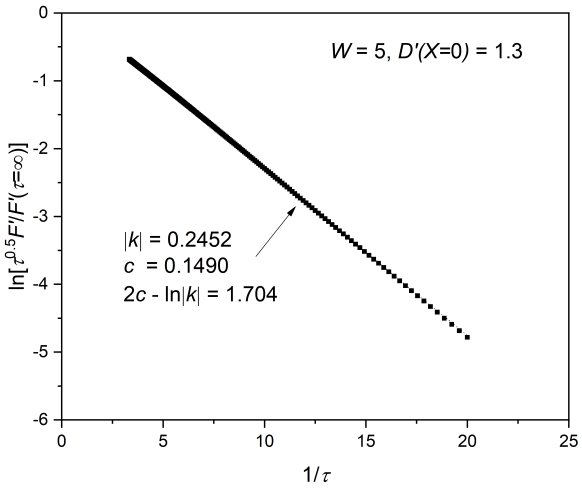

D'(X=0) = 4.5
|k| = 0.1984
c = 0.2192
2c - ln|k| = 2.056
ln[τ^0.5F'/F'(τ=∞)]
1/τ

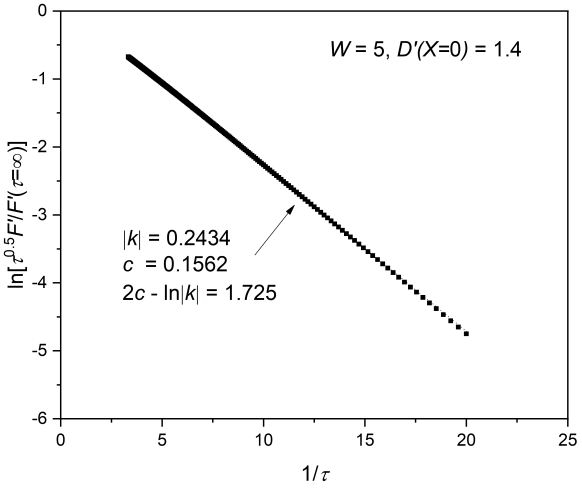
C.2 Full Model with $W = 5$

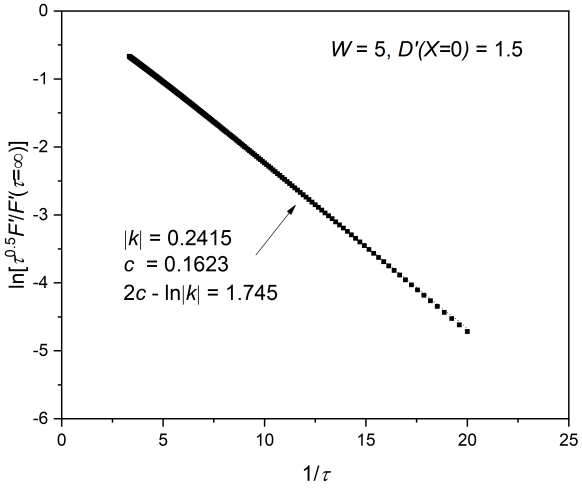


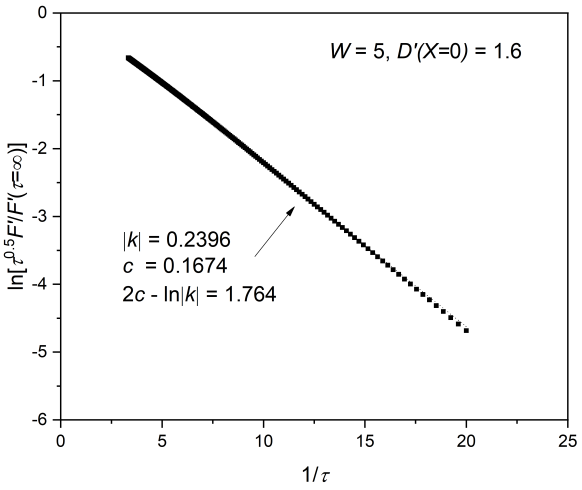


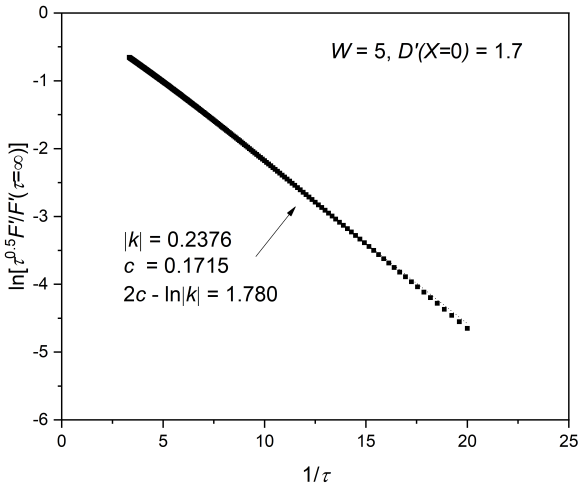


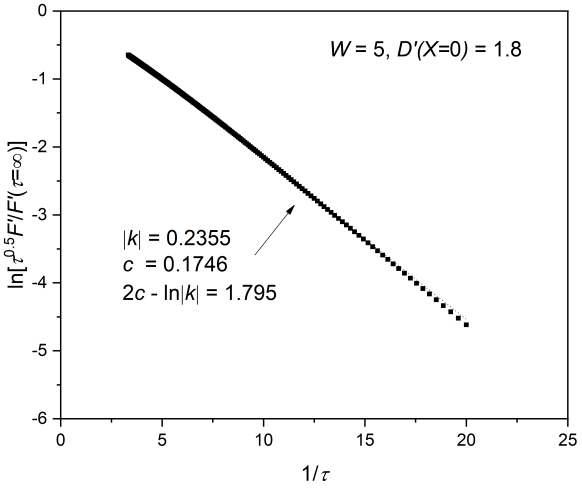


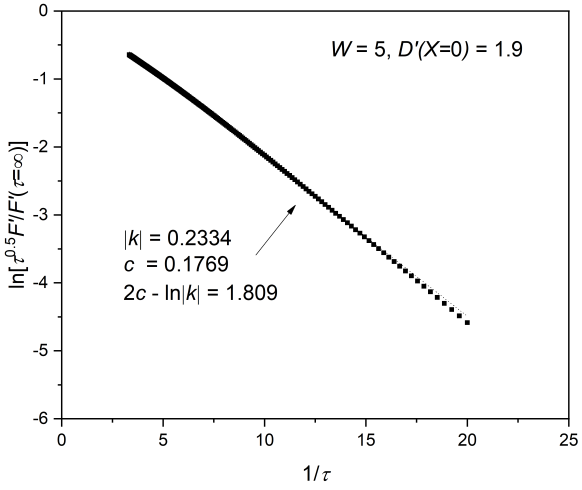


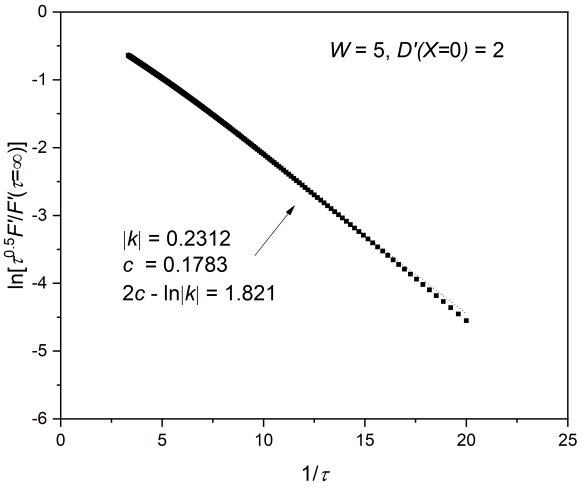


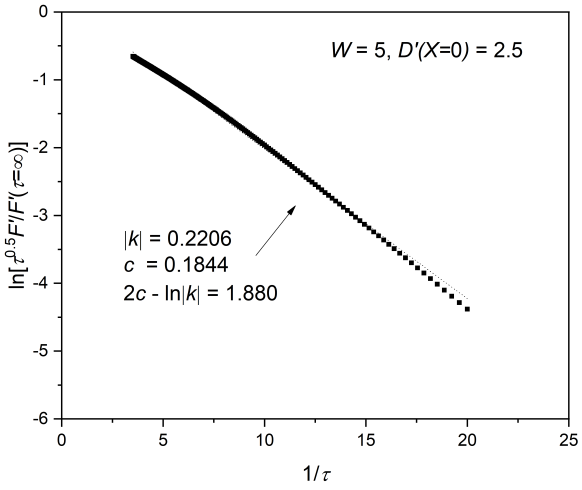

W = 5, D'(X=0) = 1.6
|k| = 0.2396
c = 0.1674
2c - ln|k| = 1.764
ln[τ^0.5F'/F'(τ=∞)]
1/τ

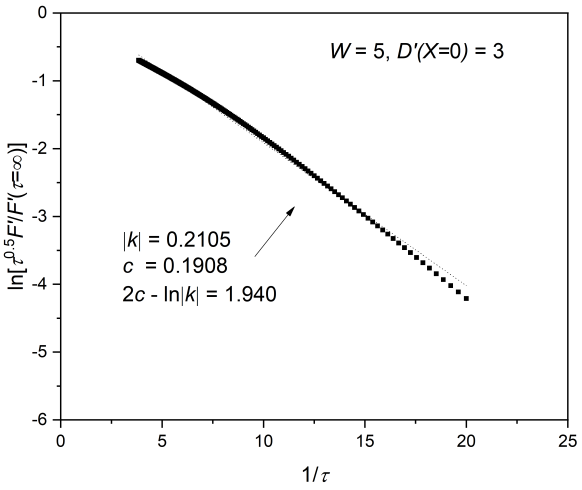

W = 5, D'(X=0) = 1.7
|k| = 0.2376
c = 0.1715
2c - ln|k| = 1.780
ln[τ^0.5F'/F'(τ=∞)]
1/τ

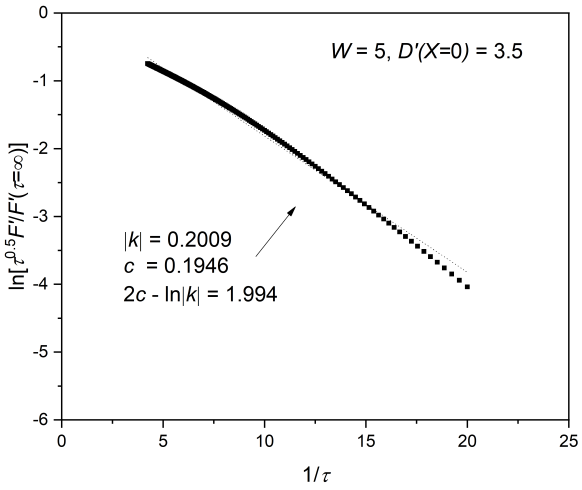

W = 5, D'(X=0) = 1.8
|k| = 0.2355
c = 0.1746
2c - ln|k| = 1.795
ln[τ^0.5F'/F'(τ=∞)]
1/τ

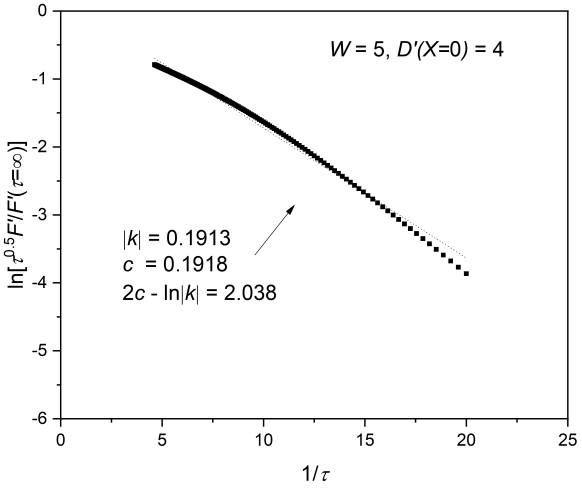

W = 5, D'(X=0) = 1.9
|k| = 0.2334
c = 0.1769
2c - ln|k| = 1.809
ln[τ^0.5F'/F'(τ=∞)]
1/τ

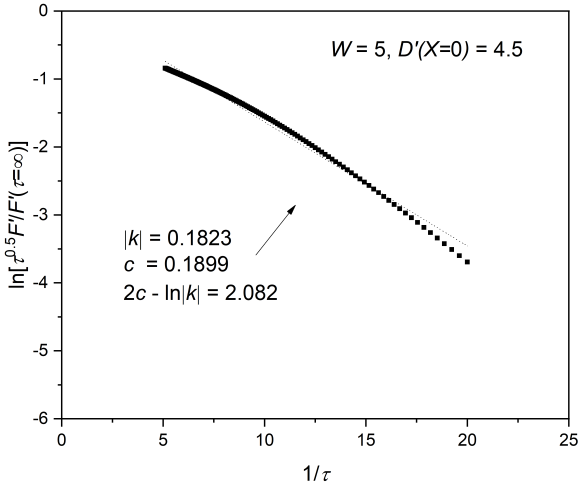

W = 5, D'(X=0) = 2
|k| = 0.2312
c = 0.1783
2c - ln|k| = 1.821
ln[τ^0.5F'/F'(τ=∞)]
1/τ


W = 5, D'(X=0) = 2.5
|k| = 0.2206
c = 0.1844
2c - ln|k| = 1.880
ln[τ^0.5F'/F'(τ=∞)]
1/τ


W = 5, D'(X=0) = 3
|k| = 0.2105
c = 0.1908
2c - ln|k| = 1.940
ln[τ^0.5 F'/F'(τ=∞)]
1/τ


W = 5, D'(X=0) = 3.5
|k| = 0.2009
c = 0.1946
2c - ln|k| = 1.994
ln[τ^0.5 F'/F'(τ=∞)]
1/τ


W = 5, D'(X=0) = 4
|k| = 0.1913
c = 0.1918
2c - ln|k| = 2.038
ln[τ^0.5 F'/F'(τ=∞)]
1/τ


W = 5, D'(X=0) = 4.5
|k| = 0.1823
c = 0.1899
2c - ln|k| = 2.082
ln[τ^0.5 F'/F'(τ=∞)]
1/τ

Appendix D

Experimental Runs Explained

Ideally, it was scheduled to carry out multiple runs with different pressures at each temperature for each type of the polymers. In fact, Run-H-5 to Run-H-8 for HDPE at 35 °C were those conducted during the first phase of the project. The progress was affected by the following factors, which are reviewed as experience for future researchers:

1) Preliminary experiments: after the rig was built and all devices were tested, a large amount of time was spent on identifying the potential problems to prevent failures during a high-pressure experiment, or determining the optimal practices to increase the operating efficiency. For instance, appropriate ways were explored on how to load and support the polymer sample in the permeation cell; the normal duration of a measurement was confirmed, so as not to spend too much time on relatively little useful data, or too little time causing a loss of important data; an optimal way was determined on how to operate the two pumps to consistently and reliably generate the high pressure as required, *etc.* In addition to the runs used for detailed analysis listed in Table 4.2, a number of preliminary runs were carried out. These were often incomplete and were used primarily for testing purposes. It will not be necessary for future researchers to undertake such a long programme of testing, troubleshooting, and familiarisation.

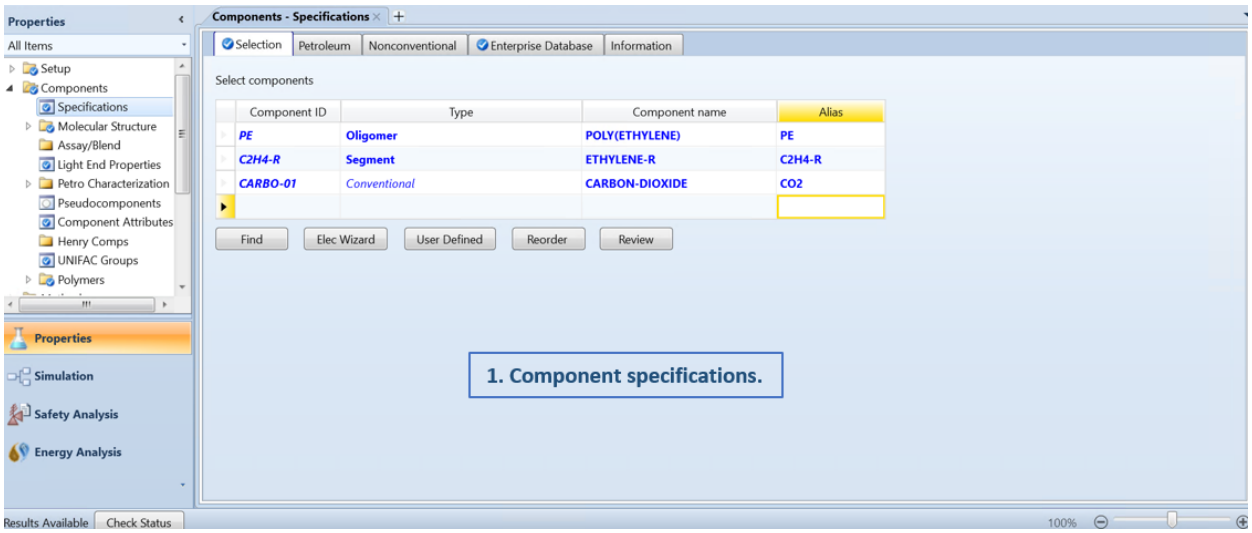
2) Operating mistakes or misoperations: given the high pressure involved and the long duration of a typical run, care and attention were required while performing the experiment.

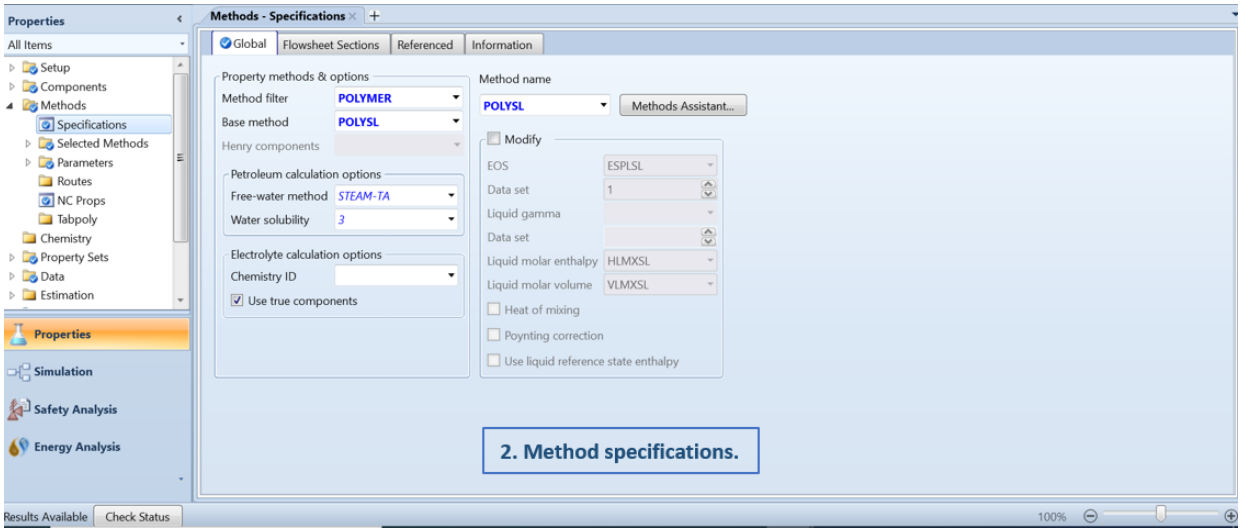
Although the safety devices implemented can securely protect the entire system in a worst case scenario when misoperations due to a lack of care occur, precious data, time and materials could be wasted. In this work, apart from the effective runs and the preliminary runs, there were also several failed runs, the data of which were not used. For example, a Sitec fitting was once tightened improperly. During the first few days, a leak was not observed when the successive experiment was operated in a low pressure range. However, after the pressure was increased to a certain higher value, the leak was identified. Consequently, the experiment was stopped, the fitting was tightened, and the run was conducted all over again. Thus, to avoid accidents or experimental failures, it is recommended to carefully check the conditions of all parts of the rig prior to a run, and to frequently examine the readings during a measurement to identify any abnormality, and to respond promptly to prevent any further loss.

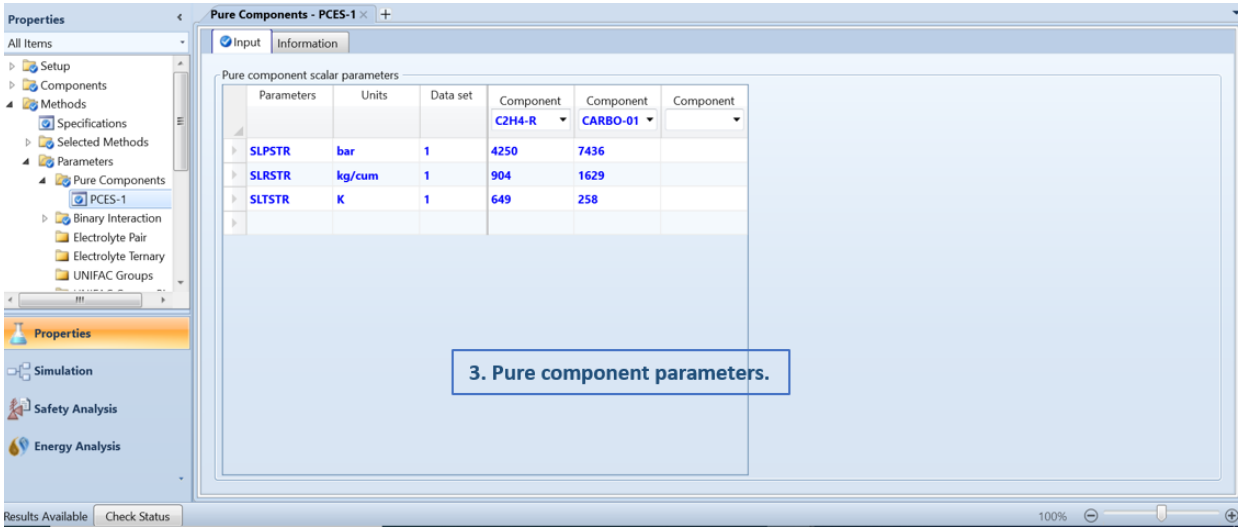
3) Disruption: it was planned to generate a set of permeation measurements for PTFE and HDPE, including repeats and comparisons between single and multiple step experiments. There was also a plan to conduct independent sorption measurements, which were dropped from this permeation project, as a result of the unexpected lockdown due to COVID-19. The lab closure allowed the development of the analytical approach and the justification behind the assumptions. This time proved to be valuable for constructing the work presented in this thesis. As work on result analysis progressed during 2020, including the work on the SL EOS, it became evident that there were inconsistencies in the measurements, in particular between Run-H-5 and the other runs conducted under the same temperature with HDPE. By this time, it was past time to begin writing up, and not suitable for conducting any further experiments. These experiments are therefore scheduled to be carried out in future projects.

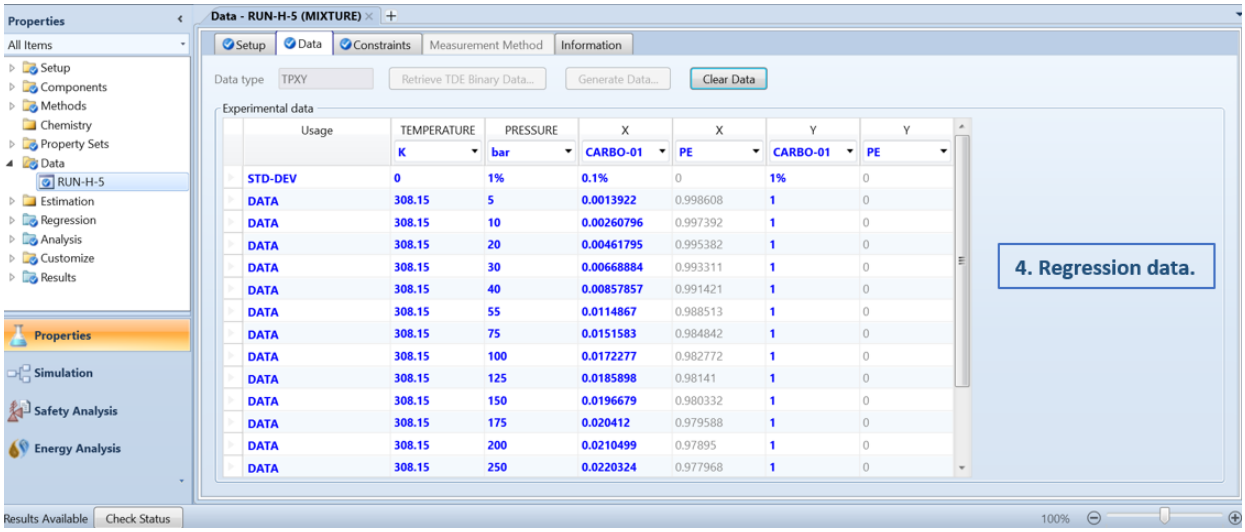
Appendix E

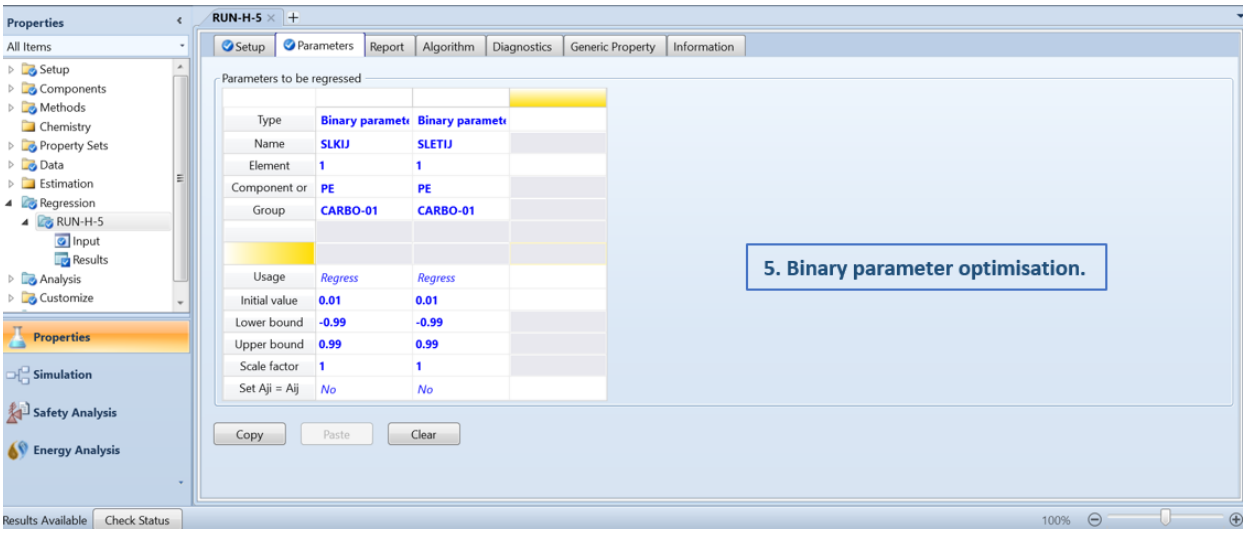
ASPEN Modelling of Solubility

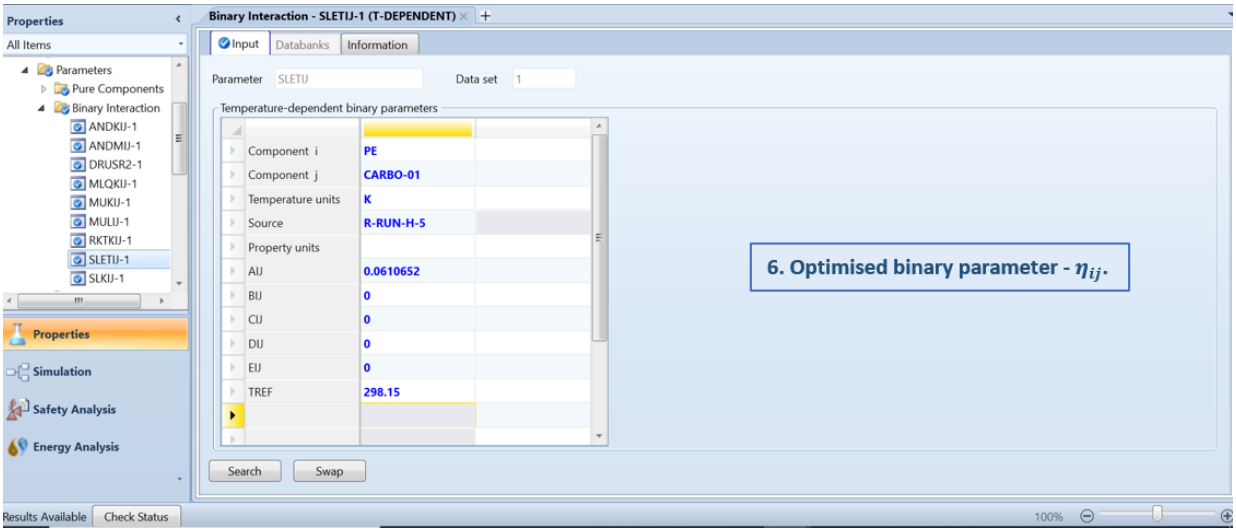


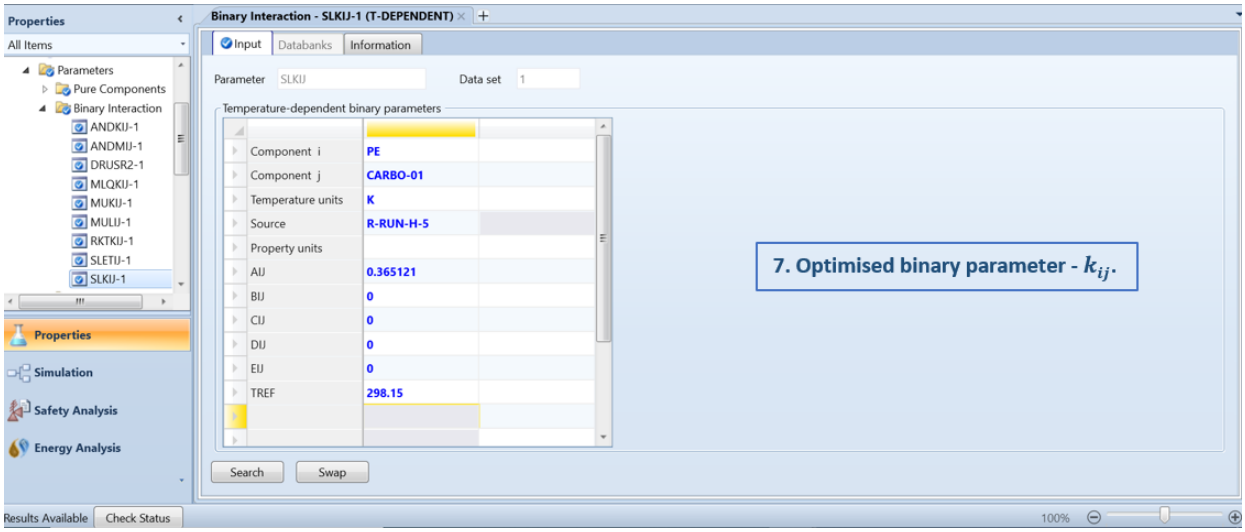


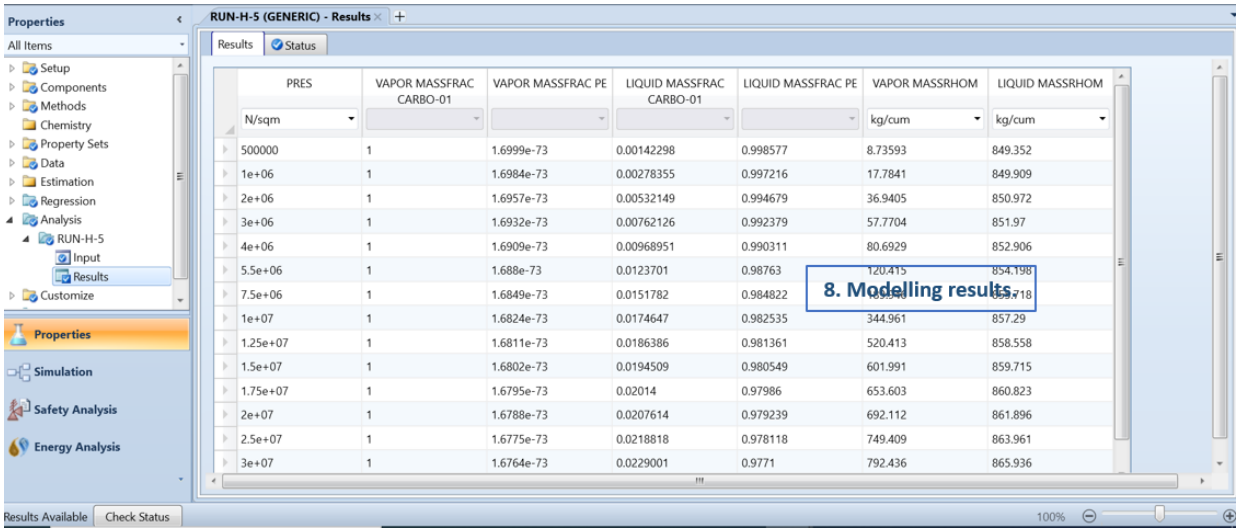

Properties
All Items
Setup
Components
Methods
Specifications
Selected Methods
Parameters
Pure Components
PCES-1
Binary Interaction
Electrolyte Pair
Electrolyte Ternary
UNIFAC Groups
Properties
Simulation
Safety Analysis
Energy Analysis
Pure Components - PCES-1
Input
Information
Pure component scalar parameters
Parameters
Units
Data set
Component
Component
Component
C2H4-R
CARBO-01
SLPSTR
bar
1
4250
7436
SLRSTR
kg/cum
1
904
1629
SLTSTR
K
1
649
258
3. Pure component parameters.
Results Available
Check Status
100%


Properties
All Items
Setup
Components
Methods
Chemistry
Property Sets
Data
RUN-H-5
Estimation
Regression
Analysis
Customize
Results
Properties
Simulation
Safety Analysis
Energy Analysis
Data - RUN-H-5 (MIXTURE)
Setup
Data
Constraints
Measurement Method
Information
Data type
TPXY
Retrieve TDE Binary Data...
Generate Data...
Clear Data
Experimental data
Usage
TEMPERATURE
PRESSURE
X
X
Y
Y
K
bar
CARBO-01
PE
CARBO-01
PE
STD-DEV 0 1% 0.1% 0 1% 0
DATA 308.15 5 0.0013922 0.998608 1 0
DATA 308.15 10 0.00260796 0.997392 1 0
DATA 308.15 20 0.00461795 0.995382 1 0
DATA 308.15 30 0.00668884 0.993311 1 0
DATA 308.15 40 0.00857857 0.991421 1 0
DATA 308.15 55 0.0114867 0.988513 1 0
DATA 308.15 75 0.0151583 0.984842 1 0
DATA 308.15 100 0.0172277 0.982772 1 0
DATA 308.15 125 0.0185898 0.98141 1 0
DATA 308.15 150 0.0196679 0.980332 1 0
DATA 308.15 175 0.020412 0.979588 1 0
DATA 308.15 200 0.0210499 0.97895 1 0
DATA 308.15 250 0.0220324 0.977968 1 0
4. Regression data.
Results Available
Check Status
100%


Properties
All Items
Setup
Components
Methods
Chemistry
Property Sets
Data
Estimation
Regression
RUN-H-5
Input
Results
Analysis
Customize
Properties
Simulation
Safety Analysis
Energy Analysis
RUN-H-5
Setup
Parameters
Report
Algorithm
Diagnostics
Generic Property
Information
Parameters to be regressed
Type Binary paramet Binary paramet
Name SLKIJ SLETIJ
Element 1 1
Component or PE PE
Group CARBO-01 CARBO-01
Usage Regress Regress
Initial value 0.01 0.01
Lower bound -0.99 -0.99
Upper bound 0.99 0.99
Scale factor 1 1
Set Aji = Aij No No
Copy
Paste
Clear
5. Binary parameter optimisation.
Results Available
Check Status
100%

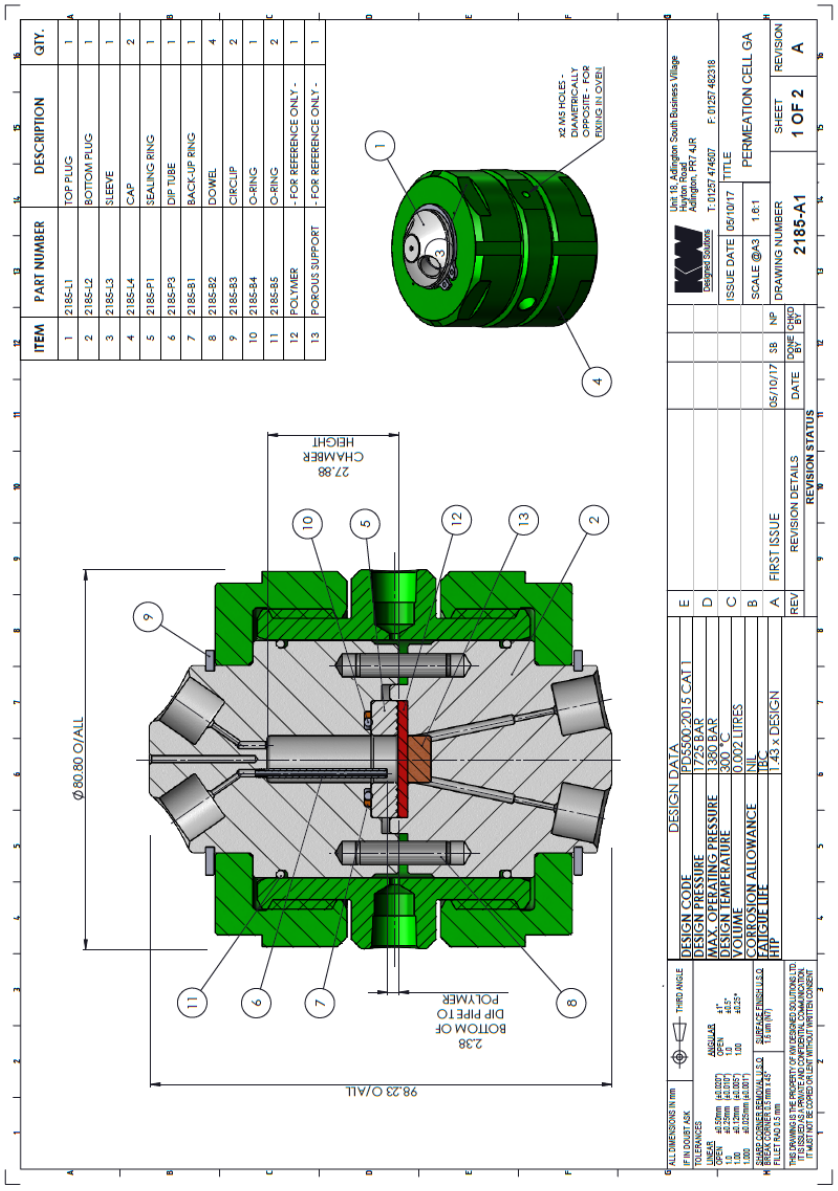

Properties
All Items
Parameters
Pure Components
Binary Interaction
ANDKIJ-1
ANDMIJ-1
DRUSR2-1
MLQKIJ-1
MUKIJ-1
MULIJ-1
RKTKIJ-1
SLETIJ-1
SLKIJ-1
Properties
Simulation
Safety Analysis
Energy Analysis
Results Available
Check Status
Binary Interaction - SLETIJ-1 (T-DEPENDENT)
Input
Databanks
Information
Parameter SLETIJ
Data set 1
Temperature-dependent binary parameters
Component i PE
Component j CARBO-01
Temperature units K
Source R-RUN-H-5
Property units
AIJ 0.0610652
BIJ 0
CIJ 0
DIJ 0
EIJ 0
TREF 298.15
Search
Swap
100%
6. Optimised binary parameter - η_{ij}.

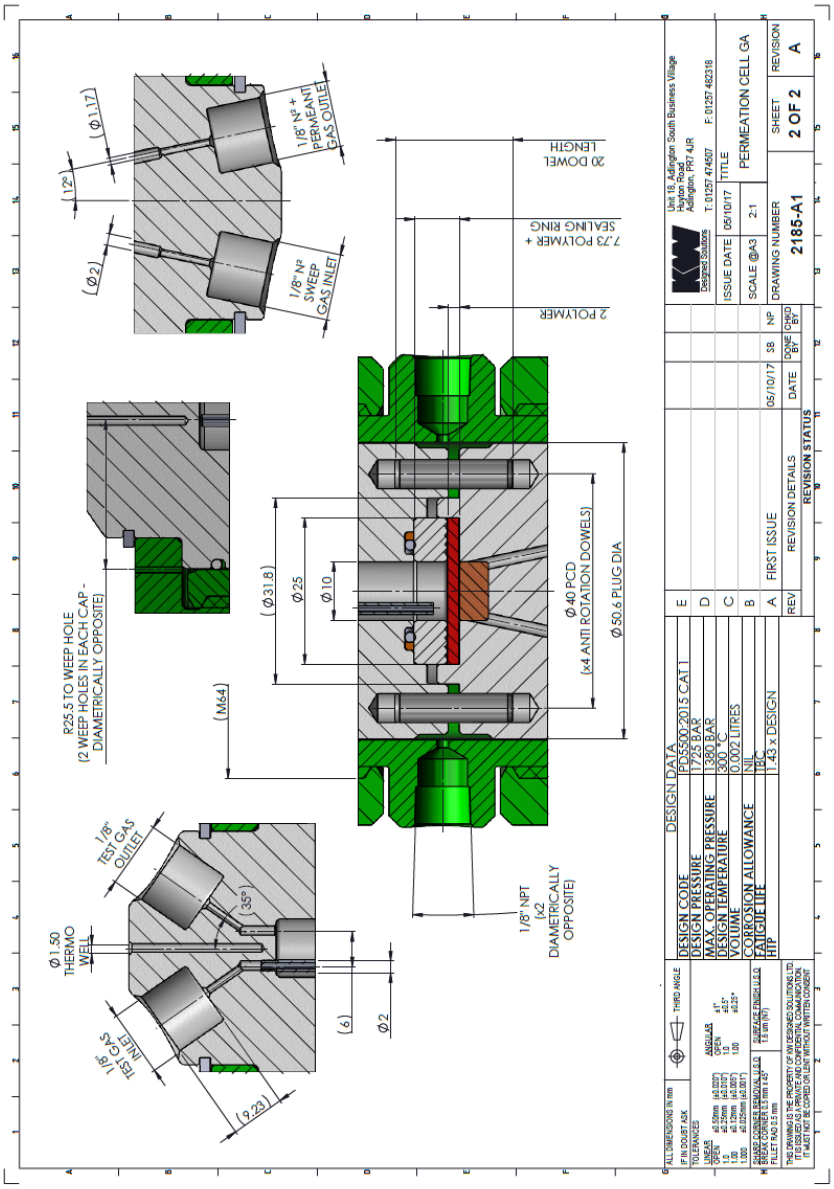

Properties
All Items
Parameters
Pure Components
Binary Interaction
ANDKIJ-1
ANDMIJ-1
DRUSR2-1
MLQKIJ-1
MUKIJ-1
MULIJ-1
RKTKIJ-1
SLETIJ-1
SLKIJ-1
Properties
Simulation
Safety Analysis
Energy Analysis
Results Available
Check Status
Binary Interaction - SLKIJ-1 (T-DEPENDENT)
Input
Databanks
Information
Parameter SLKIJ
Data set 1
Temperature-dependent binary parameters
Component i PE
Component j CARBO-01
Temperature units K
Source R-RUN-H-5
Property units
AIJ 0.365121
BIJ 0
CIJ 0
DIJ 0
EIJ 0
TREF 298.15
Search
Swap
100%
7. Optimised binary parameter - k_{ij}.


Properties
All Items
Setup
Components
Methods
Chemistry
Property Sets
Data
Estimation
Regression
Analysis
RUN-H-5
Input
Results
Customize
Properties
Simulation
Safety Analysis
Energy Analysis
Results Available
Check Status
RUN-H-5 (GENERIC) - Results
Results
Status
PRES
VAPOR MASSFRAC CARBO-01
VAPOR MASSFRAC PE
LIQUID MASSFRAC CARBO-01
LIQUID MASSFRAC PE
VAPOR MASSRHOM
LIQUID MASSRHOM
N/sqm
kg/cum
kg/cum
500000 1 1.6999e-73 0.00142298 0.998577 8.73593 849.352
1e+06 1 1.6984e-73 0.00278355 0.997216 17.7841 849.909
2e+06 1 1.6957e-73 0.00532149 0.994679 36.9405 850.972
3e+06 1 1.6932e-73 0.00762126 0.992379 57.7704 851.97
4e+06 1 1.6909e-73 0.00968951 0.990311 80.6929 852.906
5.5e+06 1 1.688e-73 0.0123701 0.98763 120.415 854.198
7.5e+06 1 1.6849e-73 0.0151782 0.984822 [illegible] 855.718
1e+07 1 1.6824e-73 0.0174647 0.982535 344.961 857.29
1.25e+07 1 1.6811e-73 0.0186386 0.981361 520.413 858.558
1.5e+07 1 1.6802e-73 0.0194509 0.980549 601.991 859.715
1.75e+07 1 1.6795e-73 0.02014 0.97986 653.603 860.823
2e+07 1 1.6788e-73 0.0207614 0.979239 692.112 861.896
2.5e+07 1 1.6775e-73 0.0218818 0.978118 749.409 863.961
3e+07 1 1.6764e-73 0.0229001 0.9771 792.436 865.936
100%
8. Modelling results.

Appendix F

Drawings of Permeation Cell




1/8" N² + PERMEANT GAS OUTLET
1/8" N² SWEEP GAS INLET
(Ø1.17)
12°
(Ø2)
30 DOWEL LENGTH
7.73 POLYMER + SEALING RING
2 POLYMER
R25.5 TO WEEP HOLE (2 WEEP HOLES IN EACH CAP - DIAMETRICALLY OPPOSITE)
(Ø31.8)
Ø25
Ø10
(M64)
Ø40 PCD (x4 ANTI ROTATION DOWELS)
Ø50.6 PLUG DIA
1/8" NPT (x2 DIAMETRICALLY OPPOSITE)
Ø1.50 THERMO WELL
1/8" TEST GAS OUTLET
35°
1/8" TEST GAS INLET
(6)
Ø2
(9.23)
DESIGN DATA
DESIGN CODE PD5500:2015 CAT 1
DESIGN PRESSURE 172.5 BAR
MAX. OPERATING PRESSURE 138.0 BAR
MAX. OUT TEMPERATURE 300°C
VOLUME 0.002 LITRES
CORROSION ALLOWANCE NIL
FATIGUE LIFE 15°C
HTP 1.43 x DESIGN
REVISION STATUS
REV REVISION DETAILS DATE DONE BY CHKD BY
A FIRST ISSUE 05/10/17 SB NP
B
C
D
E
ALL DIMENSIONS IN mm
IF IN DOUBT ASK
THIRD ANGLE
TOLERANCES
UNLESS OTHERWISE STATED
ANGULAR ±1°
OPEN ±0.5°
1.0 ±0.5mm (±0.020") 1.0 0.05
1.5 ±0.13mm (±0.005") 1.5 0.05
1.00 ±0.05mm (±0.002") 1.00 0.025
1.000 ±0.025mm (±0.001")
SURFACE FINISH 1.6 AO
1.6 um (63")
THIS DRAWING IS THE PROPERTY OF KW DEFINED SOLUTIONS LTD IT IS ISSUED AS A PRIVATE AND CONFIDENTIAL COMMUNICATION IT MUST NOT BE COPIED OR USED WITHOUT WRITTEN CONSENT
KW Defined Solutions
Unit 18, Adlington South Business Village Wigan Road Adlington, PR7 4JR
T: 01257 474507 F: 01257 482316
ISSUE DATE 05/10/17
SCALE @A3 2:1
DRAWING NUMBER 2185-A1
TITLE PERMEATION CELL GA
SHEET 2 OF 2
REVISION A

Appendix G

Access to the Data

Data underlying this thesis can be accessed at `https://data.hpc.imperial.ac.uk/resolve/?doi=9420&access=`, and used under the Creative Commons Attribution licence.

Bibliography

[1] United Nations. (2020) The race to zero emissions, and why the world depends on it. [Online]. Available: https://news.un.org/en/story/2020/12/1078612

[2] ——. (2015) Adoption of the paris agreement. [Online]. Available: http://unfccc.int/resource/docs/2015/cop21/eng/l09r01.pdf

[3] M. Darby and I. Gerretsen. (2021) Which countries have a net zero carbon goal? [Online]. Available: https://www.climatechangenews.com/2019/06/14/countries-net-zero-climate-goal/

[4] United Nations. (2021) Coronavirus global health emergency. [Online]. Available: https://www.un.org/coronavirus

[5] A. A. Olajire, "CO_2 capture and separation technologies for end-of-pipe applications – a review," *Energy*, vol. 35, no. 6, pp. 2610–2628, 2010, 7th International Conference on Sustainable Energy Technologies. [Online]. Available: https://www.sciencedirect.com/science/article/pii/S0360544210000848

[6] S. Paul, R. Shepherd, A. Bahrami, and W. Woollin, "Material selection for supercritical CO_2 transport," TWI. Newcastle: Proceeding of the International Forum on Transportation of CO2 by Pipelines, 6 2012, available at https://www.twi-global.com/technical-knowledge/published-papers/selection-of-materials-for-high-pressure-co2-transport#paul2010.

[7] ChemicaLogic. (1999) Carbon dioxide phase diagram. [Online]. Available: http://www.chemicalogic.com/Pages/DownloadPhaseDiagrams.html

[8] DNV. (2010) Offshore standard dnv-os-f101: Submarine pipeline systems. [Online]. Available: http://www.opimsoft.com/download/reference/os-f101_2010-10.pdf

[9] ZEP. (2010) The cost of CO_2 transport: post-demonstration ccs in the EU. [Online]. Available: https://www.globalccsinstitute.com/archive/hub/publications/119811/costs-co2-transport-post-demonstration-ccs-eu.pdf

[10] M. Knoope, A. Ramírez, and A. Faaij, "Investing in CO_2 transport infrastructure under uncertainty: a comparison between ships and pipelines," *International Journal of Greenhouse Gas Control*, vol. 41, pp. 174–193, 2015. [Online]. Available: https://www.sciencedirect.com/science/article/pii/S1750583615300220

[11] L. Ansaloni, B. Alcock, and T. A. Peters, "Effects of CO_2 on polymeric materials in the CO_2 transport chain: a review," *International Journal of Greenhouse Gas Control*, vol. 94, p. 102930, 2020. [Online]. Available: https://www.sciencedirect.com/science/article/pii/S1750583619305493

[12] S. M. Hesjevik, S. Olsen, and M. Seiersten, "Corrosion at high CO_2 pressure," *CORROSION 2003*, 03 2003.

[13] M. Kermani and A. Morshed, "Carbon dioxide corrosion in oil and gas production: a compendium," *Corrosion*, vol. 59, 08 2003.

[14] S. Nešić, "Key issues related to modelling of internal corrosion of oil and gas pipelines – a review," *Corrosion Science*, vol. 49, no. 12, pp. 4308–4338, 2007. [Online]. Available: https://www.sciencedirect.com/science/article/pii/S0010938X07001539

[15] R. Nyborg, *Guidelines for prediction of CO_2 corrosion in oil and gas production systems.* Institutt for energiteknikk, 2009.

[16] F. Ayello, K. J. Evans, R. Thodla, N. Sridhar *et al.*, "Effect of impurities on corrosion of steel in supercritical CO_2," *National Association of Corrosion Engineers*, 2010.

[17] B. R. Strazisar, R. R. Anderson, and C. M. White, "Degradation pathways for

monoethanolamine in a CO_2 capture facility," *Energy & Fuels*, vol. 17, no. 4, pp. 1034–1039, 2003. [Online]. Available: https://doi.org/10.1021/ef020272i

[18] A. Bello and R. O. Idem, "Pathways for the formation of products of the oxidative degradation of CO_2-loaded concentrated aqueous monoethanolamine solutions during CO_2 absorption from flue gases," *Industrial & Engineering Chemistry Research*, vol. 44, no. 4, pp. 945–969, 2005. [Online]. Available: https://doi.org/10.1021/ie049329+

[19] S. Curia, D. De Focatiis, and S. Howdle, "High-pressure rheological analysis of CO_2-induced melting point depression and viscosity reduction of poly(ε-caprolactone)," *Polymer*, vol. 69, pp. 17–24, 2015, self-Healing Polymers. [Online]. Available: https://www.sciencedirect.com/science/article/pii/S0032386115004681

[20] A. S. Michaels and H. J. Bixler, "Solubility of gases in polyethylene," *Journal of Polymer Science*, vol. 50, no. 154, pp. 393–412, 1961. [Online]. Available: https://onlinelibrary.wiley.com/doi/abs/10.1002/pol.1961.1205015411

[21] P. L. Durrill and R. G. Griskey, "Diffusion and solution of gases in thermally softened or molten polymers: Part I. development of technique and determination of data," *AIChE Journal*, vol. 12, no. 6, pp. 1147–1151, 1966. [Online]. Available: https://aiche.onlinelibrary.wiley.com/doi/abs/10.1002/aic.690120619

[22] S. A. Stern, J. T. Mullhaupt, and P. J. Gareis, "The effect of pressure on the permeation of gases and vapors through polyethylene. Usefulness of the corresponding states principle," *AIChE Journal*, vol. 15, no. 1, pp. 64–73, 1969. [Online]. Available: https://aiche.onlinelibrary.wiley.com/doi/abs/10.1002/aic.690150117

[23] W. J. Koros, D. R. Paul, and A. A. Rocha, "Carbon dioxide sorption and transport in polycarbonate," *Journal of Polymer Science: Polymer Physics Edition*, vol. 14, no. 4, pp. 687–702, 1976. [Online]. Available: https://onlinelibrary.wiley.com/doi/abs/10.1002/pol.1976.180140410

[24] R. J. Pace and A. Datyner, "Model of sorption of simple molecules in polymers," *Journal of Polymer Science: Polymer Physics Edition*, vol. 18, no. 5, pp. 1103–1124,

1980. [Online]. Available: https://onlinelibrary.wiley.com/doi/abs/10.1002/pol.1980.180180515

[25] N. Muruganandam, W. J. Koros, and D. R. Paul, "Gas sorption and transport in substituted polycarbonates," *Journal of Polymer Science Part B: Polymer Physics*, vol. 25, no. 9, pp. 1999–2026, 1987. [Online]. Available: https://onlinelibrary.wiley.com/doi/abs/10.1002/polb.1987.090250917

[26] T.-H. Kim, W. J. Koros, and G. Husk, "Temperature effects on gas permselection properties in hexafluoro aromatic polyimides," *Journal of Membrane Science*, vol. 46, no. 1, pp. 43–56, 1989. [Online]. Available: https://www.sciencedirect.com/science/article/pii/S0376738800811692

[27] R. T. Chern and C. N. Provan, "Gas-induced plasticization and the permselectivity of poly(tetrabromophenolphthalein terephthalate) to a mixture of carbon dioxide and methane," *Macromolecules*, vol. 24, no. 9, pp. 2203–2207, 1991. [Online]. Available: https://doi.org/10.1021/ma00009a011

[28] T. C. Merkel, V. I. Bondar, K. Nagai, B. D. Freeman, and I. Pinnau, "Gas sorption, diffusion, and permeation in poly(dimethylsiloxane)," *Journal of Polymer Science Part B: Polymer Physics*, vol. 38, no. 3, pp. 415–434, 2000. [Online]. Available: https://onlinelibrary.wiley.com/doi/abs/10.1002/%28SICI%291099-0488%2820000201%2938%3A3%3C415%3A%3AAID-POLB8%3E3.0.CO%3B2-Z

[29] V. I. Bondar, B. D. Freeman, and I. Pinnau, "Gas transport properties of poly(ether-b-amide) segmented block copolymers," *Journal of Polymer Science Part B: Polymer Physics*, vol. 38, no. 15, pp. 2051–2062, 2000. [Online]. Available: https://onlinelibrary.wiley.com/doi/abs/10.1002/1099-0488%2820000801%2938%3A15%3C2051%3A%3AAID-POLB100%3E3.0.CO%3B2-D

[30] H. Lin and B. D. Freeman, "Gas permeation and diffusion in cross-linked poly(ethylene glycol diacrylate)," *Macromolecules*, vol. 39, no. 10, pp. 3568–3580, 2006. [Online]. Available: https://doi.org/10.1021/ma051686o

[31] V. Wiesmet, E. Weidner, S. Behme, G. Sadowski, and W. Arlt, "Measurement and modelling of high-pressure phase equilibria in the systems polyethyleneglycol (peg)–propane, peg–nitrogen and peg–carbon dioxide," *The Journal of Supercritical Fluids*, vol. 17, no. 1, pp. 1–12, 2000. [Online]. Available: https://www.sciencedirect.com/science/article/pii/S0896844699000431

[32] Y. Sato, T. Takikawa, S. Takishima, and H. Masuoka, "Solubilities and diffusion coefficients of carbon dioxide in poly(vinyl acetate) and polystyrene," *The Journal of Supercritical Fluids*, vol. 19, no. 2, pp. 187–198, 2001. [Online]. Available: https://www.sciencedirect.com/science/article/pii/S0896844600000929

[33] Y. Sato, T. Takikawa, M. Yamane, S. Takishima, and H. Masuoka, "Solubility of carbon dioxide in ppo and ppo/ps blends," *Fluid Phase Equilibria*, vol. 194-197, pp. 847–858, 2002, proceedings of the Ninth International Conference on Properties and Phase Equilibria for Product and Process Design. [Online]. Available: https://www.sciencedirect.com/science/article/pii/S0378381201006872

[34] M. A. Jacobs, M. F. Kemmere, and J. T. Keurentjes, "Foam processing of poly(ethylene-co-vinyl acetate) rubber using supercritical carbon dioxide," *Polymer*, vol. 45, no. 22, pp. 7539–7547, 2004. [Online]. Available: https://www.sciencedirect.com/science/article/pii/S0032386104008493

[35] S. P. Nalawade, F. Picchioni, L. P. Janssen, V. E. Patil, J. T. Keurentjes, and R. Staudt, "Solubilities of sub- and supercritical carbon dioxide in polyester resins," *Polymer Engineering & Science*, vol. 46, no. 5, pp. 643–649, 2006. [Online]. Available: https://onlinelibrary.wiley.com/doi/abs/10.1002/pen.20518

[36] B. Bonavoglia, G. Storti, and M. Morbidelli, "Modeling of the sorption and swelling behavior of semicrystalline polymers in supercritical CO_2," *Industrial & Engineering Chemistry Research*, vol. 45, no. 3, pp. 1183–1200, 2006. [Online]. Available: https://doi.org/10.1021/ie050842c

[37] R. Ben-Mansour, M. Habib, O. Bamidele, M. Basha, N. Qasem, A. Peedikakkal,

T. Laoui, and M. Ali, "Carbon capture by physical adsorption: Materials, experimental investigations and numerical modeling and simulations – a review," *Applied Energy*, vol. 161, pp. 225–255, 2016. [Online]. Available: https://www.sciencedirect.com/science/article/pii/S0306261915012386

[38] G. T. Rochelle, "Amine scrubbing for CO_2 capture," *Science*, vol. 325, no. 5948, pp. 1652–1654, 2009. [Online]. Available: https://science.sciencemag.org/content/325/5948/1652

[39] R. Khalilpour, K. Mumford, H. Zhai, A. Abbas, G. Stevens, and E. S. Rubin, "Membrane-based carbon capture from flue gas: a review," *Journal of Cleaner Production*, vol. 103, pp. 286–300, 2015, carbon Emissions Reduction: Policies, Technologies, Monitoring, Assessment and Modeling. [Online]. Available: https://www.sciencedirect.com/science/article/pii/S0959652614010920

[40] R. Sabouni, H. Kazemian, and S. Rohani, "Carbon dioxide capturing technologies: a review focusing on metal organic framework materials (mofs)," *Environmental Science and Pollution Research*, vol. 21, no. 8, pp. 5427–5449, 2014.

[41] L.-S. Fan, L. Zeng, W. Wang, and S. Luo, "Chemical looping processes for CO_2 capture and carbonaceous fuel conversion – prospect and opportunity," *Energy Environ. Sci.*, vol. 5, pp. 7254–7280, 2012. [Online]. Available: http://dx.doi.org/10.1039/C2EE03198A

[42] B. Wetenhall, H. Aghajani, H. Chalmers, S. Benson, M.-C. Ferrari, J. Li, J. Race, P. Singh, and J. Davison, "Impact of CO_2 impurity on CO_2 compression, liquefaction and transportation," *Energy Procedia*, vol. 63, pp. 2764–2778, 2014, 12th International Conference on Greenhouse Gas Control Technologies, GHGT-12. [Online]. Available: https://www.sciencedirect.com/science/article/pii/S1876610214021146

[43] R. W. Baker, *Membrane technology and applications*. John Wiley & Sons, 2012.

[44] X. He and M.-B. Hägg, "Membranes for environmentally friendly energy processes," *Membranes*, vol. 2, no. 4, pp. 706–726, 2012. [Online]. Available: https://www.mdpi.com/2077-0375/2/4/706

[45] X. He, "A review of material development in the field of carbon capture and the application of membrane-based processes in power plants and energy-intensive industries," *Energy, Sustainability and Society*, vol. 8, 11 2018.

[46] J. D. Seader, E. J. Henley, and D. K. Roper, *Separation process principles*. John Wiley & Sons, 1998, vol. 25.

[47] R. Bredesen, K. Jordal, and O. Bolland, "High-temperature membranes in power generation with CO_2 capture," *Chemical Engineering and Processing: Process Intensification*, vol. 43, no. 9, pp. 1129–1158, 2004, special Issue on Membrane Reactors. [Online]. Available: https://www.sciencedirect.com/science/article/pii/S025527010400056X

[48] P. Bernardo, E. Drioli, and G. Golemme, "Membrane gas separation: A review/state of the art," *Industrial & Engineering Chemistry Research*, vol. 48, no. 10, pp. 4638–4663, 2009. [Online]. Available: https://doi.org/10.1021/ie8019032

[49] D. Paul and Y. Yampol'skii, *Polymeric gas separation membranes*. Taylor & Francis, 1993. [Online]. Available: https://books.google.co.in/books?id=2U9MqMG7cwkC

[50] L. M. Robeson, "The upper bound revisited," *Journal of Membrane Science*, vol. 320, no. 1, pp. 390–400, 2008. [Online]. Available: https://www.sciencedirect.com/science/article/pii/S0376738808003347

[51] M. Halseid, A. Dugstad, and B. Morland, "Corrosion and bulk phase reactions in CO_2 transport pipelines with impurities: Review of recent published studies," *Energy Procedia*, vol. 63, pp. 2557–2569, 2014, 12th International Conference on Greenhouse Gas Control Technologies, GHGT-12. [Online]. Available: https://www.sciencedirect.com/science/article/pii/S1876610214020931

[52] M. Mohitpour, P. Seevam, K. K. Botros, B. Rothwell, and C. Ennis, *Pipeline transportation of carbon dioxide containing impurities*. ASME Press, 01 2012. [Online]. Available: https://doi.org/10.1115/1.859834

[53] R. Thodla, A. Francois, and N. Sridhar, "Materials performance in supercritical CO_2 environments," in *CORROSION 2009*. OnePetro, 2009.

[54] I. S. Cole, P. Corrigan, S. Sim, and N. Birbilis, "Corrosion of pipelines used for CO_2 transport in ccs: Is it a real problem?" *International Journal of Greenhouse Gas Control*, vol. 5, no. 4, pp. 749–756, 2011. [Online]. Available: https://www.sciencedirect.com/science/article/pii/S1750583611000703

[55] S. Sim, I. Cole, F. Bocher, P. Corrigan, R. Gamage, N. Ukwattage, and N. Birbilis, "Investigating the effect of salt and acid impurities in supercritical CO_2 as relevant to the corrosion of carbon capture and storage pipelines," *International Journal of Greenhouse Gas Control*, vol. 17, pp. 534–541, 2013. [Online]. Available: https://www.sciencedirect.com/science/article/pii/S1750583613002612

[56] P. A. Schweitzer *et al.*, *Corrosion of polymers and elastomers*. CRC Press, 2006.

[57] T. C. Merkel and L. G. Toy, "Comparison of hydrogen sulfide transport properties in fluorinated and nonfluorinated polymers," *Macromolecules*, vol. 39, no. 22, pp. 7591–7600, 2006. [Online]. Available: https://doi.org/10.1021/ma061072z

[58] P. Noothout, F. Wiersma, O. Hurtado, D. Macdonald, J. Kemper, and K. van Alphen, "CO_2 pipeline infrastructure – lessons learnt," *Energy Procedia*, vol. 63, pp. 2481–2492, 2014, 12th International Conference on Greenhouse Gas Control Technologies, GHGT-12. [Online]. Available: https://www.sciencedirect.com/science/article/pii/S1876610214020864

[59] M. E. Parker, J. P. Meyer, and S. R. Meadows, "Carbon dioxide enhanced oil recovery injection operations technologies (poster presentation)," *Energy Procedia*, vol. 1, no. 1, pp. 3141–3148, 2009, greenhouse Gas Control Technologies 9. [Online]. Available: https://www.sciencedirect.com/science/article/pii/S1876610209007395

[60] J. Mark, *Physical properties of polymers handbook*. Woodbury, N.Y: AIP Press, 1996.

[61] Polymerdatabase. (2017) Thermo-physical properties: Calculated data. [Online]. Available: https://polymerdatabase.com/polymers/polytetrafluoroethylene.html

[62] G. Allen, G. Gee, D. Mangaraj, D. Sims, and G. J. Wilson, "Intermolecular forces and chain flexibilities in polymers: II. internal pressures of polymers," *Polymer*, vol. 1, pp.

467–476, 1960. [Online]. Available: https://www.sciencedirect.com/science/article/pii/0032386160900628

[63] R. A. Hayes, "The relationship between glass temperature, molar cohesion, and polymer structure," *Journal of Applied Polymer Science*, vol. 5, no. 15, pp. 318–321, 1961. [Online]. Available: https://onlinelibrary.wiley.com/doi/abs/10.1002/app.1961.070051511

[64] R. H. Schuster, H. M. Issel, and V. Peterseim, "Selective interactions in elastomers, a base for compatibility and polymer-filler interactions," *Rubber Chemistry and Technology*, vol. 69, no. 5, p. 769–780, 11 1996.

[65] R. Campion, B. Thomson, and H. J.A., "Elastomers for fluid containment in offshore oil and gas production: Guidelines and review," MERL Ltd, Tamworth Road, Hertford, Tech. Rep., 2005, available at https://www.hse.gov.uk/research/rrpdf/rr320.pdf.

[66] A. Bottino, G. Capannelli, S. Munari, and A. Turturro, "Solubility parameters of poly(vinylidene fluoride)," *Journal of Polymer Science Part B: Polymer Physics*, vol. 26, no. 4, pp. 785–794, 1988. [Online]. Available: https://onlinelibrary.wiley.com/doi/abs/10.1002/polb.1988.090260405

[67] A. F. Barton, *CRC handbook of solubility parameters and other cohesion parameters*. Routledge, 2017.

[68] L. Williams, *Hansen solubility parameters: a user's handbook*, 2nd ed. CRC press, 2007, ch. 10, pp. 177–201.

[69] Chemline Plastics. (2019) Chemical resistance guide. [Online]. Available: https://www.chemline.com/media/Chemline-Plastics-chemical-resistance-guide.pdf

[70] Fisher Scientific. (2021) Chemical resistance of plastics. [Online]. Available: https://www.fishersci.co.uk/gb/en/scientific-products/technical-tools/chemical-resistance-plastics.html

[71] Nylacast. (2021) Chemical resistance table. [Online]. Available: https://www.nylacast.com/wp-content/uploads/2019/04/NylacastChemicalResistanceTable19.pdf

[72] S. Ebnesajjad, "17 - chemical properties of fluoropolymers—polytetrafluoroethylene and polychlorotrifluoroethylene," in *Fluoroplastics (Second Edition)*, second edition ed., S. Ebnesajjad, Ed. Oxford: William Andrew Publishing, 2015, vol. 1, pp. 382–395. [Online]. Available: https://www.sciencedirect.com/science/article/pii/B9781455731992000173

[73] P. Mallick, "5 - thermoplastics and thermoplastic–matrix composites for lightweight automotive structures," in *Materials, Design and Manufacturing for Lightweight Vehicles*, ser. Woodhead Publishing Series in Composites Science and Engineering, P. Mallick, Ed. Woodhead Publishing, 2010, pp. 174–207. [Online]. Available: https://www.sciencedirect.com/science/article/pii/B9781845694630500055

[74] L. W. McKeen, "10 - fluoropolymers," in *The effect of UV light and weather on plastics and elastomers (third edition)*, third edition ed., ser. Plastics Design Library, L. W. McKeen, Ed. Boston: William Andrew Publishing, 2013, pp. 243–269. [Online]. Available: https://www.sciencedirect.com/science/article/pii/B9781455728510000104

[75] C. Vasile, *Handbook of polyolefins*. CRC Press, 2000.

[76] S. Selke and R. Hernandez, "Packaging: Polymers for containers," in *Encyclopedia of Materials: Science and Technology*, K. J. Buschow, R. W. Cahn, M. C. Flemings, B. Ilschner, E. J. Kramer, S. Mahajan, and P. Veyssière, Eds. Oxford: Elsevier, 2001, pp. 6646–6652. [Online]. Available: https://www.sciencedirect.com/science/article/pii/B008043152601175X

[77] J. Wijmans and R. Baker, "The solution-diffusion model: A review," *Journal of Membrane Science*, vol. 107, no. 1, pp. 1–21, 1995. [Online]. Available: https://www.sciencedirect.com/science/article/pii/037673889500102I

[78] D. R. Paul, "Further comments on the relation between hydraulic permeation and diffusion," *Journal of Polymer Science: Polymer Physics Edition*, vol. 12, no. 6, pp. 1221–1230, 1974. [Online]. Available: https://onlinelibrary.wiley.com/doi/abs/10.1002/pol.1974.180120618

[79] M. Klopffer and B. Flaconnèche, "Transport properties of gases in polymers: Bibliographic review," *Oil & Gas Science and Technology – Rev. IFP*, vol. 56, pp. 223–244, 05 2001.

[80] J. Crank and G. Park, *Diffusion in polymers*. London: Academic Press, 1968.

[81] T. Naylor, *Comprehensive polymer science. Vol.2, Polymer properties : the synthesis, characterization, reactions & applications of polymers*. Pergamon, 1989, ch. 20, pp. 643–668.

[82] H. A. Daynes and S. W. J. Smith, "The process of diffusion through a rubber membrane," *Proceedings of the Royal Society of London. Series A, Containing Papers of a Mathematical and Physical Character*, vol. 97, no. 685, pp. 286–307, 1920. [Online]. Available: https://royalsocietypublishing.org/doi/abs/10.1098/rspa.1920.0034

[83] R. M. Barrer, *Diffusion in and through solids*. Cambridge: Cambridge University Press, 1951.

[84] J. Crank, *The mathematics of diffusion*, 2nd ed. Oxford: Clarendon Press, 1975.

[85] P. Ghosh, "Thermal transitions in polymers," 2007.

[86] D. A. Edwards, "Non-fickian diffusion in thin polymer films," *Journal of Polymer Science Part B: Polymer Physics*, vol. 34, no. 5, pp. 981–997, 1996. [Online]. Available: https://onlinelibrary.wiley.com/doi/abs/10.1002/%28SICI%291099-0488%2819960415%2934%3A5%3C981%3A%3AAID-POLB16%3E3.0.CO%3B2-7

[87] T. Alfrey, E. F. Gurnee, and W. G. Lloyd, "Diffusion in glassy polymers," *Journal of Polymer Science Part C: Polymer Symposia*, vol. 12, no. 1, pp. 249–261, 1966. [Online]. Available: https://onlinelibrary.wiley.com/doi/abs/10.1002/polc.5070120119

[88] M. L. Huggins, "Solutions of long chain compounds," *The Journal of Chemical Physics*, vol. 9, no. 5, pp. 440–440, 1941. [Online]. Available: https://doi.org/10.1063/1.1750930

[89] P. J. Flory, "Thermodynamics of high polymer solutions," *The Journal of Chemical Physics*, vol. 9, no. 8, pp. 660–660, 1941. [Online]. Available: https://doi.org/10.1063/1.1750971

[90] ——, "Thermodynamics of high polymer solutions," *The Journal of Chemical Physics*, vol. 10, no. 1, pp. 51–61, 1942. [Online]. Available: https://doi.org/10.1063/1.1723621

[91] C. Hinz, "Description of sorption data with isotherm equations," *Geoderma*, vol. 99, no. 3, pp. 225–243, 2001. [Online]. Available: https://www.sciencedirect.com/science/article/pii/S0016706100000719

[92] S. Sohn and D. Kim, "Modification of langmuir isotherm in solution systems—definition and utilization of concentration dependent factor," *Chemosphere*, vol. 58, no. 1, pp. 115–123, 2005. [Online]. Available: https://www.sciencedirect.com/science/article/pii/S0045653504007520

[93] V. I. Bondar, Y. Kamiya, and Y. P. Yampol'skii, "On pressure dependence of the parameters of the dual-mode sorption model," *Journal of Polymer Science Part B: Polymer Physics*, vol. 34, no. 2, pp. 369–378, 1996. [Online]. Available: https://onlinelibrary.wiley.com/doi/abs/10.1002/%28SICI%291099-0488%2819960130%2934%3A2%3C369%3A%3AAID-POLB18%3E3.0.CO%3B2-H

[94] R. Paterson, Y. Yampol'skii, P. G. T. Fogg, A. Bokarev, V. Bondar, O. Ilinich, and S. Shishatskii, "Iupac-nist solubility data series 70. solubility of gases in glassy polymers," *Journal of Physical and Chemical Reference Data*, vol. 28, no. 5, pp. 1255–1450, 1999. [Online]. Available: https://doi.org/10.1063/1.556050

[95] P. J. Flory and J. Rehner, "Statistical mechanics of cross-linked polymer networks ii. swelling," *The Journal of Chemical Physics*, vol. 11, no. 11, pp. 521–526, 1943. [Online]. Available: https://doi.org/10.1063/1.1723792

[96] P. J. Flory, "Statistical mechanics of swelling of network structures," *The Journal of Chemical Physics*, vol. 18, no. 1, pp. 108–111, 1950. [Online]. Available: https://doi.org/10.1063/1.1747424

[97] A. Singh, B. D. Freeman, and I. Pinnau, "Pure and mixed gas acetone/nitrogen permeation properties of polydimethylsiloxane [pdms]," *Journal of Polymer Science Part B: Polymer Physics*, vol. 36, no. 2, pp. 289–301, 1998. [Online]. Available: https://onlinelibrary.wiley.com/doi/abs/10.1002/%28SICI%291099-0488%2819980130%2936%3A2%3C289%3A%3AAID-POLB8%3E3.0.CO%3B2-M

[98] R. J. Hernandez, J. R. Giacin, and E. A. Grulke, "The sorption of water vapor by an amorphous polyamide," *Journal of Membrane Science*, vol. 65, no. 1, pp. 187–199, 1992. [Online]. Available: https://www.sciencedirect.com/science/article/pii/0376738892870645

[99] R. J. Hernandez and R. Gavara, "Sorption and transport of water in nylon-6 films," *Journal of Polymer Science Part B: Polymer Physics*, vol. 32, no. 14, pp. 2367–2374, 1994. [Online]. Available: https://onlinelibrary.wiley.com/doi/abs/10.1002/polb.1994.090321407

[100] R. J. Hernandez, "Effect of water vapor on the transport properties of oxygen through polyamide packaging materials," *Journal of Food Engineering*, vol. 22, no. 1, pp. 495–507, 1994. [Online]. Available: https://www.sciencedirect.com/science/article/pii/0260877494900507

[101] E. Favre, Q. T. Nguyen, P. Schaetzel, R. Clément, and J. Néel, "Sorption of organic solvents into dense silicone membranes. part 1.—validity and limitations of flory–huggins and related theories," *J. Chem. Soc., Faraday Trans.*, vol. 89, pp. 4339–4346, 1993. [Online]. Available: http://dx.doi.org/10.1039/FT9938904339

[102] S. Matteucci, Y. Yampolskii, B. D. Freeman, and I. Pinnau, *Transport of gases and vapors in glassy and rubbery polymers.* John Wiley & Sons, Ltd, 2006, ch. 1, pp. 1–47. [Online]. Available: https://onlinelibrary.wiley.com/doi/abs/10.1002/047002903X.ch1

[103] I. C. Sanchez and R. H. Lacombe, "An elementary molecular theory of classical fluids. pure fluids," *The Journal of Physical Chemistry*, vol. 80, no. 21, pp. 2352–2362, 1976.

[104] ——, "Statistical thermodynamics of polymer solutions," *Macromolecules*, vol. 11, no. 6, pp. 1145–1156, 1978.

[105] M. G. De Angelis, T. C. Merkel, V. I. Bondar, B. D. Freeman, F. Doghieri, and G. C. Sarti, "Hydrocarbon and fluorocarbon solubility and dilation in poly(dimethylsiloxane): Comparison of experimental data with predictions of the sanchez–lacombe equation of state," *Journal of Polymer Science Part B: Polymer Physics*, vol. 37, no. 21, pp. 3011–3026, 1999.

[106] Y. Huang and D. Paul, "Physical aging of thin glassy polymer films monitored by gas permeability," *Polymer*, vol. 45, no. 25, pp. 8377–8393, 2004. [Online]. Available: https://www.sciencedirect.com/science/article/pii/S0032386104009991

[107] H. Fujita, "Diffusion in polymer-diluent systems," in *Fortschritte Der Hochpolymeren-Forschung*. Berlin, Heidelberg: Springer Berlin Heidelberg, 1961, pp. 1–47.

[108] H. Fujita and E. Maekawa, "Viscosity behavior of the system polymethyl acrylate and diethyl phthalate over the complete range of composition," *The Journal of Physical Chemistry*, vol. 66, no. 6, pp. 1053–1058, 1962. [Online]. Available: https://doi.org/10.1021/j100812a020

[109] J. S. Vrentas and J. L. Duda, "Diffusion in polymer—solvent systems. i. reexamination of the free-volume theory," *Journal of Polymer Science: Polymer Physics Edition*, vol. 15, no. 3, pp. 403–416, 1977. [Online]. Available: https://onlinelibrary.wiley.com/doi/abs/10.1002/pol.1977.180150302

[110] ——, "Diffusion in polymer–solvent systems. ii. a predictive theory for the dependence of diffusion coefficients on temperature, concentration, and molecular weight," *Journal of Polymer Science: Polymer Physics Edition*, vol. 15, no. 3, pp. 417–439, 1977. [Online]. Available: https://onlinelibrary.wiley.com/doi/abs/10.1002/pol.1977.180150303

[111] ——, "Molecular diffusion in polymer solutions," *AIChE Journal*, vol. 25, no. 1, pp. 1–24, 1979. [Online]. Available: https://aiche.onlinelibrary.wiley.com/doi/abs/10.1002/aic.690250102

[112] A. K. Doolittle, "Studies in newtonian flow. ii. the dependence of the viscosity of liquids on free-space," *Journal of Applied Physics*, vol. 22, no. 12, pp. 1471–1475, 1951. [Online]. Available: https://doi.org/10.1063/1.1699894

[113] ——, "Studies in newtonian flow. iii. the dependence of the viscosity of liquids on molecular weight and free space (in homologous series)," *Journal of Applied Physics*, vol. 23, no. 2, pp. 236–239, 1952. [Online]. Available: https://doi.org/10.1063/1.1702182

[114] H. Fujita and A. Kishimoto, "Interpretation of viscosity data for concentrated polymer solutions," *The Journal of Chemical Physics*, vol. 34, no. 2, pp. 393–398, 1961. [Online]. Available: https://doi.org/10.1063/1.1700962

[115] S. S. Kulkarni and S. A. Stern, "The diffusion of CO_2, CH_4, C_2H_4, and C_3H_8 in polyethylene at elevated pressures," *Journal of Polymer Science: Polymer Physics Edition*, vol. 21, no. 3, pp. 441–465, 1983. [Online]. Available: https://onlinelibrary.wiley.com/doi/abs/10.1002/pol.1983.180210310

[116] M. H. Cohen and D. Turnbull, "Molecular transport in liquids and glasses," *The Journal of Chemical Physics*, vol. 31, no. 5, pp. 1164–1169, 1959. [Online]. Available: https://doi.org/10.1063/1.1730566

[117] H. Fujita, "Notes on free volume theories," *Polymer Journal*, vol. 23, pp. 1499–1506, 1991.

[118] ——, "Comments on free volume theories for polymer—solvent systems," *Chemical Engineering Science*, vol. 48, no. 17, pp. 3037–3042, 1993. [Online]. Available: https://www.sciencedirect.com/science/article/pii/000925099380169Q

[119] L. S. Mossner and E. A. Grulke, "Effects of thermodynamic models on the predictions of free volume diffusion theory for concentrated polymer solutions," *Journal of Applied Polymer Science*, vol. 35, no. 4, pp. 923–936, 1988. [Online]. Available: https://onlinelibrary.wiley.com/doi/abs/10.1002/app.1988.070350408

[120] J. S. Yoon, K. L. Kim, K. H. Lee, and S. J. Maing, "Diffusion coefficient and solubility of vinyl acetate molecules in poly(vinyl acetate) matrices," *European*

Polymer Journal, vol. 28, no. 7, pp. 713–716, 1992. [Online]. Available: https://www.sciencedirect.com/science/article/pii/001430579290072A

[121] S. U. Hong, "Prediction of polymer/solvent diffusion behavior using free-volume theory," *Industrial & Engineering Chemistry Research*, vol. 34, no. 7, pp. 2536–2544, 1995. [Online]. Available: https://doi.org/10.1021/ie00046a040

[122] C. J. Guo, D. De Kee, and B. Harrison, "Free volume model and diffusion of organic solvents in natural rubber," *Journal of Applied Polymer Science*, vol. 56, no. 7, pp. 817–822, 1995. [Online]. Available: https://onlinelibrary.wiley.com/doi/abs/10.1002/app.1995.070560706

[123] S. U. Hong, "Predicting ability of free-volume theory for solvent self-diffusion coefficients in rubbers," *Journal of Applied Polymer Science*, vol. 61, no. 5, pp. 833–841, 1996. [Online]. Available: https://onlinelibrary.wiley.com/doi/abs/10.1002/%28SICI%291097-4628%2819960801%2961%3A5%3C833%3A%3AAID-APP16%3E3.0.CO%3B2-Y

[124] M. Tonge and R. Gilbert, "Testing free volume theory for penetrant diffusion in rubbery polymers," *Polymer*, vol. 42, no. 4, pp. 1393–1405, 2001. [Online]. Available: https://www.sciencedirect.com/science/article/pii/S0032386100005188

[125] G. Mauviel and E. Favre, "Free-volume theory applied to diffusion in liquids: A critical analysis," *Industrial & Engineering Chemistry Research*, vol. 43, no. 21, pp. 6847–6854, 2004. [Online]. Available: https://doi.org/10.1021/ie049719w

[126] W. Schabel, P. Scharfer, M. Kind, and I. Mamaliga, "Sorption and diffusion measurements in ternary polymer–solvent–solvent systems by means of a magnetic suspension balance—experimental methods and correlations with a modified flory–huggins and free-volume theory," *Chemical Engineering Science*, vol. 62, no. 8, pp. 2254–2266, 2007. [Online]. Available: https://www.sciencedirect.com/science/article/pii/S0009250907000310

[127] A. Mafi, A. Raisi, M. Hatam, and A. Aroujalian, "A comparative study on the free volume theories for diffusivity through polymeric membrane in pervaporation

process," *Journal of Applied Polymer Science*, vol. 131, no. 15, 2014. [Online]. Available: https://onlinelibrary.wiley.com/doi/abs/10.1002/app.40581

[128] R. P. Danner, "Measuring and correlating diffusivity in polymer–solvent systems using free-volume theory," *Fluid Phase Equilibria*, vol. 362, pp. 19–27, 2014, special Issue on PPEPPD 2013. [Online]. Available: https://www.sciencedirect.com/science/article/pii/S0378381213004524

[129] A. Chalykh, L. Titkova, A. Malkin, V. Dreval', and I. Pronin, "Comparative investigation of the diffusion and viscosity behaviour of polybutadiene solutions," *Polymer Science U.S.S.R.*, vol. 16, no. 8, pp. 2134–2144, 1974. [Online]. Available: https://www.sciencedirect.com/science/article/pii/003239507490286X

[130] T. Kinoshita, N. Okazaki, A. Takizawa, and Y. Tsujita, "Sorption and permeation of poly(n-hexyl l-glutamate) — organic solvent systems," *Polymer*, vol. 20, no. 7, pp. 791–796, 1979. [Online]. Available: https://www.sciencedirect.com/science/article/pii/0032386179901125

[131] G. Fleischer, "Temperature dependence of self diffusion of polystyrene and polyethylene in the melt. an interpretation in terms of the free volume theory," *Polymer bulletin (Berlin, Germany)*, vol. 11, no. 1, pp. 75–80, 1984.

[132] J. W. Rhim and R. Y. Huang, "On the prediction of separation factor and permeability in the separation of binary mixtures by pervaporation," *Journal of Membrane Science*, vol. 46, no. 2, pp. 335–348, 1989. [Online]. Available: https://www.sciencedirect.com/science/article/pii/S0376738800803440

[133] H. Hachisuka, S. Goto, Y. Tsujita, A. Takizawa, T. Kinoshita, and M. Miyamoto, "Gas transport properties of cured polyalkoxysilylbutadiene," *Polymer*, vol. 31, no. 2, pp. 276–280, 1990. [Online]. Available: https://www.sciencedirect.com/science/article/pii/003238619090119J

[134] M. Laguna, J. Guzmán, and E. Riande, "Transport of carbon dioxide in linear low-density polyethylene determined by permeation measurements and nmr

spectroscopy," *Polymer*, vol. 42, no. 9, pp. 4321–4327, 2001. [Online]. Available: https://www.sciencedirect.com/science/article/pii/S0032386100008090

[135] X. Gong, A. Bandis, A. Tao, G. Meresi, Y. Wang, P. Inglefield, A. Jones, and W.-Y. Wen, "Self-diffusion of water, ethanol and decafluropentane in perfluorosulfonate ionomer by pulse field gradient nmr," *Polymer*, vol. 42, no. 15, pp. 6485–6492, 2001. [Online]. Available: https://www.sciencedirect.com/science/article/pii/S0032386101001197

[136] J.-P. Hsu and S.-H. Lin, "Diffusivity of solvent in a polymer solution—expansive free volume effect," *European Polymer Journal*, vol. 41, no. 5, pp. 1036–1042, 2005. [Online]. Available: https://www.sciencedirect.com/science/article/pii/S0014305704004331

[137] A. Abbasi, M. Z. Saghir, and M. Kawaji, "An improved thermodiffusion model for ternary mixtures using fujita's free volume theory," vol. 36, no. 3, pp. 259–272, 2011. [Online]. Available: https://doi.org/10.1515/JNETDY.2011.016

[138] H. Liu, C. M. Silva, and E. A. Macedo, "Generalised free-volume theory for transport properties and new trends about the relationship between free volume and equations of state," *Fluid Phase Equilibria*, vol. 202, no. 1, pp. 89–107, 2002. [Online]. Available: https://www.sciencedirect.com/science/article/pii/S0378381202000833

[139] A. W. Thornton, K. M. Nairn, A. J. Hill, and J. M. Hill, "New relation between diffusion and free volume: I. predicting gas diffusion," *Journal of Membrane Science*, vol. 338, no. 1, pp. 29–37, 2009. [Online]. Available: https://www.sciencedirect.com/science/article/pii/S0376738809002555

[140] H. Ohashi, T. Ito, and T. Yamaguchi, "Prediction of self-diffusivity in multicomponent polymeric systems using shell-like free volume theory," *Industrial & Engineering Chemistry Research*, vol. 49, no. 22, pp. 11 676–11 681, 2010. [Online]. Available: https://doi.org/10.1021/ie101299q

[141] A. W. Thornton, K. M. Nairn, A. J. Hill, J. M. Hill, and Y. Huang, "New relation between diffusion and free volume: Ii. predicting vacancy diffusion,"

Journal of Membrane Science, vol. 338, no. 1, pp. 38–42, 2009. [Online]. Available: https://www.sciencedirect.com/science/article/pii/S0376738809002567

[142] Aspen Technology, *Aspen polymers - Polymer characterization and physical properties*, 8th ed., Aspen Technology, Burlington, MA, 12 2012.

[143] P. M. Mathias and T. W. Copeman, "Extension of the peng-robinson equation of state to complex mixtures: Evaluation of the various forms of the local composition concept," *Fluid Phase Equilibria*, vol. 13, pp. 91–108, 1983. [Online]. Available: https://www.sciencedirect.com/science/article/pii/0378381283800843

[144] P. A. Rodgers, "Pressure–volume–temperature relationships for polymeric liquids: A review of equations of state and their characteristic parameters for 56 polymers," *Journal of Applied Polymer Science*, vol. 48, no. 6, pp. 1061–1080, 1993. [Online]. Available: https://onlinelibrary.wiley.com/doi/abs/10.1002/app.1993.070480613

[145] S. M. Lambert, Y. Song, and J. M. Prausnitz, "14 equations of state for polymer systems," in *Equations of State for Fluids and Fluid Mixtures*, ser. Experimental Thermodynamics, J. Sengers, R. Kayser, C. Peters, and H. White, Eds. Elsevier, 2000, vol. 5, pp. 523–588. [Online]. Available: https://www.sciencedirect.com/science/article/pii/S1874564400800041

[146] J. E. Lennard-Jones and A. F. Devonshire, "Critical phenomena in gases - i," *Proceedings of the Royal Society of London. Series A - Mathematical and Physical Sciences*, vol. 163, no. 912, pp. 53–70, 1937. [Online]. Available: https://royalsocietypublishing.org/doi/abs/10.1098/rspa.1937.0210

[147] A. T. DiBenedetto, "Molecular properties of amorphous high polymers. i. a cell theory for amorphous high polymers," *Journal of Polymer Science Part A: General Papers*, vol. 1, no. 11, pp. 3459–3476, 1963. [Online]. Available: https://onlinelibrary.wiley.com/doi/abs/10.1002/pol.1963.100011116

[148] I. Prigogine, N. Trappeniers, and V. Mathot, "Statistical thermodynamics of r-mers and r-mer solutions," *Discussions of the Faraday Society*, vol. 15, pp. 93–107, 1953.

[149] I. Prigogine, *The molecular theory of solutions*. Amsterdam : North Holland Publishing Company, 1957.

[150] R. Simha and T. Somcynsky, "On the statistical thermodynamics of spherical and chain molecule fluids," *Macromolecules*, vol. 2, no. 4, pp. 342–350, 1969. [Online]. Available: https://doi.org/10.1021/ma60010a005

[151] C. Zhong, W. Wang, and H. Lu, "Simplified hole theory equation of state for polymer liquids," *Fluid Phase Equilibria*, vol. 86, pp. 137–146, 1993. [Online]. Available: https://www.sciencedirect.com/science/article/pii/037838129387172W

[152] W. Chapman, K. Gubbins, G. Jackson, and M. Radosz, "Saft: Equation-of-state solution model for associating fluids," *Fluid Phase Equilibria*, vol. 52, pp. 31–38, 1989. [Online]. Available: https://www.sciencedirect.com/science/article/pii/0378381289803085

[153] W. G. Chapman, K. E. Gubbins, G. Jackson, and M. Radosz, "New reference equation of state for associating liquids," *Industrial & Engineering Chemistry Research*, vol. 29, no. 8, pp. 1709–1721, 1990. [Online]. Available: https://doi.org/10.1021/ie00104a021

[154] D. Liu, H. Li, M. S. Noon, and D. L. Tomasko, "CO_2-induced pmma swelling and multiple thermodynamic property analysis using sanchez–lacombe eos," *Macromolecules*, vol. 38, no. 10, pp. 4416–4424, 2005. [Online]. Available: https://doi.org/10.1021/ma047319e

[155] R. S. Prabhakar, M. G. De Angelis, G. C. Sarti, B. D. Freeman, and M. C. Coughlin, "Gas and vapor sorption, permeation, and diffusion in poly(tetrafluoroethylene-co-perfluoromethyl vinyl ether)," *Macromolecules*, vol. 38, no. 16, pp. 7043–7055, 2005. [Online]. Available: https://doi.org/10.1021/ma050546b

[156] C. Nicolas, E. Neau, S. Meradji, and I. Raspo, "The sanchez–lacombe lattice fluid model for the modeling of solids in supercritical fluids," *Fluid Phase Equilibria*, vol. 232, no. 1, pp. 219 – 229, 2005. [Online]. Available: http://www.sciencedirect.com/science/article/pii/S0378381205000671

[157] I. Sanchez, "Statistical thermodynamics of bulk and surface properties of polymer

mixtures," *Journal of Macromolecular Science, Part B*, vol. 17, no. 3, pp. 565–589, 1980. [Online]. Available: https://doi.org/10.1080/00222348008212827

[158] J. K. Lee, S. X. Yao, G. Li, M. B. G. Jun, and P. C. Lee, "Measurement methods for solubility and diffusivity of gases and supercritical fluids in polymers and its applications," *Polymer Reviews*, vol. 57, no. 4, pp. 695–747, 2017. [Online]. Available: https://doi.org/10.1080/15583724.2017.1329209

[159] M. Minelli and M. G. De Angelis, "An equation of state (eos) based model for the fluid solubility in semicrystalline polymers," *Fluid Phase Equilibria*, vol. 367, pp. 173 – 181, 2014. [Online]. Available: http://www.sciencedirect.com/science/article/pii/S0378381214000491

[160] C. E. Rogers, *Permeation of gases and vapours in polymers*. Dordrecht: Springer Netherlands, 1985, pp. 11–73. [Online]. Available: https://doi.org/10.1007/978-94-009-4858-7_2

[161] B. Flaconnèche, J. Martin, and M. Klopffer, "Permeability, diffusion and solubility of gases in polyethylene, polyamide 11 and poly (vinylidene fluoride)," *Oil & Gas Science and Technology-revue De L Institut Francais Du Petrole - OIL GAS SCI TECHNOL*, vol. 56, pp. 261–278, 05 2001.

[162] G. Clarizia, C. Algieri, and E. Drioli, "Filler-polymer combination: A route to modify gas transport properties of a polymeric membrane," *Polymer*, vol. 45, no. 16, pp. 5671–5681, 2004. [Online]. Available: https://www.sciencedirect.com/science/article/pii/S0032386104005737

[163] Y. Sato, K. Fujiwara, T. Takikawa, Sumarno, S. Takishima, and H. Masuoka, "Solubilities and diffusion coefficients of carbon dioxide and nitrogen in polypropylene, high-density polyethylene, and polystyrene under high pressures and temperatures," *Fluid Phase Equilibria*, vol. 162, no. 1, pp. 261–276, 1999. [Online]. Available: https://www.sciencedirect.com/science/article/pii/S0378381299002174

[164] J. Park and D. Paul, "Correlation and prediction of gas permeability in glassy polymer membrane materials via a modified free volume based group contribution method,"

Journal of Membrane Science, vol. 125, no. 1, pp. 23–39, 1997. [Online]. Available: https://www.sciencedirect.com/science/article/pii/S0376738896000610

[165] L. Ansaloni, M. Minelli, M. Giacinti Baschetti, and G. Sarti, "Effect of relative humidity and temperature on gas transport in matrimid®: Experimental study and modeling," *Journal of Membrane Science*, vol. 471, pp. 392–401, 2014. [Online]. Available: https://www.sciencedirect.com/science/article/pii/S0376738814006358

[166] J. L. Lundberg, "Diffusivities and solubilities of methane in linear polyethylene melts," *Journal of Polymer Science Part A: General Papers*, vol. 2, no. 9, pp. 3925–3931, 1964. [Online]. Available: https://onlinelibrary.wiley.com/doi/abs/10.1002/pol.1964.100020909

[167] Y. Naito, K. Mizoguchi, K. Terada, and Y. Kamiya, "The effect of pressure on gas permeation through semicrystalline polymers above the glass transition temperature," *Journal of Polymer Science Part B: Polymer Physics*, vol. 29, no. 4, pp. 457–462, 1991. [Online]. Available: https://onlinelibrary.wiley.com/doi/abs/10.1002/polb.1991.090290408

[168] Y. Naito, Y. Kamiya, K. Terada, K. Mizoguchi, and J. S. Wang, "Pressure dependence of gas permeability in a rubbery polymer," *Journal of Applied Polymer Science*, vol. 61, no. 6, pp. 945–950, 1996. [Online]. Available: https://onlinelibrary.wiley.com/doi/abs/10.1002/%28SICI%291097-4628%2819960808%2961%3A6%3C945%3A%3AAID-APP8%3E3.0.CO%3B2-H

[169] A. S. Michaels and R. B. Parker Jr., "Sorption and flow of gases in polyethylene," *Journal of Polymer Science*, vol. 41, no. 138, pp. 53–71, 1959. [Online]. Available: https://onlinelibrary.wiley.com/doi/abs/10.1002/pol.1959.1204113805

[170] A. Peterlin, "Dependence of diffusive transport on morphology of crystalline polymers," *Journal of Macromolecular Science, Part B*, vol. 11, no. 1, pp. 57–87, 1975. [Online]. Available: https://doi.org/10.1080/00222347508217855

[171] C. H. Klute, "Diffusion of small molecules in semicrystalline polymers: Water in polyethylene," *Journal of Applied Polymer Science*, vol. 1, no. 3, pp. 340–350, 1959. [Online]. Available: https://onlinelibrary.wiley.com/doi/abs/10.1002/app.1959.070010312

[172] J. L. Budzien, J. D. McCoy, D. H. Weinkauf, R. A. LaViolette, and E. S. Peterson, "Solubility of gases in amorphous polyethylene," *Macromolecules*, vol. 31, no. 10, pp. 3368–3371, 1998. [Online]. Available: https://doi.org/10.1021/ma971786x

[173] A. S. Michaels and H. J. Bixler, "Flow of gases through polyethylene," *Journal of Polymer Science*, vol. 50, no. 154, pp. 413–439, 1961. [Online]. Available: https://onlinelibrary.wiley.com/doi/abs/10.1002/pol.1961.1205015412

[174] B. Flaconnèche, J. Martin, and M. Klopffer, "Transport properties of gases in polymers: Experimental methods," *Oil & Gas Science and Technology-revue De L Institut Francais Du Petrole - OIL GAS SCI TECHNOL*, vol. 56, pp. 245–259, 05 2001.

[175] R. Felder and G. Huvard, "17. permeation, diffusion, and sorption of gases and vapors," in *Polymers*, ser. Methods in Experimental Physics, R. Fava, Ed. Academic Press, 1980, vol. 16, pp. 315–377. [Online]. Available: https://www.sciencedirect.com/science/article/pii/S0076695X08605360

[176] Y. Kamiya, T. Hirose, K. Mizoguchi, and Y. Naito, "Gravimetric study of high-pressure sorption of gases in polymers," *Journal of Polymer Science Part B: Polymer Physics*, vol. 24, no. 7, pp. 1525–1539, 1986. [Online]. Available: https://onlinelibrary.wiley.com/doi/abs/10.1002/polb.1986.090240711

[177] B. I. Chaudhary and A. I. Johns, "Solubilities of nitrogen, isobutane and carbon dioxide in polyethylene," *Journal of Cellular Plastics*, vol. 34, no. 4, pp. 312–328, 1998. [Online]. Available: https://doi.org/10.1177/0021955X9803400403

[178] A. S. Michaels, W. R. Vieth, and J. A. Barrie, "Diffusion of gases in polyethylene terephthalate," *Journal of Applied Physics*, vol. 34, no. 1, pp. 13–20, 1963. [Online]. Available: https://doi.org/10.1063/1.1729054

[179] W. Vieth, J. Howell, and J. Hsieh, "Dual sorption theory," *Journal of Membrane Science*, vol. 1, pp. 177–220, 1976. [Online]. Available: https://www.sciencedirect.com/science/article/pii/S037673880082267X

[180] W. J. Koros and D. R. Paul, "Design considerations for measurement of gas sorption in polymers by pressure decay," *Journal of Polymer Science: Polymer Physics Edition*, vol. 14, no. 10, pp. 1903–1907, 1976. [Online]. Available: https://onlinelibrary.wiley.com/doi/abs/10.1002/pol.1976.180141014

[181] ——, "CO_2 sorption in poly(ethylene terephthalate) above and below the glass transition," *Journal of Polymer Science: Polymer Physics Edition*, vol. 16, no. 11, pp. 1947–1963, 1978. [Online]. Available: https://onlinelibrary.wiley.com/doi/abs/10.1002/pol.1978.180161105

[182] S. A. Stern and A. H. De Meringo, "Solubility of carbon dioxide in cellulose acetate at elevated pressures," *Journal of Polymer Science: Polymer Physics Edition*, vol. 16, no. 4, pp. 735–751, 1978. [Online]. Available: https://onlinelibrary.wiley.com/doi/abs/10.1002/pol.1978.180160415

[183] W. J. Koros, "Model for sorption of mixed gases in glassy polymers," *Journal of Polymer Science: Polymer Physics Edition*, vol. 18, no. 5, pp. 981–992, 1980. [Online]. Available: https://onlinelibrary.wiley.com/doi/abs/10.1002/pol.1980.180180506

[184] P. K. Davis, G. D. Lundy, J. E. Palamara, J. L. Duda, and R. P. Danner, "New pressure-decay techniques to study gas sorption and diffusion in polymers at elevated pressures," *Industrial & Engineering Chemistry Research*, vol. 43, no. 6, pp. 1537–1542, 2004. [Online]. Available: https://doi.org/10.1021/ie034075y

[185] D. Li, T. Liu, L. Zhao, and W. Yuan, "Solubility and diffusivity of carbon dioxide in solid-state isotactic polypropylene by the pressure-decay method," *Industrial & Engineering Chemistry Research*, vol. 48, no. 15, pp. 7117–7124, 2009. [Online]. Available: https://doi.org/10.1021/ie8019483

[186] M. W. Fitch, W. J. Koros, R. L. Nolen, and J. R. Carnes, "Permeation of several gases through elastomers, with emphasis on the deuterium/hydrogen pair," *Journal of Applied Polymer Science*, vol. 47, no. 6, pp. 1033–1046, 1993. [Online]. Available: https://onlinelibrary.wiley.com/doi/abs/10.1002/app.1993.070470610

[187] S. A. Stern, G. R. Mauze, and H. L. Frisch, "Tests of a free-volume model for the permeation of gas mixtures through polymer membranes. CO_2-C_2H_4, CO_2-C_3H_8, and C_2H_4-C_3H_8 mixtures in polyethylene," *Journal of Polymer Science: Polymer Physics Edition*, vol. 21, no. 8, pp. 1275–1298, 1983. [Online]. Available: https://onlinelibrary.wiley.com/doi/abs/10.1002/pol.1983.180210802

[188] R. T. Chern, W. J. Koros, B. Yui, H. B. Hopfenberg, and V. T. Stannett, "Selective permeation of CO_2 and CH_4 through kapton polyimide: Effects of penetrant competition and gas-phase nonideality," *Journal of Polymer Science: Polymer Physics Edition*, vol. 22, no. 6, pp. 1061–1084, 1984. [Online]. Available: https://onlinelibrary.wiley.com/doi/abs/10.1002/pol.1984.180220610

[189] L. M. Costello and W. J. Koros, "Temperature dependence of gas sorption and transport properties in polymers: measurement and applications," *Industrial & engineering chemistry research*, vol. 31, no. 12, pp. 2708–2714, 1992.

[190] E. Sada, H. Kumazawa, P. Xu, and S.-T. Wang, "Permeation of mixed gases in glassy polymer membranes," *Journal of Applied Polymer Science*, vol. 40, no. 7-8, pp. 1391–1399, 1990. [Online]. Available: https://onlinelibrary.wiley.com/doi/abs/10.1002/app.1990.070400725

[191] E. Sada, H. Kumazawa, and J.-S. Wang, "Permeation of binary gas mixture through glassy polymer membranes with concentration-dependent diffusivities," *Journal of Polymer Science Part B: Polymer Physics*, vol. 30, no. 1, pp. 105–111, 1992. [Online]. Available: https://onlinelibrary.wiley.com/doi/abs/10.1002/polb.1992.090300111

[192] L. M. Costello and W. J. Koros, "Comparison of pure and mixed gas carbon dioxide and methane permeabilities in polycarbonate: effect of temperature," *Industrial*

& Engineering Chemistry Research, vol. 32, no. 10, pp. 2277–2280, 1993. [Online]. Available: https://doi.org/10.1021/ie00022a012

[193] Direct Plastics. (2021) PTFE - material data sheet. [Online]. Available: https://www.directplastics.co.uk/pub/pdf/datasheets/PTFE%20Data%20Sheet.pdf

[194] ——. (2021) HDPE natural - material data sheet. [Online]. Available: https://www.directplastics.co.uk/pub/pdf/datasheets/HDPE%20Natural%20Data%20Sheet.pdf

[195] Y. Kong and J. Hay, "The measurement of the crystallinity of polymers by dsc," *Polymer*, vol. 43, no. 14, pp. 3873–3878, 2002. [Online]. Available: https://www.sciencedirect.com/science/article/pii/S0032386102002355

[196] M. Keating, L. Malone, and W. Saunders, "Annealing effect on semi-crystalline materials in creep behavior," *Journal of Thermal Analysis and Calorimetry*, vol. 69, no. 1, pp. 37 – 52, 25 Jul. 2002. [Online]. Available: https://akjournals.com/view/journals/10973/69/1/article-p37.xml

[197] S. Z. Cheng, *Handbook of thermal analysis and calorimetry: applications to polymers and plastics*. Elsevier, 2002.

[198] F. Sarrasin, P. Memari, M. Klopffer, V. Lachet, C. T. Condat, B. Rousseau, and E. Espuche, "Influence of high pressures on CH_4, CO_2 and H_2S solubility in polyethylene: Experimental and molecular simulation approaches for pure gas and gas mixtures. modelling of the sorption isotherms," *J. Membr. Sci.*, vol. 490, pp. 380 – 388, 2015. [Online]. Available: http://www.sciencedirect.com/science/article/pii/S0376738815003713

[199] R. E. Kesting and A. K. Fritzsche, *Polymeric gas separation membranes*. New York ; Chichester: Wiley & Sons, 1993.

[200] U. Parasu Veera, "Mass transport models for a single particle in gas-phase propylene polymerisation," *Chem. Eng. Sci.*, vol. 58, no. 9, pp. 1765 – 1775, 2003. [Online]. Available: http://www.sciencedirect.com/science/article/pii/S0009250903000058

[201] J. Adewole, L. Jensen, U. Al-Mubaiyedh, N. von Solms, and I. Hussein, "Transport properties of natural gas through polyethylene nanocomposites at high temperature and pressure," *J. Polym. Res.*, vol. 19, 02 2012.

[202] B. Craster and T. Jones, "Permeation of a range of species through polymer layers under varying conditions of temperature and pressure: In situ measurement methods," *Polymers (Basel)*, vol. 11, no. 6, p. 1056, 06 2019.

[203] A. Kreituss and H. L. Frisch, "Free-volume estimates in heterogeneous polymer systems. i. diffusion in crystalline ethylene–propylene copolymers," *J. Polym. Sci. Polym. Phys. Ed.*, vol. 19, no. 5, pp. 889–905, 1981. [Online]. Available: https://onlinelibrary.wiley.com/doi/abs/10.1002/pol.1981.180190515

[204] M. J. Hayes and G. S. Park, "The diffusion of benzene in rubber. part 2.—high concentration of benzene," *Trans. Faraday Soc.*, vol. 52, pp. 949–955, 1956. [Online]. Available: http://dx.doi.org/10.1039/TF9565200949

[205] S. A. Stern, S. S. Kulkarni, and H. L. Frisch, "Tests of a "free-volume" model of gas permeation through polymer membranes. i. pure CO_2, CH_4, C_2H_4, and C_3H_8 in polyethylene," *J. Polym. Sci. Polym. Phys. Ed.*, vol. 21, no. 3, pp. 467–481, 1983. [Online]. Available: https://onlinelibrary.wiley.com/doi/abs/10.1002/pol.1983.180210311

[206] E. Sada, H. Kumazawa, P. Xu, and H. Nishikawa, "Gas transport in rubbery polymers," *J. Appl. Polym. Sci.*, vol. 33, no. 8, pp. 3037–3044, 1987. [Online]. Available: https://onlinelibrary.wiley.com/doi/abs/10.1002/app.1987.070330835

[207] W. A. Rogers, R. S. Buritz, and D. Alpert, "Diffusion coefficient, solubility, and permeability for helium in glass," *J. Appl. Phys.*, vol. 25, no. 7, pp. 868–875, 1954. [Online]. Available: https://doi.org/10.1063/1.1721760

[208] C. S. Venable and T. Fuwa, "The solubility of gases in rubber and rubber stock and effect of solubility on penetrability," *Journal of Industrial & Engineering Chemistry*, vol. 14, no. 2, pp. 139–142, 1922. [Online]. Available: https://doi.org/10.1021/ie50146a022

[209] P. L. Durrill and R. G. Griskey, "Diffusion and solution of gases into thermally softened or molten polymers: Part ii. relation of diffusivities and solubilities with temperature pressure and structural characteristics," *AIChE Journal*, vol. 15, no. 1, pp. 106–110, 1969. [Online]. Available: https://aiche.onlinelibrary.wiley.com/doi/abs/10.1002/aic.690150124

[210] R. G. Wissinger and M. E. Paulaitis, "Swelling and sorption in polymer–CO_2 mixtures at elevated pressures," *Journal of Polymer Science Part B: Polymer Physics*, vol. 25, no. 12, pp. 2497–2510, 1987. [Online]. Available: https://onlinelibrary.wiley.com/doi/abs/10.1002/polb.1987.090251206

[211] R. Soleimani, A. H. Saeedi Dehaghani, A. Rezai-Yazdi, S. A. Hosseini, S. P. Hosseini, and A. Bahadori, "Evolving an accurate decision tree-based model for predicting carbon dioxide solubility in polymers," *Chemical Engineering & Technology*, vol. 43, no. 3, pp. 514–522, 2020. [Online]. Available: https://onlinelibrary.wiley.com/doi/abs/10.1002/ceat.201900096

[212] J. M. Prausnitz, "Regular solution theory for gas-liquid solutions," *AIChE Journal*, vol. 4, no. 3, pp. 269–272, 1958. [Online]. Available: https://aiche.onlinelibrary.wiley.com/doi/abs/10.1002/aic.690040307

[213] C. P. Ribeiro and B. D. Freeman, "Sorption, dilation, and partial molar volumes of carbon dioxide and ethane in cross-linked poly(ethylene oxide)," *Macromolecules*, vol. 41, no. 23, pp. 9458–9468, 2008. [Online]. Available: https://doi.org/10.1021/ma801478c

[214] Y. Wang, Y. Yang, and M. Tao, "Understanding free volume characteristics of ethylene-propylene-diene monomer (epdm) through molecular dynamics simulations," *Materials*, vol. 12, p. 612, 02 2019.

[215] Y. Sato, T. Takikawa, A. Sorakubo, S. Takishima, H. Masuoka, and M. Imaizumi, "Solubility and diffusion coefficient of carbon dioxide in biodegradable polymers," *Industrial & Engineering Chemistry Research*, vol. 39, no. 12, pp. 4813–4819, 2000. [Online]. Available: https://doi.org/10.1021/ie0001220

[216] J. Chen, T. Liu, W. Yuan, and L. Zhao, "Solubility and diffusivity of CO_2 in polypropylene/micro-calcium carbonate composites," *The Journal of Supercritical Fluids*, vol. 77, pp. 33–43, 2013. [Online]. Available: https://www.sciencedirect.com/science/article/pii/S0896844613000685

[217] I. Ushiki, S. Hayashi, S. ichi Kihara, and S. Takishima, "Solubilities and diffusion coefficients of carbon dioxide and nitrogen in poly(methyl methacrylate) at high temperatures and pressures," *The Journal of Supercritical Fluids*, vol. 152, p. 104565, 2019. [Online]. Available: https://www.sciencedirect.com/science/article/pii/S0896844619302360

[218] I. Ushiki, Y. Yoshino, S. Hayashi, S. ichi Kihara, and S. Takishima, "Measurement and modeling of solubilities and diffusion coefficients of carbon dioxide in poly(ethylene-co-acrylic acid)," *The Journal of Supercritical Fluids*, vol. 158, p. 104733, 2020. [Online]. Available: https://www.sciencedirect.com/science/article/pii/S0896844619307351

[219] C. Guo and D. de Kee, "Effect of molecular size and free volume on diffusion in liquids," *Chemical Engineering Science*, vol. 46, no. 8, pp. 2133 – 2141, 1991. [Online]. Available: http://www.sciencedirect.com/science/article/pii/000925099180171T

[220] C. Yeom and R. Huang, "A new method for determining the diffusion coefficients of penetrants through polymeric membranes from steady state pervaporation experiments," *Journal of Membrane Science*, vol. 68, no. 1, pp. 11 – 20, 1992. [Online]. Available: http://www.sciencedirect.com/science/article/pii/037673889280146B

[221] M. L. Williams, R. F. Landel, and J. D. Ferry, "The temperature dependence of relaxation mechanisms in amorphous polymers and other glass-forming liquids," *Journal of the American Chemical Society*, vol. 77, no. 14, pp. 3701–3707, 1955. [Online]. Available: https://doi.org/10.1021/ja01619a008

[222] R. Simha and R. F. Boyer, "On a general relation involving the glass temperature and coefficients of expansion of polymers," *The Journal of Chemical Physics*, vol. 37, no. 5, pp. 1003–1007, 1962. [Online]. Available: https://doi.org/10.1063/1.1733201

[223] F. A. Quinn and L. Mandelkern, "Thermodynamics of crystallization in high polymers: poly-(ethylene)," *Journal of the American Chemical Society*, vol. 80, no. 13, pp. 3178–3182, 1958. [Online]. Available: https://doi.org/10.1021/ja01546a003

[224] F. C. Stehling and L. Mandelkern, "The glass temperature of linear polyethylene," *Macromolecules*, vol. 3, no. 2, pp. 242–252, 1970. [Online]. Available: https://doi.org/10.1021/ma60014a023

[225] Y. Tsujita, T. Nose, and T. Hata, "Thermodynamic properties of polyethylene and eicosane. i. p–v–t relations and internal pressure," *Polymer Journal*, vol. 3, no. 5, pp. 581–586, 1972.

[226] D. Isăcescu, I. Ionescu, M. Leca, C. Roncea, D. Mihăţă, and E. Rizescu, "Studies in the field of polyethylene—v. correlations between compressibility, crystallinity and molecular weight of high pressure natural polyethylenes," *European Polymer Journal*, vol. 7, no. 7, pp. 913 – 932, 1971. [Online]. Available: http://www.sciencedirect.com/science/article/pii/0014305771900553

[227] T. Hatakeyama, T. Hashimoto, and H. Kanetsuna, "Compressibility of polyethylene under pressure up to 5000 kg/cm2," *Colloid and polymer science*, vol. 252, no. 1, pp. 15–19, 1974.

[228] T. Ito, "Compressibility of the polymer crystal," *Polymer*, vol. 23, no. 10, pp. 1412–1434, 1982. [Online]. Available: https://www.sciencedirect.com/science/article/pii/0032386182902397

[229] M. Lorenzen, M. Hanfland, and A. Mermet, "Poly(tetrafluoroethylene) under pressure: X-diffraction studies," *Nuclear Instruments and Methods in Physics Research Section B: Beam Interactions with Materials and Atoms*, vol. 200, pp. 416–420, 2003, proceedings of the E-MRS 2002 Symposium I on Synchrotron Radiation and Materials Science. [Online]. Available: https://www.sciencedirect.com/science/article/pii/S0168583X02017329

[230] K. Gauter and R. A. Heidemann, "Modeling polyethylene-solvent mixtures with the sanchez–lacombe equation," *Fluid Phase Equilibria*, vol. 183-184, pp. 87 – 97,

2001, proceedings of the fourteenth symposium on thermophysical properties. [Online]. Available: http://www.sciencedirect.com/science/article/pii/S037838120100423X

[231] M. A. Bashir, M. Al-haj Ali, V. Kanellopoulos, J. Seppälä, E. Kokko, and S. Vijay, "The effect of pure component characteristic parameters on sanchez–lacombe equation-of-state predictive capabilities," *Macromolecular Reaction Engineering*, vol. 7, no. 5, pp. 193–204, 2013. [Online]. Available: https://onlinelibrary.wiley.com/doi/abs/10.1002/mren.201200054

[232] A. Kitagishi, S. Takizawa, Y. Sato, and H. Inomata, "Measurement and prediction of solubilities and diffusion coefficients of ethylene in rubbery propylene copolymers," *Fluid Phase Equilibria*, vol. 492, pp. 110 – 117, 2019. [Online]. Available: http://www.sciencedirect.com/science/article/pii/S0378381219301414

[233] M. L. Williams, J. S. Dickmann, J. C. Hassler, and E. Kiran, "Volumetric properties and solubility parameters of cyclohexane + CO_2 mixtures at high pressures and their modeling with the sanchez–lacombe equation of state," *Industrial & Engineering Chemistry Research*, vol. 56, no. 30, pp. 8748–8766, 2017. [Online]. Available: https://doi.org/10.1021/acs.iecr.7b01287

[234] D. R. Paul, "Gas sorption and transport in glassy polymers," *Berichte der Bunsengesellschaft für physikalische Chemie*, vol. 83, no. 4, pp. 294–302, 1979. [Online]. Available: https://onlinelibrary.wiley.com/doi/abs/10.1002/bbpc.19790830403

[235] R. A. Pasternak, M. V. Christensen, and J. Heller, "Diffusion and permeation of oxygen, nitrogen, carbon dioxide, and nitrogen dioxide through polytetrafluoroethylene," *Macromolecules*, vol. 3, no. 3, pp. 366–371, 1970. [Online]. Available: https://doi.org/10.1021/ma60015a020

[236] E. Aionicesei, M. Škerget, and e. Knez, "Measurement and modeling of the CO_2 solubility in poly(ethylene glycol) of different molecular weights," *Journal of Chemical & Engineering Data*, vol. 53, no. 1, pp. 185–188, 2008. [Online]. Available: https://doi.org/10.1021/je700467p

[237] Z. Chen, K. Cao, Z. Yao, and Z. Huang, "Modeling solubilities of subcritical and supercritical fluids in polymers with cubic and non-cubic equations of state," *The Journal of Supercritical Fluids*, vol. 49, no. 2, pp. 143–153, 2009. [Online]. Available: https://www.sciencedirect.com/science/article/pii/S0896844609000023

[238] J. Chen, T. Liu, L. Zhao, and W. Yuan, "Determination of CO_2 solubility in isotactic polypropylene melts with different polydispersities using magnetic suspension balance combined with swelling correction," *Thermochimica Acta*, vol. 530, pp. 79–86, 2012. [Online]. Available: https://www.sciencedirect.com/science/article/pii/S0040603111005958

[239] Z. Lei, H. Ohyabu, Y. Sato, H. Inomata, and R. L. Smith, "Solubility, swelling degree and crystallinity of carbon dioxide–polypropylene system," *The Journal of Supercritical Fluids*, vol. 40, no. 3, pp. 452–461, 2007. [Online]. Available: https://www.sciencedirect.com/science/article/pii/S0896844606002026

[240] M. A. Mukaddam, E. Litwiller, and I. Pinnau, "Gas sorption, diffusion, and permeation in nafion," 2015. [Online]. Available: http://hdl.handle.net/10754/596253

[241] K. Toi, G. Morel, and D. R. Paul, "Gas sorption and transport in poly(phenylene oxide) and comparisons with other glassy polymers," *Journal of Applied Polymer Science*, vol. 27, no. 8, pp. 2997–3005, 1982. [Online]. Available: https://onlinelibrary.wiley.com/doi/abs/10.1002/app.1982.070270823

[242] B. J. Story and W. J. Koros, "Sorption of CO_2/CH_4 mixtures in poly(phenylene oxide) and a carboxylated derivative," *Journal of Applied Polymer Science*, vol. 42, no. 9, pp. 2613–2626, 1991. [Online]. Available: https://onlinelibrary.wiley.com/doi/abs/10.1002/app.1991.070420926

[243] C. C. Hu, Y. J. Fu, K. R. Lee, R. C. Ruaan, and J. Y. Lai, "Effect of sorption behavior on transport properties of gases in polymeric membranes," *Polymer*, vol. 50, no. 22, pp. 5308–5313, 2009. [Online]. Available: https://www.sciencedirect.com/science/article/pii/S0032386109007915

[244] S. Areerat, Y. Hayata, R. Katsumoto, T. Kegasawa, H. Egami, and M. Ohshima, "Solubility of carbon dioxide in polyethylene/titanium dioxide composite under high pressure and temperature," *Journal of Applied Polymer Science*, vol. 86, no. 2, pp. 282–288, 2002. [Online]. Available: https://onlinelibrary.wiley.com/doi/abs/10.1002/app.10944

[245] Y. Li, C. Park, H. Li, and J. Wang, "Measurement of the pvt property of pp/co2 solution," *Fluid Phase Equilibria*, vol. 270, no. 1, pp. 15–22, 2008. [Online]. Available: https://www.sciencedirect.com/science/article/pii/S0378381208001830

[246] D. D. Liu and J. M. Prausnitz, "Solubilities of gases and volatile liquids in polyethylene and in ethylene-vinyl acetate copolymers in the region 125-225 °c," *Industrial & Engineering Chemistry Fundamentals*, vol. 15, no. 4, pp. 330–335, 1976. [Online]. Available: https://doi.org/10.1021/i160060a018

[247] N. Wang, K. Hattori, S. Takishima, and H. Masuoka, "Measurement and prediction of vapor-liquid equilibrium ratios for solutes at infinite dilution in CO_2+polyvinyl acetate system at high pressures," *KAGAKU KOGAKU RONBUNSHU*, vol. 17, no. 6, pp. 1138–1145, 1991.

[248] N. Wang, S. Ishida, S. Takishima, and H. Masuoka, "Sorption measurement of nitrogen in polystyrene at high pressure and its correlation by a modified dual-sorption model," *KAGAKU KOGAKU RONBUNSHU*, vol. 18, no. 2, pp. 226–232, 1992.

[249] F. Doghieri and G. C. Sarti, "Nonequilibrium lattice fluids: a predictive model for the solubility in glassy polymers," *Macromolecules*, vol. 29, no. 24, pp. 7885–7896, Jan. 1996.

[250] Y. Sato, M. Wang, S. Takishima, H. Masuoka, T. Watanabe, and Y. Fukasawa, "Solubility of butane and isobutane in molten polypropylene and polystyrene," *Polymer Engineering & Science*, vol. 44, no. 11, pp. 2083–2089, 2004. [Online]. Available: https://onlinelibrary.wiley.com/doi/abs/10.1002/pen.20213

[251] S. Kazarian, "Polymer processing with supercritical fluids," *Polymer science series CC/C of vysokomolekuliarnye soedineniia*, vol. 42, no. 1, pp. 78–101, 2000.

[252] S. P. Nalawade, F. Picchioni, and L. Janssen, "Supercritical carbon dioxide as a green solvent for processing polymer melts: Processing aspects and applications," *Progress in Polymer Science*, vol. 31, no. 1, pp. 19–43, 2006. [Online]. Available: https://www.sciencedirect.com/science/article/pii/S0079670005001085

[253] D. L. Tomasko, H. Li, D. Liu, X. Han, M. J. Wingert, L. J. Lee, and K. W. Koelling, "A review of CO_2 applications in the processing of polymers," *Industrial & Engineering Chemistry Research*, vol. 42, no. 25, pp. 6431–6456, 2003. [Online]. Available: https://doi.org/10.1021/ie030199z

[254] Y. P. Handa, J. Roovers, and F. Wang, "Effect of thermal annealing and supercritical fluids on the crystallization behavior of methyl-substituted poly(aryl ether ether ketone)," *Macromolecules*, vol. 27, no. 19, pp. 5511–5516, 1994. [Online]. Available: https://doi.org/10.1021/ma00097a035

[255] Z. Zhong, S. Zheng, and Y. Mi, "High-pressure dsc study of thermal transitions of a poly(ethylene terephthalate)/carbon dioxide system," *Polymer*, vol. 40, no. 13, pp. 3829–3834, 1999. [Online]. Available: https://www.sciencedirect.com/science/article/pii/S0032386198005941

[256] K. Mizoguchi, T. Hirose, Y. Naito, and Y. Kamiya, "CO_2−induced crystallization of poly(ethylene terephthalate)," *Polymer*, vol. 28, no. 8, pp. 1298–1302, 1987. [Online]. Available: https://www.sciencedirect.com/science/article/pii/0032386187904411

[257] S. Lambert and M. Paulaitis, "Crystallization of poly(ethylene terephthalate) induced by carbon dioxide sorption at elevated pressures," *The Journal of Supercritical Fluids*, vol. 4, no. 1, pp. 15–23, 1991, proceedings of the Symposium on Supercritical Fluids. [Online]. Available: https://www.sciencedirect.com/science/article/pii/0896844691900263

[258] S. G. Kazarian, N. H. Brantley, and C. A. Eckert, "Applications of vibrational spectroscopy to characterize poly(ethylene terephthalate) processed with supercritical CO_2," *Vibrational Spectroscopy*, vol. 19, no. 2, pp. 277–283, 1999. [Online]. Available: https://www.sciencedirect.com/science/article/pii/S0924203198000733

[259] X. Liao, A. V. Nawaby, and P. S. Whitfield, "Carbon dioxide-induced crystallization in poly(l-lactic acid) and its effect on foam morphologies," *Polymer International*, vol. 59, no. 12, pp. 1709–1718, 2010. [Online]. Available: https://onlinelibrary.wiley.com/doi/abs/10.1002/pi.2910

[260] Y. T. Shieh and Y. G. Lin, "Equilibrium solubility of CO_2 in rubbery eva over a wide pressure range: effects of carbonyl group content and crystallinity," *Polymer*, vol. 43, no. 6, pp. 1849–1856, 2002. [Online]. Available: https://www.sciencedirect.com/science/article/pii/S0032386101007765

[261] O. Fleming, K. Chan, and S. Kazarian, "FT-IR imaging and raman microscopic study of poly(ethylene terephthalate) film processed with supercritical CO_2," *Vibrational Spectroscopy*, vol. 35, no. 1, pp. 3–7, 2004, the 2nd International Conference on Advanced Vibrational Spectroscopy (ICAVS-2). [Online]. Available: https://www.sciencedirect.com/science/article/pii/S0924203103001437

[262] O. S. Fleming and S. G. Kazarian, "Confocal raman microscopy of morphological changes in poly(ethylene terephthalate) film induced by supercritical CO_2," *Applied Spectroscopy*, vol. 58, no. 4, pp. 390–394, 2004, pMID: 15104807. [Online]. Available: https://doi.org/10.1366/000370204773580211